Winter 2003

Numerical Study of Two-Dimensional Secondary Injection Into a Mach 3.5 Freestream

Stephen C. Coghill
Old Dominion University

NUMERICAL STUDY OF TWO-DIMENSIONAL SECONDARY INJECTION INTO A MACH 3.5 FREESTREAM

by

Stephen C. Coghill
B.S. August 1999, Old Dominion University

A Thesis Submitted to the Faculty of
Old Dominion University in Partial Fulfillment of the
Requirement for the Degree of

MASTER OF SCIENCE

MECHANICAL ENGINEERING

OLD DOMINION UNIVERSITY
December 2003

Approved by:

Dr. Surendra N. Tiwari (Director)

Dr. Taj O. Mohieldin (Co-Director)

Dr. Sushil K. Chaturvedi (Member)

ABSTRACT

NUMERICAL STUDY OF TWO-DIMENSIONAL SECONDARY INJECTION INTO A MACH 3.5 FREESTREAM

Stephen C. Coghill
Old Dominion University, 2003
Director: Dr. Surendra N. Tiwari
Co-Director: Dr. Taj O. Mohieldin

Upstream interaction within a dual-mode scramjet engine is investigated numerically. The upstream interaction is investigated by increasing the freestream-to-injector pressure ratio. The constant area duct and sudden expansion geometries are used to achieve these results. Analysis using the symmetry boundary condition is compared to the full boundary condition for the constant area duct. Numerical analysis of the Mach 3.5 freestream is conducted using normal sonic injection of nitrogen gas to create the upstream interaction. Comparisons, where applicable, are made to experimental results. Due to the high speed of the flowfield, oblique shockwaves are present causing numerical convergence difficult to achieve. The flowfield symmetry assumptions break down due to the high shear stresses present in the boundary layer separation region. As the freestream-to-injector pressure ratio is increased this separation region begins to move upstream within the isolator region. This study proves that the upstream interaction is not related to reacting flows, but rather to the high turbulent shear stresses that are present in the boundary layer separation regions.

ACKNOWLEDGMENTS

I would like to give my appreciation to all my professors who encouraged and helped me through my undergraduate and graduate years here at Old Dominion University. Without them my future as an engineer would have never been possible.

I would like to thank my committee members for their support and encouragement. I would not have been able to progress this far if it were not for my co-advisor Dr. Taj O. Mohieldin. He has encouraged, taught, and guided me since I was an undergraduate student in the Mechanical Engineering Technology program. It has been a great pleasure and experience to study under Dr. Surendra N. Tiwari. He was my instructor for a majority of my graduate classes and I must say that I am honored to have learned from a great scholar. I would also like to thank Dr. Sushil K. Chaturvedi for being a member of my committee.

I want to thank all my friends that have been there to answer my questions and gave me their valuable advice. I express my thanks and love to my mother and father for being there and supporting me. I want to thank my wife, Heidi, for supporting me through my studies and understanding the late nights that I had to stay up to finish this study. While finishing this study my beautiful daughter Kathyraine Mae was born. She has filled my life with fulfillment and joy.

This study has been supported by the NASA Langley Research Center in Hampton, Virginia through the Old Dominion University Research Foundation under NASA Grant NAG-1-2266. The grant, given by the Hyper-X Program Office at NASA/LaRC, supported students conducting numerical simulations of mixing and combustion in scramjet engines.

TABLE OF CONTENTS

LIST OF TABLES

LIST OF FIGURES

NOMENCLATURE

Symbol	
CAD	Computer Aided Drafting
CFD	Computational Fluid Dynamics
CFL	Courant number
DOS	Disk Operated System
E	Internal energy
$\vec{F}$	External body force(s)
$\vec{g}$	Gravity
G_b	Generation of turbulence kinetic energy due to buoyancy
G_k	Generation of turbulence kinetic energy due to the mean velocity gradients
H	Hydrogen
h	Enthalpy
$\vec{J}_j$	Diffusion flux of species j
JNAL	Japan National Aerospace Laboratory
K	Temperature
kPa	Pressure
LES	Large Eddy Simulation
M	Mach number
Menter BSL	Turbulence model
Menter SST	Turbulence model
N	Nitrogen
NAL	National Aerospace Laboratory
NASA	National Aeronautics and Space Administration
O	Oxygen
P	Pressure
R_i	Net rate of production by chemical reaction
RNG	Turbulence model
Scramjet	Supersonic combustion ramjet

S_i	Rate of creation from the dispersed phase
S_ε	user-defined source term
S_κ	user-defined source terms
VULCAN	Viscous Upwind aLgorithm for Complex flow ANalysis
Y_i	Local mass fraction for each species
Y_M	Contribution of the fluctuating dilation in compressible turbulence to the overall dissipation rate

Subscripts

2	Number of atoms
back	Backpressure
j	Jet
t	Total or stagnation
total	Total
o	Stagnation or total
s	Static

Superscripts

1	Reference number
°	Degrees

Greek

$\kappa-\varepsilon$	Turbulence model
κ_{eff}	Effective conductivity
$q-\omega$	Turbulence model
$\vec{\upsilon}$	Mass average velocity vector
ρ	Density
$\bar{\bar{\tau}}$	Stress tensor
$\propto_\varepsilon$	inverse effective Prandtl numbers for ε
$\propto_\kappa$	inverse effective Prandtl numbers for κ

SECTION 1

INTRODUCTION

1.1 Motivation*

Ever since the Wright brothers took off in their engine-powered airplane one hundred years ago, man has continued to conquer and push the envelope of speed and altitude in aviation. Much has been accomplished since that time. During World War II the jet engine was designed and tested and eventually put into production. The jet engine allowed man to climb to new heights in conquering the quest for speed. Much research was put into the jet engine during this period. Through research, the design of the jet engine allowed aviator's to push the envelope to crack the sound barrier. This was a major breakthrough since scientists at that time thought this was impossible to accomplish. From the 1940's through the 1950's, major research and experimentation was conducted in aeronautics to go faster than anyone had ever thought. The SR-71, which was designed in the 1950's, still holds the speed record for an air-breathing engine at over Mach 3. Sources say that a scramjet-powered engine would propel an aircraft from New York City to Japan in 1.5 hours. With aircraft like this, business transactions would help boost the economy and decrease package delivery time.

Supersonic combustion research has been conducted at NASA Langley Research Center since 1960.[1] At hypersonic speeds, the performance of the engine decreases due to the effects of real gases and other losses. Also, due to high temperatures and pressures, structural integrity begins to fail. So to prevent this from happening the design must be so that the speed of air entering the scramjet engine is at supersonic speed. Some of the major difficulties encountered through experimental research of the scramjet engine are mixing efficiency and complete combustion of the fuel. NASA has studied hypersonic air breathing propulsion for nearly 60 years.[2-6] The quest was to conquer hypersonic flight through the utilization of the "scramjet" engine, otherwise known as the supersonic combustion ramjet engine. The advantage

* The AIAA Journal format has been followed in preparing this thesis.

of the scramjet engine is that, like the turbo jet engine, it has no moving. It uses the oxygen in the atmosphere as the oxidizer and the aircraft carries the fuel. This allows the aircraft to fly faster and farther. Many tests have been performed on the scramjet engine. However, due to the fact that these experiments have been conducted on the ground, inaccurate results can occur. Because a scramjet engine performs high in the atmosphere, there are different boundary conditions as opposed to ground boundary conditions. The inaccuracy can affect combustion, boundary layer formation, and fuel mixing characteristics.

Computational Fluid Dynamics, otherwise known as "CFD", has been used extensively in the research of scramjet technology.[4] Without CFD the amount of money to conduct research in this area would be astronomical. Currently, CFD has been used to validify experimental results. Getting accurate results through CFD allows engineers to create experiments through CFD, and to cut down the costs of setting up and performing the actual experiments.

The motivation of this study is to show that the complex flowfield can be understood more completely and that the upstream interaction, due to boundary layer separation, is not related to reacting flows. Now that computers have grown faster in CPU speed and are capable of holding more memory, computation of these complex flowfields can be shown more clearly. As a result, computational time is reduced and more cases or models can be conducted.

1.2 Background of the Study

1.2.1 Review of Research

During operation of the scramjet engine there are various operating conditions such as startup, mid-range, and full power operation. Here we will concentrate on the mid-range aspect of the scramjet engine. The term used during the mid-range operation is known as "dual mode". Dual mode means that there is a transition between the subsonic and supersonic conditions within the combustor during flight. There has been much research concerning the dual mode combustor.[7-13] In Japan there has been research on the scramjet engine.[7, 14-16] Matsuo et al.[7] used numerical

methods for various cases. They concluded that special attention must be focused on the modeling of turbulence and temperature fluctuation effect of the Reynolds-averaged simulations.

1.2.2 Flat Plate Studies

Supersonic flows over a flat plate or through a constant area with normal sonic or supersonic injection of different gases have been experimentally and numerically conducted by scientists and engineers for many years.[17-43] Early research on secondary injection into supersonic flows was conducted by Spaid and Zukoski.[17-18] Their research found that the static pressure in the separated region immediately downstream of the jet nozzle exit is usually lower than the pressure just upstream of separation. However, near reattachment, pressures in this region depends upon the Mach number and mass flow rate of injectant, as well as the injectant fluid properties.

The penetration of gases into supersonic flow has been investigated by Billig et al[9-11] in the mid 1960's. In their experiments, they researched the analytical prediction of the behavior of gaseous jets issuing transversely through a surface into a freestream. For underexpanded jets exhausting into the freestream, it was shown that the shock structure, if any, caused in the jet itself, by underexpansion can have a profound effect upon penetration. It was found that by increasing the injection pressure above the level of effective back pressure there was an 8-10% gain in penetration. By increasing the injection to supersonic, penetration increased 10-15% over sonic injection. Further study of sonic and supersonic injection into a freestream was conducted by the Povinelli brothers.[22] They concluded that the effect of injection Mach number on penetration increased with downstream distance and that an increase of approximately 30% in penetration of a Mach 4 injectant occurred over a sonic one. Also, jet penetration was proportional to the jet total to effective back pressure ratio raised to the one-half power.

Recent study into mixing phenomena in supersonic flows has been conducted by Aso et al.[23-25] using two and three-dimensional analysis. Their studies proved that the bowshock wave/turbulent boundary layer interaction induces the boundary layer

separation in front of the injection. They found that in the interaction region surface, pressure begins to increase in front of the separation point, then to a plateau in front of the injector, finally decreasing significantly below freestream static level just after the injector and then increasing again showing local pressure peak. Also, they showed that the separation length and penetration height increase with an increase in injector pressure to freestream pressure ratio. Results found using a three-dimensional injector showed complicated flow structures that were quite different from the two-dimensional study.

Toda et al.[26] has used computational schemes to model various turbulence models relating to injection into a supersonic freestream. Their models showed that the effects of the turbulence models on the flow structures mainly appear in the upstream separation region and that the flowfield behind the injection does not depend on turbulence since all the numerical results were in good agreement with experimental data. Toda et al. also concluded that all the turbulence models gave reasonable results, but that more modifications in the turbulence models would have to be done to give a more accurate solution. McClinton et al.[27] used an injection ramp scheme, very similar to that of Abdel-Salam et al., [11] to analyze flow losses and thrust potential in supersonic combustors. Their research showed that flow losses in supersonic mixing and reacting flows are caused by a combination of coupled complex phenomena, such as shocks, separation, friction, etc. They found that by using a non-reacting flow the mixing was highest using the swept ramp injector, lowest for the unswept injector, and intermediate for the 30° angled flush injector.

Turbulent mixing experimentation by Gerlinger et al.[28]and Holderman et al.[29] have also been conducted. Gerlinger et al. used the low-Reynolds-number q-ω turbulence model for a flat plate where nitrogen gas injected transversely. They found that this model was far superior to the κ-ε turbulence model because of its high numerical stability. Holderman et al. used different injector shape and configurations in their experiments. They found that the momentum-flux ratio and orifice geometry affect mixing performance significantly and that the mixing rate is a function of slot orientation.

Donald Rizzetta[31] used numerical simulation to recreate the slot injection experiments by Aso et al.[23] Rizzetta used the κ-ε turbulence model in his numerical scheme, low-Reynolds number terms, and a compressibility correction. His results as compared to Aso et al. showed similar agreement between numerical and experimental data. Grasso and Magi[32] used the Favre-averaged Navier-Stokes equations for a multicomponent mixture of gases and the k-ε turbulence model that properly accounted for low Reynolds effects to numerically simulate transverse gas injection into supersonic flow. Their work proved that the low Reynolds number model could adequately represent the detail of the complex flow pattern. Also, they showed that comparison with experimental data indicated that the model adequately resolves the interaction of the bow shock with the boundary layer.

Baurle et al.[34], Kallenberg et al.[35] have also presented papers on numerical study of jet injection into supersonic freestreams. Baurle et al used three different turbulence models: the Wilcox κ-ω model, Menter-SST model, and the Menter-BSL model. They concluded that most of the turbulence model results follow the same trends as the experimental results, although the Menter-SST model predicted a larger separation region and at a location further upstream of jet interaction. The κ-ω and BSL models had better overall predictions in terms of surface pressure comparisons. All models overpredicted the penetration heights by as much as 25% as compared to experimental results. Kallenberg et al. have used large eddy simulation(LES) as their turbulence model in a three-dimensional supersonic flow. Their results showed that the two-dimensional separation length was approximately 3 times as long as the three-dimensional results. Hubbard et al.[36] performed experiments studying the effects of jet-to-freestream momentum ratio, jet, and freestream Mach numbers, and pressure and density ratios at the jet exit. They found that penetration is strongly dependent on the momentum ratio, weakly dependent on Mach number and pressure ratio, and independent of density ratio.

Using the VULCAN CFD code, Rodriguez[38] recreates the experiments 13 and 14 by Spaid and Zukoski.[18] He created three cases of a fine, medium, and a course grid for comparisons. Using various turbulence schemes, Rodriguez found that the Wilcox κ-ω model showed much more agreement than the κ-ε model. He found that the

Menter BSL turbulence model gave the worst approximation. He stated that the SST turbulence model limits the increase of shear stress with turbulence energy in adverse pressure gradients, which allows an earlier separation of the boundary layer. The pressure level he found was over predicted by 15% and the upstream interaction length is under predicted by approximately 22% for the medium and fine grids. Rodriguez found that the upstream interactions were underpredicted and pressures were higher than the experimental data for the highest injectant pressure experiment run, which was run 14 in Spaid and Zukoski.

1.2.3 Upstream Interaction Studies

Olynciw et al.[8] conducted research on one quarter and full scaled versions of the Japanese combustor to investigate the upstream interaction in the isolator. Their research showed that the symmetric assumption fails in that the upstream interaction on the bottom wall proceeds upstream further than the top wall. They also concluded that the presence of an oblique shock train significantly slowed the numerical convergence.

Abdel-Salam et al.[9-11] investigated the mixing processes using three-dimensional analyses. One numerical study[9] used raised and relieved ramps to investigate the mixing efficiency. They concluded that the unswept relieved ramp gave a higher mixing rate the unswept raised ramp and that the swept ramp gave better results in the non-reacting and reacting flows than using unswept ramps. In another study using the Japanese combustor geometry Abdel-Salam et al.[10] used a different fuel injector positioning scheme. The results given showed no upstream interaction but the upstream interaction did show up in calculations. They concluded that this might be due to the new fuel injector arrangement. Their final study[11] investigated the boundary layer formation within the isolator. Non-reacting and reacting cases were conducted. They found that boundary layer thickness in the reacting case affected the upstream interaction. No upstream interaction was found using uniform inlet boundary conditions, however asymmetric flow was found when using an inlet profile.

Rodriguez et al.[12-13] are among other researchers that have conducted research using the Japanese combustor design include. Rodriguez et al. modeled three-dimensional and other various geometries in his studies. They found in the three-dimensional case that wall pressures were found to be within acceptable tolerances with experimental data. A curious phenomenon occurred when non-symmetric boundary conditions were solved. The overall upstream interaction was larger than using the half-height results. They concluded that this might be due to the 'buckling' of the 'inviscid' core flow between the upstream circulating regions. Rodriguez[13] used various geometries to investigate the upstream interactions in his other study. He found that it was impossible to produce a basic symmetric solution. The results showed that with the large separation regions interacting with oblique shock trains that non-symmetric perturbations occurred. He also found that flows that are under high compression appear to be unstable and the perturbations would be amplified to such an extent that flow symmetry collapses regardless of what computational scheme is used.

1.2.4 Backward Facing Step/ Sudden Expansion Studies

The basic design of the backward facing step has been studied experimentally and numerically over the years. The backward facing step is a common feature of most scramjet engines. In some studies there have been accounts where asymmetric separation near abrupt changes of the geometry have occurred. [7,44-49] The sudden expansion experiments are very similar to the backward or rear facing steps. To qualify as a sudden expansion study, the step height to domain height ratio has to be at least 1:2.

Subsonic flows over two-dimensional rearward-facing steps have been investigated by Abbott and Kline.[48] They observed the asymmetry of the turbulent flow downstream for double step geometry with large expansions. As the isolator to expansion ratio was reduced, results approached that of a single step geometry. Also, no effect on flow pattern or reattachment length is found for a wide range of Reynolds numbers and turbulence intensities, provided the flow is fully turbulent

before the step. Uenishi et al.[49] modeled laminar air at a mach 3.5 over a rearward-facing step using numerical simulation. They found that the unsteady flow was related to boundary layer thickness approaching the step.

Durst and Whitelaw[47] used flow visualization and laser-Doppler anemometry in their sudden expansion experiments. Their results proved that symmetric flows can exist in two-dimensional, plane, symmetric, sudden expansion ducts for only a limited range of Reynolds numbers. At high Reynolds numbers, the results show eddy-like patterns that alternate from one side to the other with consequent of the mean flow. They found that asymmetric flow was caused by the phenomenon of disturbances generated at the edge of the expansion and amplified in the shear layers.

There have been others who have conducted research on backward facing steps using other methods of study.[44-46] Yang[44], for example, used a new error indicator and an extended locally implicit scheme with anisotropic dissipation model on a quad-tri mesh over a backward-facing step. By using this method, Yang was able to show that the adaptive solution was more accurate. Ghia and Papp[45] performed numerical research comparing the RNG and Chien turbulence models for flow over a backward-facing step. Ghia and Papp showed both turbulence models predict the mean flow base pressure adequately. However, they found that the critical defect of both models was their inability to predict the correct magnitude and trend of the normal Reynolds stress components. They also said that the RNG model most closely approached that of experimental data. Using laser-induced fluorescence visualization techniques, Graves and McDaniel[46] conducted research on three fuel injection configurations: 1) injection from one orifice into a constant-area duct, 2) injection behind a backward-facing step, and 3) injection from staged orifices behind a backward-facing step. All three cases did not have chemical reactions. They found that the staged injection improved injectant penetration over the other two injectant configurations.

1.3 Objectives of the Study

The objective of this study is to numerically investigate the upstream interaction of a dual-mode scramjet engine. By using a non-reacting flowfield we increase the

backpressure, either using fuel injectors or by applying a backpressure at the exit, to create an asymmetric upstream interaction. First, we investigate the upstream interaction in half and full constant area duct cases. The upstream interaction will move upstream as the freestream to injector pressure ratio is increased. Both half and full constant area duct studies are evaluated to compare the upstream interaction of each. From this we apply the sudden expansion geometry to investigate the upstream interaction using the same boundary conditions. Further, we use the constant area duct with an applied backpressure to further investigate the upstream interaction. Finally, we use the fore mentioned constant area duct with a diffuser attached to see how the upstream interaction reacts.

While using a low freestream to injector pressure ratio, it was shown that the upstream interaction was symmetric, but as that ratio increased the asymmetry of the upper and lower upstream interaction was seen. The asymmetry was also shown in the sudden expansion and the constant area duct with and without a diffuser. By seeing these results, we can prove that asymmetric results are not directly related to a reacting flow.

SECTION 2

THEORETICAL FORMULATION

This section provides a description of the physical problem, numerical procedure, flowfield features, and governing equations. A discussion of the following is provided.

2.1 Physical Problem

2.1.1 Experimental Arrangement

Experiments were conducted by Spaid and Zukoski at the Jet Propulsion Laboratory, California Institute of Technology (CIT) in the 20-inch supersonic wind tunnel.[17-18] Fig. 2.1 shows the geometry of their experiment. Their measurements were conducted in British units. For convenience, all measurements have been converted to SI units. The series of experiments included the sonic injection of gaseous nitrogen and helium at various freestream Mach numbers. Experimental data consisted of test-section flow conditions, schlieren photographs, static pressure distributions on the test section wall in the injection region, concentration measurements in the flow, and injectant total pressure and mass flow rate. The dimensions of the experimental model consisted of a length of .4572 meter and a width of .4445 meter. The width of the slot was 0.2667 millimeter with a length of .1524 meter. End plates having glass inserts were sometimes mounted at either end of the slot to create a flowfield that would be as nearly two-dimensional as possible. The experiments were conducted at Mach numbers of 2.61, 3.5, and 4.54. Measured quantities consisted of test-section flow parameters, jet-reservoir flow parameters, and static pressure distributions on the surface of the plate near the jet.

Experiments for the sudden expansion diverging scramjet were performed at the National Aerospace Laboratory in Japan. Fig. 2.2 shows the CAD drawing of the scramjet engine used at the National Aerospace Laboratory. Fig. 2.2 shows the CAD drawing of the scramjet engine used at the National Aerospace Laboratory. The dimensions of the scramjet engine included an isolator height of 0.032 m and a length of 0.22 m. The dimensions of the scramjet engine included an isolator height of 0.032 m and a length of 0.22 m.

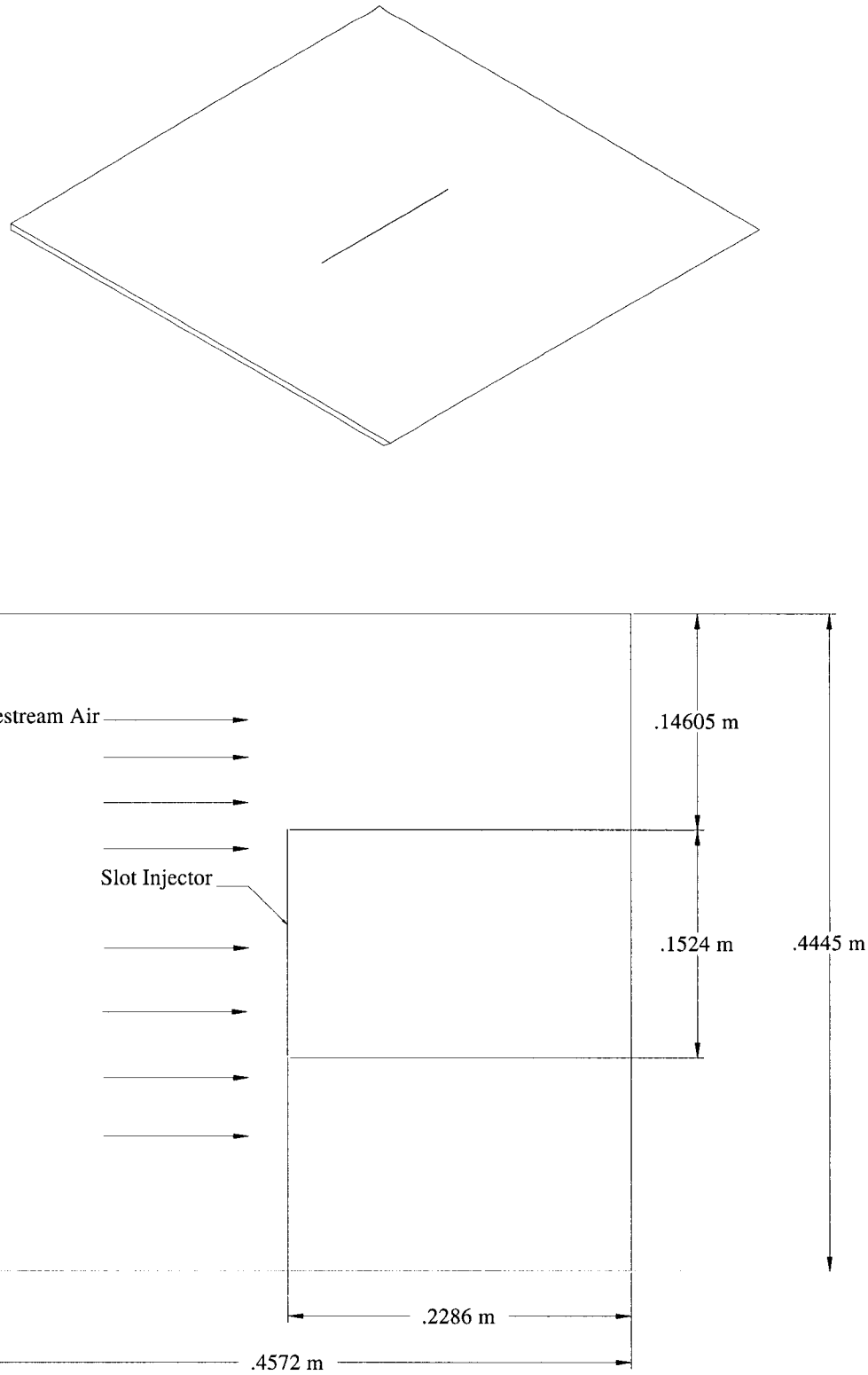

Figure 2.1 CAD drawing of Spaid and Zukoski experimental model.

The backward facing steps had a height of 3.2 mm or 10 times the isolator height. The sidewalls diverge at an angle of 1.7° after 0.096 m downstream of the backward-facing step. Their experiment consisted of combustion, so the experiment was insulated to mitigate combustor-facility interaction and to prevent the combustion induced pressure wave from propagating upstream into the nozzle. To simulate the high temperature air entering, a hydrogen vitiation air heater was used. The Mach number of the freestream air was set at 2.5. The total temperature was set at 2000 K and at a total pressure of 1013.25 kPa. Mole fractions consisted of O_2=20%, N_2=55%, and H_2O=25%. The fuel injectors were located 0.0128 m from the steps. The lower wall consisted of five fuel injectors and the top wall consisted of four fuel injectors equally spaces 0.032 m apart. The upper injectors and three center injectors on the bottom had a diameter of 4.0 mm. The outer lower injectors had a diameter of 2.8 mm. Hydrogen gas was used as the injectant in the experiments at total temperature of 280 K.

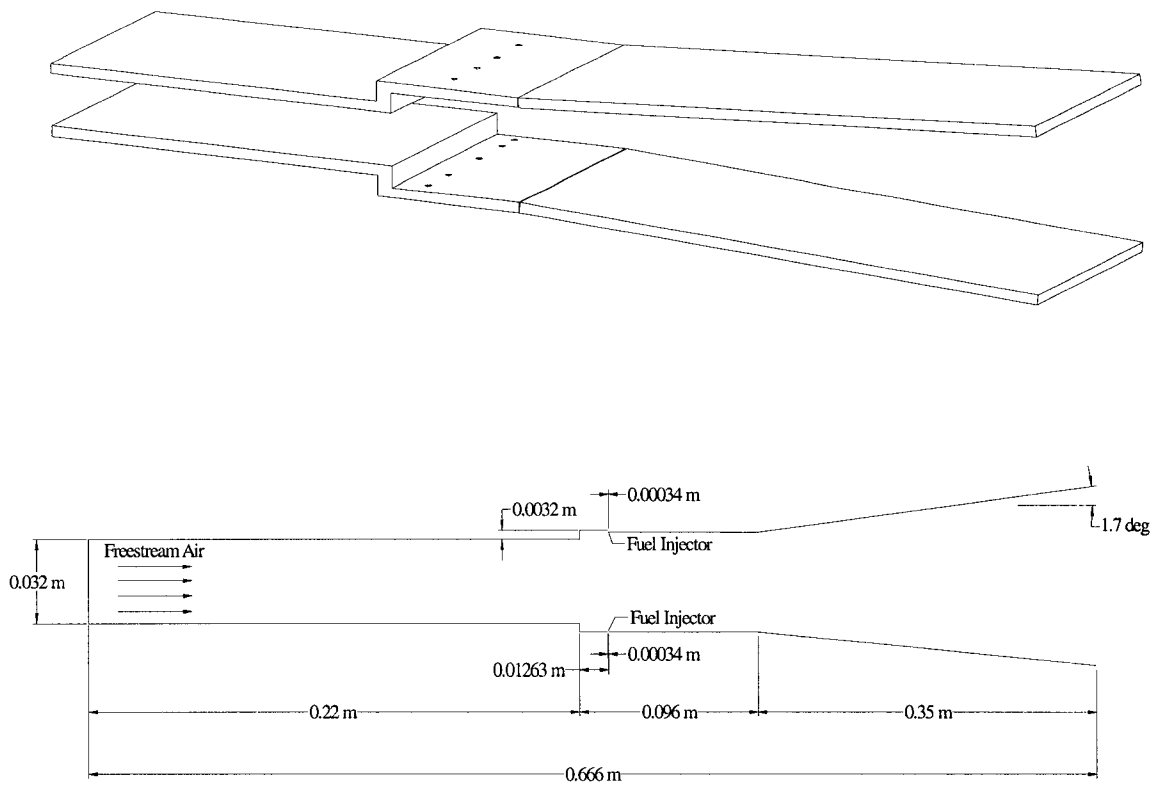

Figure 2.2 Three and two-dimensional CAD drawing of Japanese NAL sudden expansion experiment with divergent nozzle.

2.1.2 Numerical Model

Beginning with the modeling of the Spaid and Zukoski domain, the half duct geometry was created and jet-to-jet symmetry was assumed. This is shown in Fig. 2.3. Three cases were run for this domain. The first case was run at a pressure ratio (Po_{jet}/P) of 120.2. The second case was run at a pressure ratio (Po_{jet}/P) of 240.6. And the third case was run at a pressure ratio (Po_{jet}/P) of 481.2. The first case represents test case 13 from Spaid and Zukoski.[18] Freestream conditions consisted of air at a Mach number of 3.5 and at a total temperature of 566 K. Nitrogen was sonically injected transversely through a jet of a width of 0.2667 mm. The next three cases involved the whole computational domain, shown in Fig. 2.4, where no symmetry conditions exist and each of the three pressure ratios were numerically solved. For the half duct the inlet height was 0.1143 m with a length of 0.4572 m. The injector was located midway in the duct with a diameter of 0.2667 mm.

The sudden expansion case involves similar geometry from the National Aerospace Laboratory's model. The difference between the numerical model and the NAL model is that the numerical model does not have a 1.7° diverging nozzle downstream. Rather the downstream expansion is of constant area. This is shown in Fig. 2.5. The isolator height was 0.032 m high and a length of 0.22m. The step height was 10 times that of the isolator height. The steps had a height of 3.2 mm. The injectors were located 0.0128m downstream from the steps at a diameter of 0.34 mm. The length of the sudden expansion duct beginning from the step was 0.446 m long.

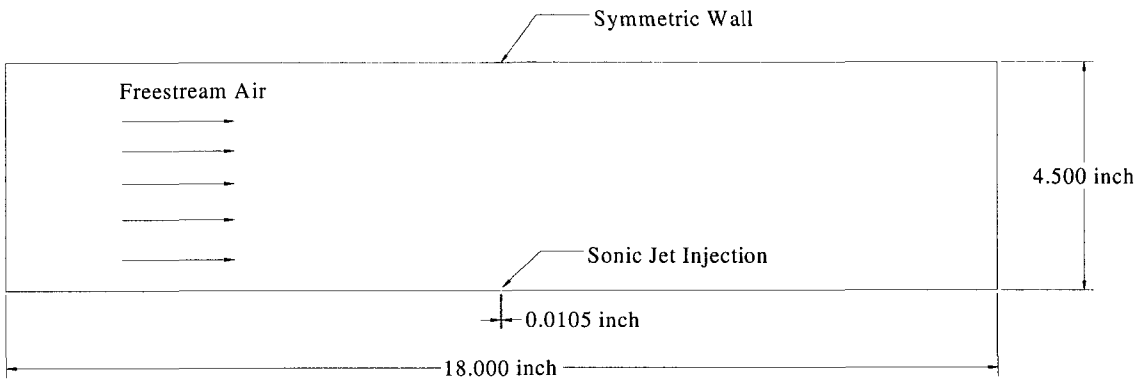

Figure 2.3 Half duct geometry.

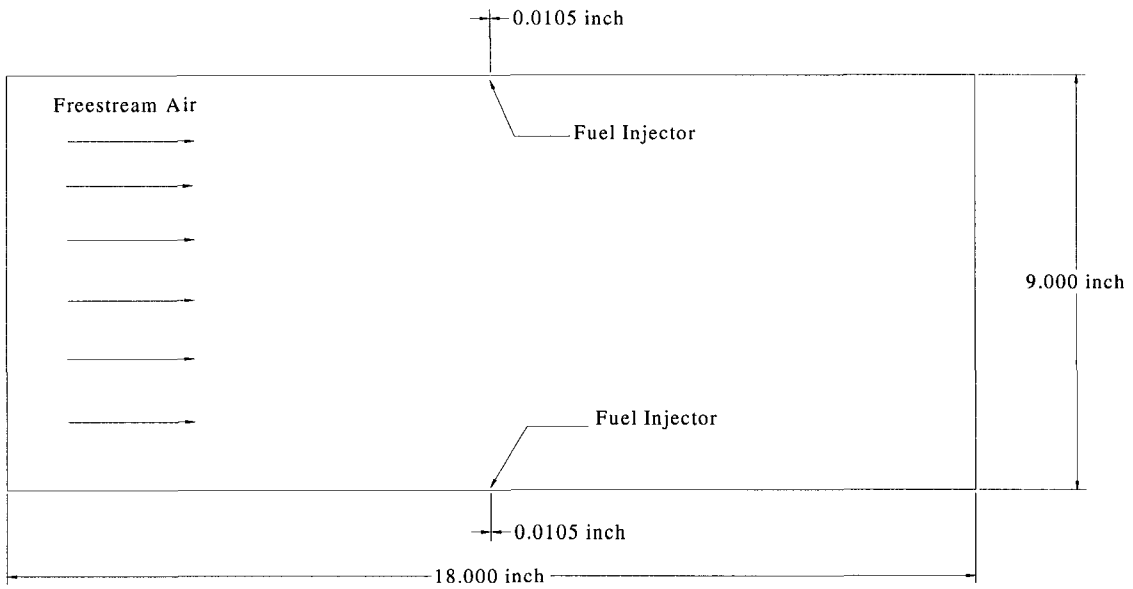

Figure 2.4 Full duct geometry.

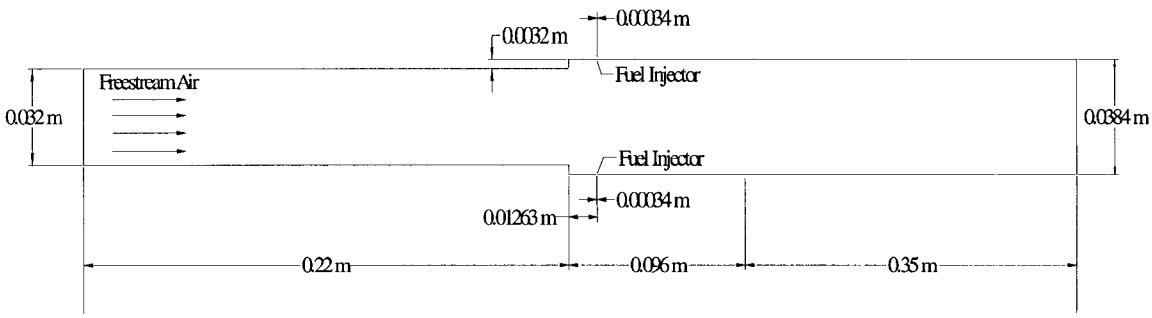

Figure 2.5 Sudden expansion duct with non-converging nozzle.

2.2 Flowfield Features

As the flowfield enters the isolator, it is at supersonic speed. In the combustion chamber region there is a breakdown in the flow due to oblique shock trains, due to the injection of gases, which creates turbulent regions. These regions can either be subsonic or supersonic. Thus, the term "dual-mode" comes into effect. As stated earlier, the term dual-mode means that the speed of air in the chamber goes from a transition from subsonic to supersonic or vice-versa. When the aircraft is in the dual-mode state, flight Mach numbers range from 5 to 8.

2.2.1 Design

The design of the dual-mode scramjet engine can be critical. Most scramjet engines use the backward-facing step design. This design allows for increasing the mixing in the combustion chamber due to the expansion of the flow. Also, the step creates a recirculating region that helps allow flame-holding stability. The isolator region creates a boundary layer region. Unstart may occur if the isolator is not long enough. So, in order to prevent unstart, the isolator must be long enough so that the separation shock does not extend out of the isolator. In order to prevent this, the boundary conditions must be adjusted by changing the design of the engine. However, having a long isolator or combustion chamber will increase the cost and weight of the flight vehicle.

2.2.2 Flow Dynamics of the Two-Dimensional Duct Model

When the underexpanded injection of secondary gas is injected normally into the supersonic freestream, the secondary flow expands rapidly through a strong Prandtl-Meyer fan within the freestream and interacts with the freestream.[17] Then the shock system, consisting of the Mach disk and barrel shock waves, are generated. By the blockage of these shocks to the freestream, a strong bow shock wave is formed in front of the injector. Also, ahead of the injection, the boundary layer separation occurs due to the interaction between the shock waves and the boundary layer, and it leads to the generation of the separation shock. This boundary layer separation is one of the characteristic phenomena when secondary flow is injected into a supersonic freestream. If the bow shock is fully established, the separation shock may interact with it. Behind the injector, a recompression shock following the boundary layer reattachment may exist. Therefore, the flowfield is complex, where various shock/shock interactions and shock wave/ boundary layer interactions can be observed around the injection.[26] Fig. 2.6 shows how the injection of the gas creates the boundary layer separation and how a recirculation region is formed between the separation and the injector.

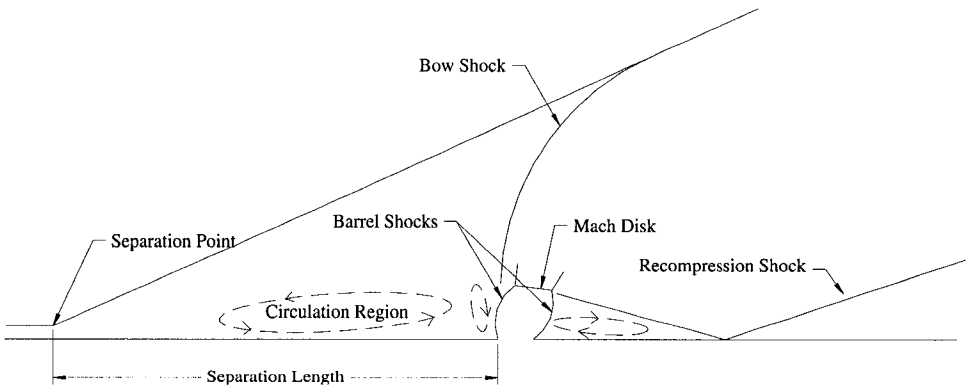

Figure 2.6 Flow characteristics of two-dimensional duct.

2.2.3 Flow Dynamics of the Sudden Expansion Model

The flow dynamics for the sudden expansion model are similar to the duct model. As the air flows through the isolator the boundary layer begins to thicken as the air approaches the expansion step. As a result of the pressure change, and expansion, the boundary layer begins to separate and drift upstream. Then, as the air passes over the steps, the flow expands through a Prandtl-Meyer fan. After the step a recirculating region is established before the injectors. The nitrogen injector is underexpanded and is injected normally at a sonic speed into the flow. The results from this are that a Mach disk and barrel shock waves are formed, as in the duct model. The injection of the gas is like a source that diverts the flowfield so that a separation bow shock is formed upstream of the injector. This bow shock redirects the incoming airflow so that the barrel shock waves and the Mach disk is reflected over so that the injectant is kept parallel to the wall. Downstream of the injector the boundary layer will reattach itself to the wall through a recompression shock. After this the flow continues downstream through the constant area duct. However, if the geometry were diverging after the injection the flow would accelerate to supersonic speeds. Figure 2.7 below shows the typical flowfield of the sudden expansion duct. As you can see the flowfield separates on the bottom first and then the top separates. It has been shown through experimentation and numerical simulation that this phenomenon oscillates from the bottom wall to the top wall. Fig. 2.7 shows the phenomena when the separation occurs on the bottom wall first.

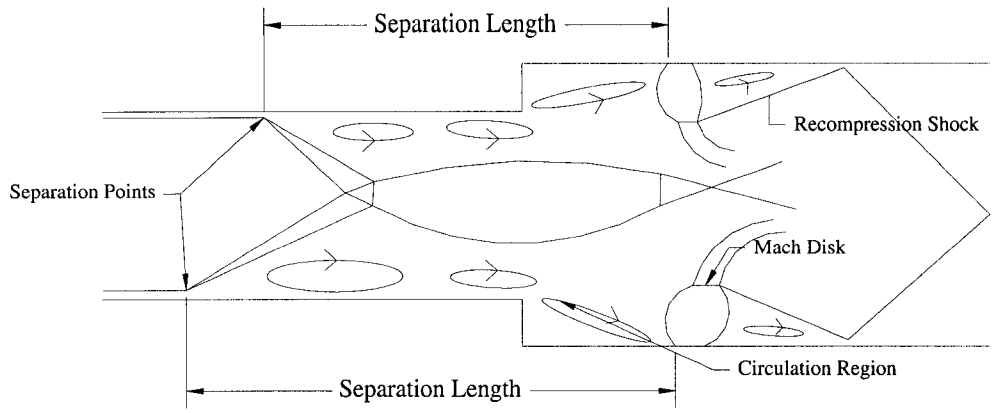

Figure 2.7 Typical flowfield characteristics of sudden expansion geometry.

2.3 Governing Equations

The governing equations used in the following numerical models are the continuity, momentum, energy, and the species transport equations. Given below are the equations.

Continuity
$$\frac{\partial}{\partial t}\rho = -\nabla \cdot \left(\rho \vec{v}\right) \tag{2.3a}$$

Momentum
$$\frac{\partial}{\partial t}\left(\rho \vec{v}\right) + \nabla \cdot \left(\rho \vec{v}\vec{v}\right) = \nabla p + \nabla \cdot \left(\bar{\bar{\tau}}\right) + \rho \vec{g} + \vec{F} \tag{2.3b}$$

Energy
$$\frac{\partial}{\partial t}(\rho E) + \nabla \cdot \left(\vec{v}(\rho E + p)\right) = \nabla \cdot \left(k_{eff} \nabla T - \sum_j h_j \vec{J}_j + \left(\bar{\bar{\tau}}_{eff} \cdot \vec{v}\right)\right)_h \tag{2.3c}$$

Species
$$\frac{\partial}{\partial t}(\rho Y_i) + \nabla \cdot \left(\rho \vec{v} Y_i\right) = -\nabla \cdot \vec{J}_i + R_i + S_i \tag{2.3d}$$

In Eqs. (2.3a-d), ρ is the density, t is time, $\vec{v}$ is the mass average velocity vector, p is the static pressure $\bar{\bar{\tau}}$ is the stress tensor, $\vec{g}$ is gravity, $\vec{F}$ is the external body force(s), E is the internal energy, κ_{eff} is the effective conductivity, h is the enthalpy, $\vec{J}_j$ is the diffusion flux of species j, Y_i is the local mass fraction for each of the species, R_i is the net rate of production by chemical reaction, and S_i is the rate of creation by addition

from the dispersed phase plus any user-defined sources. The above equations are programmed in FLUENT and are solved numerically for each of the numerical models.

2.4 Numerical Procedure

This section describes the computational fluid dynamics code, geometry and mesh setup, and boundary conditions.

2.4.1 Geometry and Mesh Creation

The pre-processor called GAMBIT version 2.0[50] was used to create the geometries and meshes for all models in this study. GAMBIT is a DOS based computer program that takes input from the user to create geometry to be meshed and then exported to FLUENT. After the geometry is created you then mesh the edges. The meshed edges can be adjusted using various aspect ratios. This is very important when dealing with flows with a boundary layer. GAMBIT has the capability of creating structured and unstructured grids. And in some instances both structured and unstructured grids may be used in the same model. The unstructured grid may include hexahedral, tetrahedral, pyramid and prism elements. In this study both structured and unstructured two-dimensional grids have been created.

2.4.2 FLUENT CFD Code

The models used in this study have been processed by FLUENT version 5.5. FLUENT is a CFD code that is based on the finite element method, where the domain is discretized into a finite set of control volumes for three-dimensional cases or cells for two-dimensional cases. The FLUENT solver has the following modeling capabilities.[51]

- flows in 2D or 3D geometries using unstructured solution-adaptive triangular/tetrahedral, quadrilateral/hexahedral, or mixed (hybrid) grids that include prisms (wedges) or pyramids
- incompressible or compressible flows
- steady-state or transient analysis

- inviscid, laminar, and turbulent flows
- Newtonian or non-Newtonian flow
- convective heat transfer, including natural and forced
- coupled conduction/convective heat transfer
- radiation heat transfer
- chemical species mixing and reaction, including combustion sub-models and surface deposition reaction models

These are just a listed few abilities that FLUENT can perform. More can be read in the FLUENT user's guide.[51]

2.4.2.1 Single vs. Double Precision

In FLUENT you have the option to either use a single or double precision solver. In most applications using the single precision is adequate, but if your geometry has features of very disparate length scales or enclosures connected by small diameter pipes using the double precision solver would be best. In all studies contained in this paper, the single precision solver has been used.

2.4.2.2 Solver Formulation

Within FLUENT you have two solver formulations to choose from, the segregated and the coupled formulations. The segregated and coupled differ in the way they solve the continuity, momentum, energy, and species equations. The segregated solves these equations individually from one another, while the coupled solver solves the equations simultaneously. The segregated solver is used mainly in incompressible and mildly compressible flows. The coupled solver is better suited for high-speed compressible flows. In both the segregated and coupled solution methods the discrete, non-linear governing equations are linearized to produce a system of equations for the dependent variables in every computational cell or volume. The resultant linear system is then solved to yield an updated flow-field solution. For each solver you have the option of choosing the implicit or explicit method. The implicit method is described as where for a given variable, the unknown value in each cell is computed using a relation that

includes both existing and unknown values from neighboring cells. Therefore, each unknown will appear in more than one equation in the system, and these equations must be solved simultaneously to give the unknown quantities. The explicit method is described as where for a given variable, the unknown value in each cell is computed using a relation that includes only existing values. Therefore, each unknown will appear in only one equation in the system and the equations for the unknown value in each cell can be solved one at a time to give the unknown quantities. All the studies presented in this paper have used the coupled implicit solver formulation.

2.4.2.3 Turbulence Modeling

FLUENT version 5.5 has the choice of four turbulence models to choose from. The Spalart-Allmaras model, κ-ε model, Reynolds stress model, and large eddy simulation turbulence models. The κ-ω model is now available in FLUENT version 6.0 with the above fore mentioned models. For brevity we will concentrate on the κ-ε model. This model has been chosen for all the cases in this study. Within the κ-ε model there are three versions: the standard, RNG, and realizable models. In this study the RNG κ-ε model has been used. This model was derived using a rigorous statistical technique called renormalization group theory. Below are the transport equations for the RNG κ-ε model.

$$\frac{\partial}{\partial t}(\rho\kappa)+\frac{\partial}{\partial \chi_i}(\rho\kappa u_i)=\frac{\partial}{\partial \chi_j}\left(\alpha_\kappa \mu_{eff}\frac{\partial \kappa}{\partial \chi_j}\right)+G_\kappa+G_b-\rho\varepsilon-Y_M+S_\kappa \tag{2.4a}$$

and

$$\frac{\partial}{\partial t(\rho\varepsilon)}+\frac{\partial}{\partial \chi_i}(\rho\varepsilon u_i)=\frac{\partial}{\partial \chi_j}\left(\alpha_\varepsilon \mu_{eff}\frac{\partial \varepsilon}{\partial \chi_j}\right)+C_{1\varepsilon}\frac{\varepsilon}{\kappa}(G_\kappa+C_{3\varepsilon}G_b)-C_{2\varepsilon}\rho\frac{\varepsilon^2}{\kappa}-R_\varepsilon+S_\varepsilon \tag{2.4b}$$

In Eqs. (2.4a-b), G_κ represents the generation of turbulence kinetic energy due to the mean velocity gradients. G_b is the generation of turbulence kinetic energy due to buoyancy. Y_M represents the contribution of the fluctuating dilation in compressible turbulence to the overall dissipation rate. The quantities α_κ and α_ε are the inverse effective Prandtl numbers for κ and ε, respectively. S_κ and S_ε are the user-defined source terms.

Constants are derived using RNG theory. A more in depth analysis of this turbulence model as well as other turbulence models can be found in FLUENT's user manual.[51]

2.4.2.4 Discretization

Discretization can be defined as the method used to convert the governing equations to algebraic equations that can be solved numerically. There are six discretization schemes: the first-order, power-law, second-order, QUICK, central-differencing, and the linearized forms. For brevity the first and second-order schemes are described here since they are used in all the studies. Upwinding means that the face value is derived from quantities in the cell upstream, or "upwind," relative to the direction of the normal velocity. When using first-order accuracy, the quantities at the cell faces are determined by assuming that the cell-center values of any field variable represent a cell-average value and hold throughout the entire cell; the face quantities are identical to the cell quantities. Thus when first-order upwinding is selected, the face value is set equal to the cell-center value in the upstream cell. When using second-order accuracy, quantities at cell faces are computed using a multidimensional linear reconstruction approach. In this approach, higher-order accuracy is achieved at cell faces through a Taylor series expansion of the cell-centered solution about the cell centroid.

2.4.3 Computational Procedure

The single precision solver has been used in all studies. The coupled implicit scheme has been used for all studies. Turbulence was modeled using the RNG κ-ε model with standard wall functions. Discretization consisted of using the first-order upwind schemes at the beginning and then changing to second-order once the model had iterated for a determined amount. The Courant number (CFL) controls the time stepping scheme. Using a large time step leads to faster convergence, however for some flows using a low CFL will keep the model stable. For all studies, a CFL of 0.1 was used to start the models. After monitoring each model individually, the CFL was changed due to residual convergence.

2.4.4 Boundary Conditions

Vitiated air at Mach 3.5 with a total temperature of 566 K has been numerically studied. The original study by Spaid and Zukoski used boundary conditions as shown in Table 2.1. Boundary conditions conducted afterwards used these values reduced by a factor of two. These other boundary conditions are shown in section 4. The injectant boundary condition was kept the same for all cases run here. Nitrogen gas was injected normal to the freestream at sonic velocity. The sonic nitrogen jet(s) had a total pressure of 379.90 kPa, static pressure of 200.64 kPa, and a total temperature of 525 K.

At the walls, a no-slip boundary condition was used. The viscous κ-ε model constant values given by FLUENT were used at the walls. Due to supersonic flow at the outlet of all geometries, FLUENT no longer uses the specified pressure given for the outlet. The pressure at the outlet is extrapolated from the flow in the interior. All models were initialized from the incoming vitiated air.

For the sudden expansion validation model used by Rodriguez[13] different boundary conditions have been used. The boundary conditions are shown in Section 3.1. Boundary conditions at the inlet consists of air at Mach 2.50 and at a P_{total}=310 kPa. A backpressure was applied to the sudden expansion model with a P_{back} of 80 kPa. Walls are adiabatic with no-slip conditions applied.

In the test section validation model the boundary conditions are given in Section 3.2. Carroll and Dutton[52] conducted this numerical validation experimentally in 1990 and Rodriguez[13] also conducted a numerical validation in 2001. Boundary conditions at the inlet consists of air at Mach 2.45 and at a P_{total}=310 kPa. A backpressure of 108.5 kPa is applied at the exit of the test section to achieve the upstream oblique shock separation. Walls are adiabatic with no-slip conditions applied.

Table 2.1 Boundary conditions used in the Spaid and Zukoski experiment.

	Freestream Air	Nitrogen Injectant
M	3.5	1.0
P_t (kPa)	240.627	379.901
P_s (kPa)	3.158	200.637
T_t (K)	314.44	291.67
T_s (K)	91.67	243.33
Velocity (m/s)	670.56	317.906

SECTION 3

COMPUTER CODE VALIDATIONS

3.1 Sudden Expansion Validation Study

3.1.1 Results and Discussion

Numerical results are presented using the sudden expansion geometry used by Rodriguez[13]. The study performed uses sudden expansion geometry with an applied backpressure at the exit of 80 kPa. This backpressure simulates the blocking effect that using injectors or combustion would create. The purpose of this study is to validate the results found by Rodriguez[13]. He found that by applying the given uniform backpressure at the outlet, asymmetric results are found. The computational grid, in Fig. 3.1, consists of 36,354 triangular cells. Boundary conditions for the validation are shown in Table 3.1.

Figure 3.2 shows the Mach number, normalized static pressure, and velocity vector and streamline contours. The Mach number contours are in good agreement with those found by Rodriguez[13]. Note here that Rodriguez used the VULCUN code from NASA Langley to conduct his research while applying the diagonal approximate-factorization (DAF) computational scheme in his study. Normalized static pressure contours, in Fig. 3.2b, as well as Mach number contours are consistent with those from the sudden expansion models with injection. The symmetry breaks down where the upper wall separates further than the lower wall. Velocity vector and stream line contours shown in Fig. 3.2c show the classic recirculation region as predicted with the models with injection. We see that the larger recirculation region on the upper wall bends the flowfield. As a result, there is a large recirculation region downstream of the upper step.

Figures 3.3-3.5 show the normalized static pressure and velocity along the x-axis plots. The classic pressure rise due to the separation shock is present in Fig. 3.3. We see that the top separates first followed by the bottom. Pressure rises due to the separation shock is approximately 350%. Figures 3.4 and 3.5 show the velocity along the x-axis. We find that the top separates at approximately 0.0562m and the bottom separates at approximately 0.07m. The difference between the top and bottom is 0.0138m. At the steps of the geometry we see that the velocity increases rapidly on the bottom and

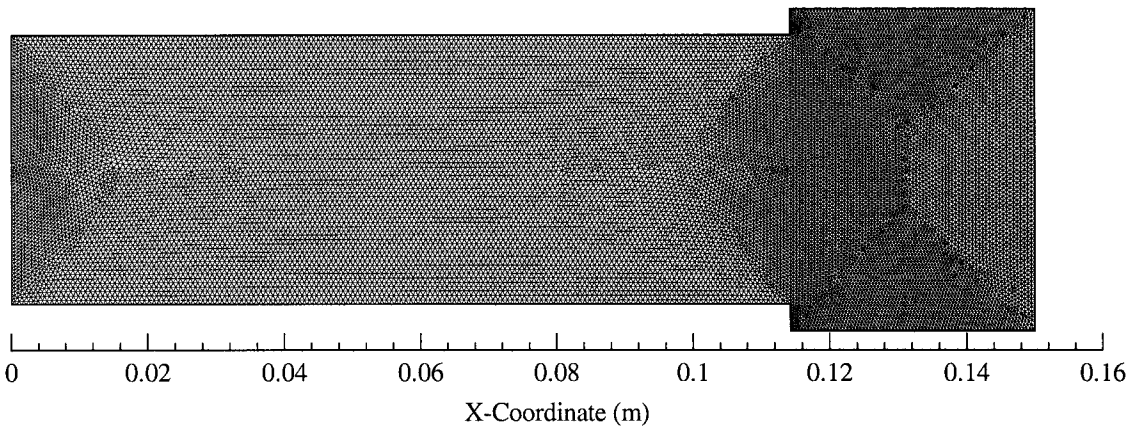

Figure 3.1 Geometry and grid for P_{back} of 80 kPa.

Table 3.1 Boundary conditions for P_{back} of 80 kPa

	Freestream air
M	2.50
P_t (kPa)	310
T_t (K)	295
P_{back} (kPa)	80

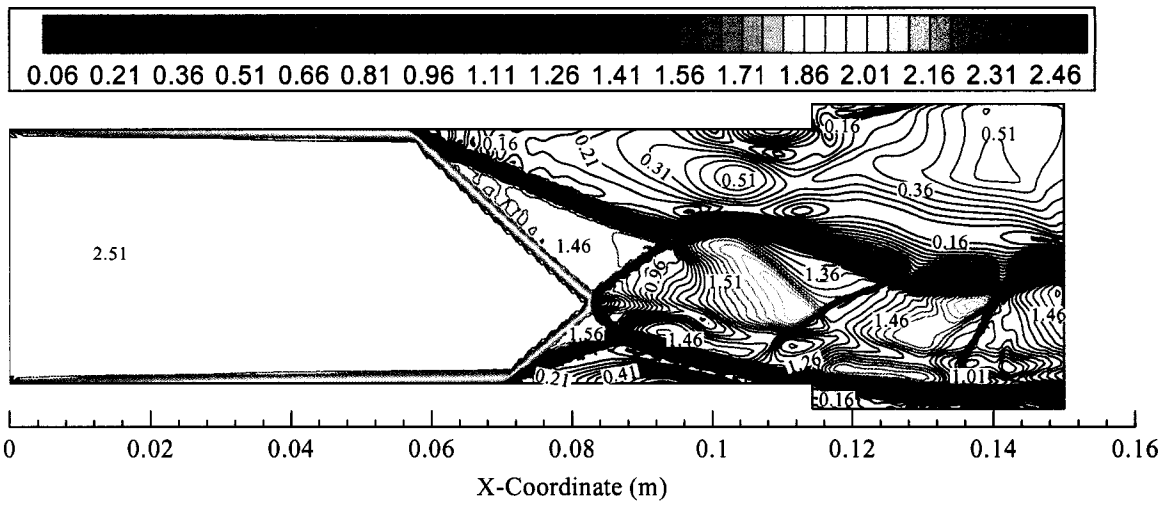

a. Mach number contours

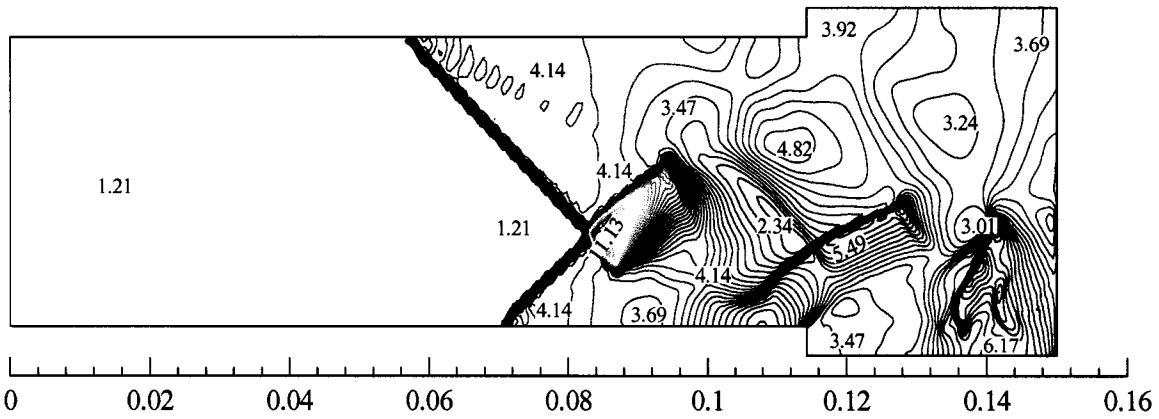

b. Normalized static pressure contours

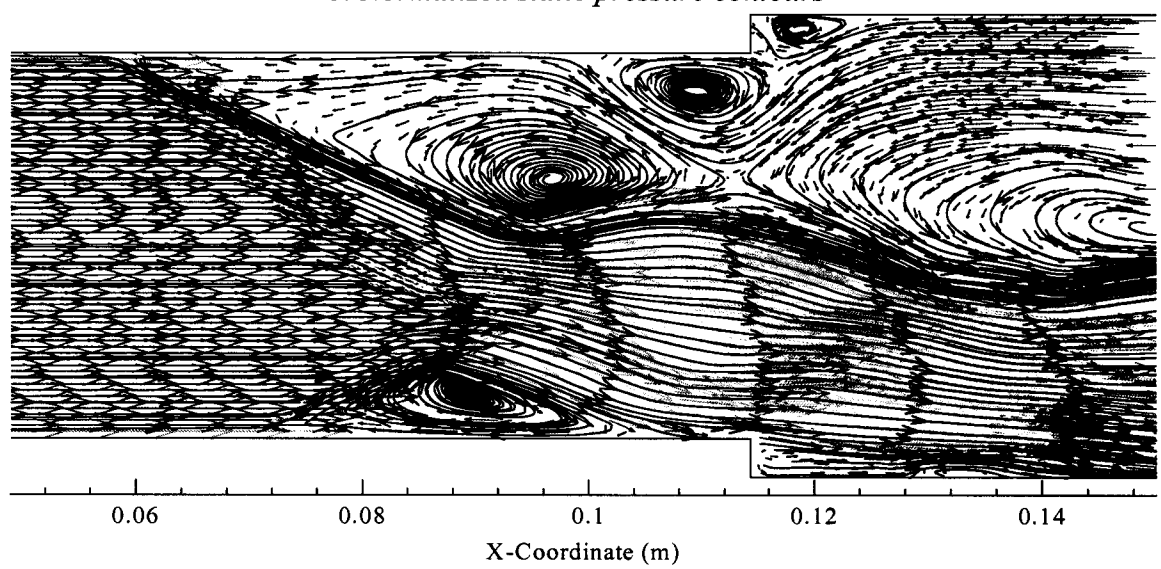

c. Velocity vector and streamline contour plot

Figure 3.2 Contour plots of using a P_{back} of 80 kPa.

decreases rapidly at the top. This is due to the large recirculation bubble upstream. The recirculation region causes the flowfield to bend, as stated previously; this causes large changes in velocity after the steps.

With the presence of a backpressure, symmetry of the flowfield is found to be untrue. The cause of the asymmetry may be attributed to turbulent shear stresses within these recirculation regions. These perturbations change as the numerical model progresses, where the separation region grows and then collapses upon itself, then moving upstream and then retreating downstream. Convergence cannot be achieved due to the oblique shock-trains created within the flowfield along with shock-boundary layer interactions causing separation shocks.

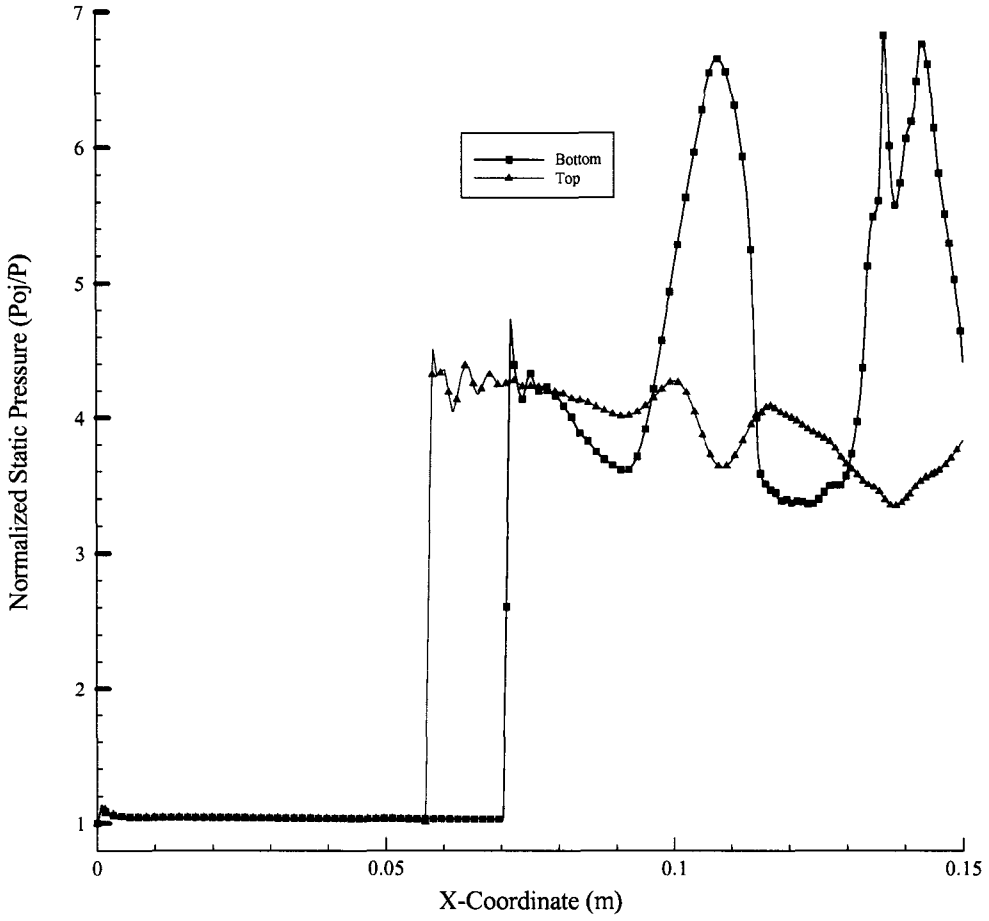

Figure 3.3 Normalized static pressure plot, sudden expansion duct P_{back}=80 kPa.

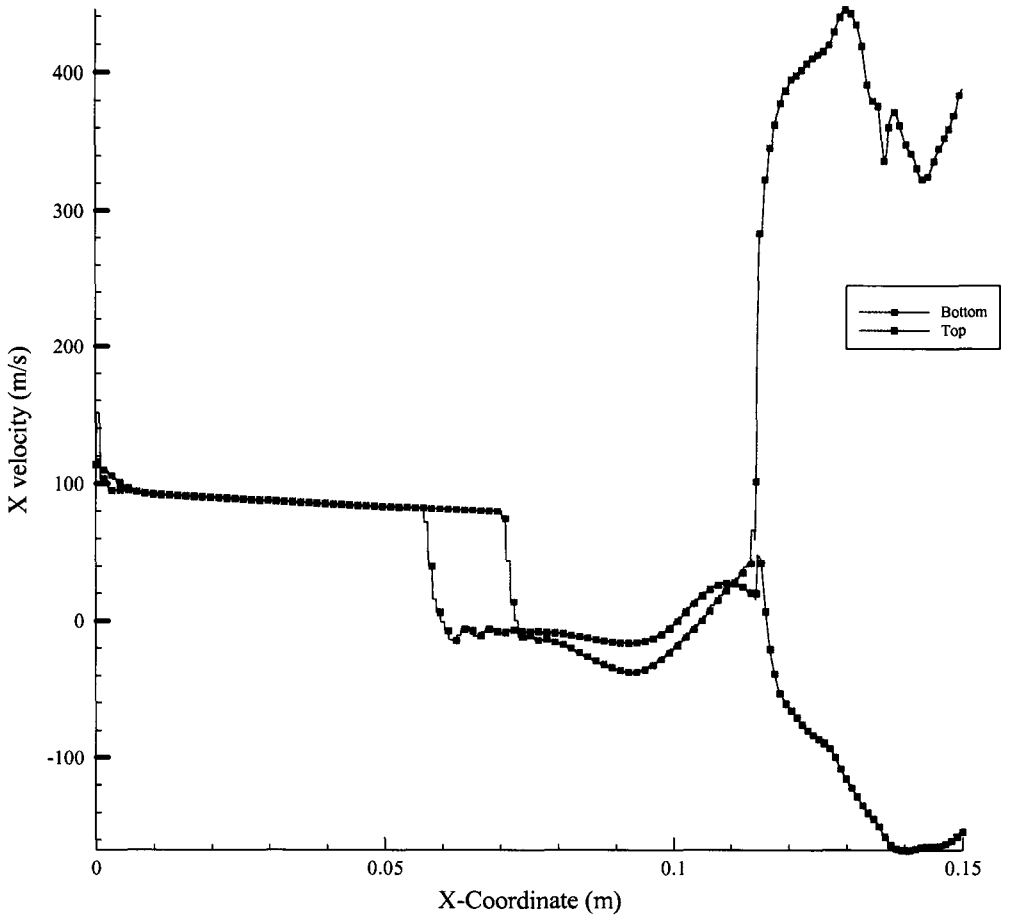

Figure 3.4 X velocity plot comparison, sudden expansion duct with P_{back}=80 kPa.

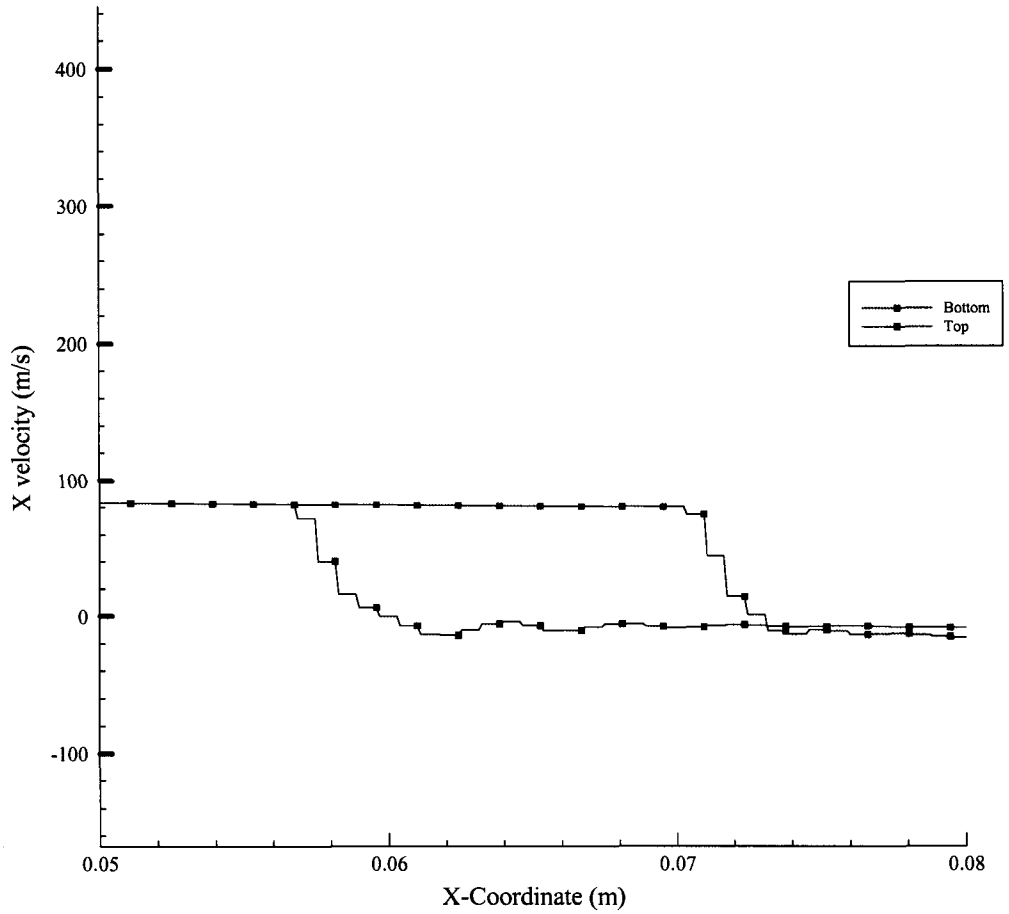

Figure 3.5 X velocity plot showing boundary layer separation, sudden expansion duct with P_{back}=80 kPa.

3.2 Test Section Isolator Validation Study

3.2.1 Introduction

Numerical study has been conducted on a diffusing test section duct with applied backpressure at the exit. This study is a validation of the experimental and numerical studies conducted by Rodriguez[13] and Carroll and Dutton[52]. The experiment was conducted using a supersonic wind tunnel assembly. The wind tunnel geometry consisted of a stagnation chamber, with a height of 101.6 mm, which was connected downstream to a convergent-divergent nozzle, then followed downstream with the diffusing test section isolator, and finally the isolator connected to the adjustable exit diffuser.

This section investigates the numerical study of the test section isolator region only. Initial boundary conditions are imposed at the inlet. These values are given in Table 3.2. Air is the only species used at a Mach number of 2.45. A backpressure of 108.5 kPa is applied to the outlet of the test section. This backpressure was found by Carroll and Dutton as the ideal value following the oblique shock train. Figure 3.5 shows the grid used for the numerical study. The length of the isolator is 754mm with a height of 38.1mm. The walls of the test section diffuse at an angle of 0.25 degrees. This was done in the experiment to give a zero axial pressure gradient in the fully started test section. An unstructured grid of 32,722cells has been used. Comparisons to the experimental[52] and numerical[13] experiments are investigated.

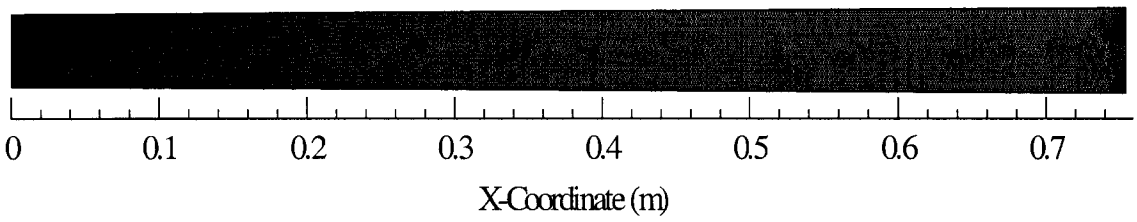

Figure 3.6 Geometry and grid for test section isolator

Table 3.2 Boundary conditions for test section isolator

	Freestream air
M	2.45
P_t (kPa)	310
T_t (K)	295
P_{back} (kPa)	108.5

3.2.2 Results and Discussion

Figure 3.7 presents results for Mach number, normalized static pressure, and vector and streamline contour plots. Figure 3.7a shows the Mach number contours. The results presented in the Rodriguez study include only the front half of the isolator-diffuser domain. The results in Fig. 3.7a show good agreement in the asymmetric shock structure compared to Rodriguez[40]. Rodriguez used the 1998 Wilcox κ-ω turbulence model in his numerical study, as for the numerical study conducted here the RNG κ–ε turbulence scheme was used. Figure 3.7a shows that the top wall separates first followed by the bottom wall. Throughout the entire numerical iteration the separation shock oscillated up and downstream, never reaching an equilibrium state. This is due to the turbulent nature of the freestream reacting to the applied backpressure.

Figure 3.7b shows the normalized static pressure contour plot. Here as in the Mach number figure we can see the upstream interaction and the asymmetric flowfield. Pressure ratios decrease across the shock, with lower ratios in the recirculation regions. The top separates at approximately 0.031m and the bottom separates at approximately 0.0295m. Observation of the numerical model at various iteration values showed the separation shock oscillating upstream and then downstream never reaching an equilibrium state. The top separation shock always separated before the bottom one. Further downstream we see that the Mach numbers decrease due to the shock train upstream.

Velocity vector and streamlines are presented in Fig. 3.7c. The recirculation regions are shown. The top region is much larger since the top has separated first and the angle the shock has taken is very steep. Smaller circulation regions are shown downstream, especially at the top. This can be attributed to the turbulent nature of the flowfield near the walls.

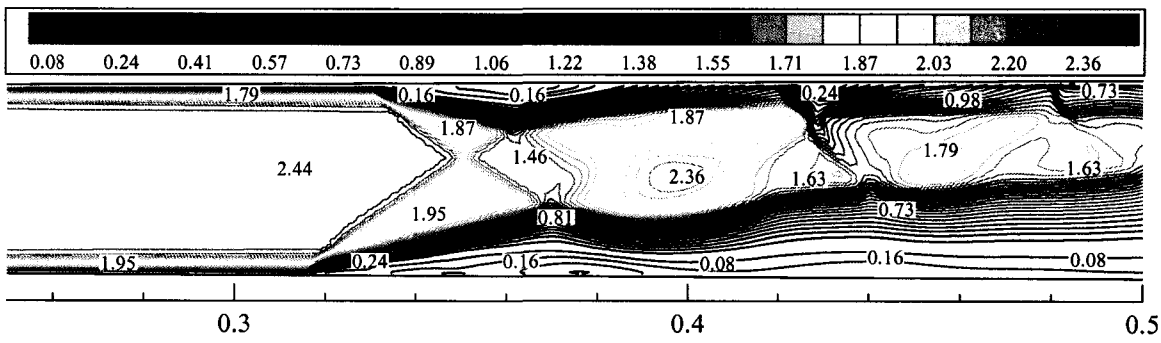

a. Mach number contours

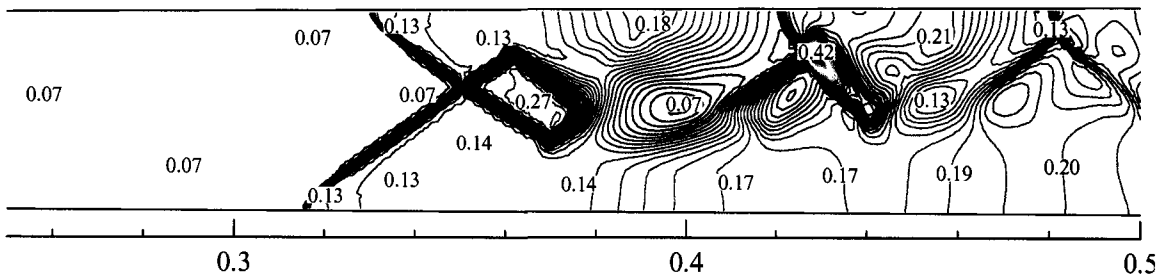

b. Normalized static pressure contours

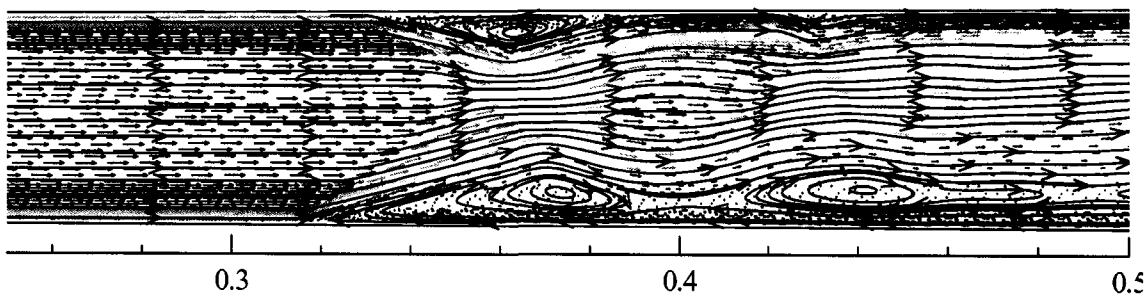

c. Velocity vector and streamline contour plot

Figure 3.7 Contour plots of test section isolator.

Figure 3.8 shows results of the normalized static pressure plot. We see that where the asymmetry occurs that normalized pressure ratio increases approximately by 283%. Comparison to Rodriguez[40] and experimental results show fair agreement.

Velocity along the x-axis is shown in Figs. 3.9 and 3.10. The top region is shown to separate at approximately 0.064m and the bottom at 0.075m. The difference is that the top separates 0.011m further upstream. Further downstream we see the velocity oscillate. This is due to the recirculation regions present near the walls.

The presence of a backpressure at the exit produces evident asymmetric results. Using a cold flow, we find that the asymmetric boundary layer separation is not related to combustion, but rather the turbulent shear stresses buckling the flowfield. Further investigation will include a diffuser connected to the isolator with the same backpressure applied at the exit.

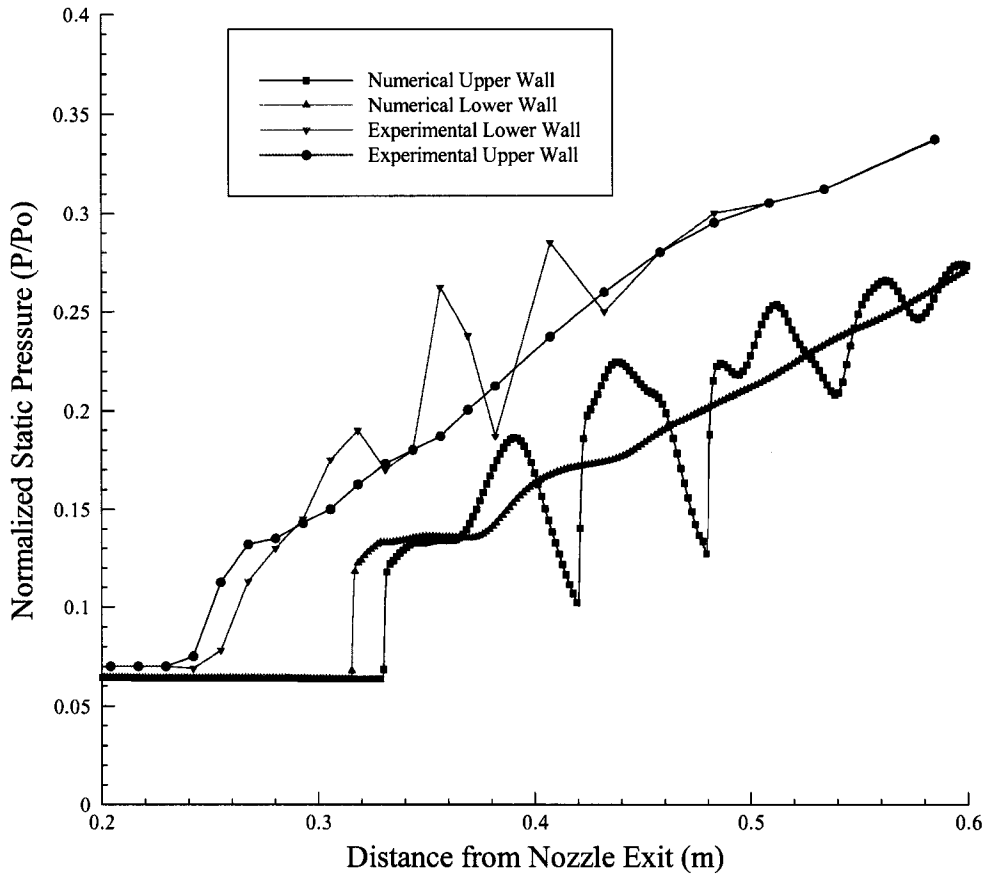

Figure 3.8 Normalized static pressure plot

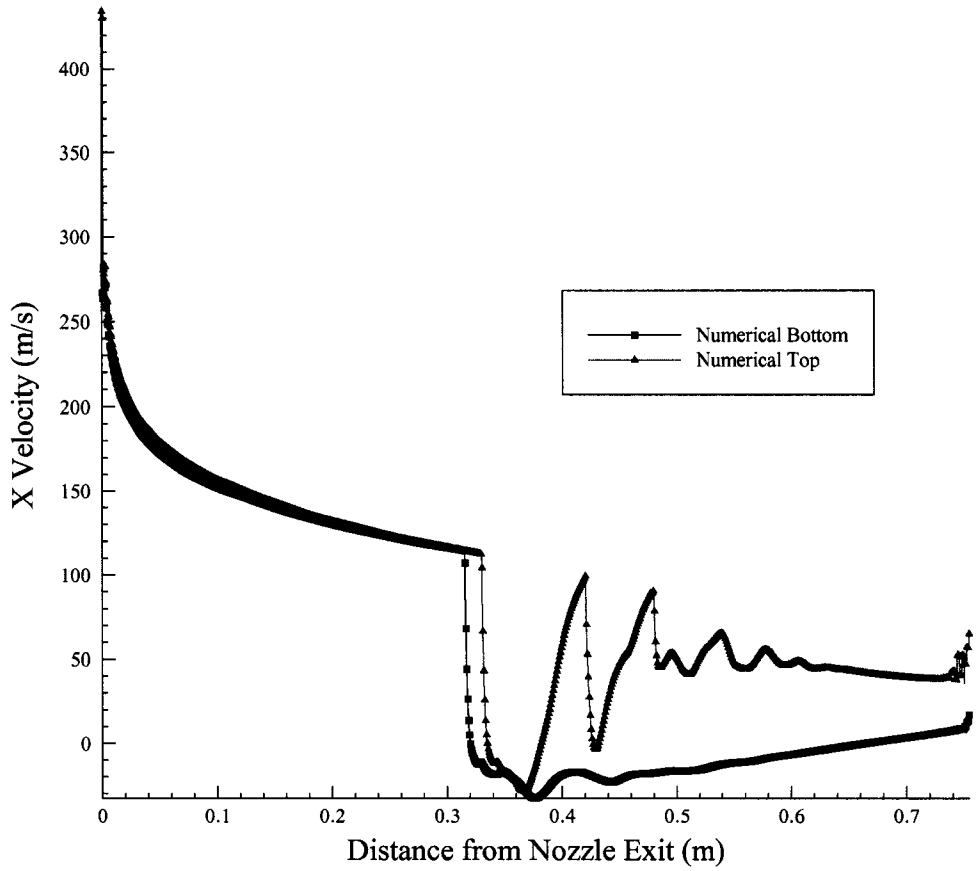

Figure 3.9 X Velocity plot comparison.

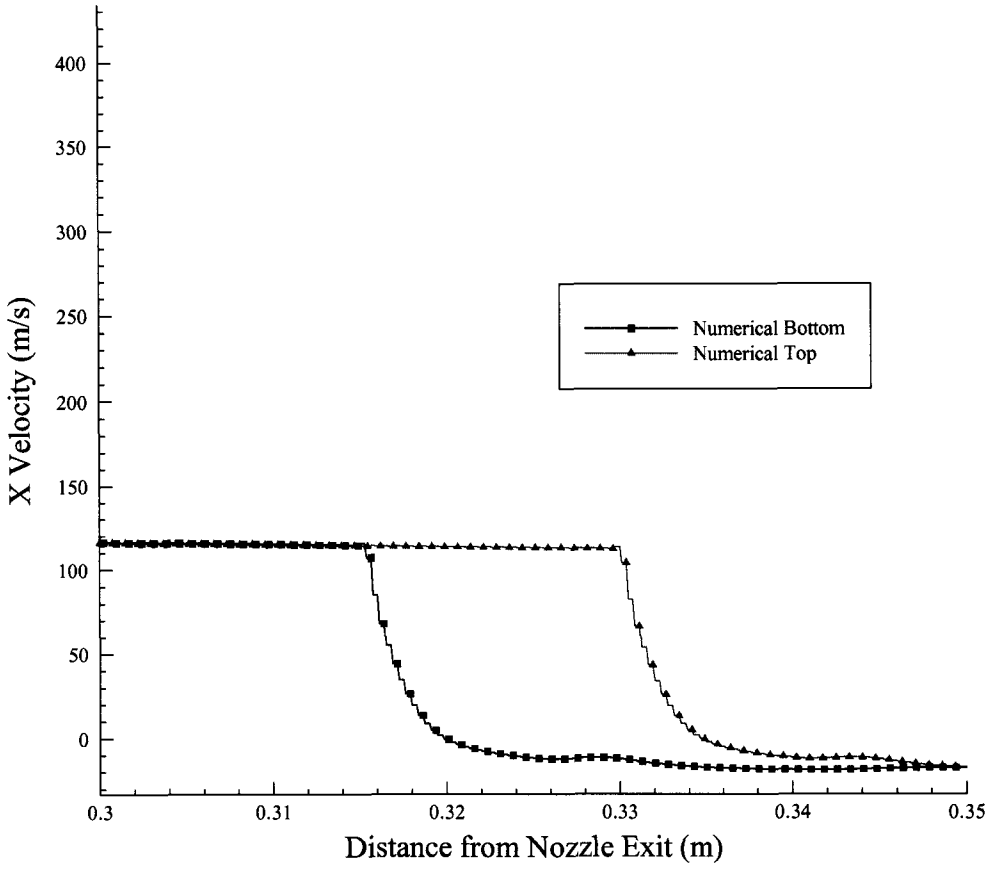

Figure 3.10 X Velocity showing boundary layer separation.

SECTION 4

HALF AND FULL DUCT RESULTS AND DISCUSSION

In this section, the results are shown for both the half and full duct constant area models. All models shown are two-dimensional. The results for the first case, $Po_j/P=120.2$, are compared from data obtained from Spaid and Zukoski[18] case number 13. Also Mohieldin et al.[8] conducted the same case number study as a CFD code validation.

4.1 Introduction

A study using computational fluid dynamics has been conducted on a two-dimensional transverse slot injection to observe the upstream interaction due to sonically injected Nitrogen into the Mach 3.5 free-stream. Spaid and Zukoski[17-18] have investigated this flowfield experimentally through a series of experiments. Rodriguez[38] and Mohieldin[8] have investigated this flowfield numerically by using the geometry and boundary conditions of Spaid and Zukoski. The actual experiment was constructed using a flat plate with a slot for the Nitrogen injection. End plates were used to give two-dimensional results. The results found numerically from the FLUENT CFD code have been compared to the experimental results for case 13 from the Spaid and Zukoski experiment.

4.2 Experimental Apparatus

The study of the interaction of gaseous Nitrogen from a transverse slot with supersonic vitiated free-stream air was conducted at the 20-inch supersonic wind tunnel in the Jet Propulsion Laboratory, California Institute of Technology during the late 1960's. Their study used supersonic vitiated free-stream air at Mach numbers of 2.61, 3.50, and 4.54. Nitrogen and Helium was used as injectants during the nineteen experiments. The gases were injected into the free-stream through an underexpanded sonic slot. End plates, made of glass, were added to each end of the slot for a couple of experiments to maintain two-dimensional results. Test-section flow and jet-reservoir

parameters, as well as static-pressure distributions on the surface of the plate near the jet were measured. For purposes of this study case 13 in Table 1 from Spaid and Zukoski[18] has been studied numerically.

4.3 Numerical Model

Half duct and full duct geometries have been numerically modeled using FLUENT version 5.5. Figure 4.1 shows the half duct geometry and computational mesh domain. Figure 4.2 shows the full duct geometry and computational mesh domain. The experiment conducted by Spaid and Zukoski used English units. For this study those units have been converted to SI units. The flat plate is 0.2286 m long with the injector in the middle at a diameter of 0.2667 mm. The height of the half duct was 0.1143 m, while the full duct was twice as high at a height of 0.2286 m. The computational mesh used a structured grid. At the wall boundaries and at the injector(s) the mesh aspect ratio decreased to produce more accurate boundary layers and shockwaves. The computational mesh domain size for the half duct consisted of 93,000 cells, while the full duct consisted of 186,000 cells.

Boundary conditions used in the half and full duct models are shown in Tables 4.1-4.3. At the walls no-slip and adiabatic boundary conditions were applied. Initialization for each model was performed at the air inlet. In all cases due to the low temperatures reaching convergence was difficult. The reason for this is that since the gas temperatures are so low, they lie outside the range of validity of the thermodynamic charts. Turbulence modeling was achieved by using the RNG $\kappa-\varepsilon$ turbulence scheme. A turbulent intensity of 1% was used as a constant throughout all models run. CFL numbers for all models began at 0.1 and steadily increased due to convergence criteria for each model.

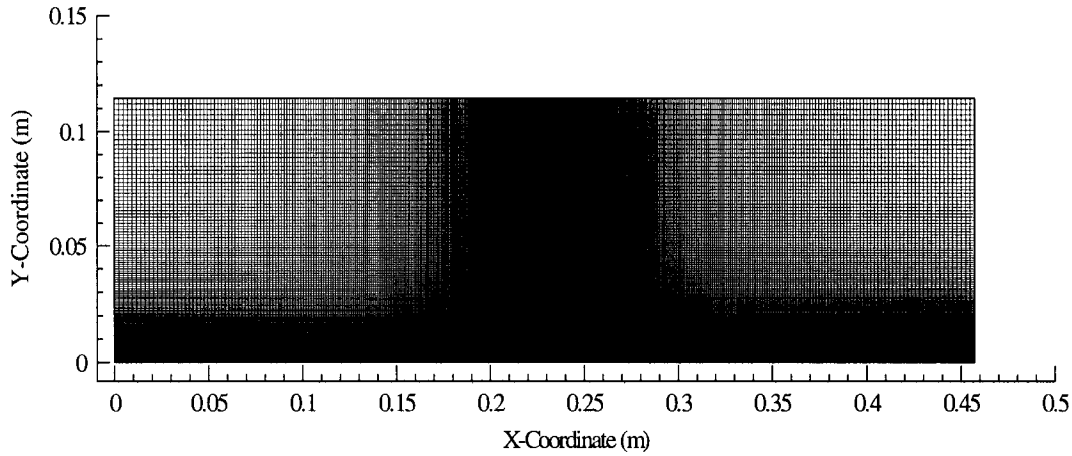

Figure 4.1 Half duct with normal injection and top symmetry.

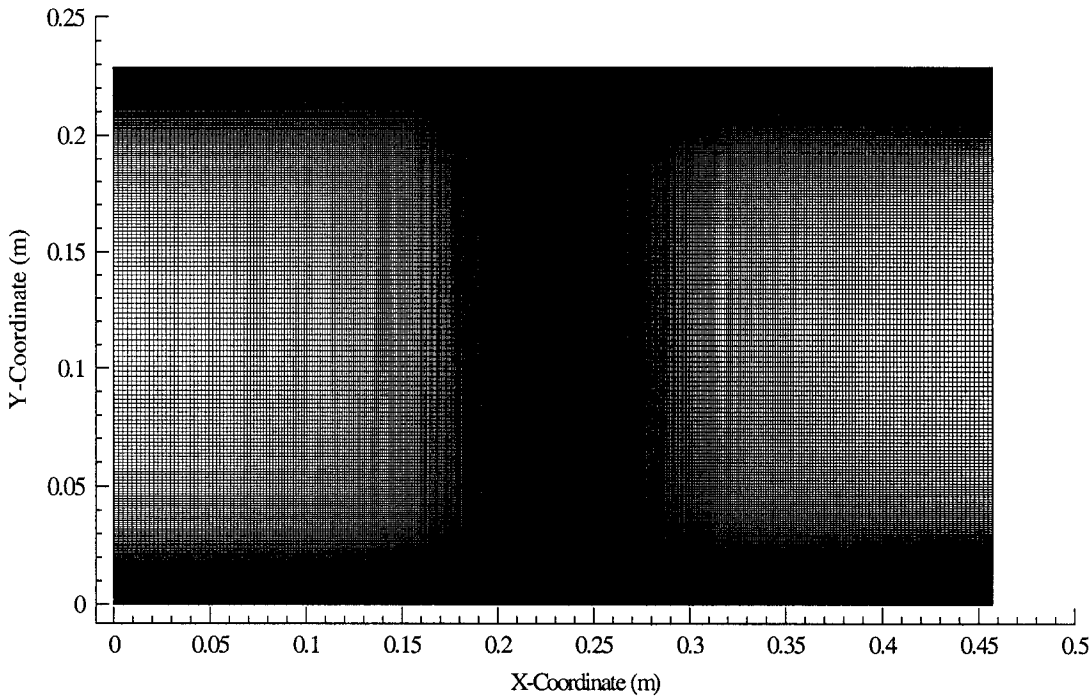

Figure 4.2 Full duct with opposed perpendicular injection.

4.4 Half and Full Duct Results

4.4.1 Results for $Po_j/P = 120.2$

Presented here is the investigation of transverse sonic injection of Nitrogen into a two-dimensional supersonic non-reacting flowfield. The half and full duct domains are investigated. Using the normalized wall pressure plot by Spaid and Zukoski[18], we compare the experimental results with that of the numerical data. Further investigation into the upstream interaction is studied by increasing the freestream-to-injector ratio.

The normalized wall static pressures for $Po_j/P=120.2$ are shown in Fig. 4.3. The normalization of the static pressure is achieved by taking the freestream air static pressure found by computation and dividing that by the given freestream air static pressure as shown in Table 4.1. The numerical results show acceptable agreement with the experimental data of Spaid and Zukoski[18]. The numerical comparison between the half and full duct are almost identical, where the half duct is slightly over predicted. A 1% turbulence intensity was used in achieving this result numerically. Greater accuracy may have been achieved if a higher turbulence intensity is used. The over prediction of the numerical model may be due to the turbulence scheme used or the fact that we have uniform boundary conditions with calorically perfect gases assumed.

Figures 4.4 and 4.5 show the velocity in the x-coordinate direction at a point 0.254 mm from the top and bottom walls. Figure 4.5 shows the separation region where the boundary layer separates from the wall. Figure 4.4 shows the whole domain of each of the half and full ducts. The separation occurs when there is a sharp drop in the velocity. In this case both the half and full duct models show good agreement in the data. But for clarity, we zoom in on the separation region and see the top and bottom boundary layer of the full duct begins to separate approximately 0.5 mm before the boundary layer of the half duct. From this we begin to see the importance of modeling the entire geometry.

Table 4.1 Boundary conditions used in the Spaid and Zukoski experiment.

	Freestream Air	Nitrogen Injectant
M	3.5	1.0
P_t (kPa)	240.627	379.901
P_s (kPa)	3.158	200.637
T_t (K)	314.44	291.67
T_s (K)	91.67	243.33
Velocity (m/s)	670.56	317.906

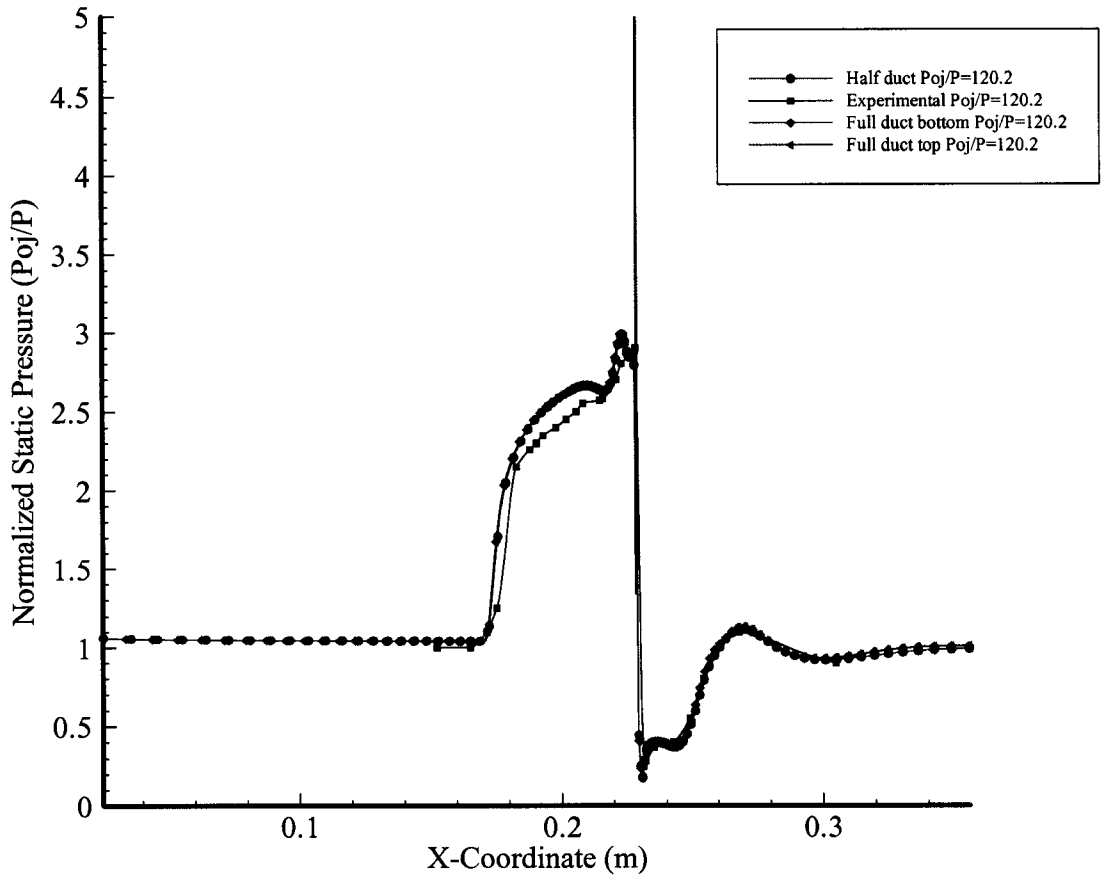

Figure 4.3 Wall normalized static pressure plot for $P_{oj}/P=120.2$.

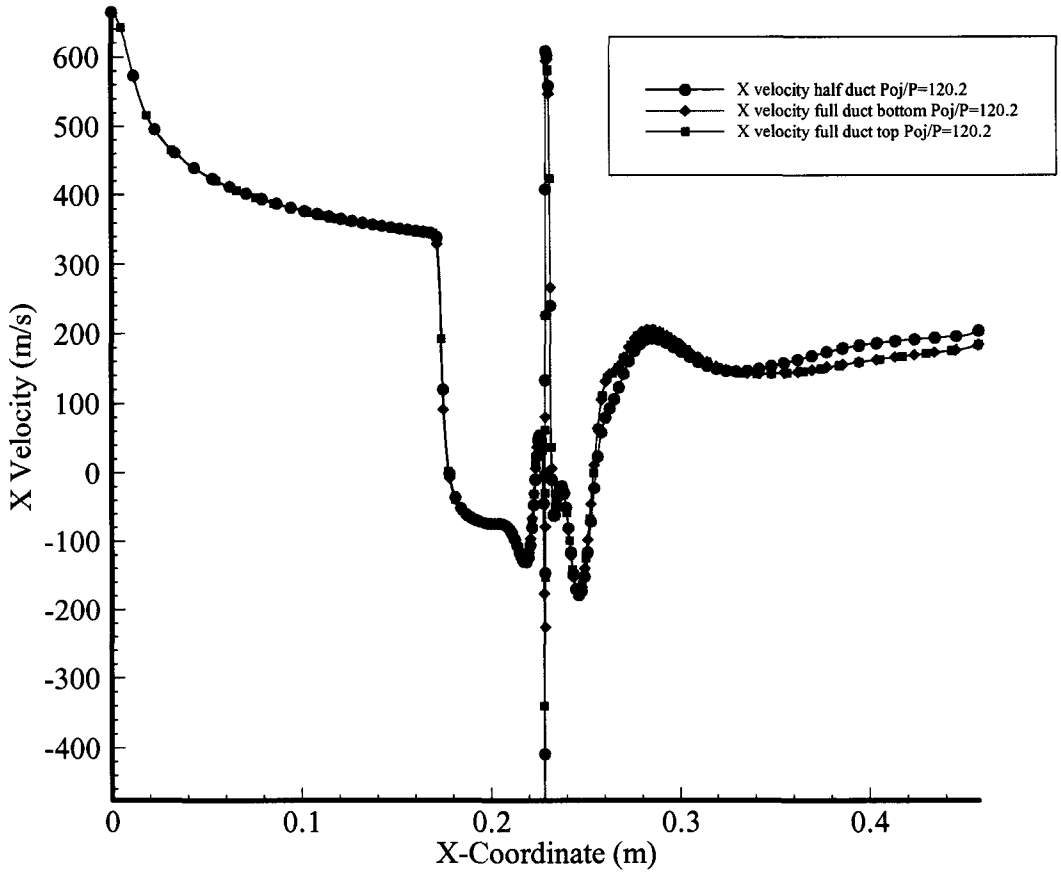

Figure 4.4 X velocity plot at 0.254 mm from wall for $Po_j/P=120.2$.

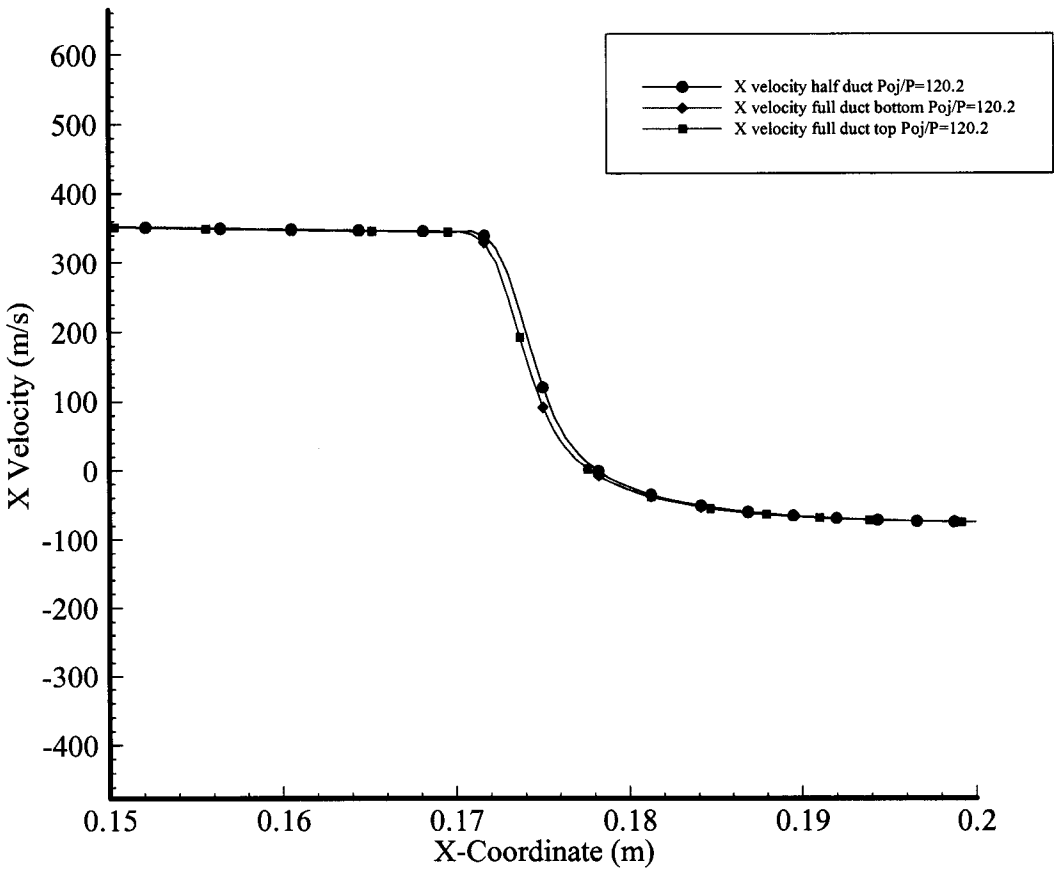

Figure 4.5 X velocity plot of separation region at 0.254 mm from walls for Po_j/P=120.2.

Figures 4.6 and 4.7 show the Mach number contours for both the half and full duct geometries. Figure 4.6 shows the Mach number contours for the whole domain while Fig. 4.7 shows the Mach number contours for the separation region. The Mach contours in Fig. 4.6 clearly show how the injection causes the flow to separate, due to blocking the incoming airflow, causing the bow shock, and how the flow Mach number is subsonic within the separation or circulation region. As the Nitrogen is injected, the barrel shocks are evident and the Mach disc is present in Fig. 4.7. Within the circulation region the wall pressure increases. This is evident in Fig. 4.3. The comparison between the half and full Mach contours show almost identical results. The full duct shows Mach number symmetry between the top and bottom walls.

The normalized static pressure contours plots are presented in Figs. 4.8 and 4.9. The freestream air normalizes the flow. Figure 4.8 shows the entire domain. You can also see the separation shock and bow shocks clearly in the figures. By comparing the half and full duct, we find that there is very little deviation between the two models. Since the flow is fully turbulent it is very difficult to achieve convergence. This is one reason why we see that the normalized results in the freestream do not result in unity. The other reason could be when the data is taken. The wall pressures may be steady; however there may be fluctuations in the flow, thus giving varying normalized results. In Fig. 4.9, the increase in the circulation region can be directly compared to Fig. 4.3. As the flow separates, the wall pressure rises in the circulation region until it reaches the injector where the pressure then rapidly decreases and then increases to normalized conditions.

Nitrogen mole fraction contours are shown in Figs. 4.10 and 4.11. The recirculating region, due to the separation shock, convects the injected Nitrogen upstream and circulates it in a clockwise direction. This is shown clearer in Fig. 4.11. Due to the low freestream to injectant pressure ratio, the penetration of the Nitrogen into the freestream is close to the walls in both the half and full duct cases.

Finally, the velocity vector and streamline contour plots are given in Figs. 4.12 and 4.13. Figure 4.12 shows the entire domain and how the flow affects the separation shock by the injected Nitrogen. We look at Fig.4.13 to get a closer view of the vortices created by the blockage caused by the injected Nitrogen. The vortices are formed upstream of the injector. This recirculation region is caused by the blockage of the

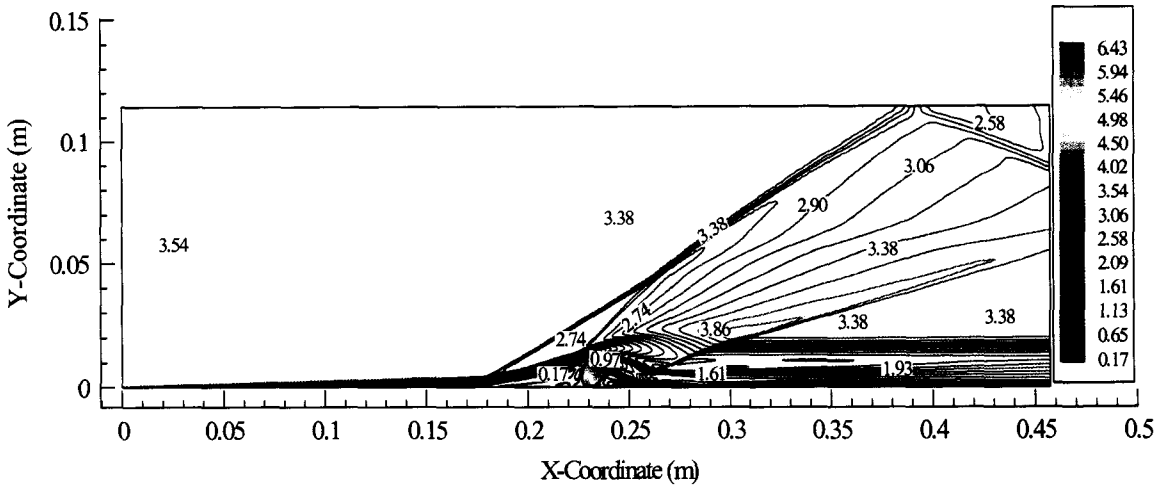

a. Mach number contour plot for half duct geometry.

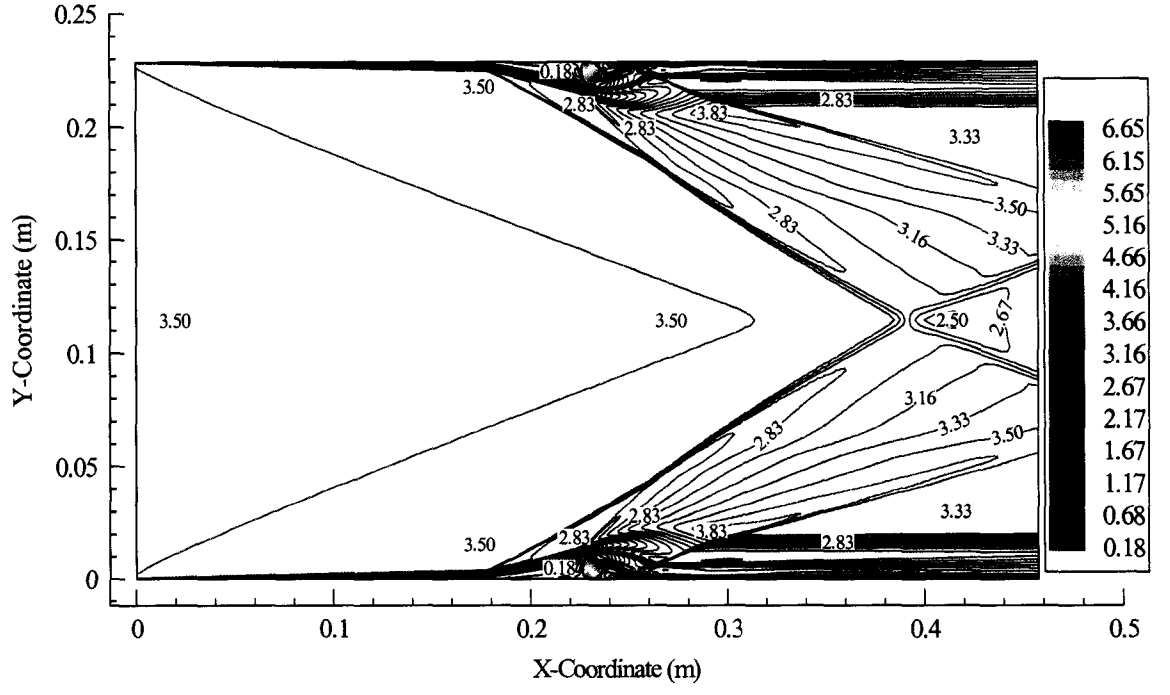

b. Mach number contour plot for full duct geometry.

Figure 4.6 Mach number contour plots for the entire geometry domain, $Po_j/P=120.2$.

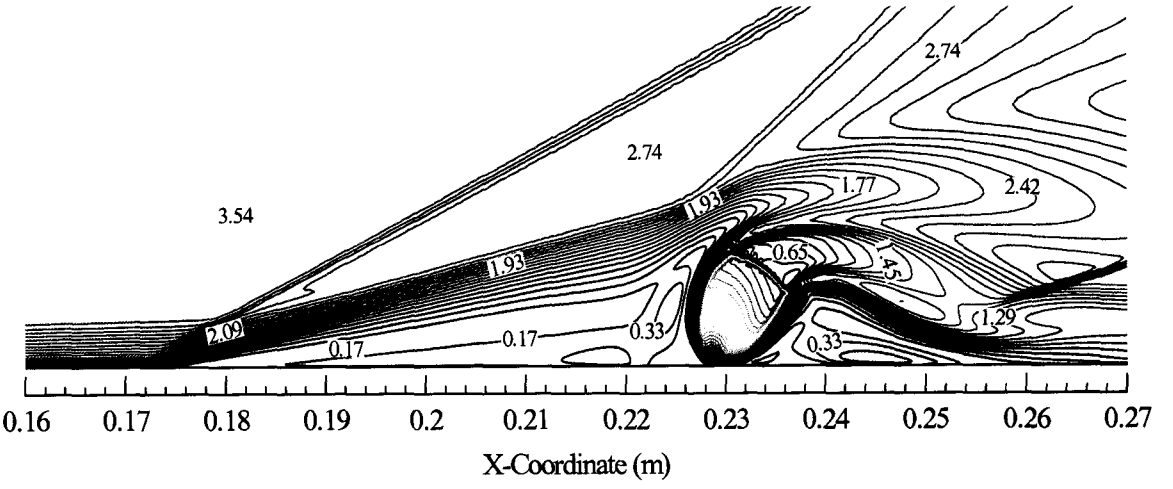

a. Bottom half duct injection

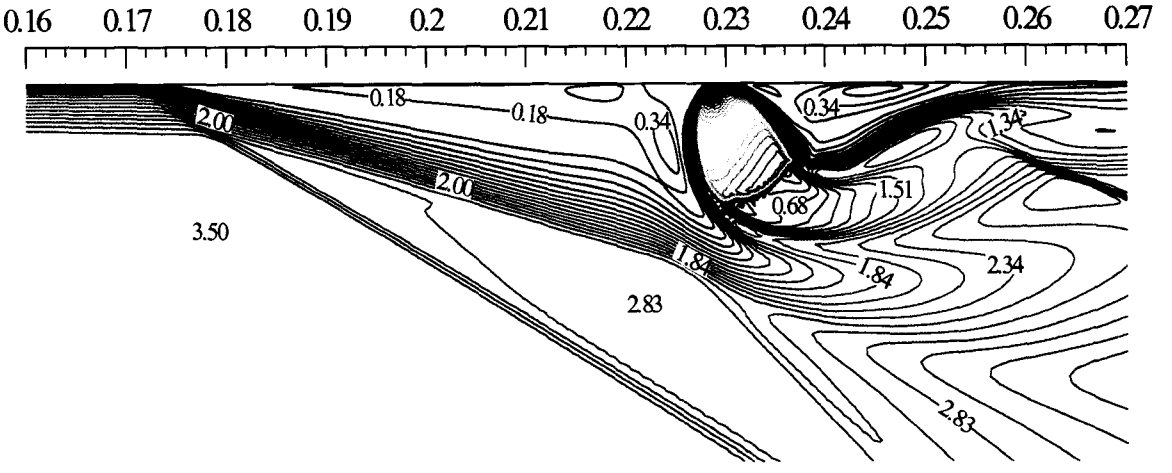

b. Top full duct injection

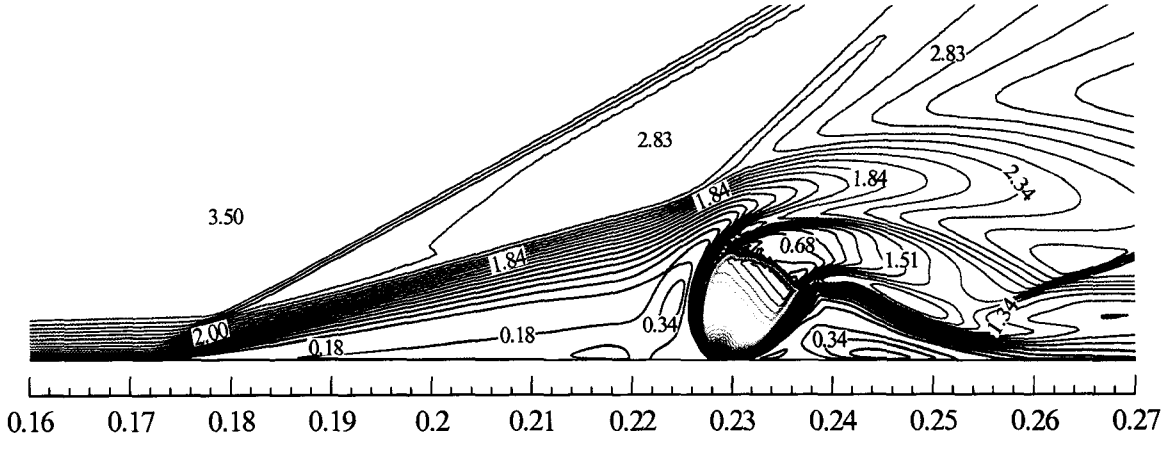

c. Bottom full duct injection

Figure 4.7. Mach number contour plots for half and full duct geometries, $Po_j/P=120.2$.

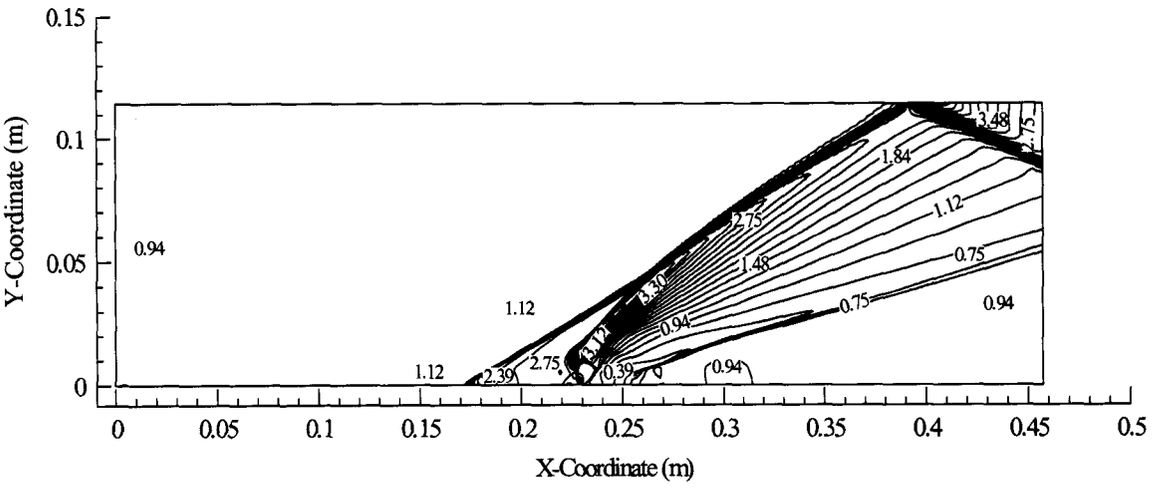

a. Normalized static pressure contour plot for half duct geometry.

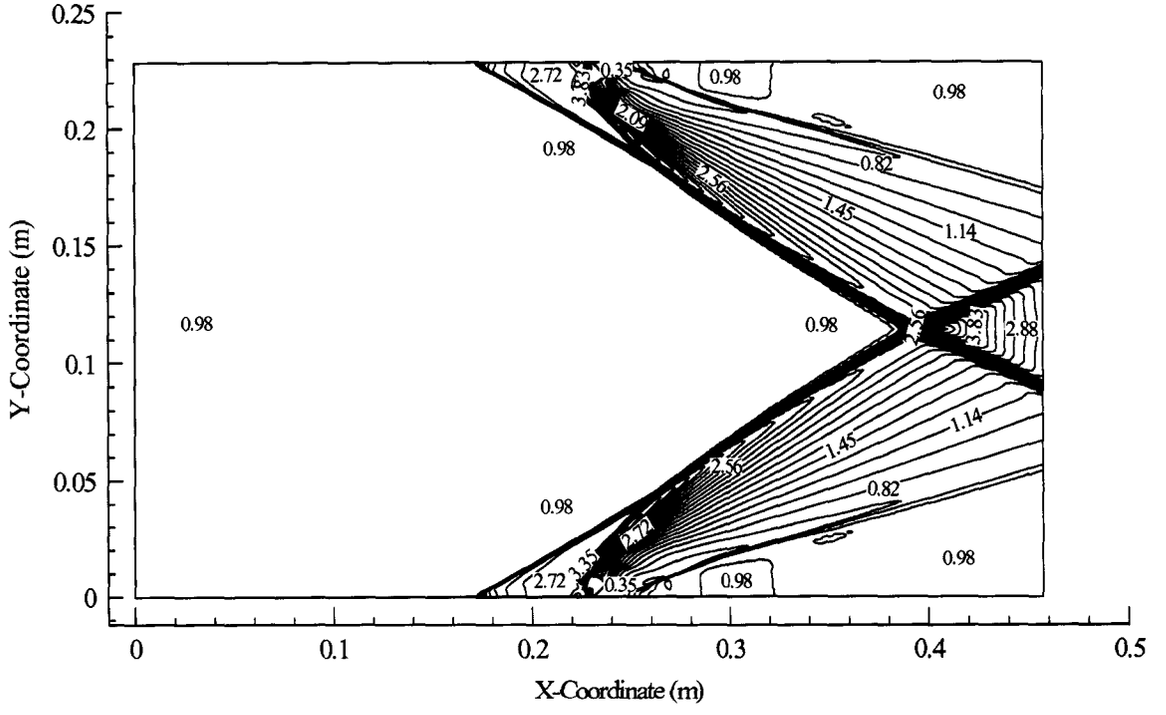

b. Normalized static pressure contour plot for full duct geometry.

Figure 4.8 Normalized static pressure contour plots for the entire geometry domain, $Po_j/P=120.2$.

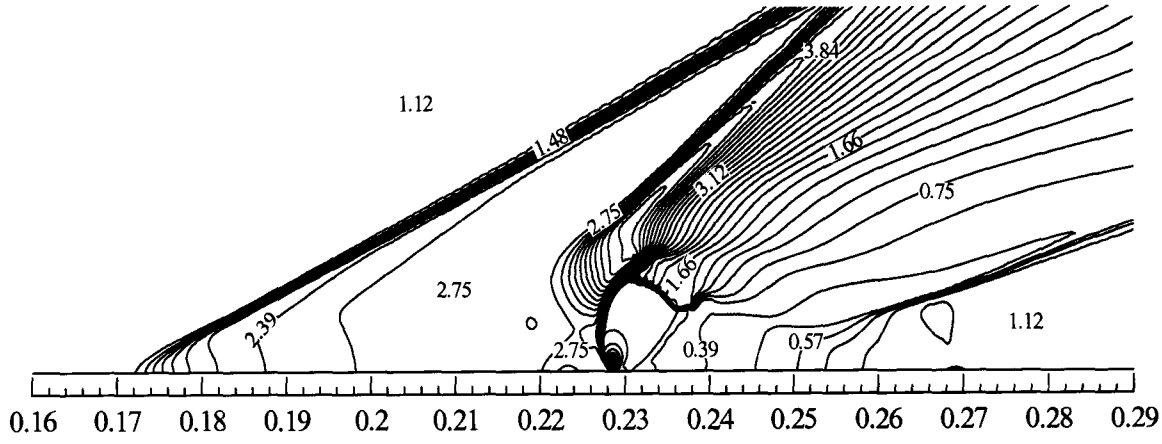

a. Bottom half duct injection

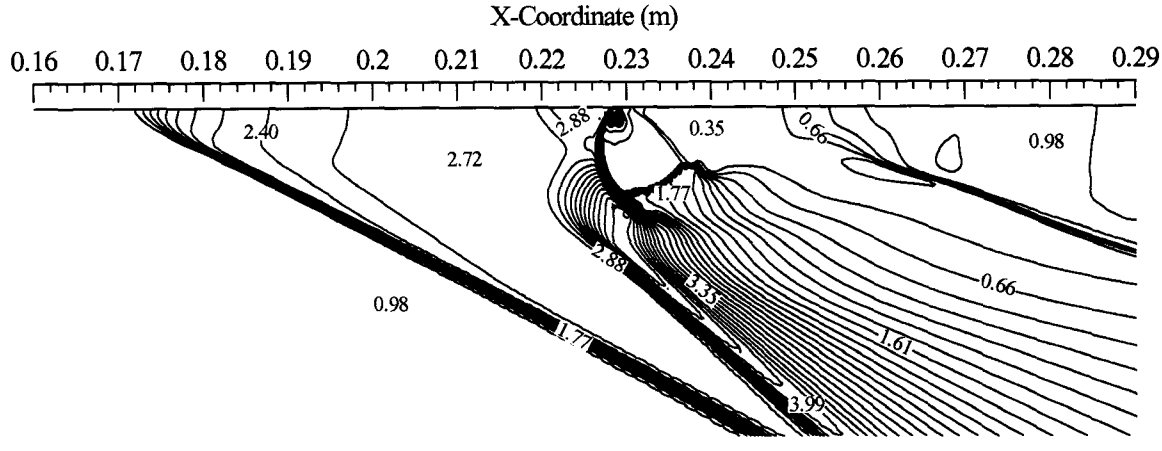

b. Top full duct injection

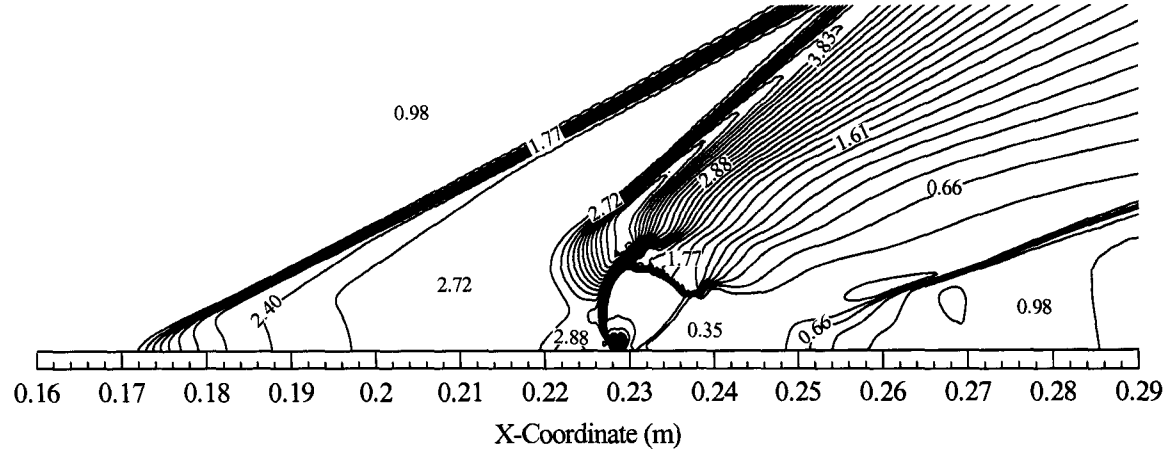

c. Bottom full duct injection

Figure 4.9. Normalized static pressure contour plots for half and full duct geometries, $Po_j/P=120.2$.

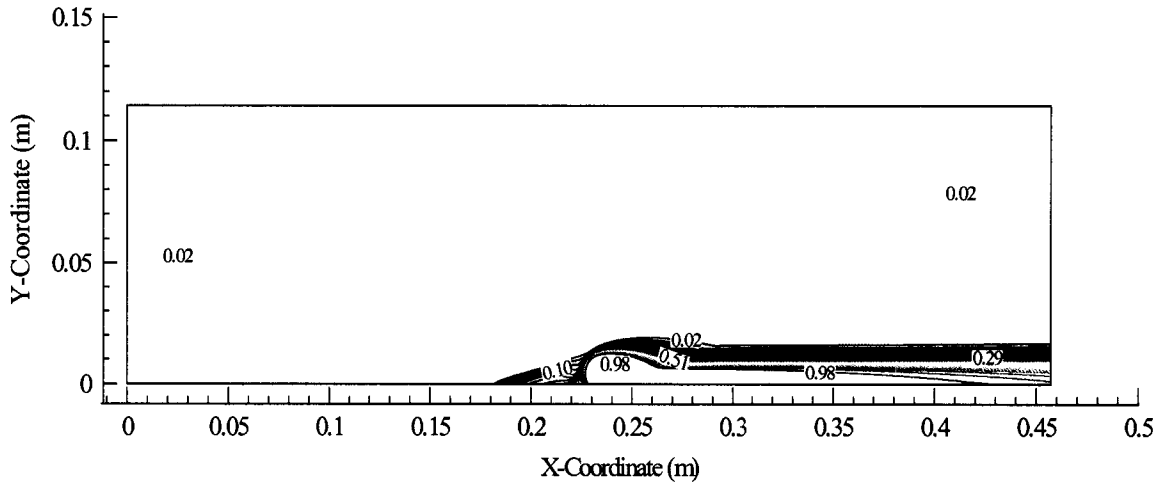

a. Nitrogen mole fraction contour plot for half duct geometry.

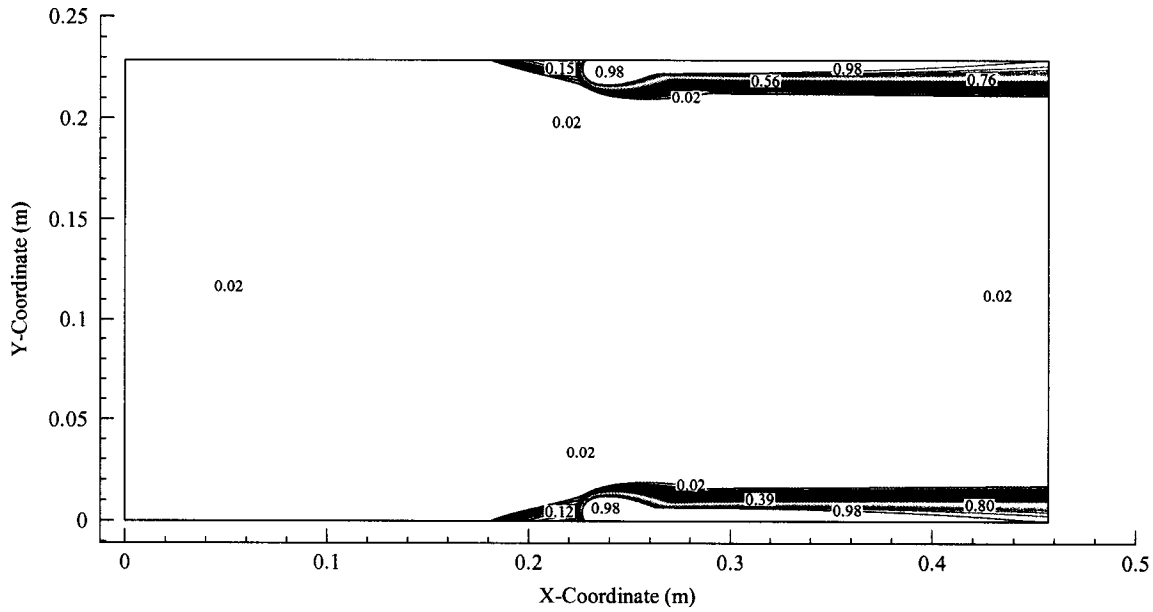

b. Nitrogen mole fraction contour plot for full duct geometry.

Figure 4.10 Nitrogen mole fraction contour plots for the entire geometry domain, $Po_j/P=120.2$.

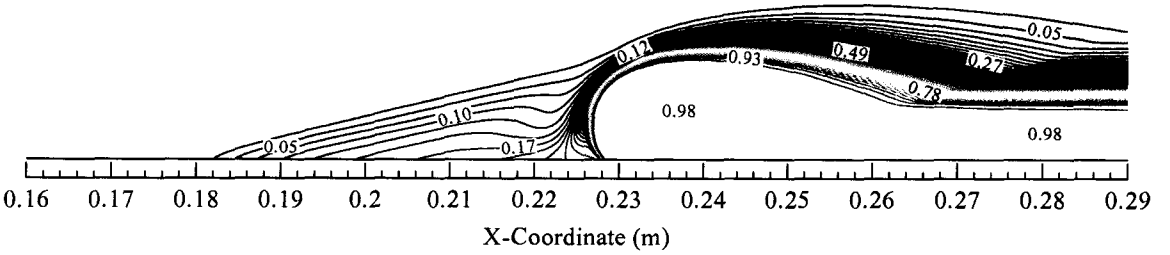

a. Bottom half duct injection

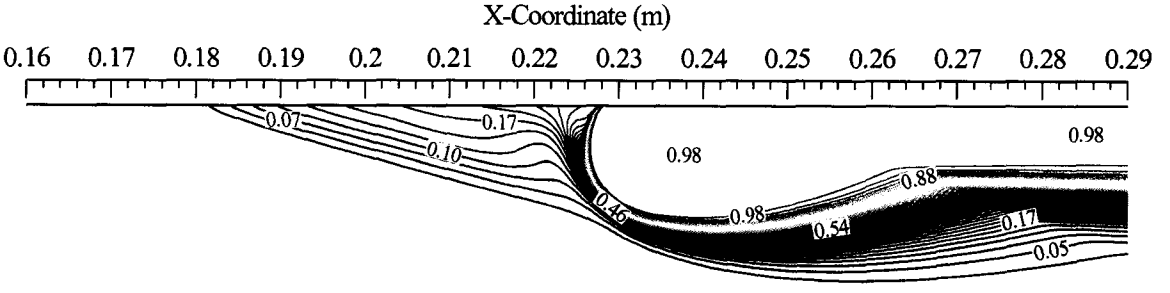

b. Top full duct injection

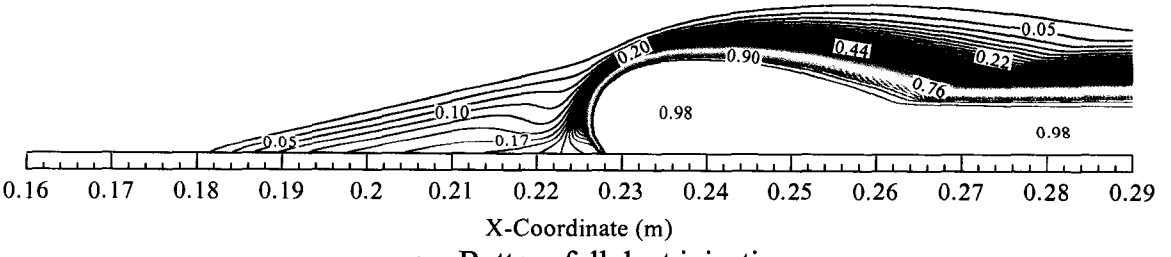

c. Bottom full duct injection

Figure 4.11 Nitrogen mole fraction contours plots for $Po_j/P=120.2$.

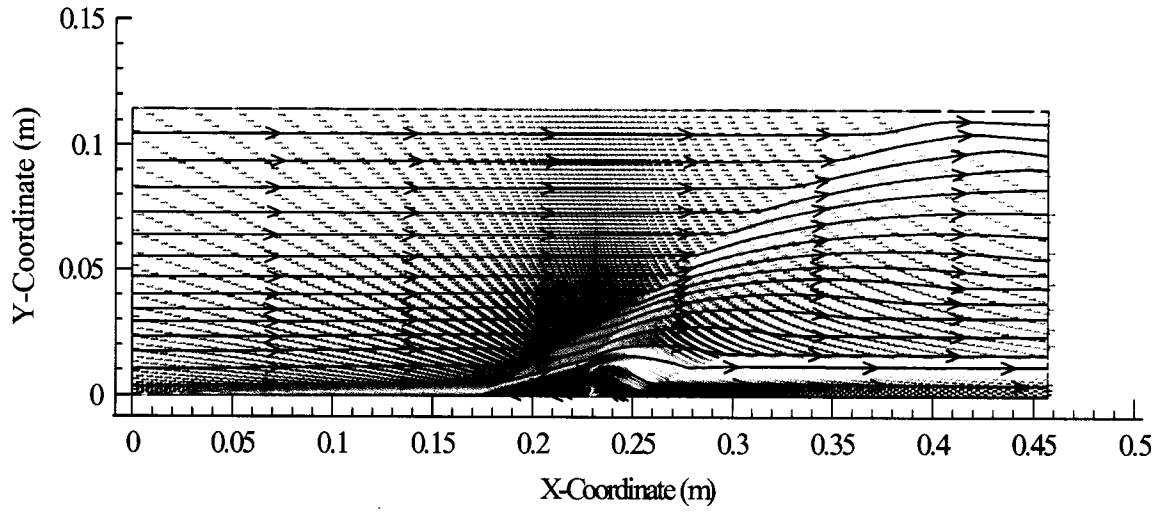

a. Velocity vector and streamline plot for half duct geometry.

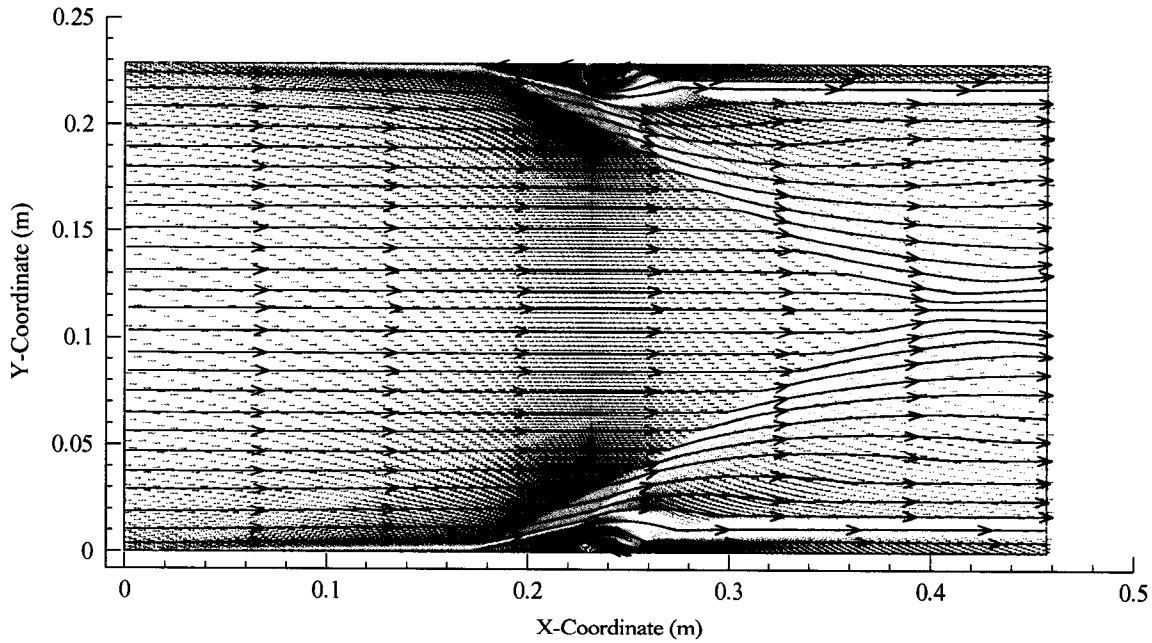

b. Velocity vector and streamline plot for full duct geometry.

Figure 4.12 Velocity vector and streamline plot for the entire geometry domain, $Po_j/P=120.2$.

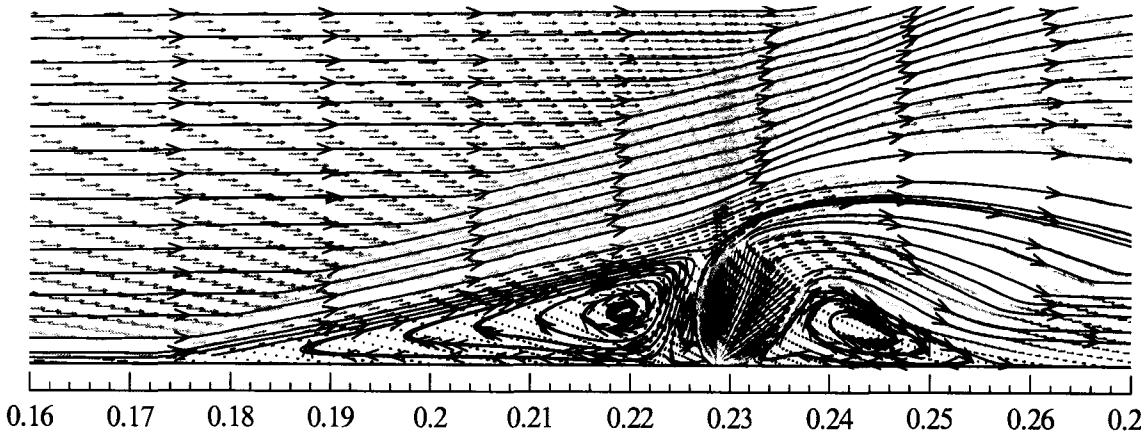

a. Bottom half duct injection

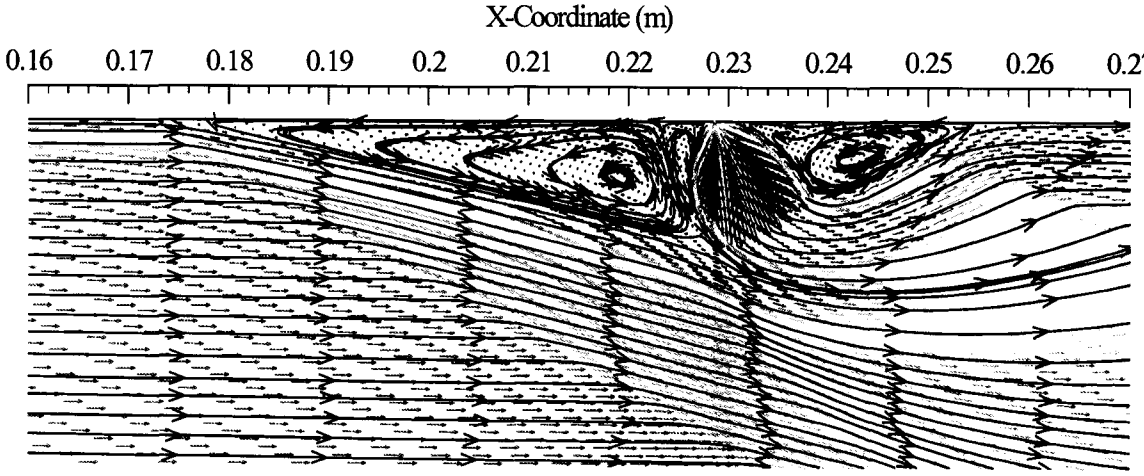

b. Full duct top injection

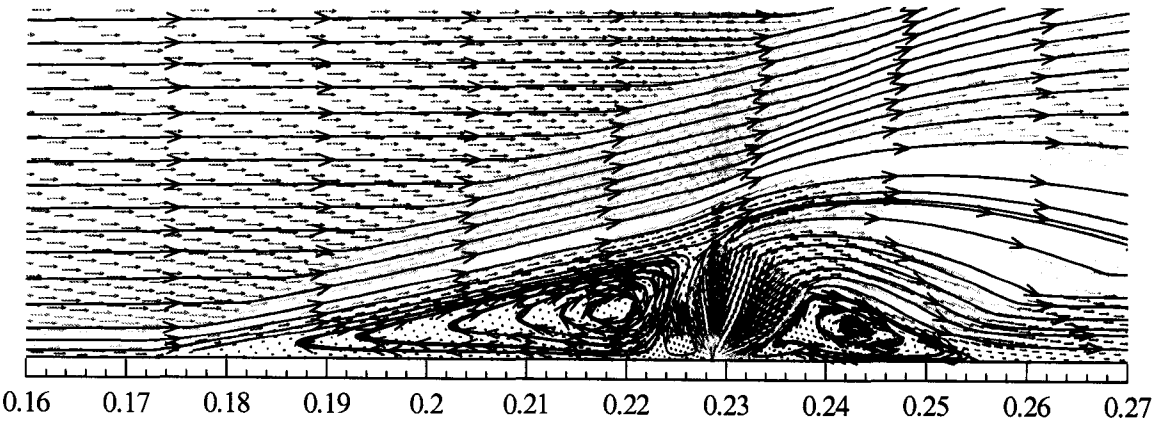

c. Full duct bottom injection

Figure 4.13 Velocity vector and streamline plots for Po_j/P=120.2.

freestream flow causing it to separate from the wall. The velocity in this circulation region is subsonic, due to the separation shock. Downstream of the injector we have a recompression shock that reattaches itself to the boundary layer. Within this recompression shock we also have a recirculation region and that region is also subsonic.

4.4.2 Results for $Po_j/P = 240.4$

The next model increases the freestream to injector pressure ratio by decreasing the total and absolute pressures of the freestream flow. The freestream static and total pressure was divided by a factor of two. Table 4.2 shows the boundary conditions for this numerical model.

Figure 4.14 shows the wall normalized static pressure plot for $Po_j/P=240.4$. The plot shows that the half duct and full duct, top and bottom, does not deviate from each other. The separated flow, due to the increase in pressure ratio, has moved further upstream. Figures 4.15 and 4.16 give the velocity in the x-coordinate direction. In Fig. 4.15, we examine how the separation has moved upstream and that the separation points of both cases look exact. However in Fig. 4.16 we can see that the separation of the full duct begins slightly further upstream. The distance can be shown as approximately 0.25 mm. This distance is much closer together than for $Po_j/P=120.2$.

Mach numbers contours are presented in Figs. 4.17 and 4.18. The injector is beginning to "bloom" as the pressure ratio increases. If we compare Fig. 4.7 and 4.18, we see how the barrel shocks begin to expand outwards. There is very little change in Mach number within the recirculating regions as compared to $Po_j/P=120.2$. The only difference between the two is shown in Figs. 4.7 and 4.17. Within the injected region we see that the Mach number has increased from 6.65 to 7.47. We can see how far upstream the separation shock has proceeded. There are slight differences between the half and full duct models. The Mach numbers for the full show symmetric agreement between the top and bottom walls. The difference between Mach numbers for the half and full duct could be attributed to residual stoppage.

Table 4.2 Half pressure boundary conditions.

	Freestream Air	Nitrogen Injectant
M	3.5	1.0
P_t (kPa)	120.314	379.901
P_s (kPa)	1.579	200.637
T_t (K)	314.44	291.67
T_s (K)	91.67	243.33
Velocity (m/s)	670.56	317.906

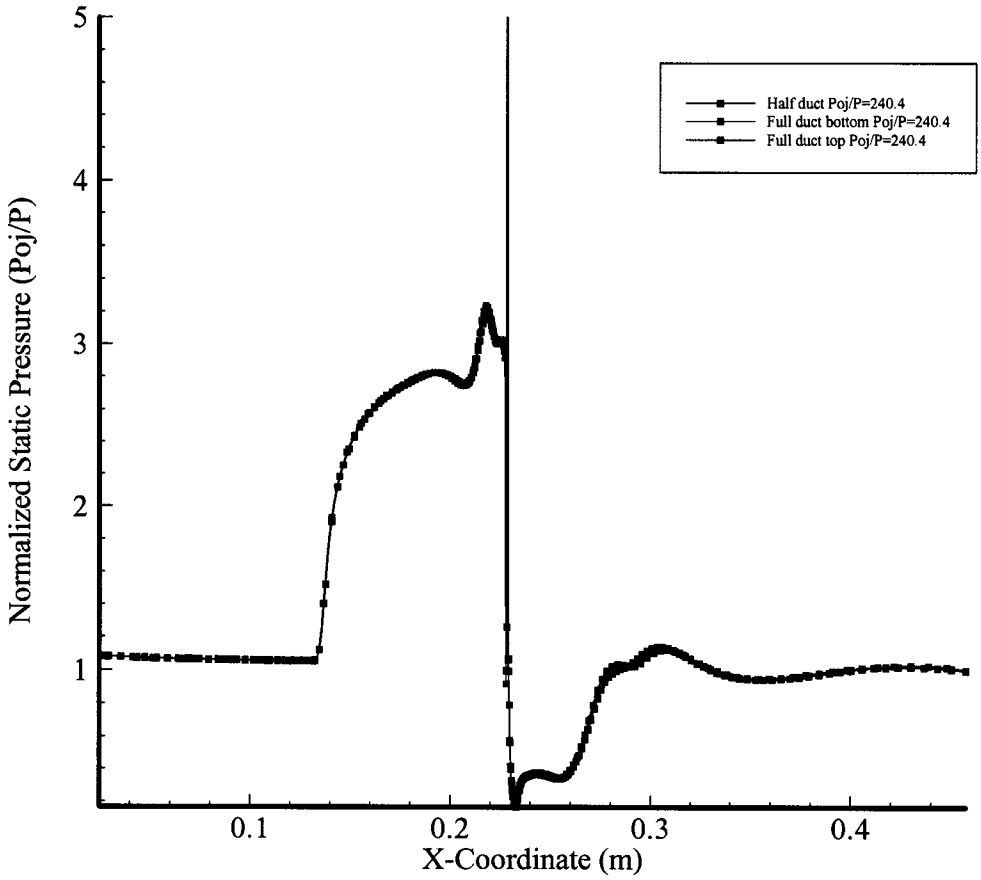

Figure 4.14 Wall normalized static pressure plot for $P_{oj}/P=240.4$.

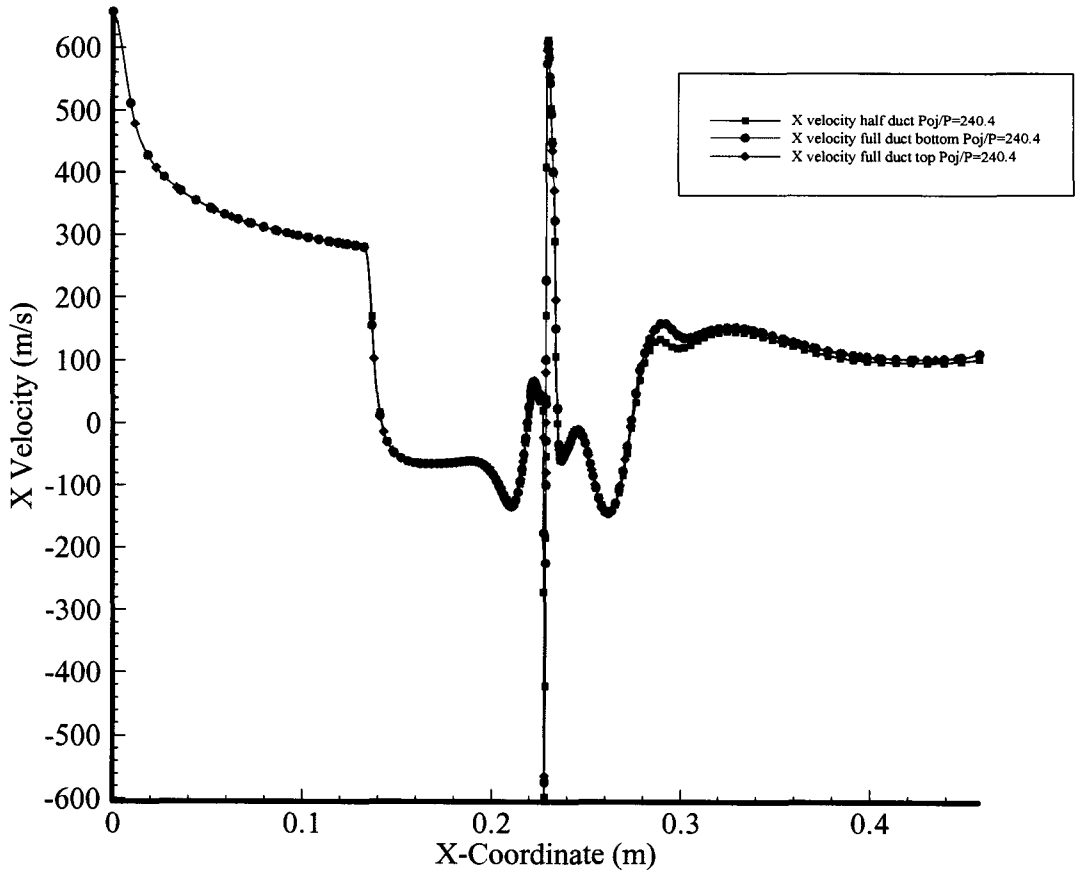

Figure 4.15 X velocity plot at 0.254 mm from wall for Po_j/P=240.4.

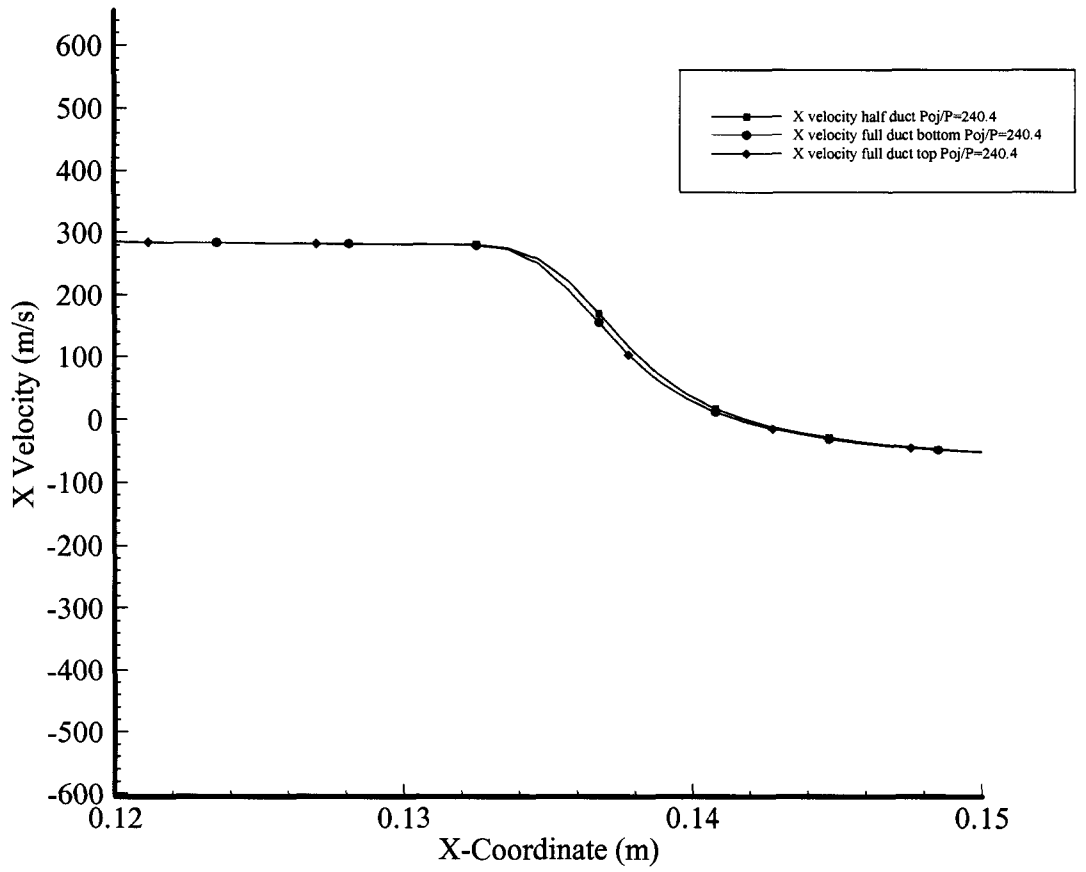

Figure 4.16 X velocity plot of separation region at 0.254 mm from wall for Po_j/P=240.4.

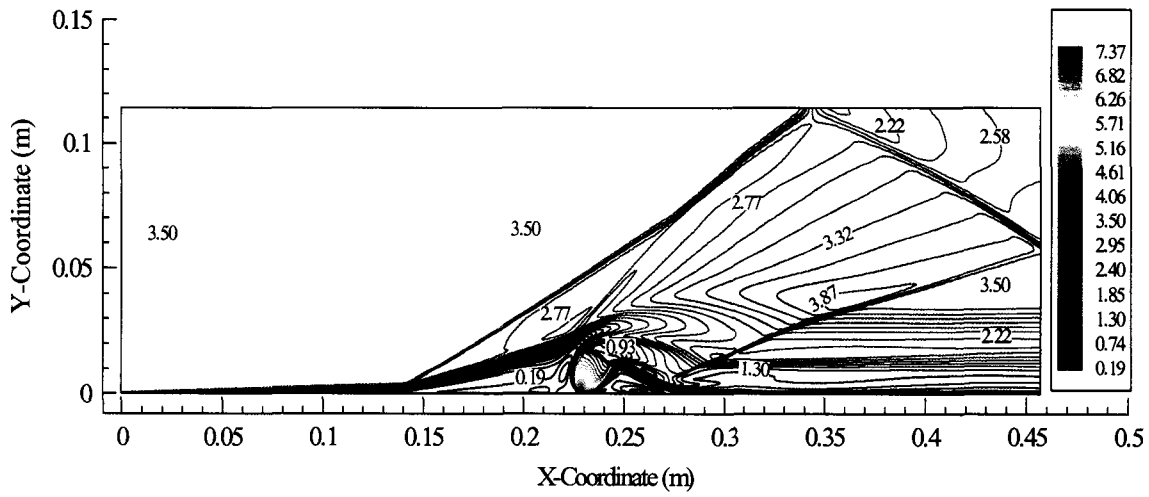

a. Mach number contour plot for half duct geometry.

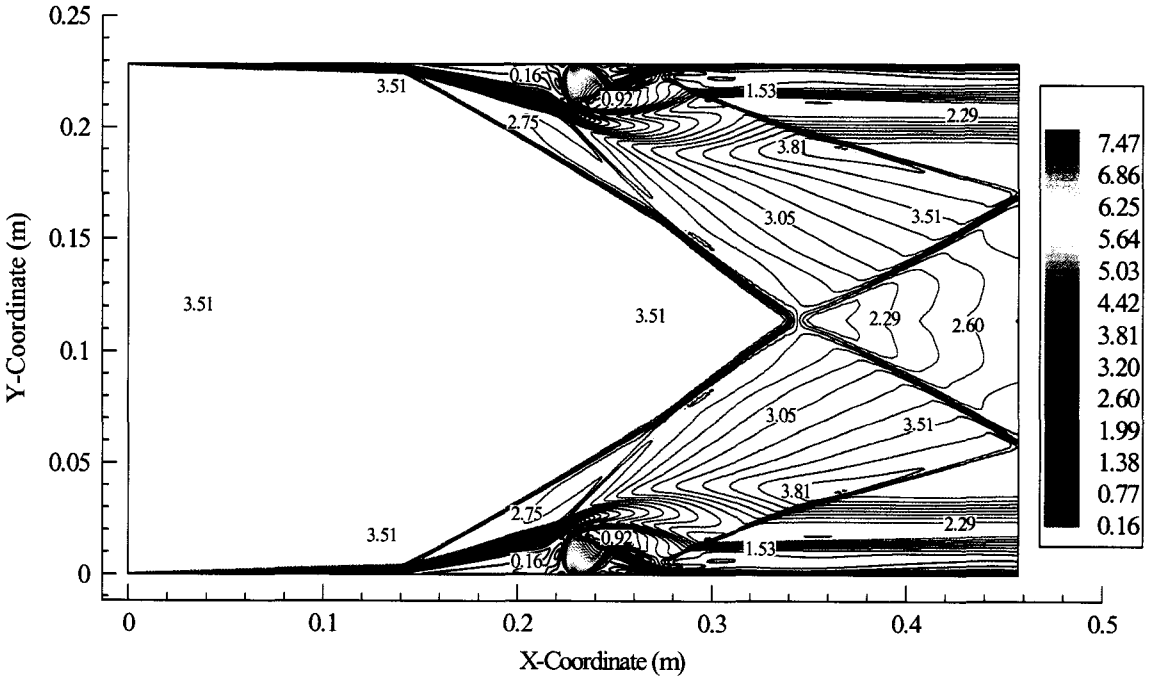

b. Mach number contour plot for full duct geometry.

Figure 4.17 Mach number contour plots for the entire geometry domain, Po_j/P=240.4.

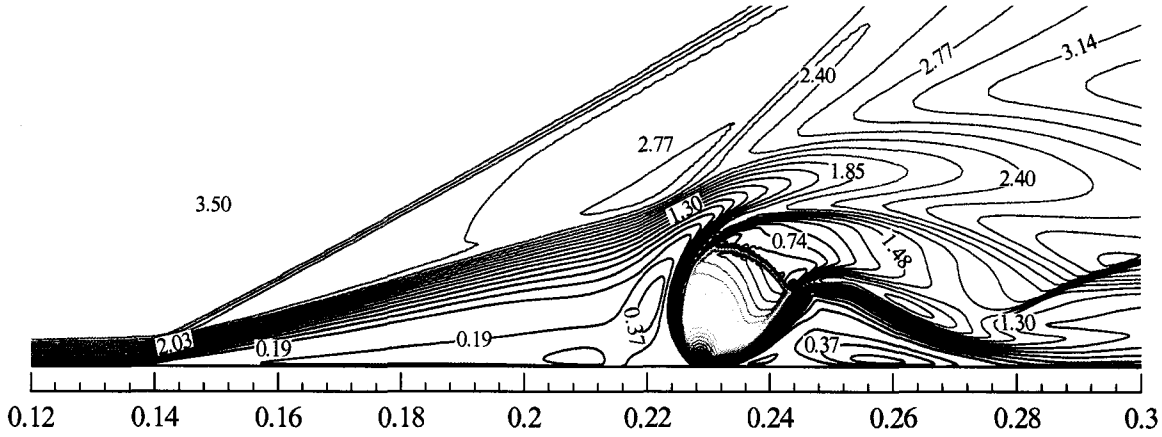

a. Bottom half duct injection

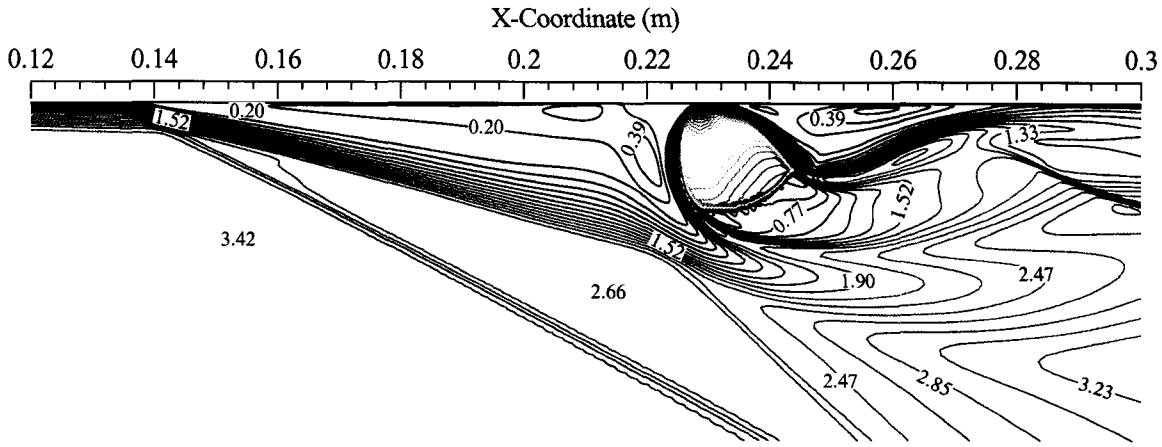

b. Top full duct injection

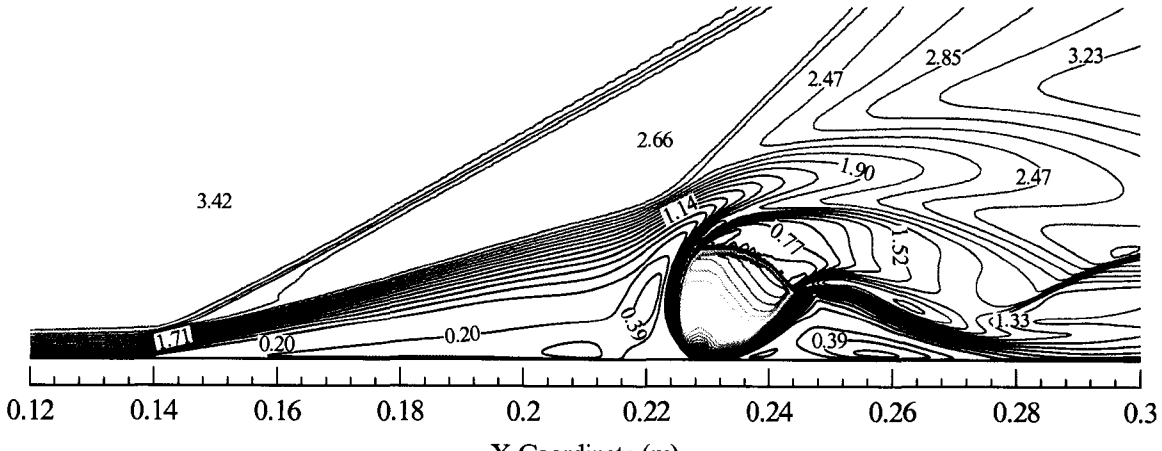

c. Bottom full duct injection

Figure 4.18 Mach number contour plots for half and full duct geometries, Po_j/P=240.4.

Figures 4.19 and 4.20 show the normalized static pressure contour plots for $Po_j/P=240.4$. Again we see how the separation shock has moved upstream due to the increase in pressure ratio and how the injector region is "blooming". The data shown by the full duct shows symmetric results and the difference between the half and full duct are minimal.

Nitrogen mole fraction contour are given in Figs 4.21 and 4.22. The increase in penetration height is due to the increase in pressure ratio. The upstream interaction convects the Nitrogen upstream into the larger recirculation region. Figure 4.22 shows this much clearer. The half and full ducts show nearly identical results.

Velocity vector and streamline contour plots are presented in Figs. 4.23 and 4.24. Figure 4.24 shows the "budding" or "fanning" of the injector region. The half duct tends to be bending more and slightly narrower than the full duct. This could be due to symmetry boundary condition applied to the top of the half duct. Vortices are present within the separated regions. These vortices are further elongated due to the increase upstream as well as downstream.

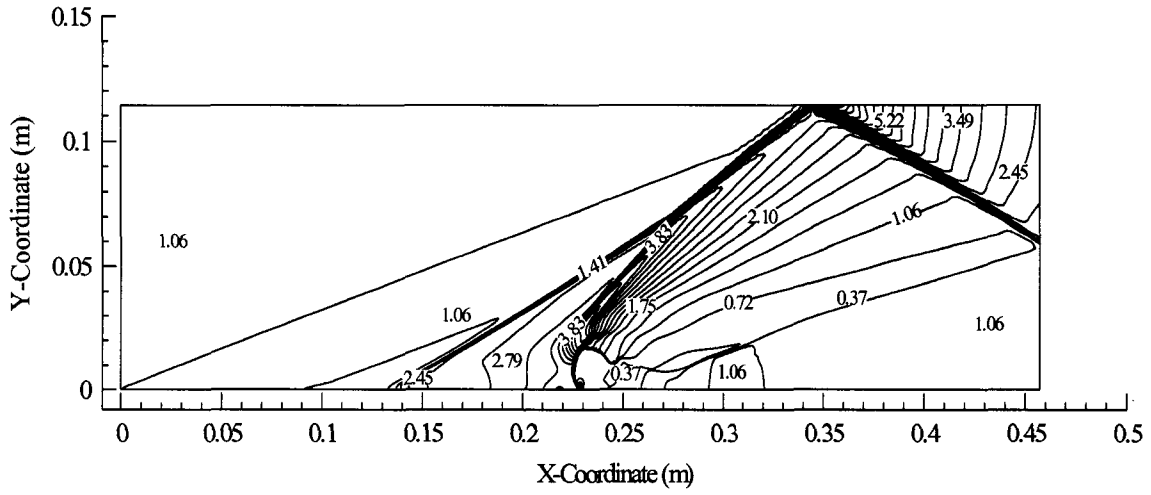

a. Normalized static pressure contour plot for half duct geometry.

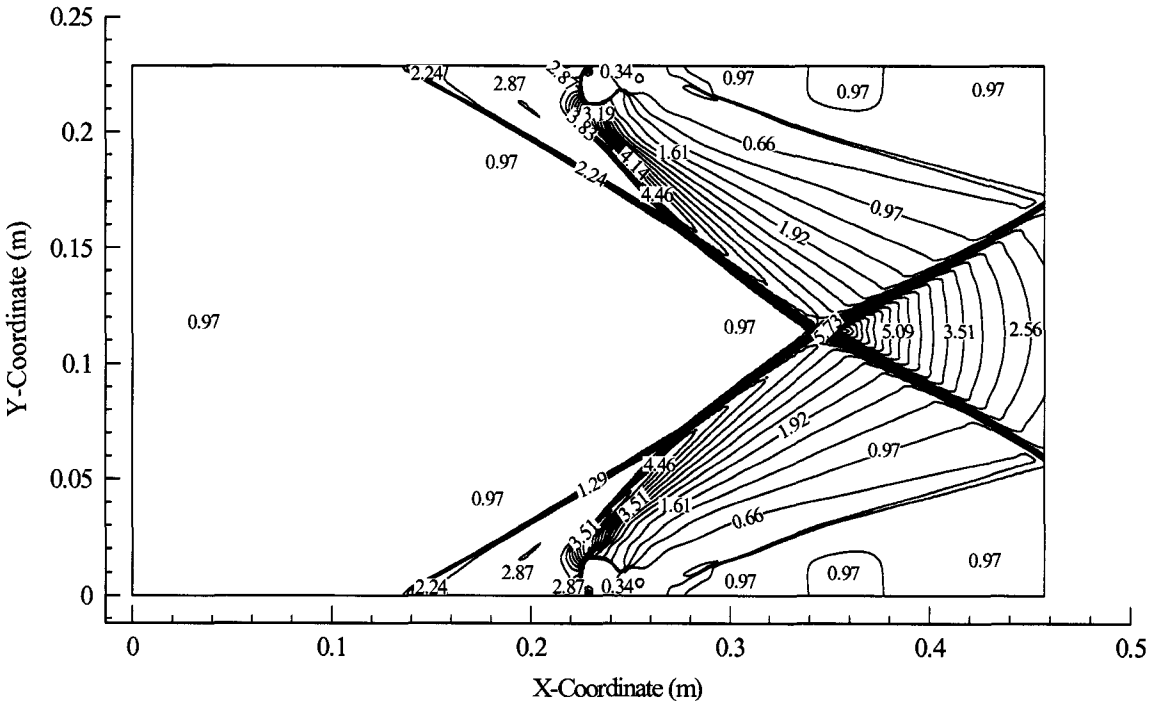

b. Normalized static pressure contour plot for full duct geometry.

Figure 4.19 Normalized static pressure contour plots for the entire geometry domain, $Po_j/P=240.4$.

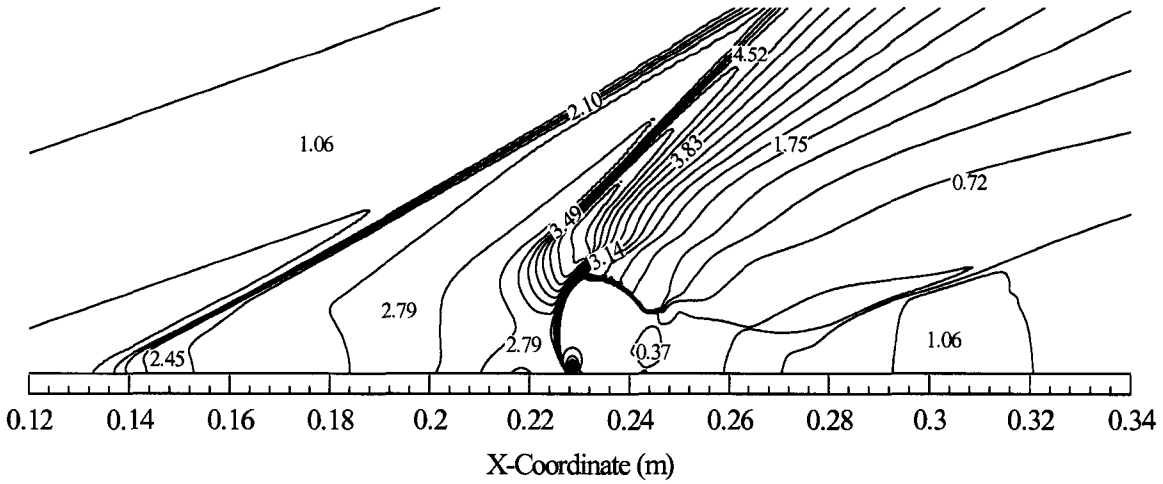

a. Bottom half duct injection

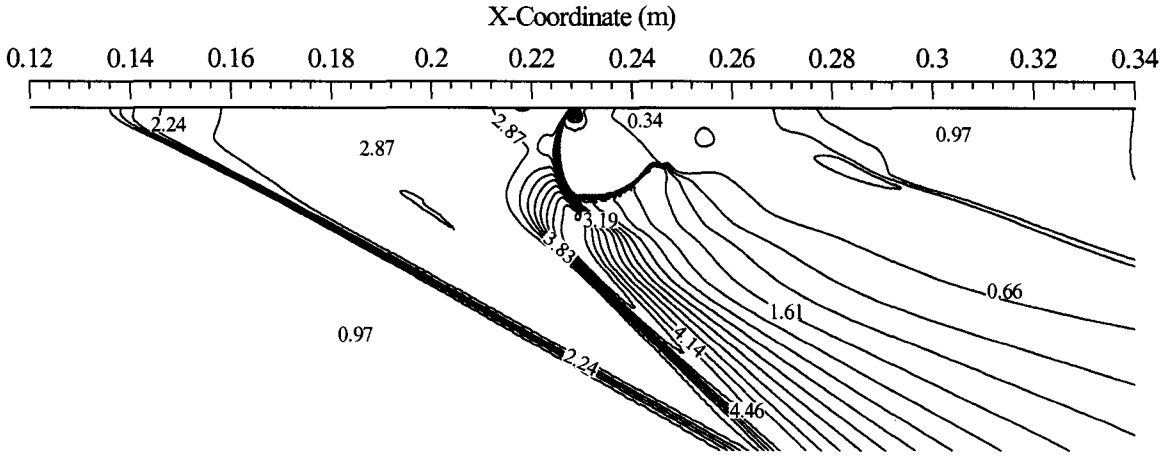

b. Top full duct injection

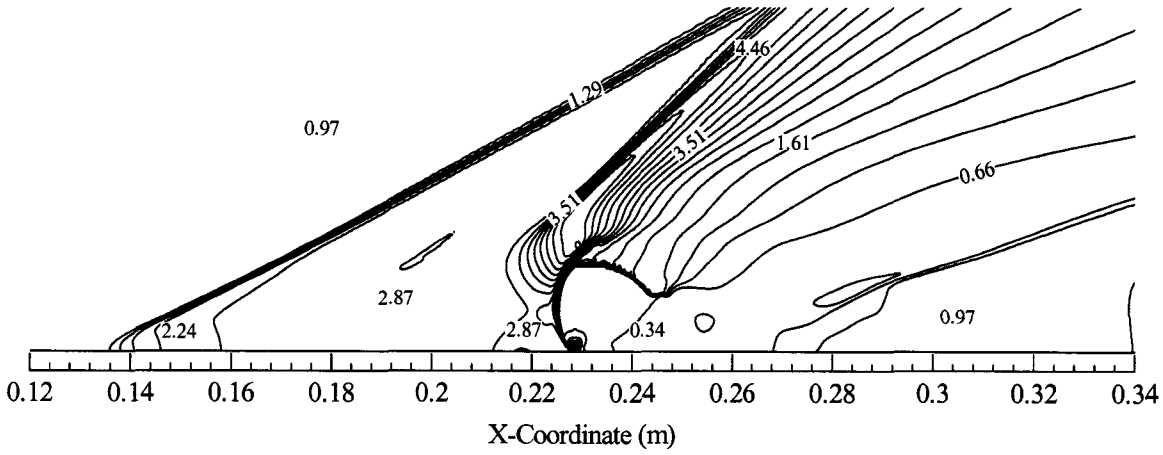

c. Bottom full duct injection

Figure 4.20 Normalized static pressure contour plots for half and full duct geometries, $Po_j/P=240.4$.

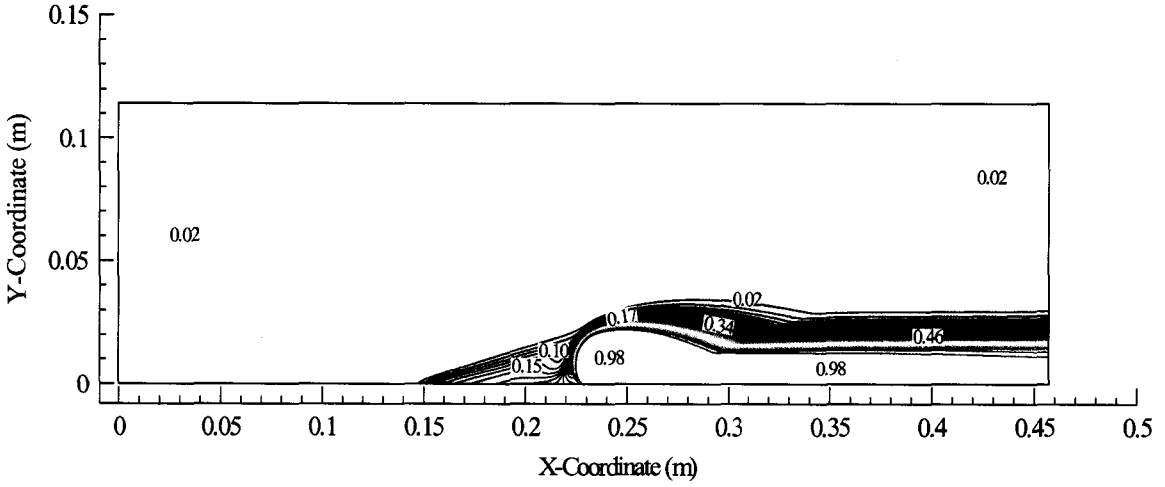

a. Nitrogen mole fraction contour plot for half duct geometry.

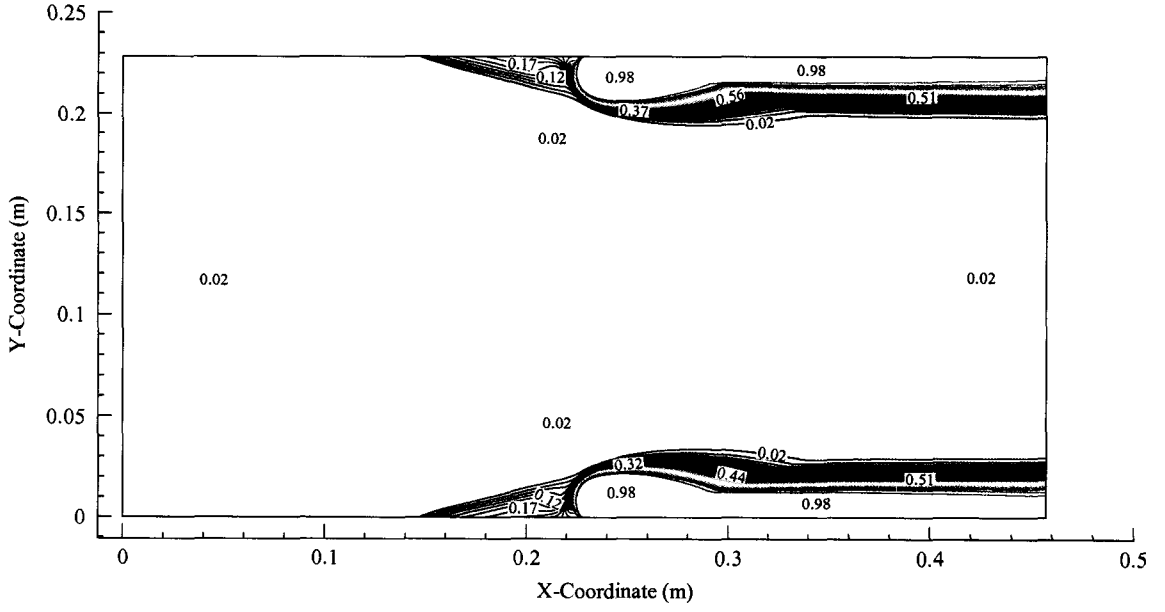

b. Nitrogen mole fraction contour plot for full duct geometry.

Figure 4.21 Nitrogen mole fraction contour plots for the entire geometry domain, $Po_j/P=240.4$.

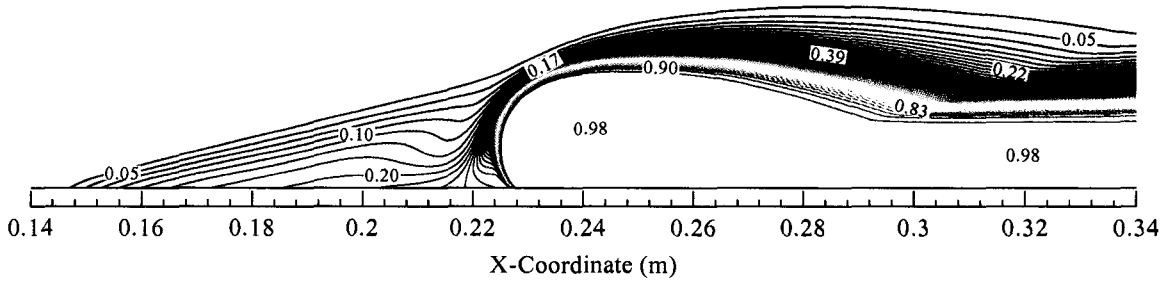

a. Bottom half duct injection

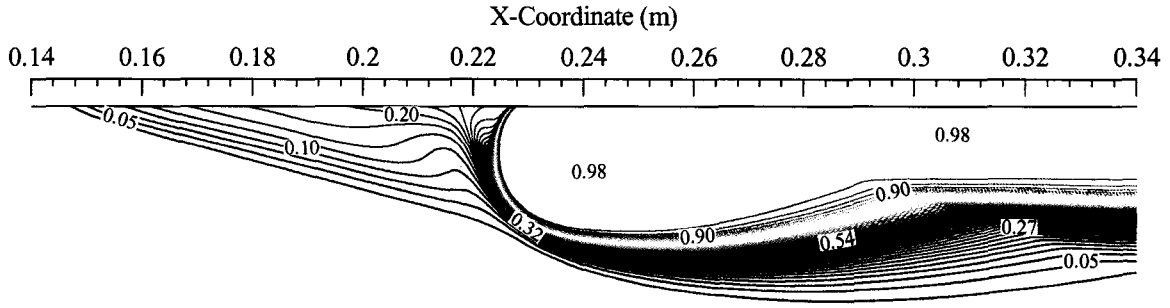

b. Top full duct injection

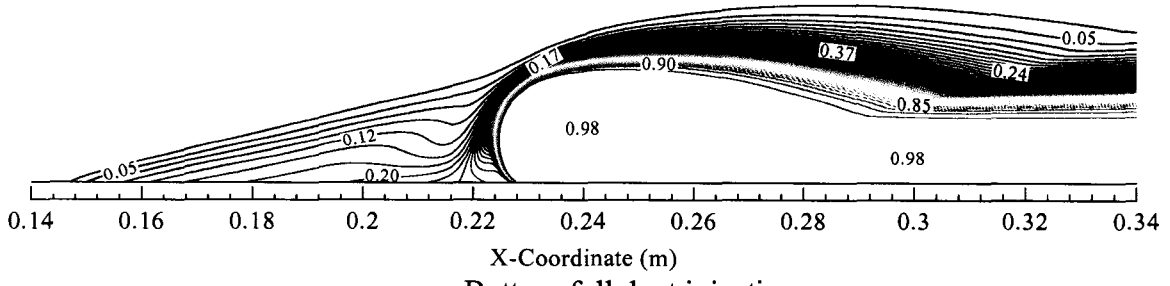

c. Bottom full duct injection

Figure 4.22 Nitrogen mole fraction contours plots for Po_j/P=240.4.

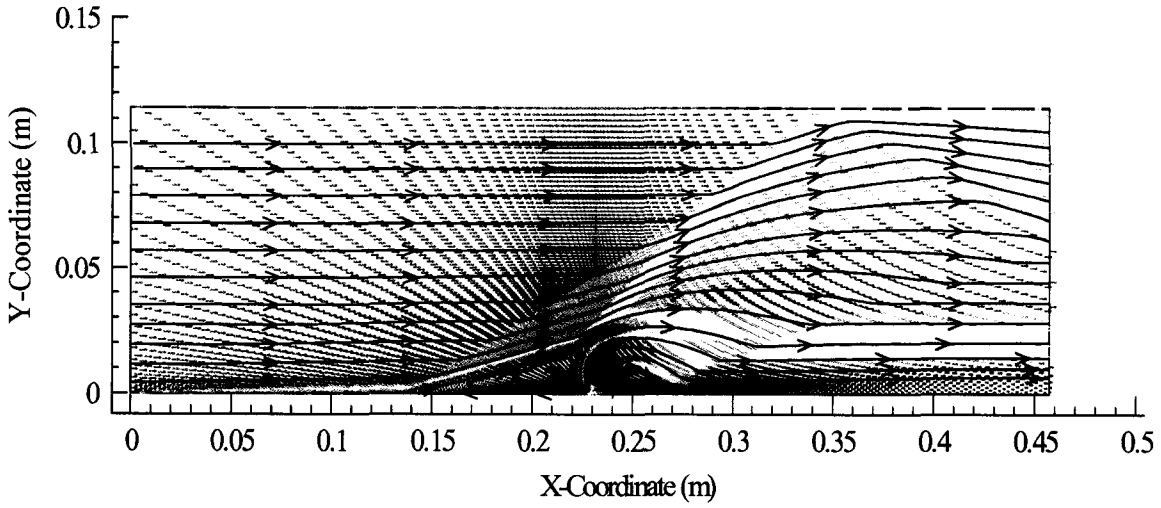

a. Velocity vector and streamline plot for half duct geometry.

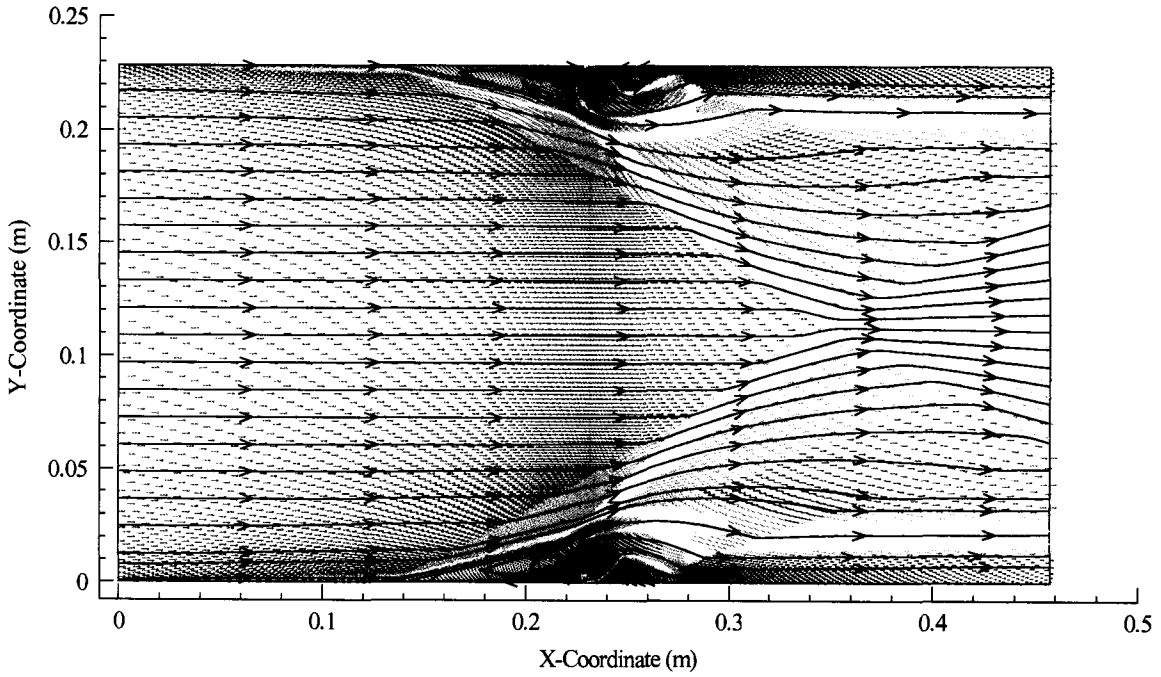

b. Velocity vector and streamline plot for full duct geometry.

Figure 4.23 Velocity vector and streamline plot for the entire geometry domain, $Po_j/P=240.4$.

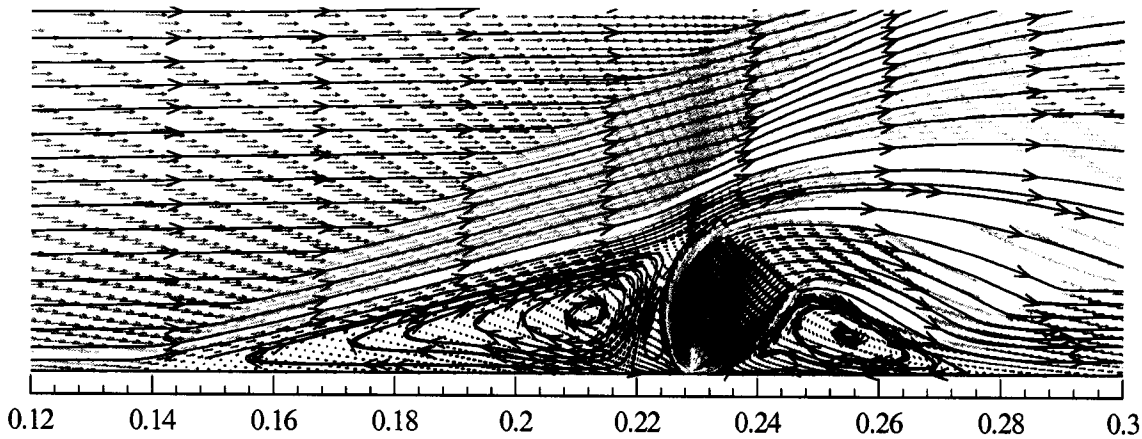

a. Bottom half duct injection

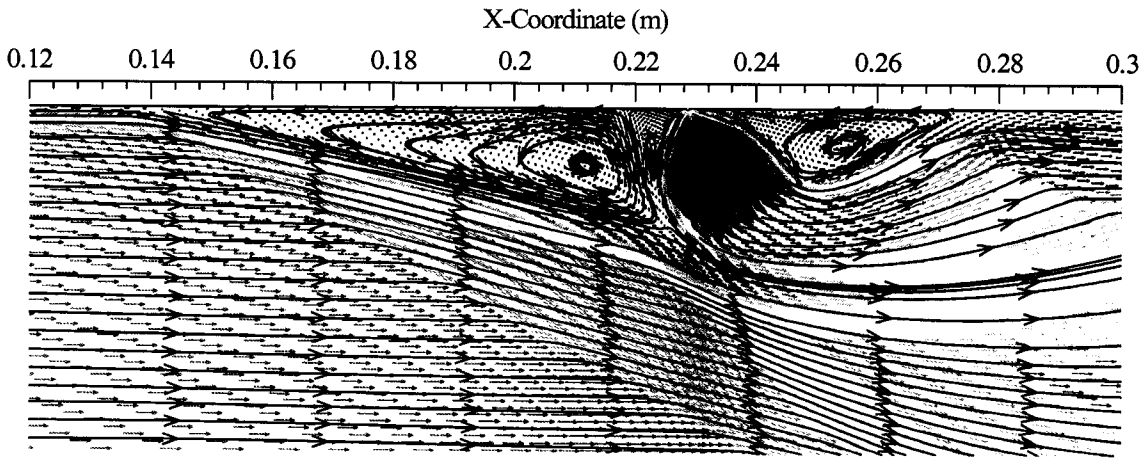

b. Full duct top injection

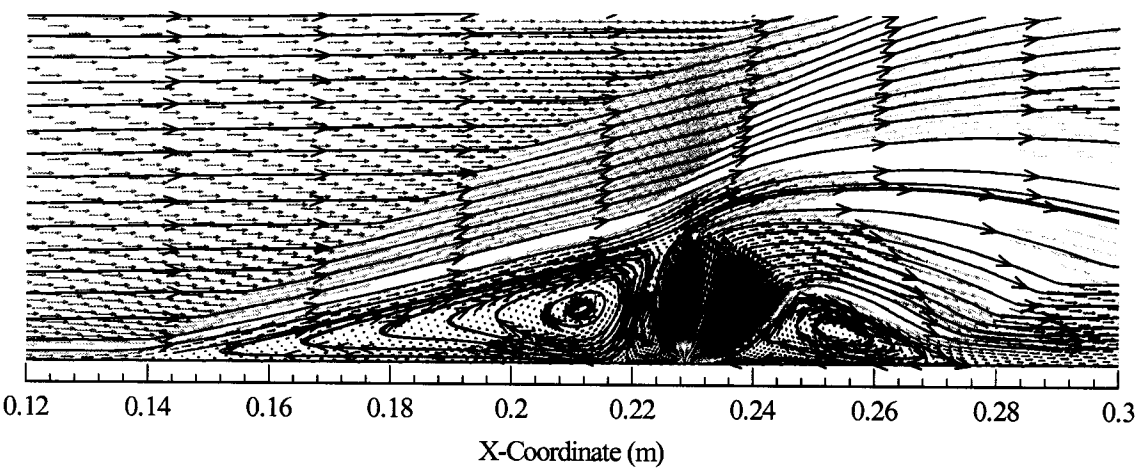

c. Full duct bottom injection

Figure 4.24 Velocity vector and streamline plots from $Po_j/P=240.4$.

4.4.3 Results for $Po_j/P = 480.8$

The final model increases the freestream to injector pressure ratio by decreasing the total and absolute pressures of the freestream flow. The freestream static and total pressure was divided by a factor of four. Table 4.3 shows the boundary conditions for this numerical model.

The normalized static pressure plot for both the half and full duct cases are presented in Fig. 4.25. Results show that as the pressure ratio increases, the boundary layer separation moves upstream. The half duct case shows that the upstream interaction occurs further downstream than the full duct model. The full duct model shows that the bottom separation region is slightly further upstream. Downstream of the injector we see the full duct large pressure fluctuations. The cause of this is that the domain is not long enough to produce the reattachment shock downstream. The half duct in this region is much more stable due to the top symmetry boundary condition.

Figures 4.26 and 4.27 show the velocity plot in the x-coordinate direction. As the pressure ratio increased you can see much clearer where the separations occurs. This is evident in Fig. 4.27. Numerical results show that the half duct case separated at approximately 0.06 m. Comparing this to the full duct results we find that the top of the full duct separates at approximately 0.0425 m and the bottom at 0.04 m. This shows that by using a full geometry domain at increasing pressure ratios we will produce much more accurate results as opposed to using a half geometry domain. Also, it shows that as the pressure ratio increases, boundary layer separation for the top and bottom regions produce much more apparent asymmetric results.

Table 4.3 Quarter pressure boundary conditions.

	Freestream Air	Nitrogen Injectant
M	3.5	1.0
P_t (kPa)	60.157	379.901
P_s (kPa)	0.789	200.637
T_t (K)	314.44	291.67
T_s (K)	91.67	243.33
Velocity (m/s)	670.56	317.906

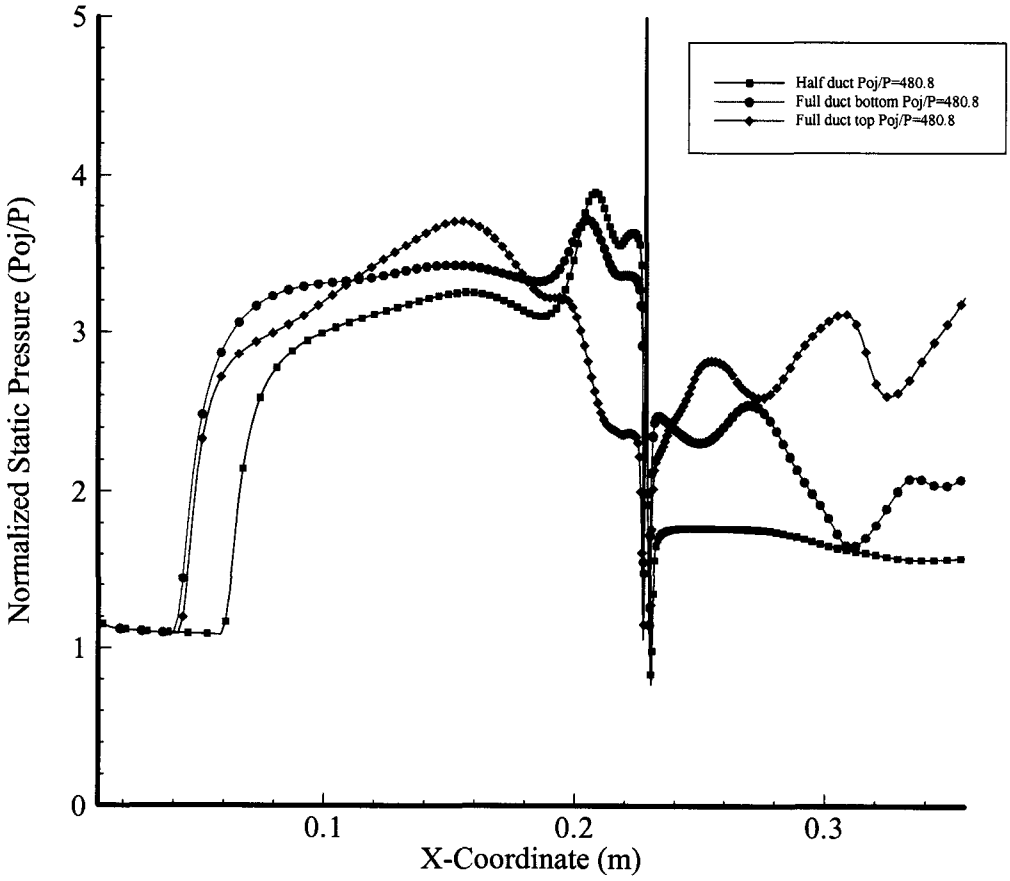

Figure 4.25 Wall normalized static pressure plot for P_{oj}/P=480.8.

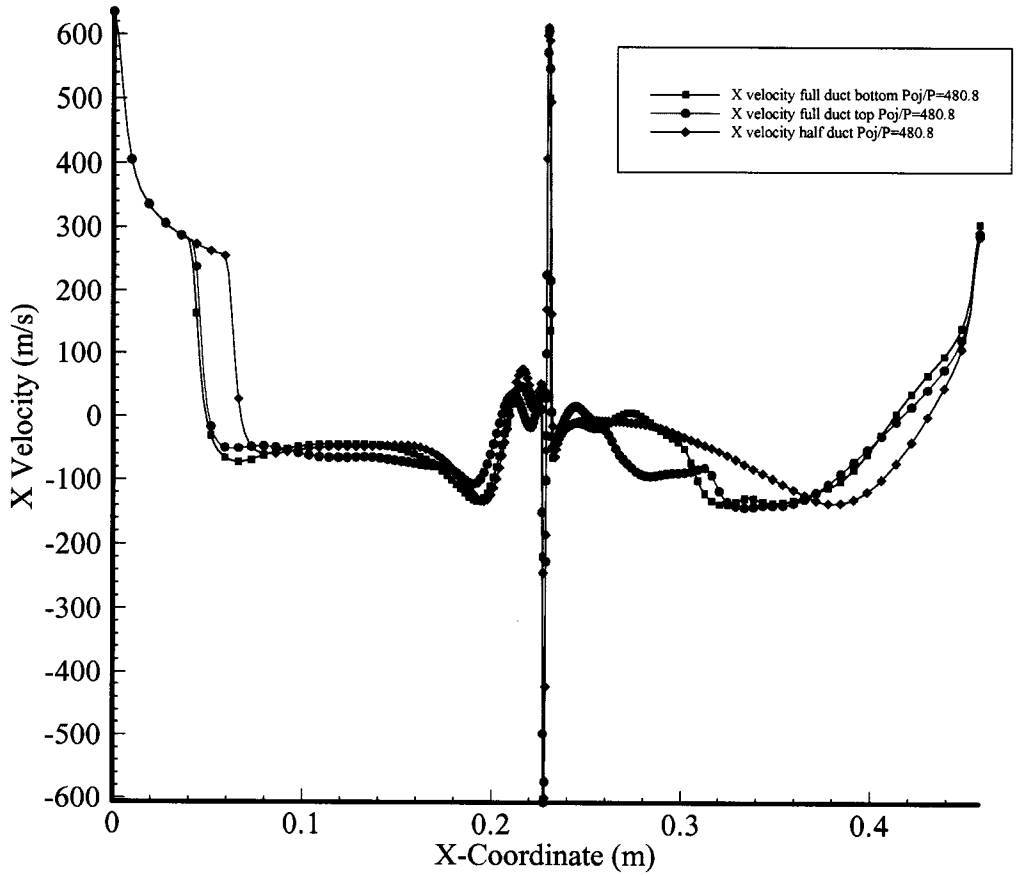

Figure 4.26 X velocity plot at 0.254 mm from walls for Po_j/P=480.8.

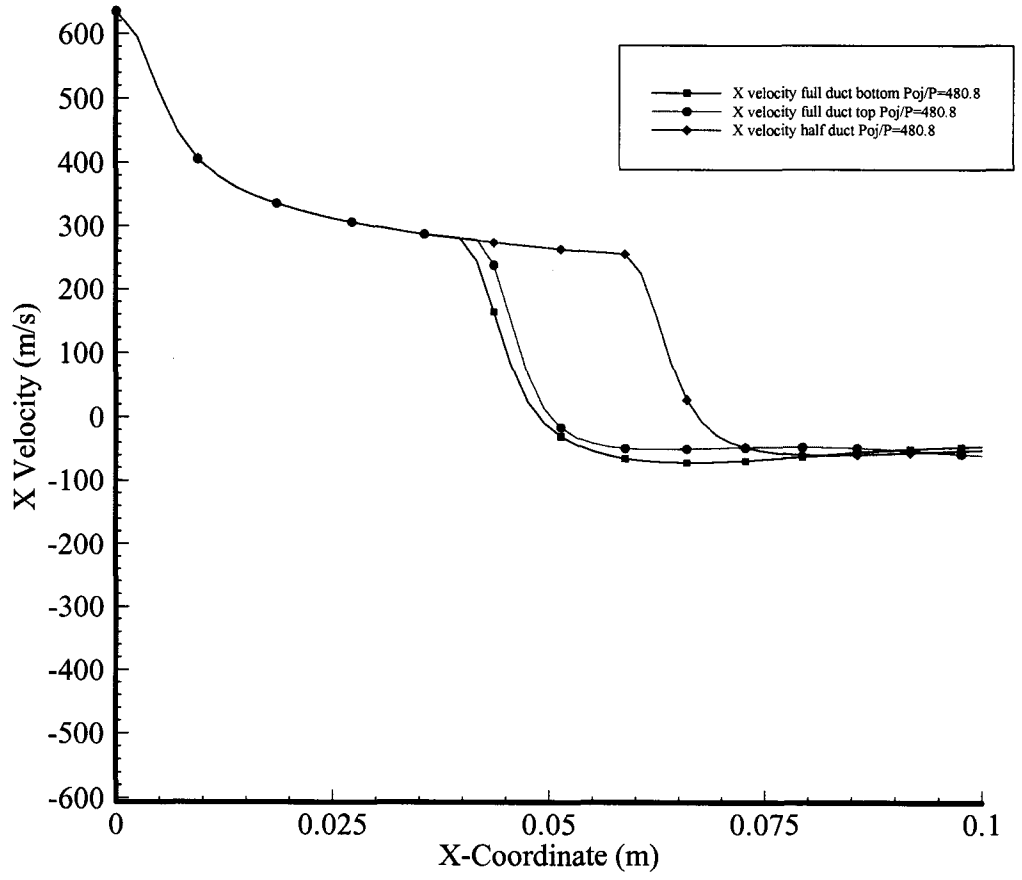

Figure 4.27 X velocity plot of separation region at 0.254 mm from wall for Po_j/P=480.8.

Mach number contours are given in Figs. 4.28 and 4.29. Comparisons between the Mach numbers however show acceptable agreement between the two models. On the x-coordinate we can see much clearer the difference where the boundary layer separates on both the half and full duct models. However, the boundary layer separation is not apparent to the naked eye in the full duct model. In the injectant region the "bloom" is much more erect. This is due to the higher pressure ratio.

Figures 4.30 and 4.31 show the contours for the normalized static pressure. Note how the normalized pressure increases in the shock/shock region. Also, due to the high pressure ratio, the bow shock begins to interact with the separation shock. Upstream, normalized pressure should be in proximity of unity. However, due to turbulence or residual convergence, this is not so.

Mole fraction of N_2 contours are presented in Figs. 4.32 and 4.33. The effect of the high pressure ratio affects the penetration height of the injectant. This is evident in Figs. 4.32 and 4.33. In both figures we see for the full duct that the recirculation region upstream of the injector shows higher mole fractions than compared to the half duct. The cause of this can be attributed to the high level of turbulent mixing occurring within the recirculating regions, as opposed to the half duct where there is lower turbulent mixing occurring in the recirculation region. This may be caused by the top symmetry boundary condition. However, leeward of the injector, we see that the mole fraction of Nitrogen is lower for the full duct. This can be attributed to the fact that the recompression shock has not fully developed due to the geometry. Therefore, the recirculating flow is not allowed be fully develop.

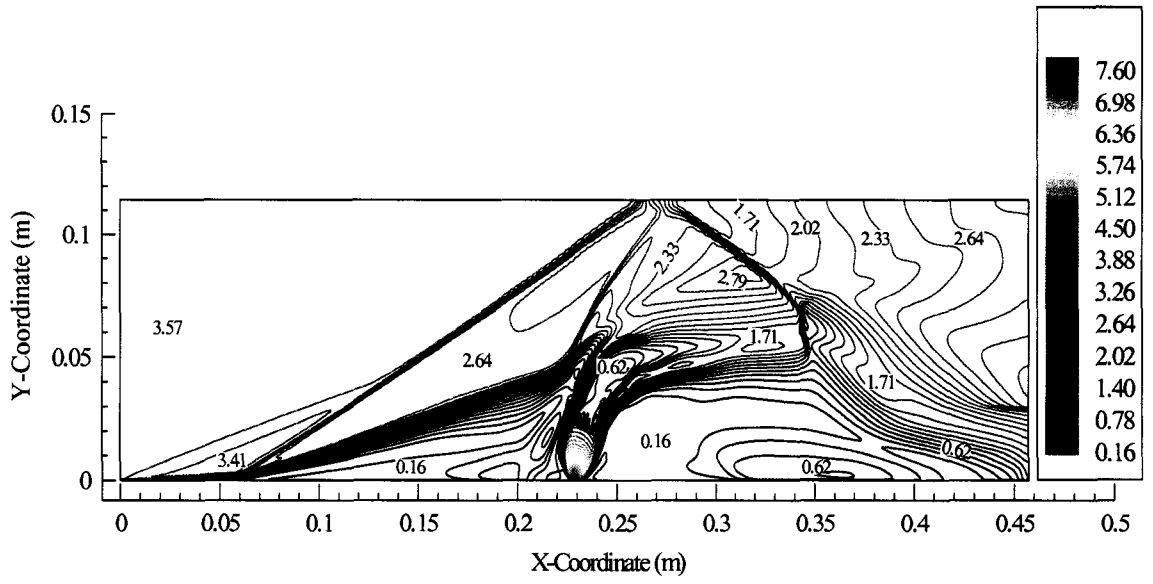

a. Mach number contour plot for half duct geometry.

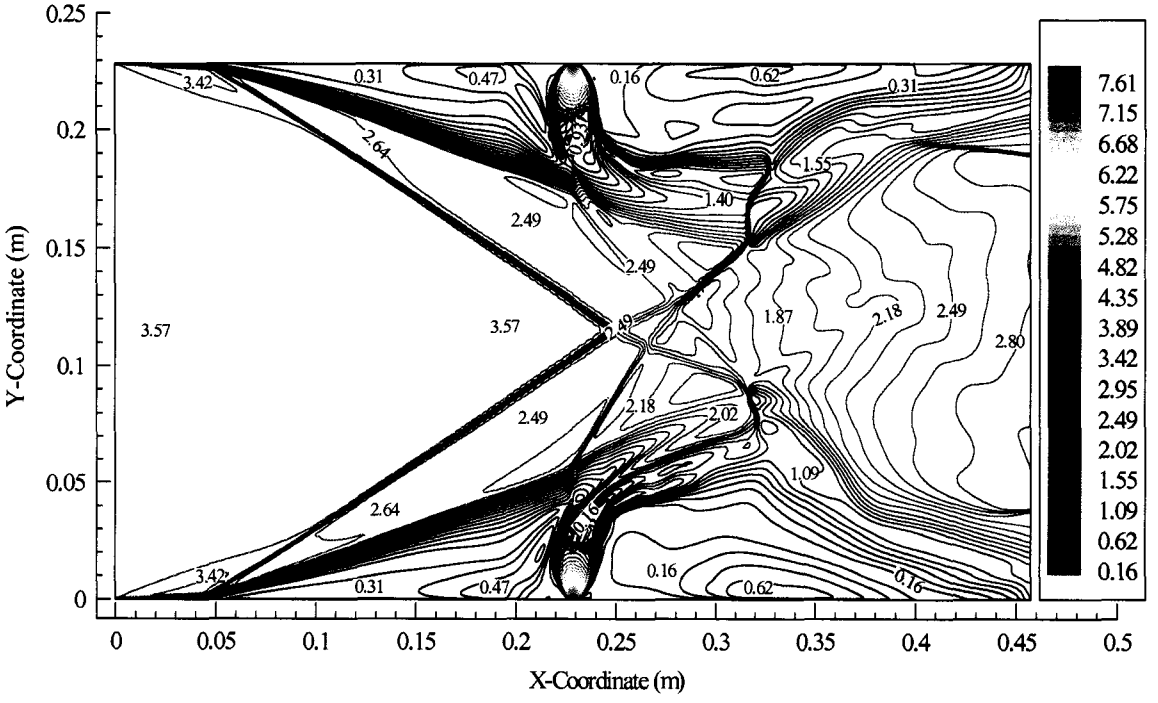

b. Mach number contour plot for full duct geometry.

Figure 4.28 Mach number contour plots for the entire geometry domain, Po_j/P=480.8.

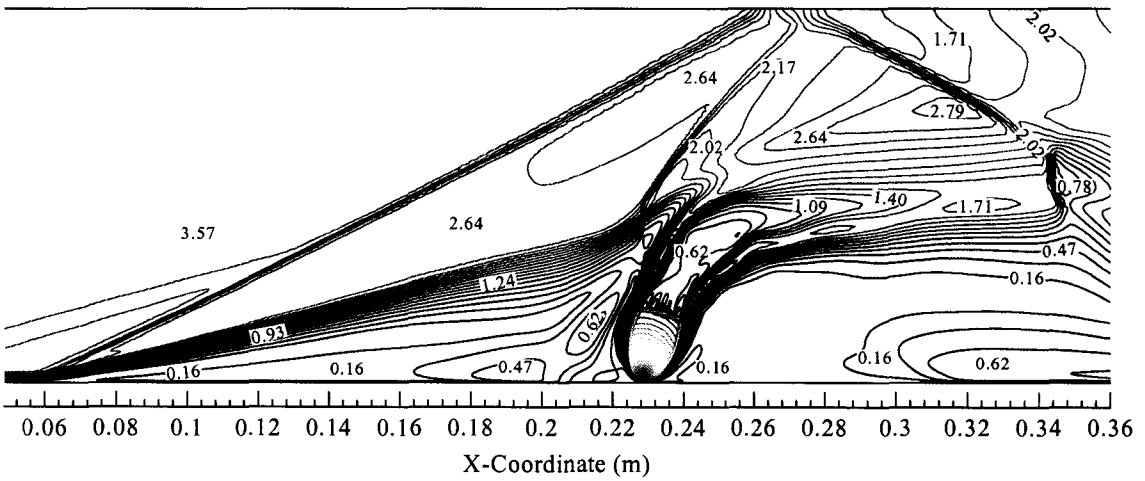

a. Bottom half duct injection

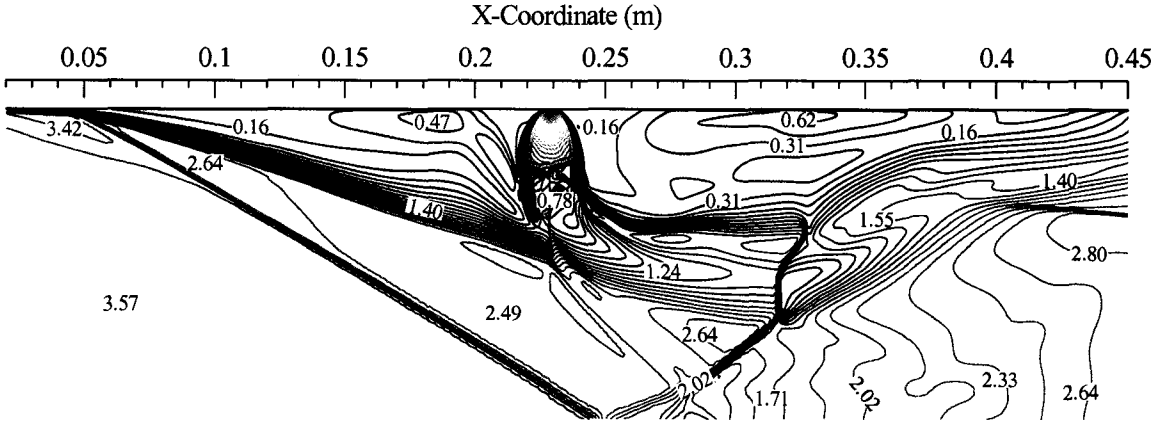

b. Top full duct injection

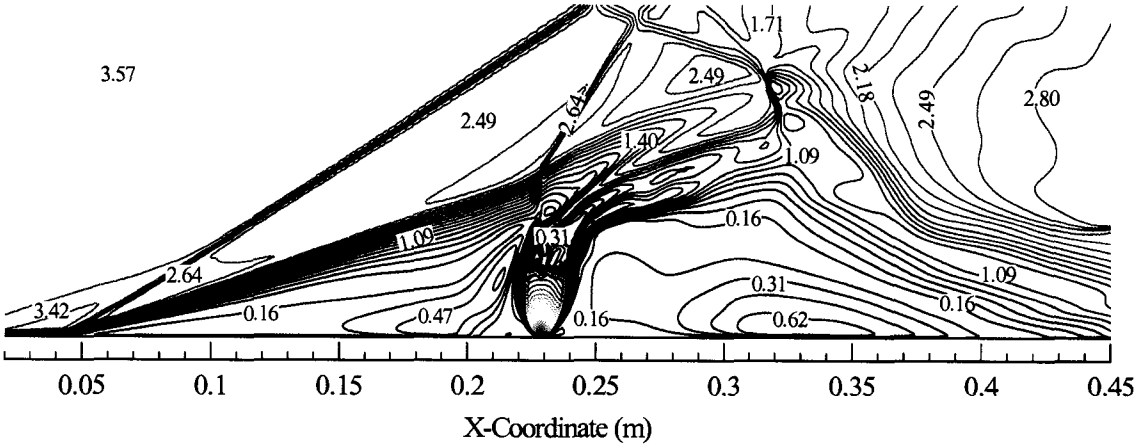

c. Bottom full duct injection

Figure 4.29 Mach number contour plots for half and full duct geometries, Po_j/P=480.8.

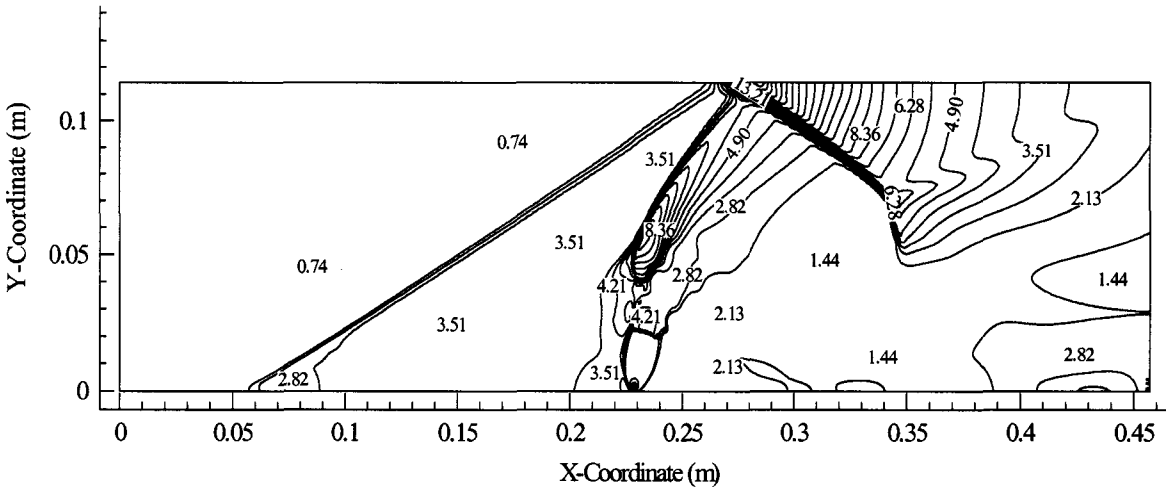

a. Normalized static pressure contour plot for half duct geometry.

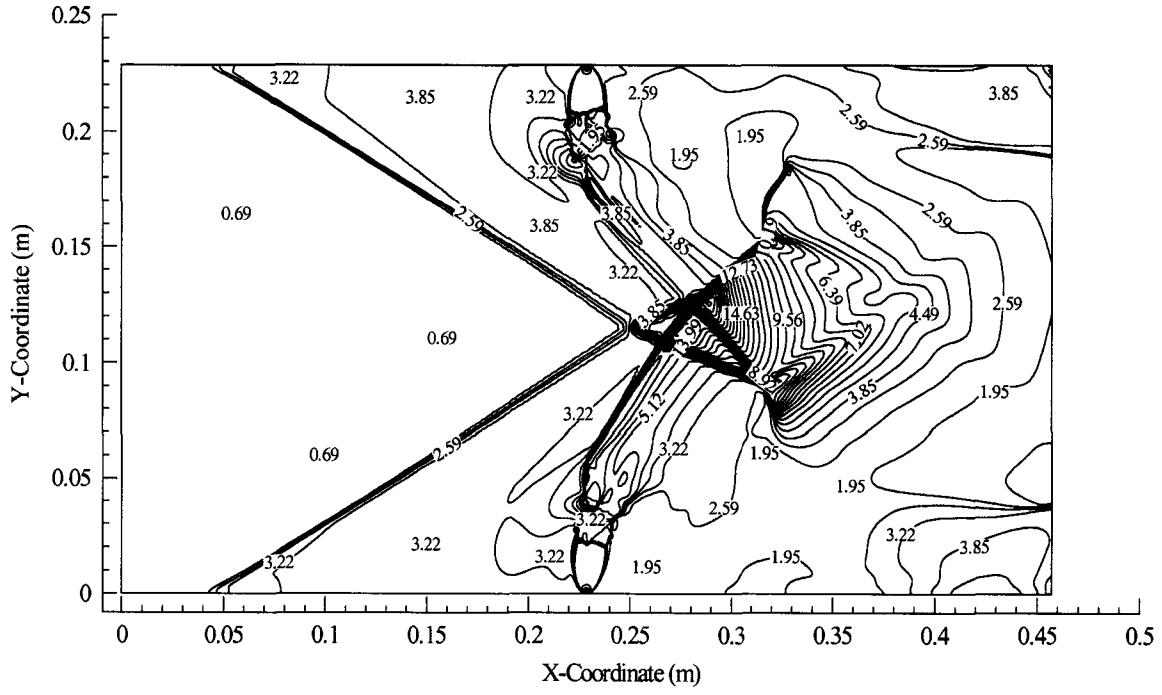

b. Normalized static pressure contour plot for full duct geometry.

Figure 4.30 Normalized static pressure contour plots for the entire geometry domain, $Po_j/P=480.8$.

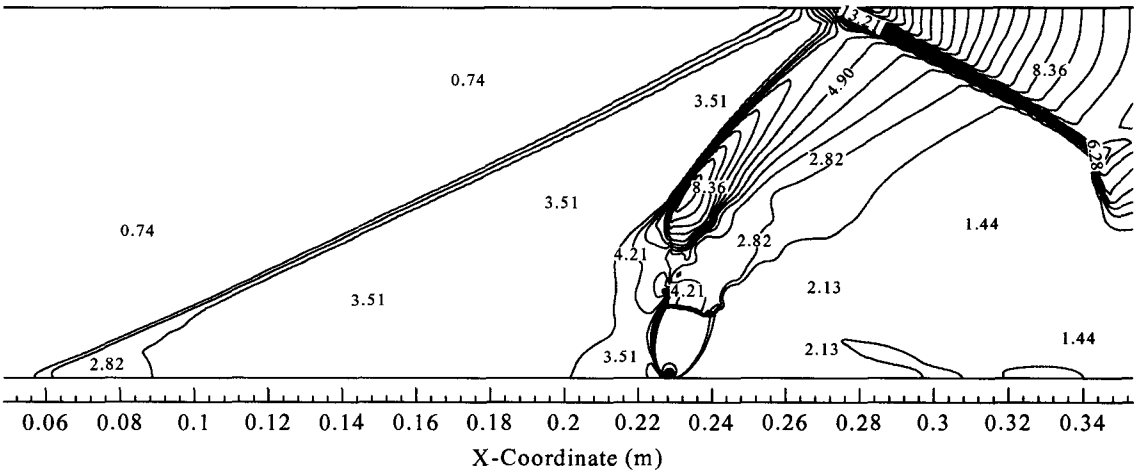

a. Bottom half duct injection

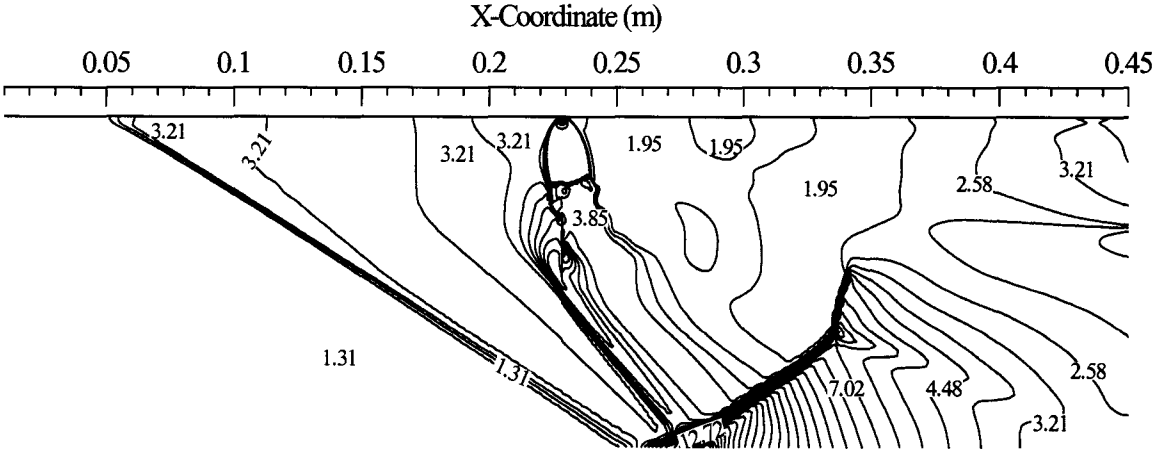

b. Top full duct injection

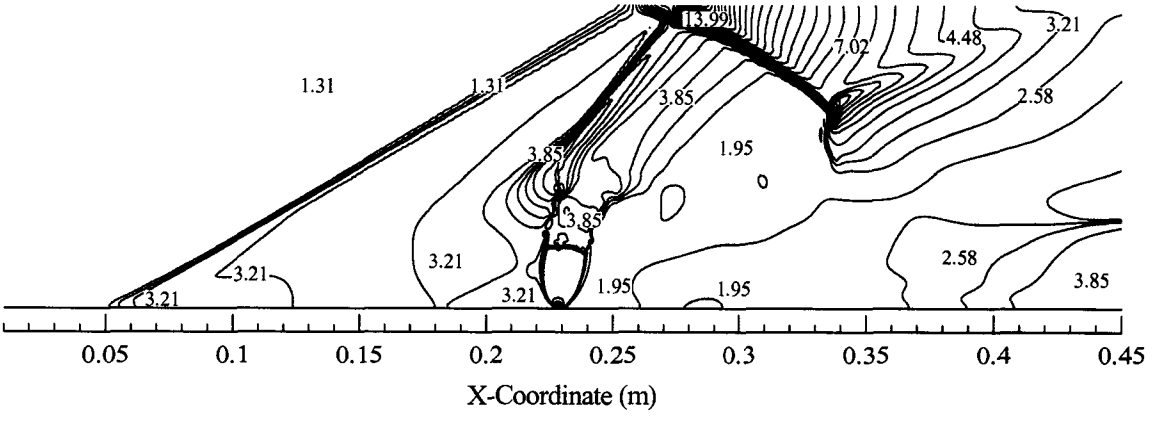

c. Bottom full duct injection

Figure 4.31 Normalized static pressure contour plots for half and full duct geometries, P_{oj}/P=480.8.

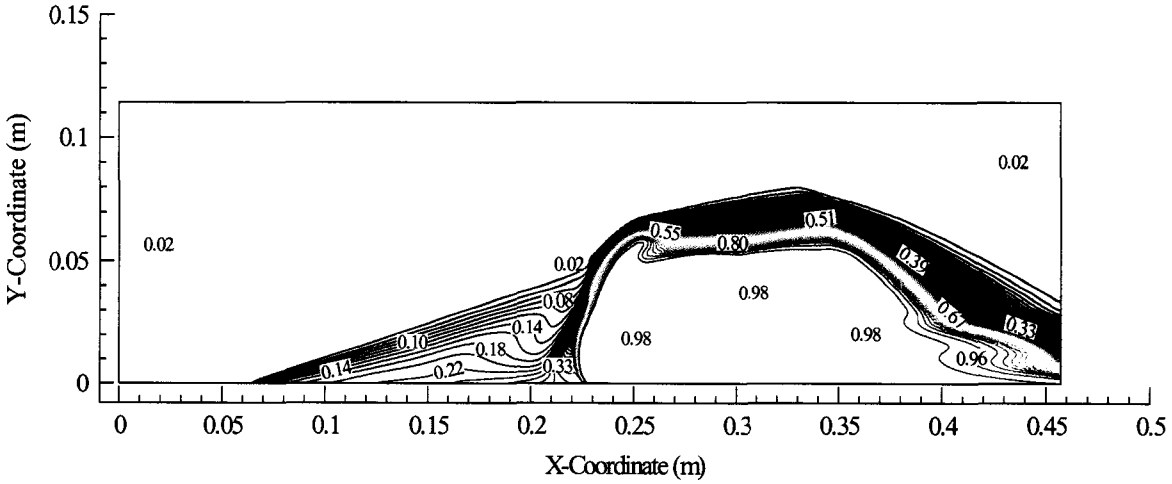

a. Mole fraction of N_2 contour plot for half duct geometry.

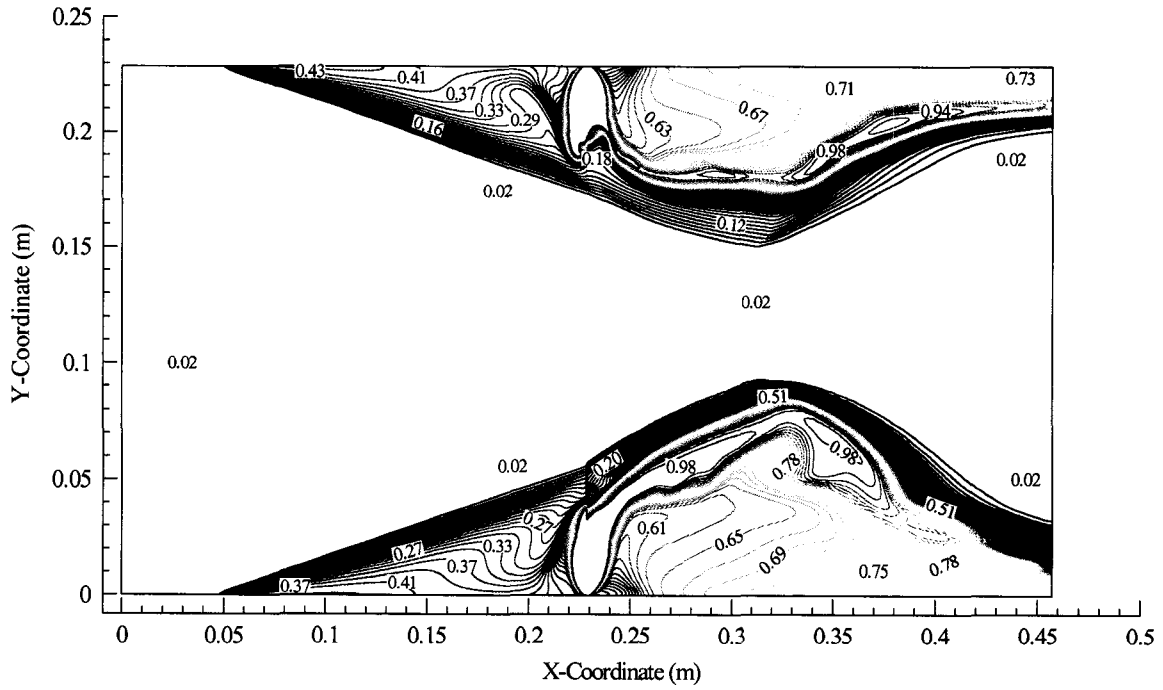

b. Mole fraction of N_2 contour plot for full duct geometry.

Figure 4.32 Mole fraction of N_2 contour plots for the entire geometry domain, Po_j/P=480.8.

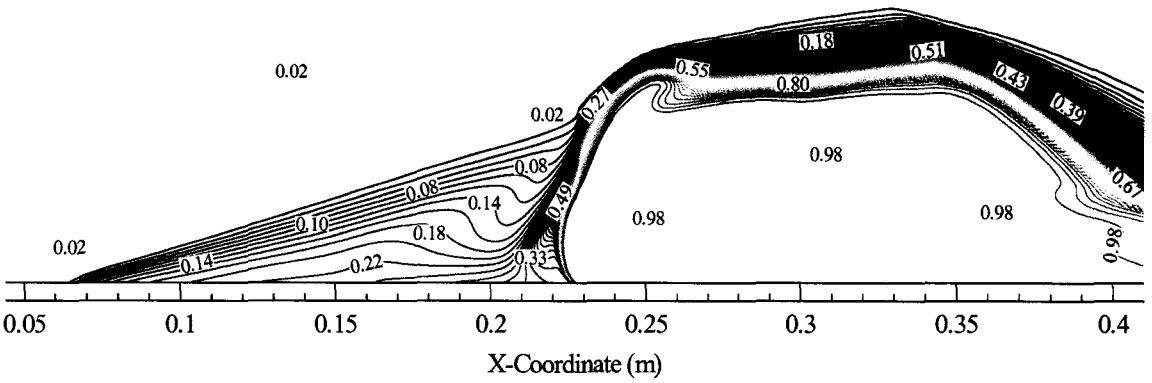

a. Bottom half duct injection

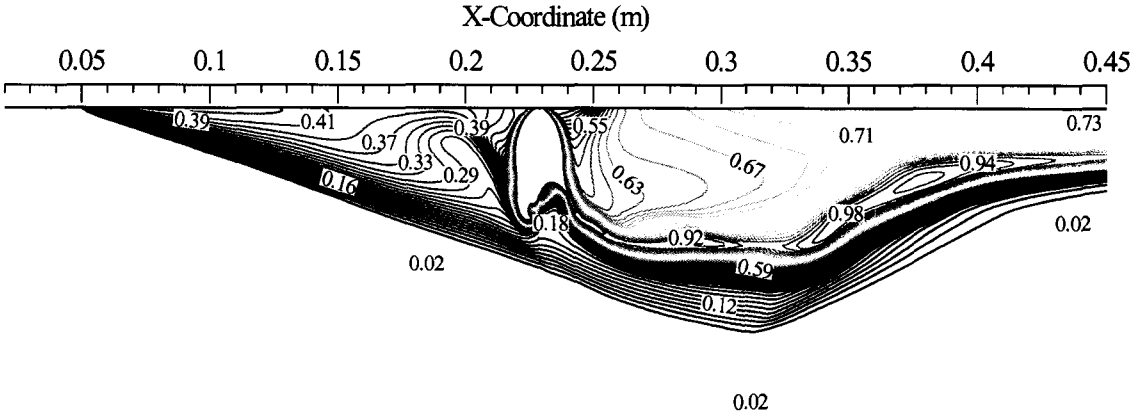

b. Top full duct injection

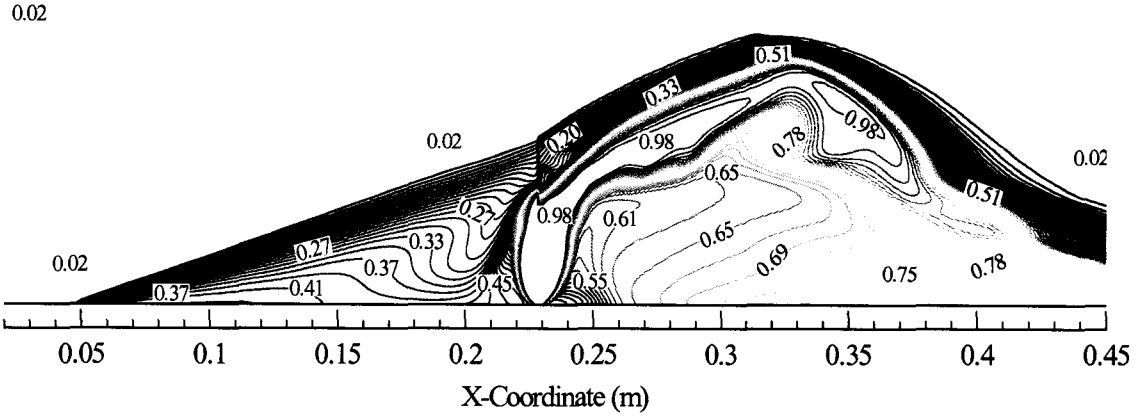

c. Bottom full duct injection

Figure 4.33 Mole fraction of N_2 contour plots for half and full duct geometries, Po_j/P=480.8.

Figures 4.34 and 4.35 give the velocity vector and streamline plots. The large recirculating regions can be seen. The large pressure ratio causes the recirculation region leeward of the injector to be very large as compared to the previous pressure ratios. The upstream recirculating regions appear to be similar in all the figures, however the leeward recirculating regions show asymmetric streamlines. The half duct shows two circulating regions within the recompression shock. This can be attributed to the turbulent mixing after the injector.

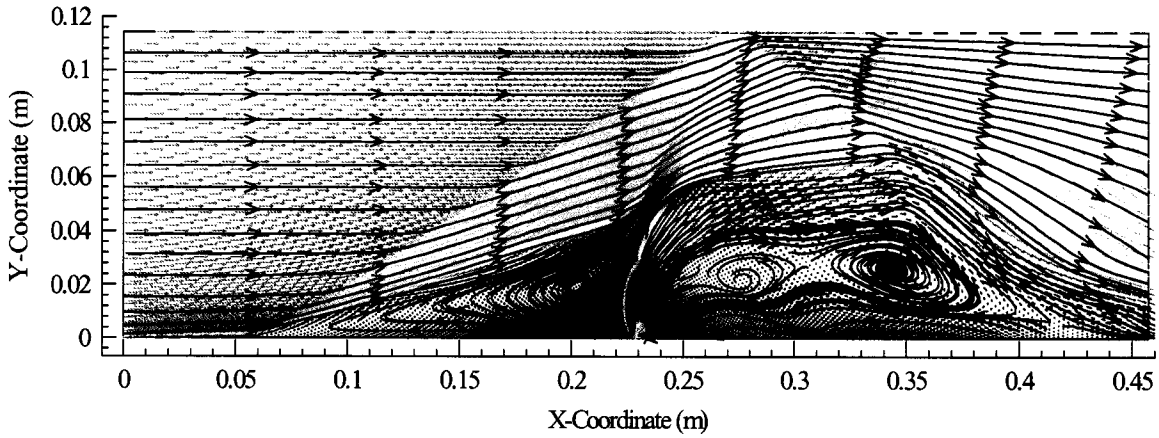

a. Velocity vector and streamline plot for half duct geometry.

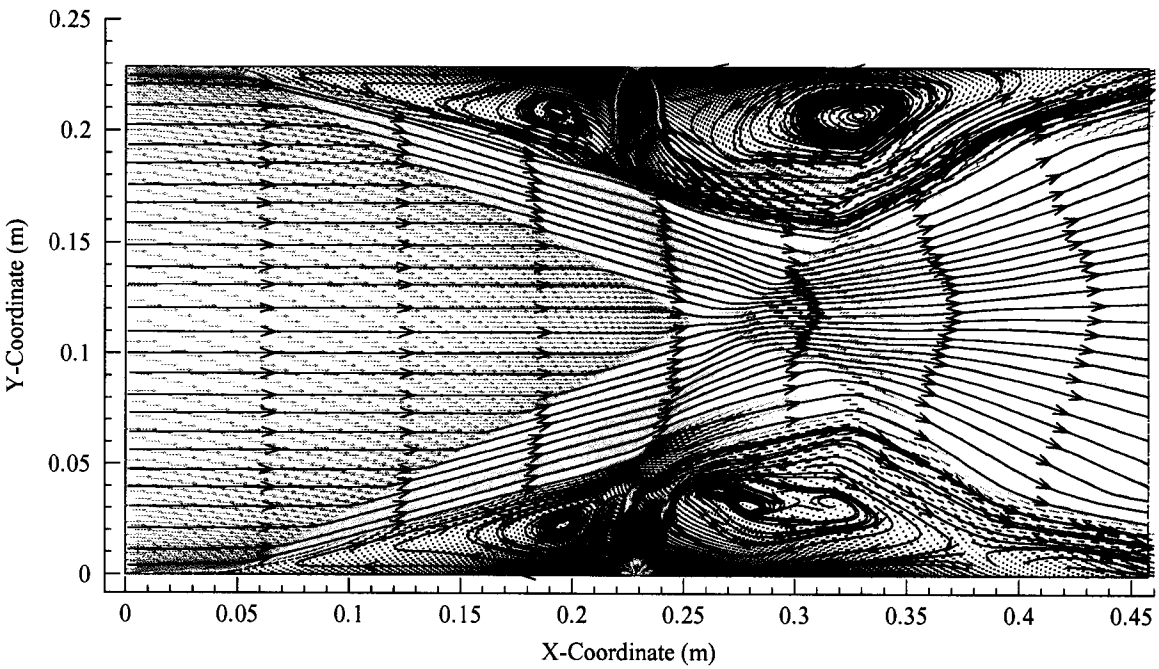

b. Velocity vector and streamline plot for full duct geometry.

Figure 4.34 Velocity vector and streamline plots for the entire geometry domain, Po_j/P=480.8.

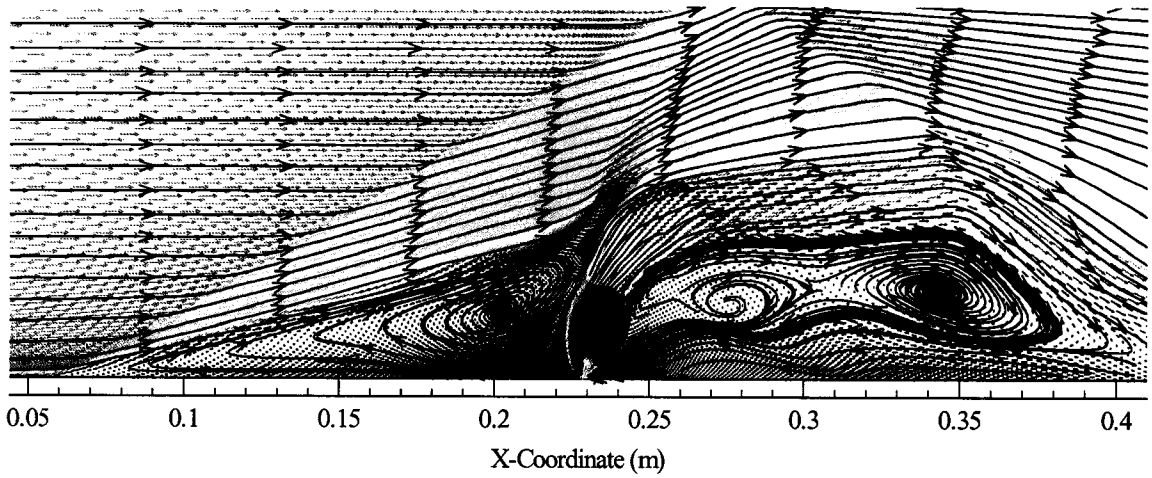

a. Bottom half duct injection

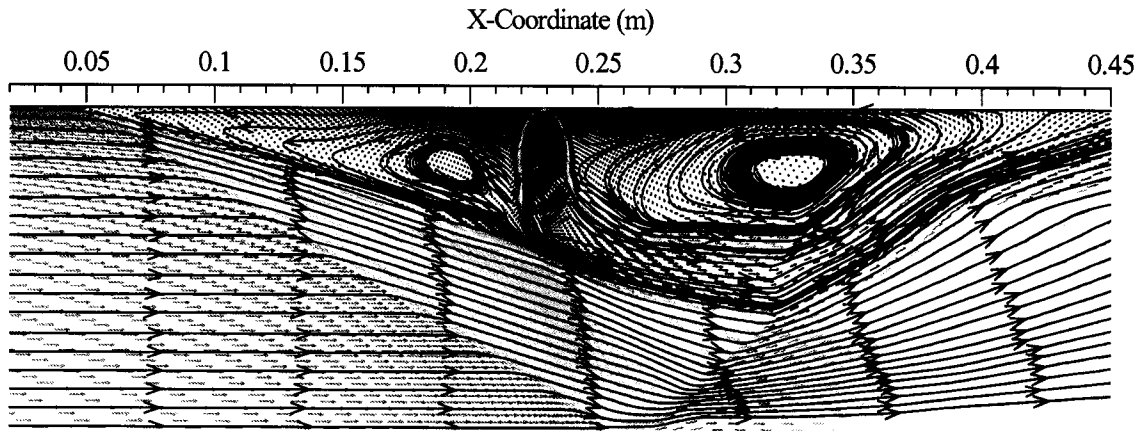

b. Top full duct injection

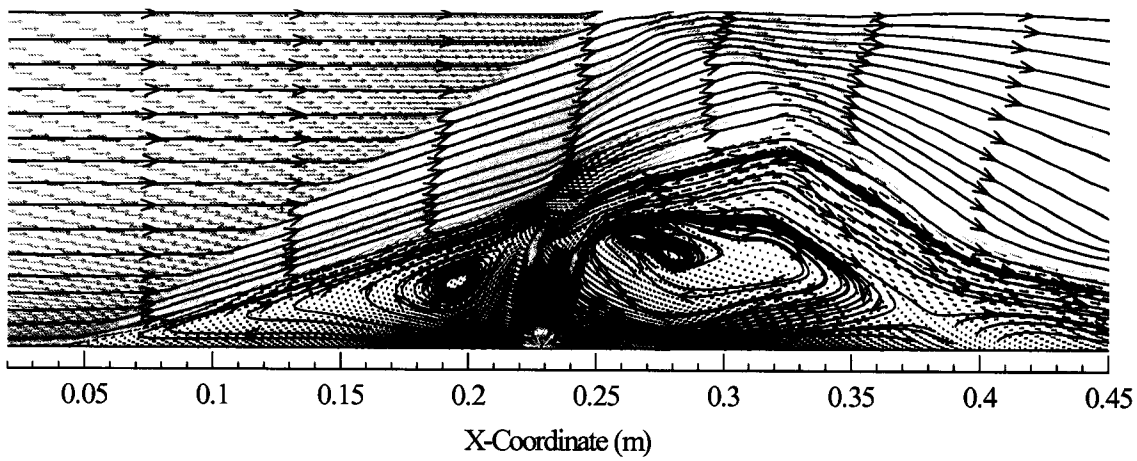

c. Bottom full duct injection

Figure 4.35 Velocity vector and streamline plots for half and full duct geometries, Po_j/P=480.8.

4.4.4 Combined Results

This section shows the combined x-y plot results of wall pressures and velocity along the x-coordinate for both models. It is shown how each study changes as the pressure ratio is increased. Also, plots of separation point versus length and pressure ratio versus separation length are compared.

Figure 4.36 shows the normalized static pressure plot for the half duct case. Notice how the pressure rises much more upstream as the pressure ratio is increased. Experimental results from Spaid and Zukoski[8] show acceptable agreement with the $Po_j/P=120.2$ case. The numerical study is slightly over-predicted. This could be attributed to the turbulence model chosen for this case. Figure 4.37 presents results for the wall normalized static pressure for the full duct case. Again notice how the pressure rises upstream as the pressure ratio increases. For the $Po_j/P=120.2$ and $Po_j/P=240.4$ cases the pressure rise is symmetrical. However, the $Po_j/P=480.8$ cases shows asymmetric results. This result can be related to the rise in pressure ratio affecting the flowfield in a way that stresses within the flowfield can produce the asymmetric upstream interaction. If the pressure were to be increased, you would be able to see asymmetric results where the distance of separation between the top and bottom walls would be greater.

Velocity plots along the x-coordinate at a distance of 0.254 mm are present in Figs. 4.38 and 4.39. We can see that the separation points in figure 4.38 follow an almost linear path. This is also evident in Fig. 4.39. It is shown how the separation point moves further upstream as the pressure ratio increases. In Fig. 4.39 for the $Po_j/P=480.8$ case it is shown that the bottom separates upstream slightly than the top. Leeward of the injector for the same case we see that the velocity does not follow the same path as the other pressure ratios. This is due to the fact that the recompression shock does not have the room to reattach due to the geometry of the model. If geometry leeward of the injector was long to accommodate this then we would see that the velocity would decrease like the others, but would peak further downstream and then become steady. This is the same for the half duct case, $Po_j/P=480.8$, in Fig. 4.38.

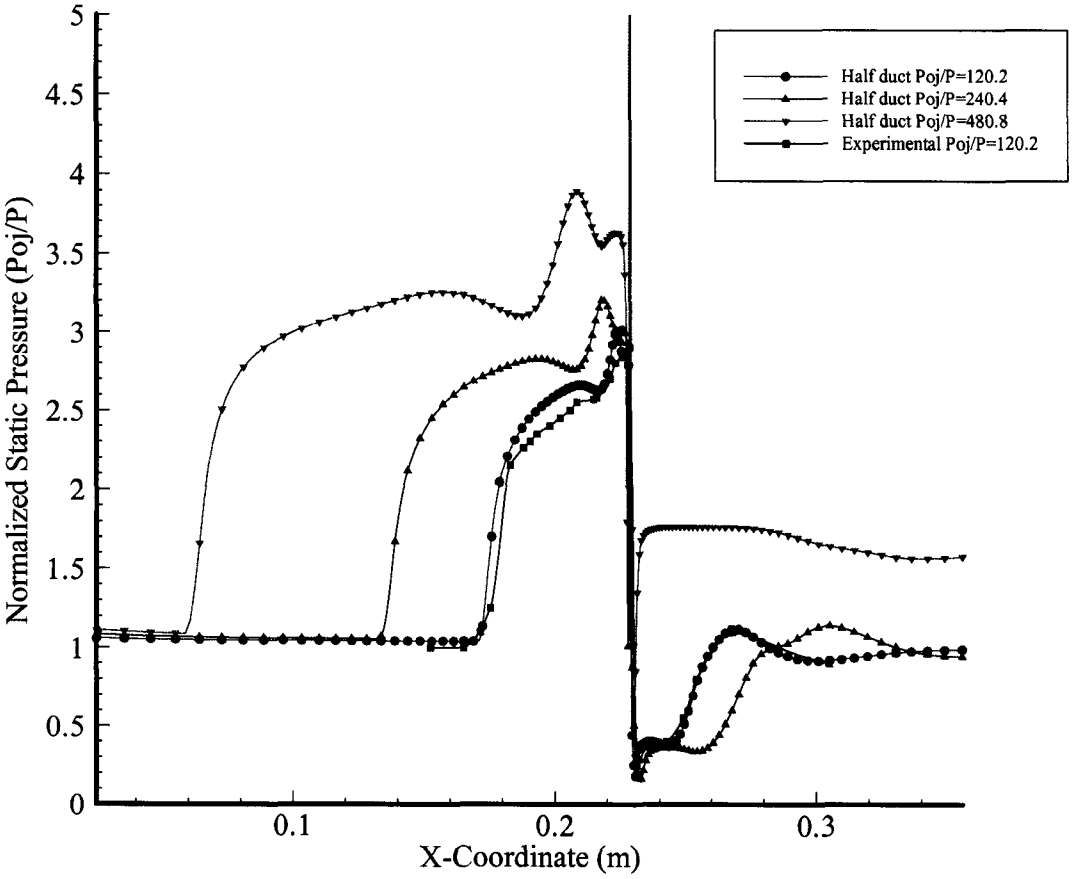

Figure 4.36 Wall normalized static pressure plot, half duct cases.

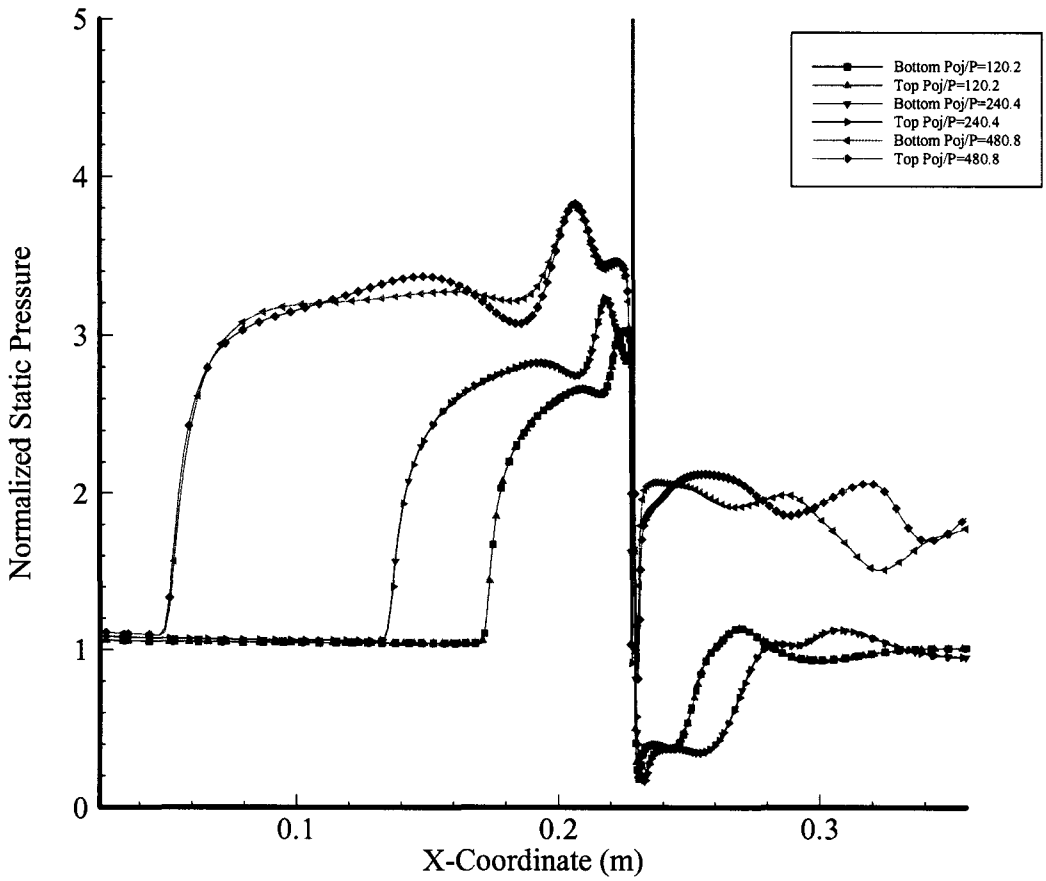

Figure 4.37 Wall normalized static pressure plot, full duct cases.

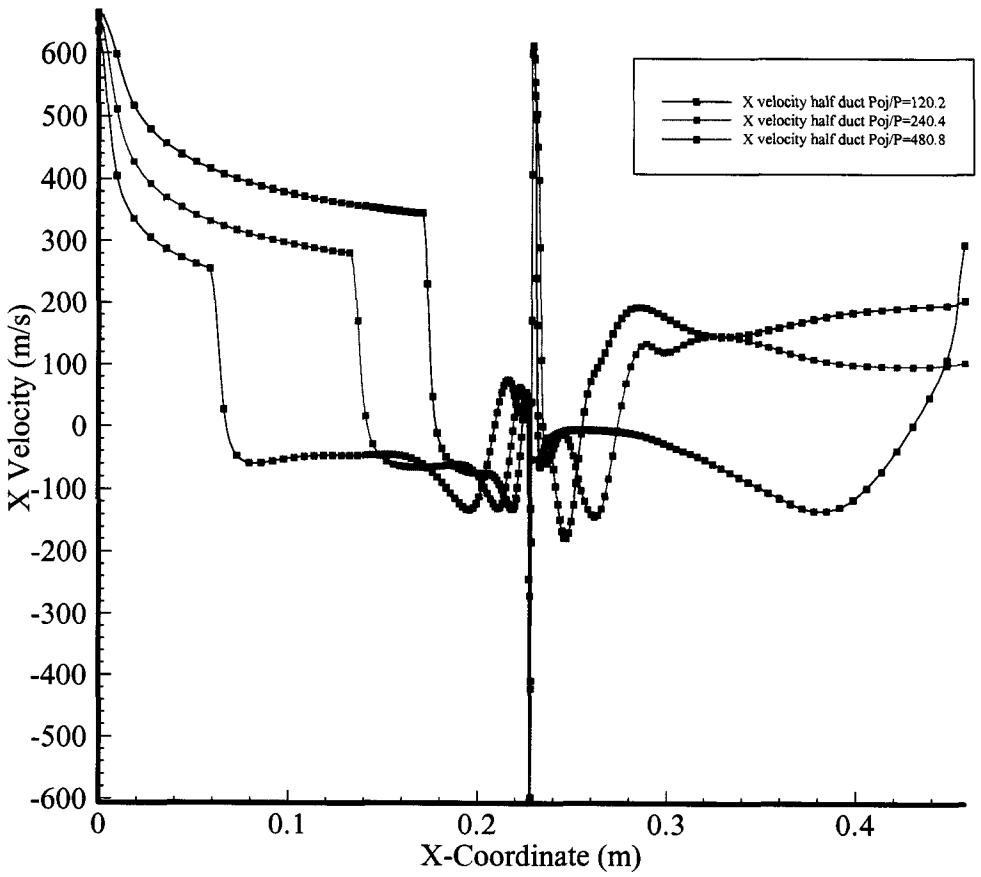

Figure 4.38 Velocity plot at 0.254mm from wall, half duct cases.

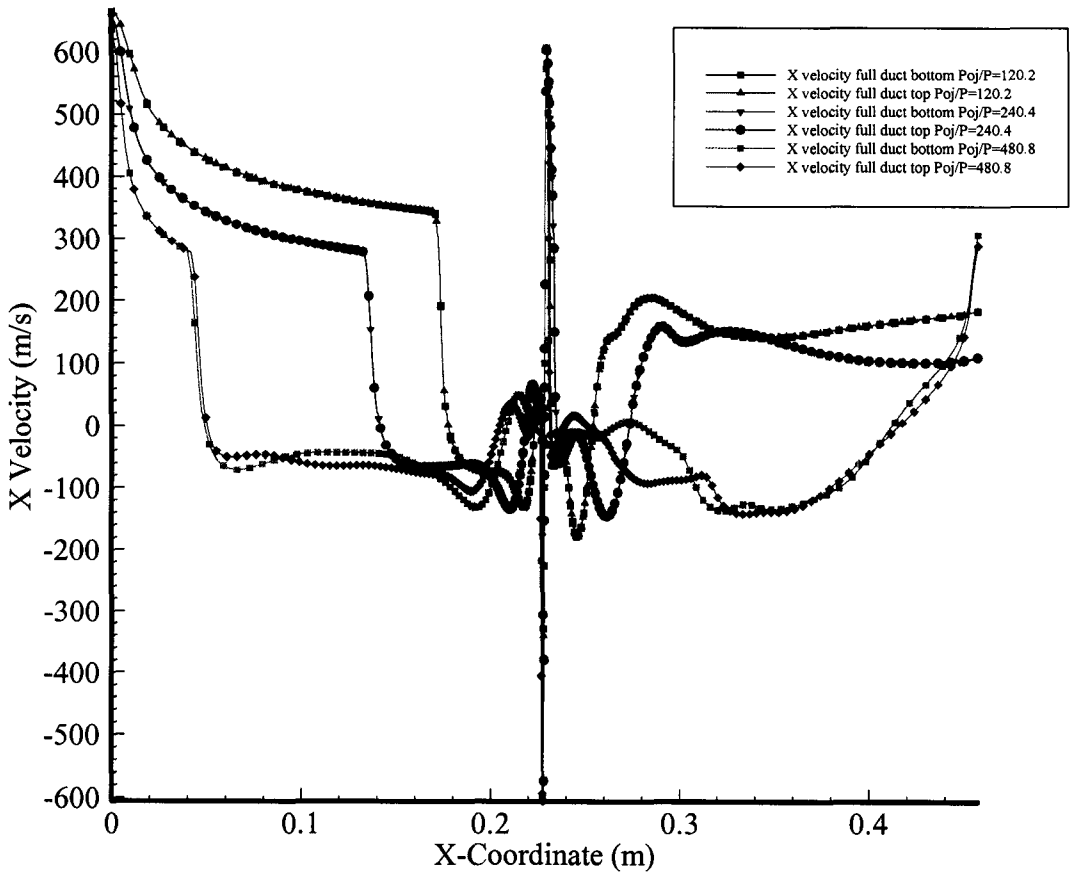

Figure 4.39 X velocity plot at 0.254mm from wall, full duct cases.

Figure 4.40 is a CAD drawing showing the flowfield with separation point and length described. Figure 4.41 shows the plot of separation point versus distance. The plots show a linear relationship between the pressure ratios. We see each pressure ratio and the half and full duct models where the separation point occurs. It has been shown that as the pressure ratio increases stresses within the flow causes the upstream interaction to become more asymmetric.

Pressure ratio versus separation length has been investigated in Fig. 4.42. It is shown that this relationship is linear for the half duct and curvilinear for the full duct. This phenomena has been studied by Aso et al.[13-15] and have shown similar results using different boundary conditions.

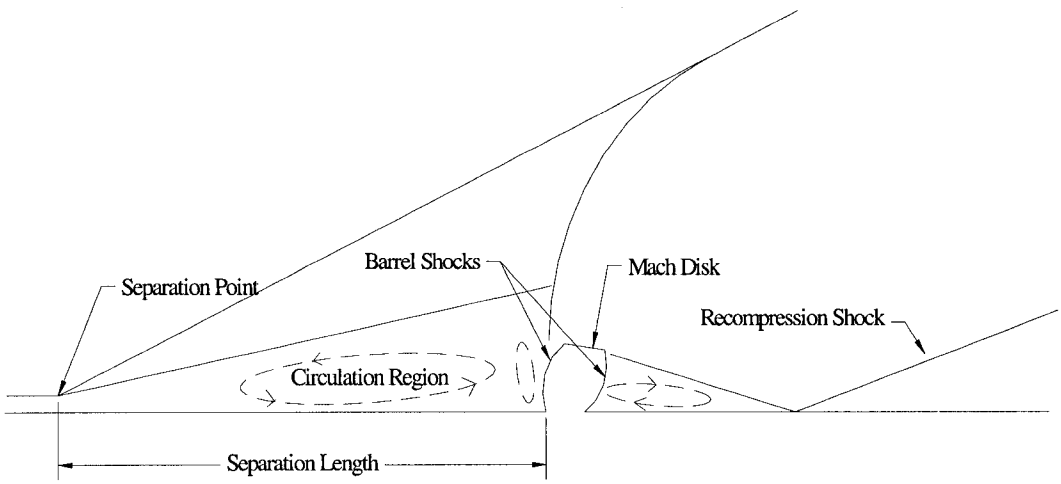

Figure 4.40 CAD sketch describing flowfield with separation point and length shown.

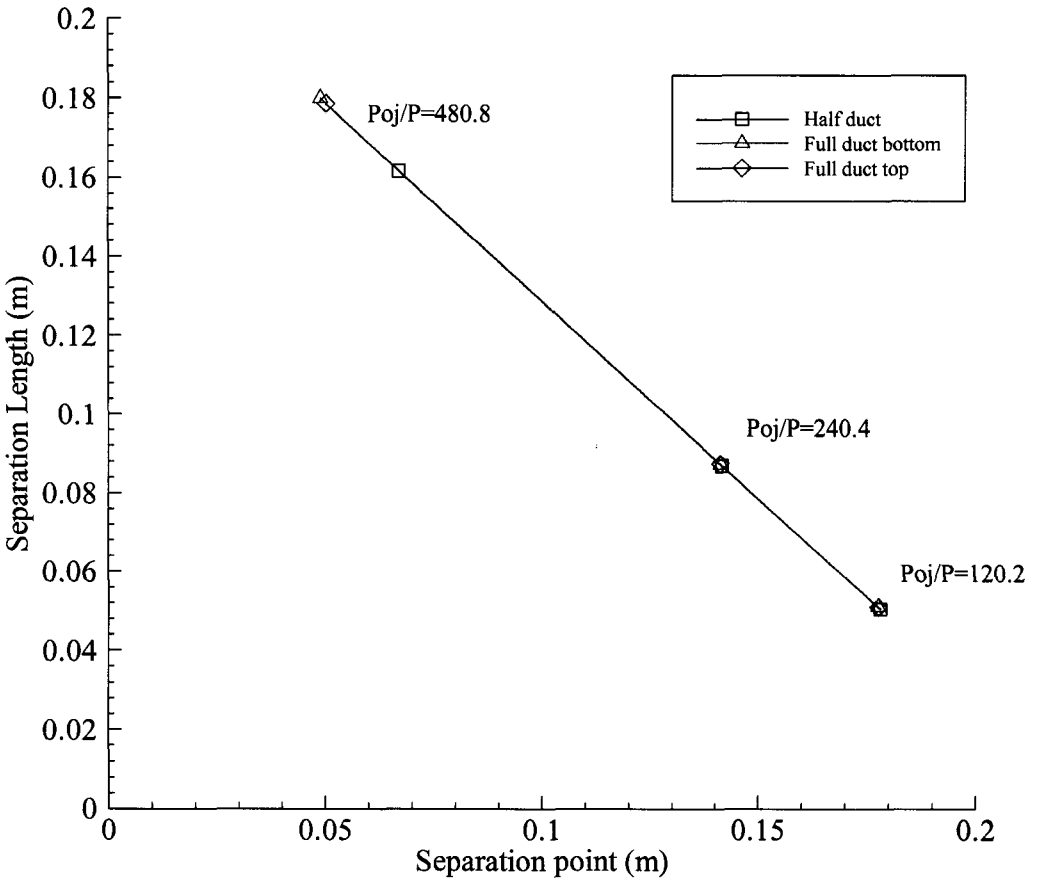

Figure 4.41 Separation point versus separation length for all pressure ratios.

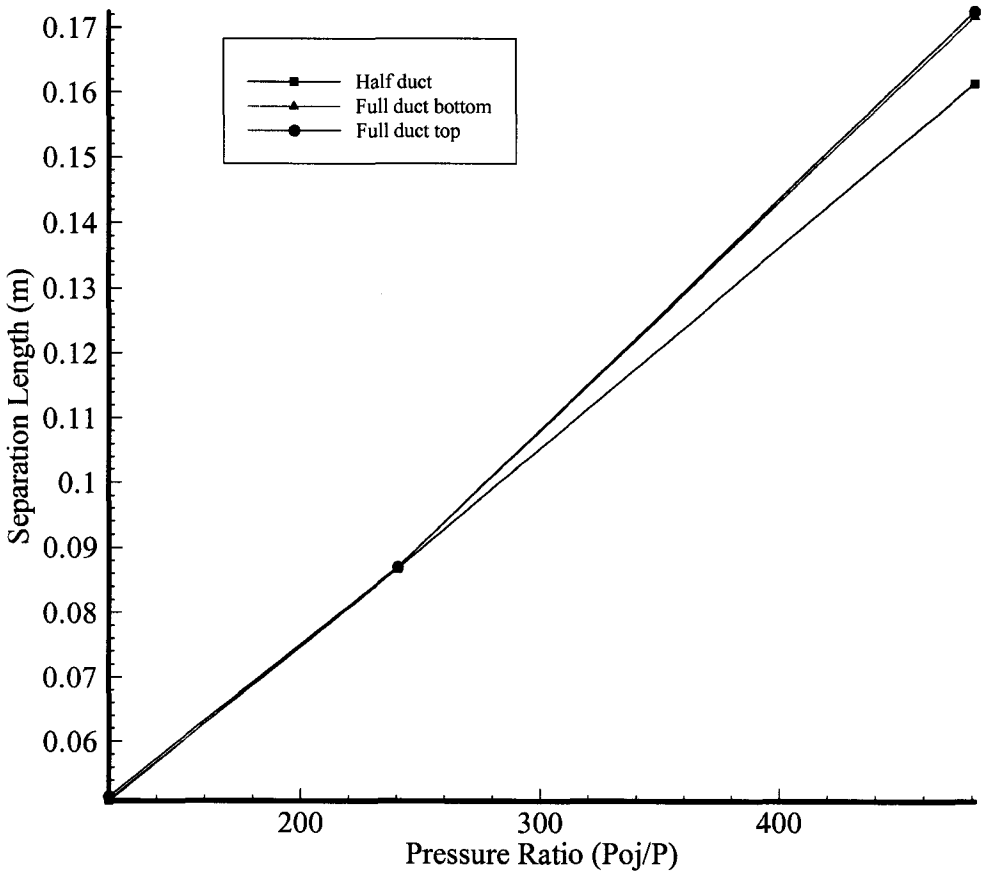

Figure 4.42 Change of upstream separation length versus pressure ratio.

4.5 Long Isolator Duct Results for $Po_j/P = 480.8$

This section gives results for the $Po_j/P=480.8$ model with a long isolator region. The original region had a length of 0.2286 m from the injector to the inlet. The geometry presented here adds an additional 0.2286 m to the original inlet giving the total distance from the injector to the inlet of 0.4572 m. Boundary conditions have not changed, only the geometry has. Figure 4.43 shows the new geometry and grid used. Grid size for this case is 70,500 cells. Table 4.6 shows the boundary conditions used for this model.

Figure 4.44 shows the Mach number contours for 30,000 and 40,000 iterations. If we compare the two, we see that the separation point is further downstream for the 40,000 iteration model. Also notice how the bow shock interacts more in Fig. 4.44b. The recompression shock is still large as shown in previous figures and, therefore, produces the same results.

Normalized static pressure contour plots are shown in Fig. 4.45. Notice how the pressure rises across the separation shock and how much larger the pressure rise is for the 40,000 iteration case. Figure 4.45a shows approximate symmetric results, while after 10,000 iterations these values change showing asymmetric results. You can see the contours on the top wall of the Fig. 4.45b extends further upstream than the bottom wall.

Figure 4.46 investigates the mole fraction of N_2. Both figures show how the pressure ratio affects penetration height. Figure 4.46a produces much more symmetric results while Fig. 4.46b gives asymmetric results. Also, in the bottom recirculation region in the same figure, we see a large concentration of N_2. This may be attributed to turbulent shearing in the region causing more than one region of circulation.

Velocity vector and streamline contour plots are given in Fig. 4.47. It is shown in Fig. 4.47a the symmetry of the flowfield. After further iterations we see the asymmetry flowfield develop. Within the recirculation regions there are multiple vortices, especially in the bottom region. We can see that with the increased pressure ratio the flowfield within this recirculating "bubble" becomes increasingly unstable as compared to lower pressure ratios.

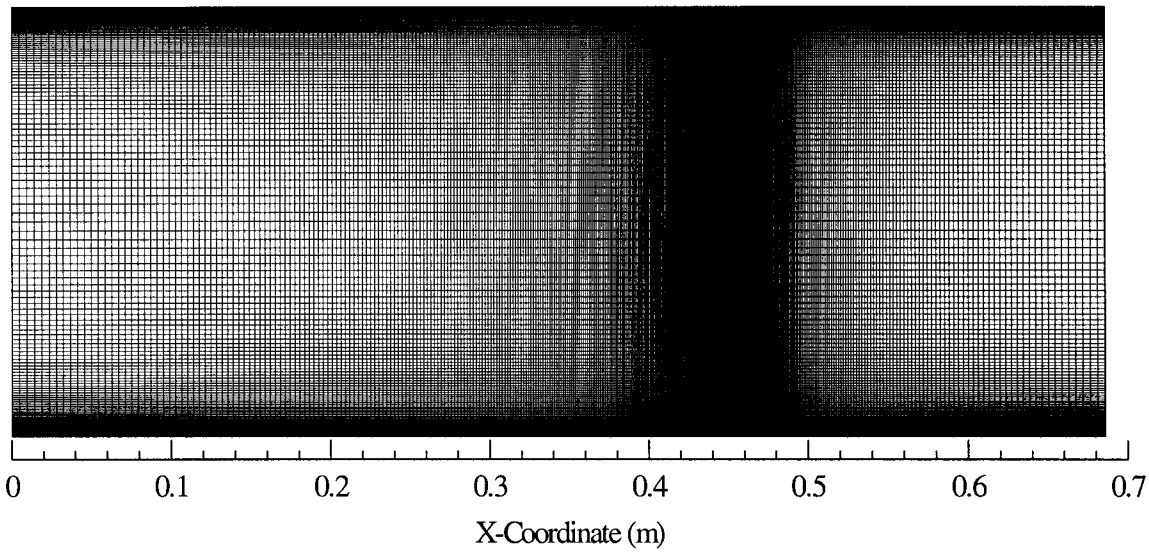

Figure 4.43 Geometry and grid for long isolator.

Table 4.4 Boundary conditions for long isolator

	Freestream Air	Nitrogen Injectant
M	3.5	1.0
P_t (kPa)	60.157	379.901
P_s (kPa)	0.789	200.637
T_t (K)	314.44	291.67
T_s (K)	91.67	243.33
Velocity (m/s)	670.56	317.906

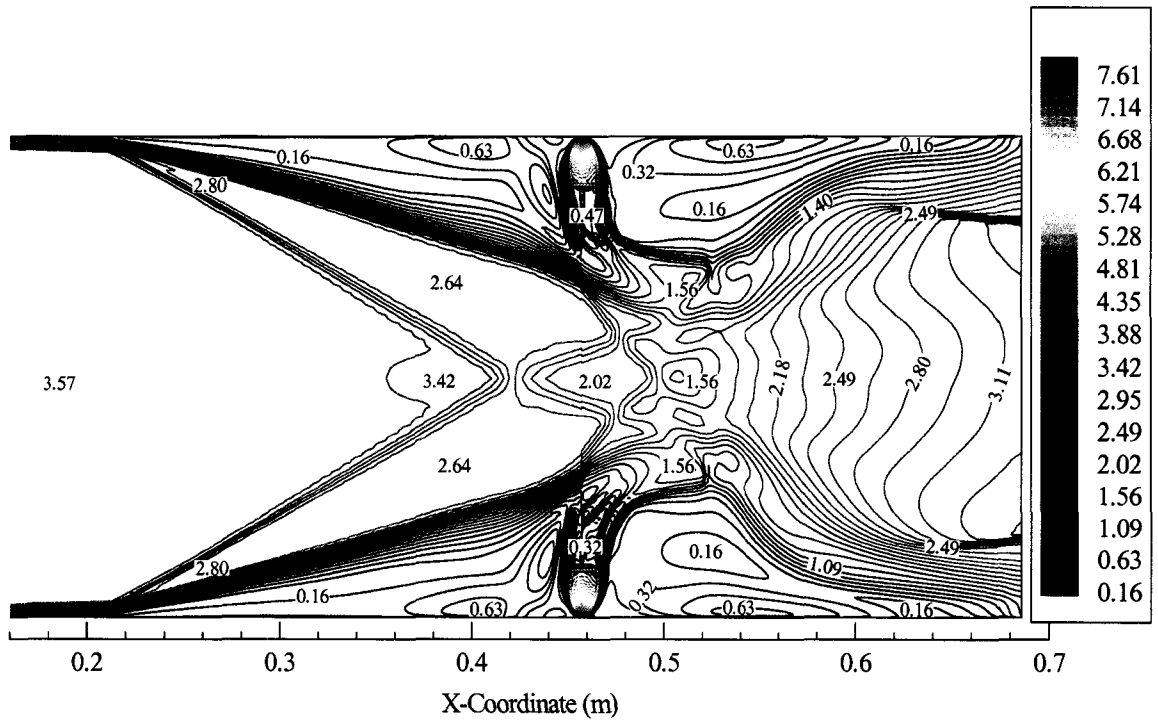

a. 30,000 iterations

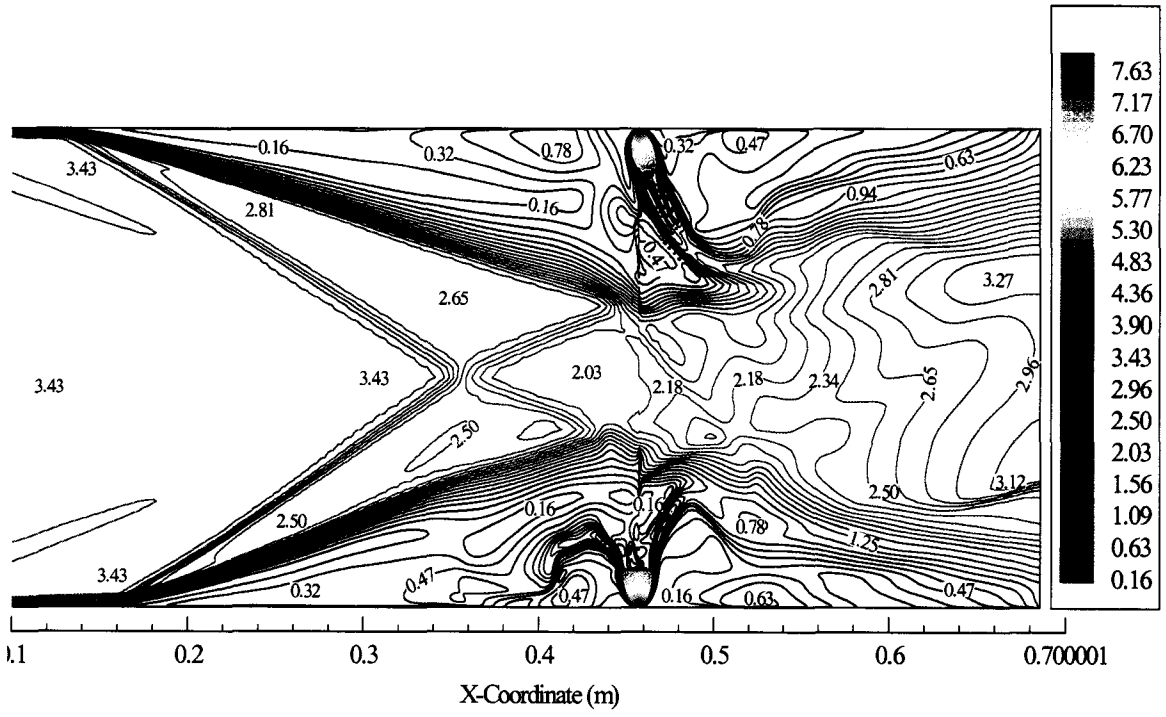

b. 40,000 iterations

Figure 4.44 Mach number contours for Po_j/P=480.8.

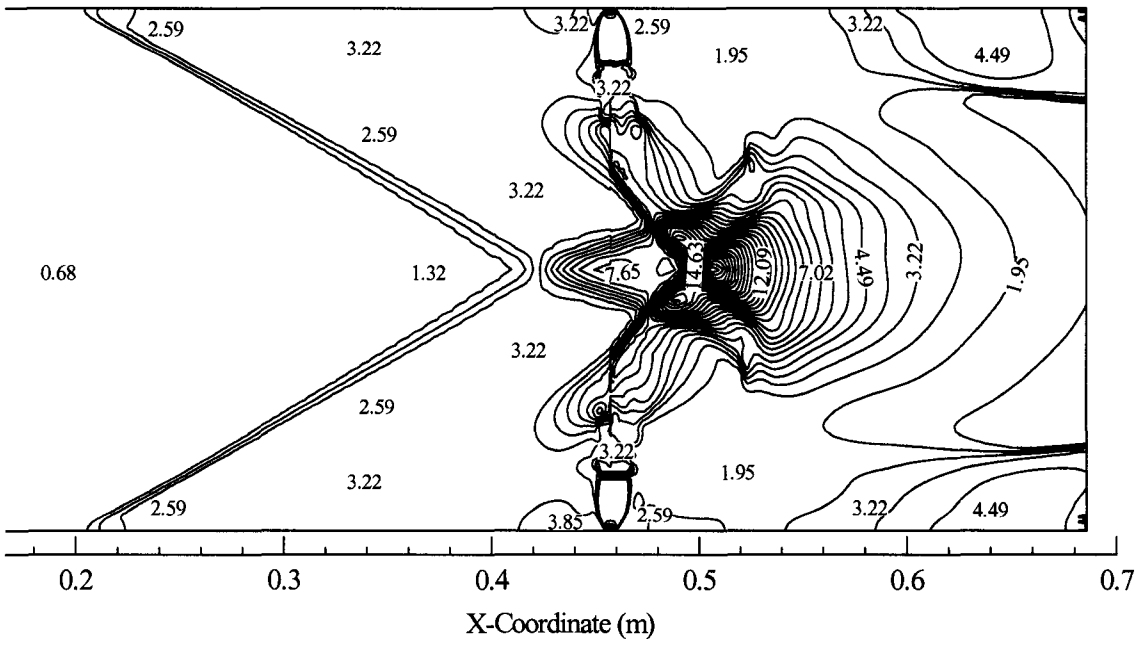

a. 30,000 iterations

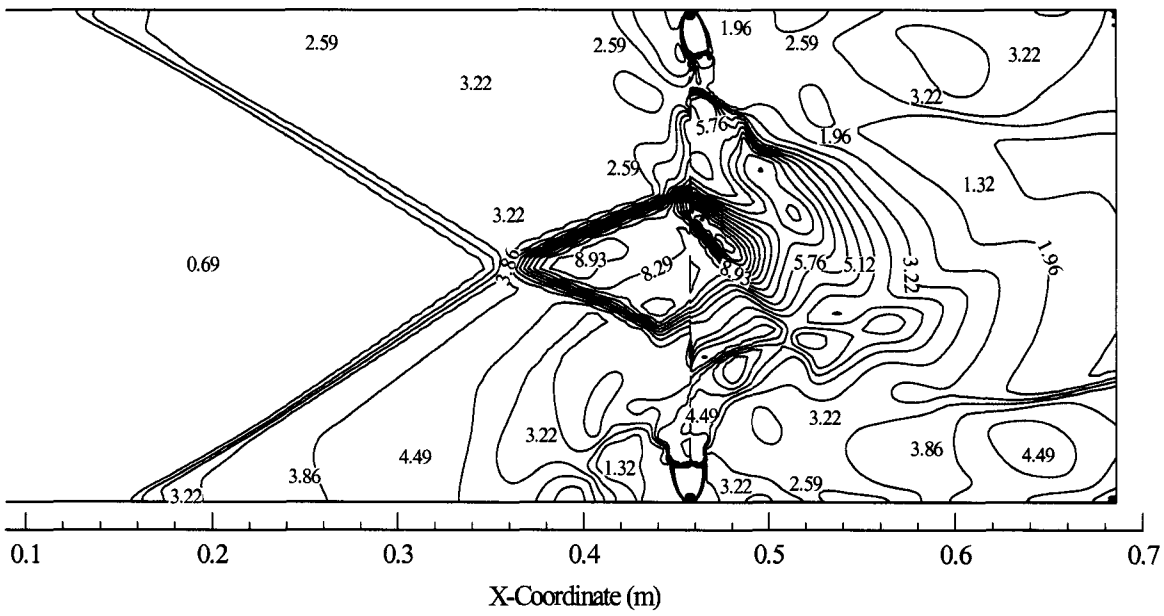

b. 40,000 iterations

Figure 4.45 Normalized static pressure contours for Po_j/P=480.8.

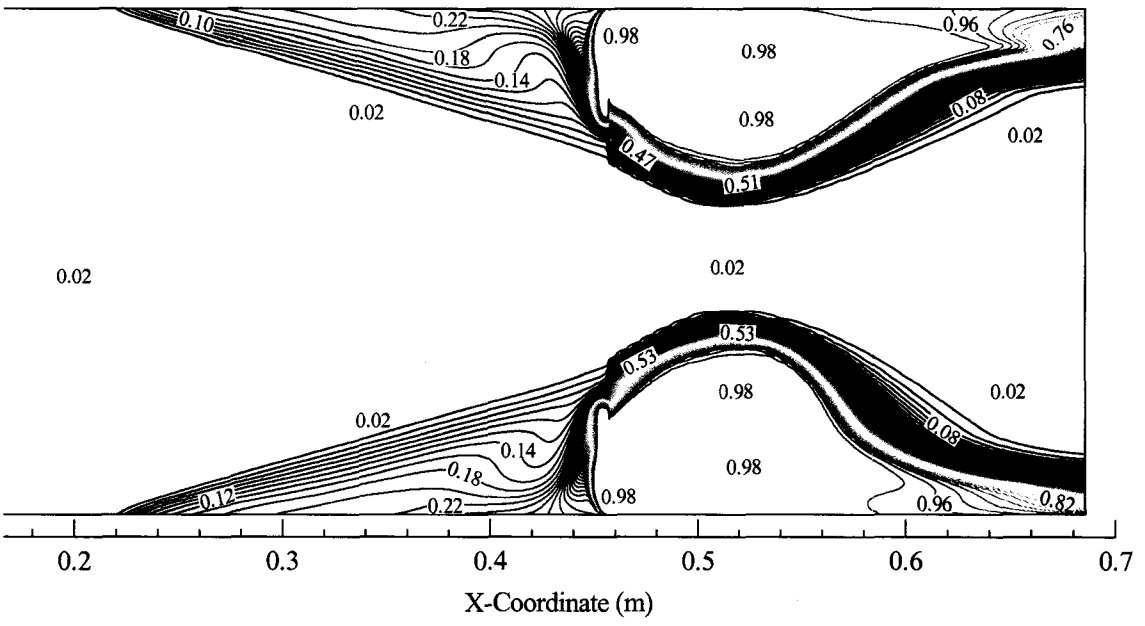

a. 30,000 iterations

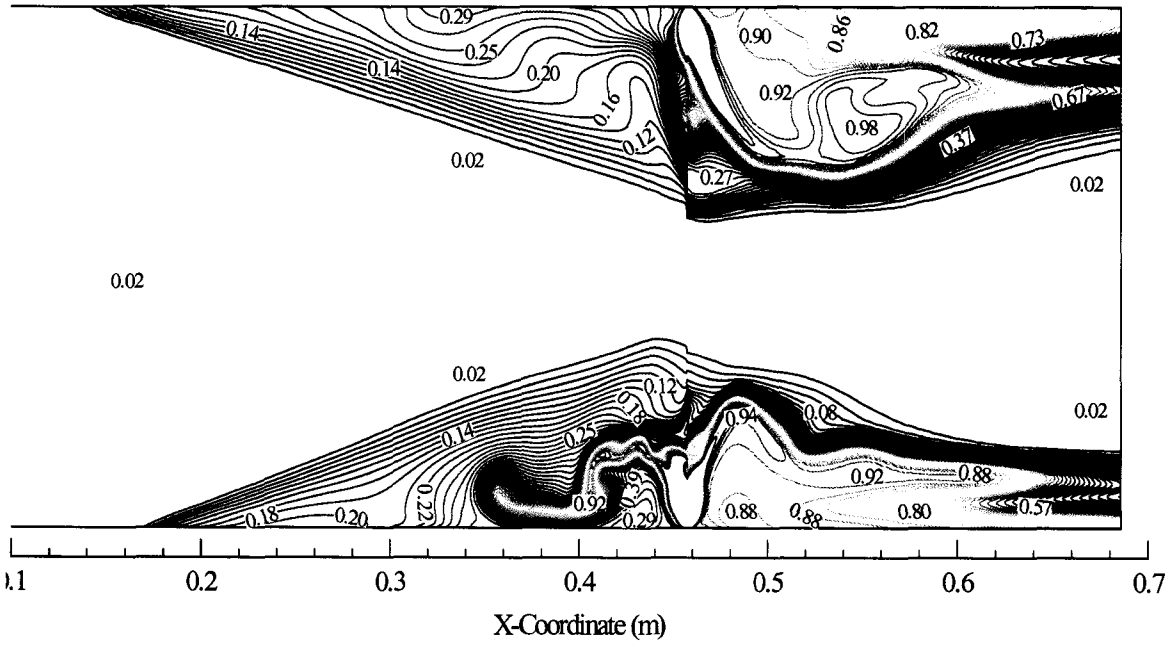

b. 40,000 iterations

Figure 4.46 Mole fraction of N_2 contours for Po_j/P=480.8.

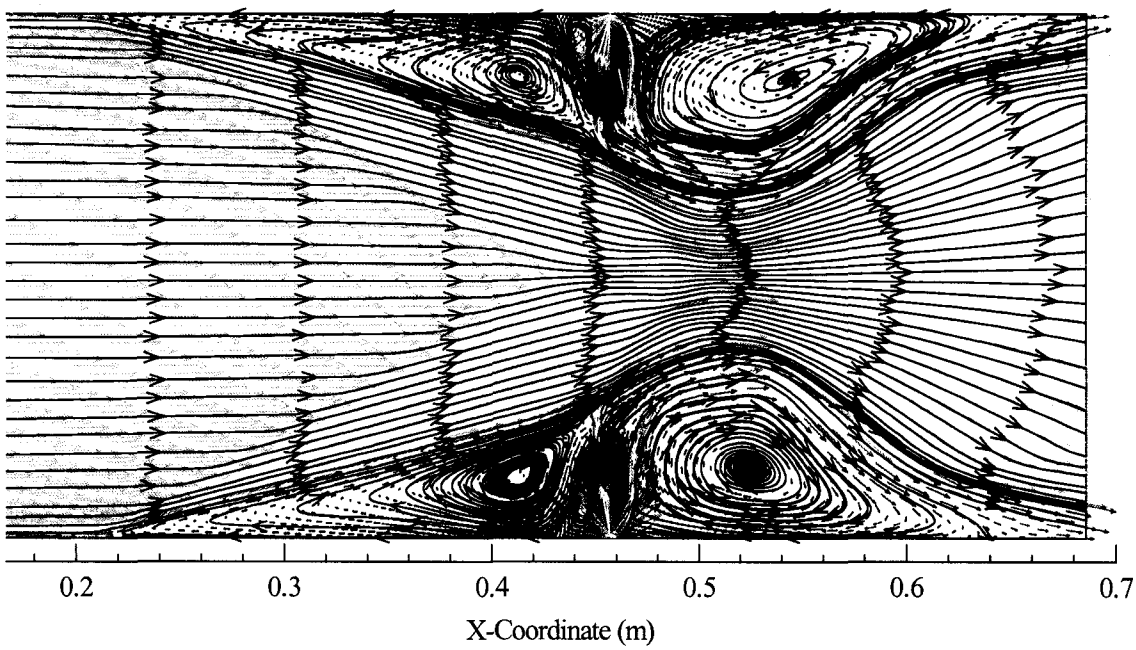

a. 30,000 iterations

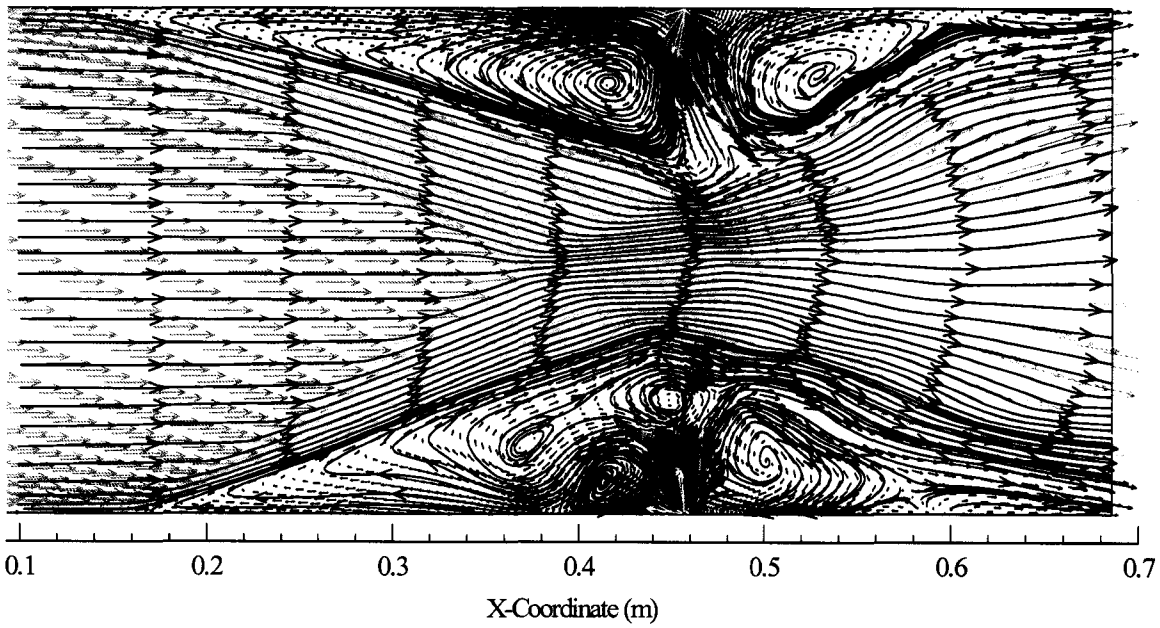

b. 40,000 iterations

Figure 4.47 Velocity vector and streamline contour plots for Po_j/P=480.8.

In the next figures, normalized static pressure and velocity along the x-coordinate plots are presented. Figure 4.48-4.50 show the normalized static pressure plots along the top and bottom walls. Figure 4.50 combines Figs. 4.48 and 4.49 to show the difference between the 30,000 and 40,000 iteration models. The increase in pressure due to the separation shock has moved further downstream and also the separation goes from nearly symmetric to asymmetric. Notice how the bottom wall pressure plot for the 40,000 model increases more than the top wall.

Figures 4.51-4.55 show the velocity along the x-coordinate for both the 30,000 and 40,000 iteration models. Figure 4.51 show the entire domain plot for the 30,000 iteration study. Notice that the top and bottom walls present near symmetric results. To verify this Fig. 4.52 shows that the top wall separates approximately 0.0025 m. before the bottom wall. This is not visible to the naked eye on the previous figures, but proves that asymmetric conditions are present. Figures 4.53 and 4.54 show the velocity along the x-coordinate for the 40,000 iteration model. It is shown how the flow separates further upstream at the top wall as compared to the bottom wall separating first in the 30,000 iteration model. We see how the flow becomes unsteady within the recirculation region. As we look at the boundary layer separates in Fig. 4.54 we can compute the difference between when the top separates and when the bottom does. From the figure it can be shown that the top separates at approximately 0.122 m and the bottom separates at approximately 0.152 m. That is a 0.130 m difference. This is clearly visible to the naked eye as opposed to the 30,000 iteration model. Finally, we combine all the velocity figures to produce Fig. 4.55. Here we can see the difference between the 30,000 iteration and 40,000 models. Again we see the 40,000 iteration model shows asymmetric results as opposed to the nearly symmetric 30,000 iteration model.

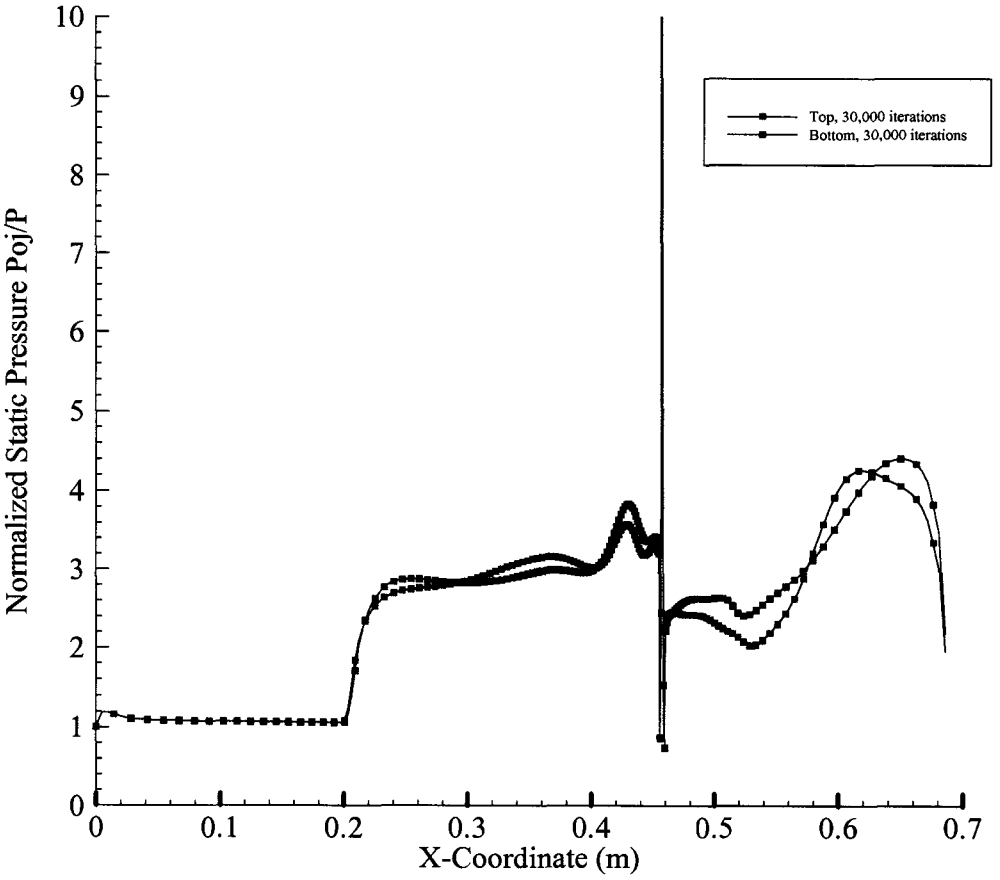

Figure 4.48 Normalized static pressure plot using the long isolator after 30,000 iterations, P_{oj}/P=480.8.

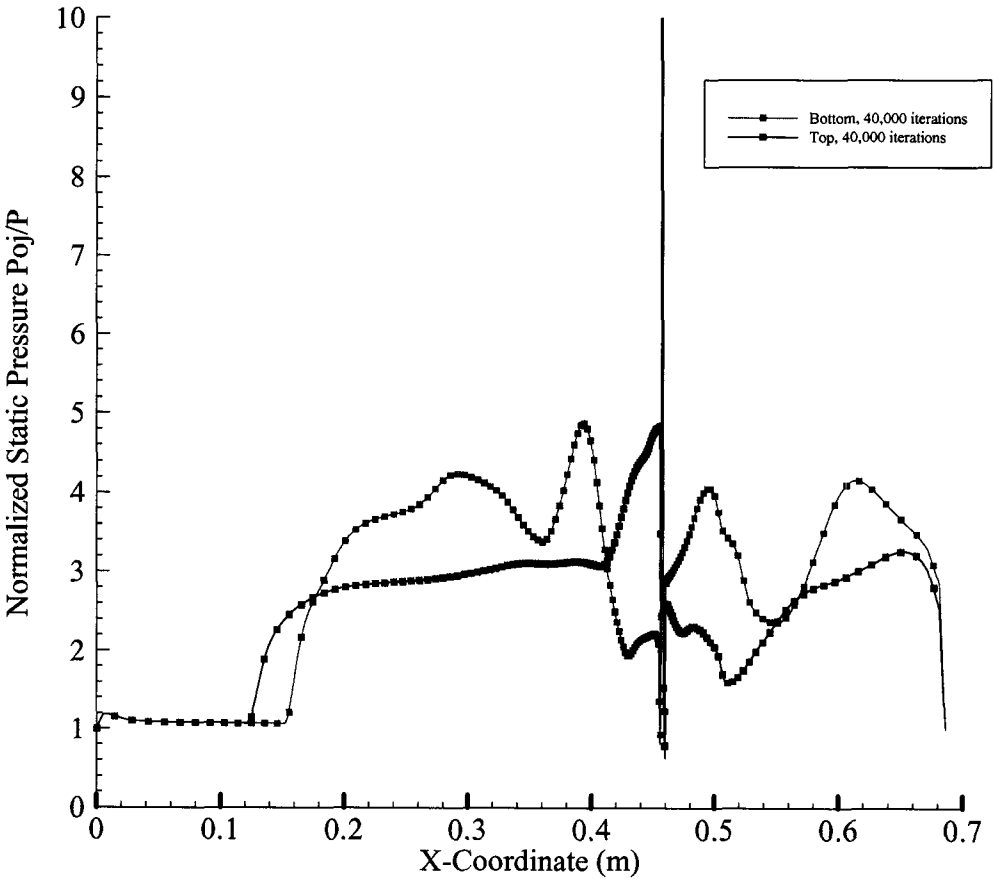

Figure 4.49 Normalized static pressure plot using the long isolator after 40,000 iterations, P_{oj}/P=480.8.

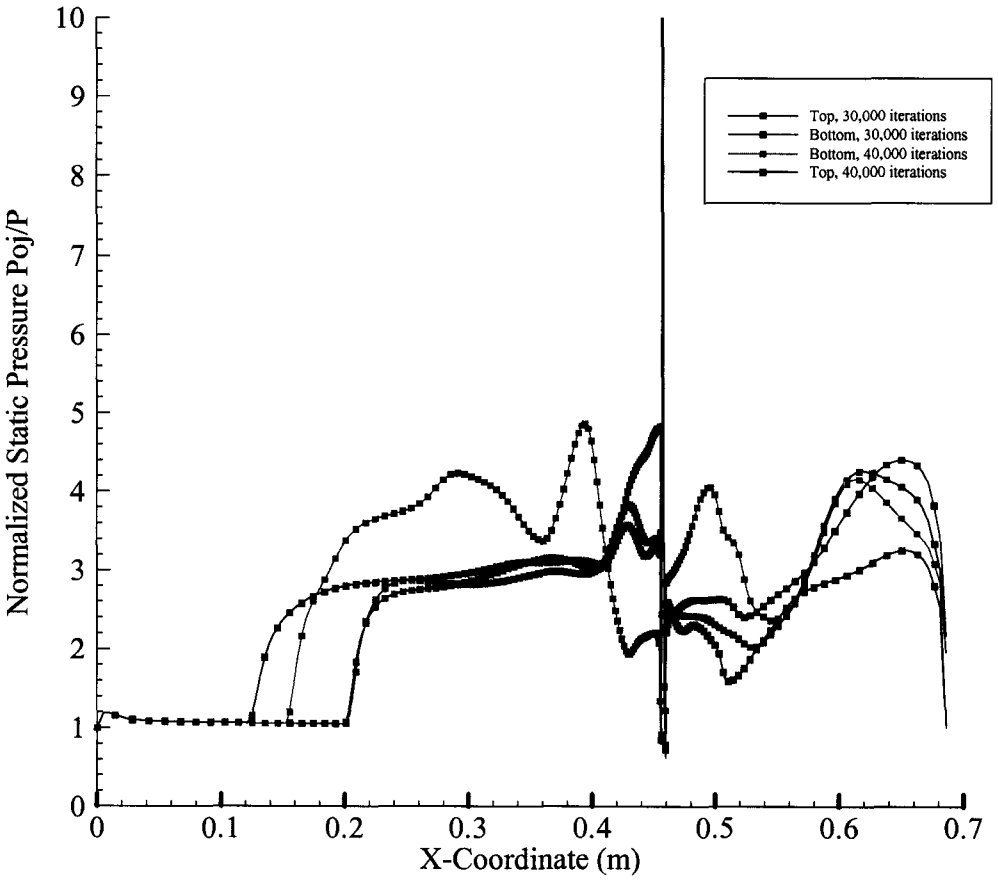

Figure 4.50 Normalized static pressure plot comparison using the long isolator, Po_j/P=480.8.

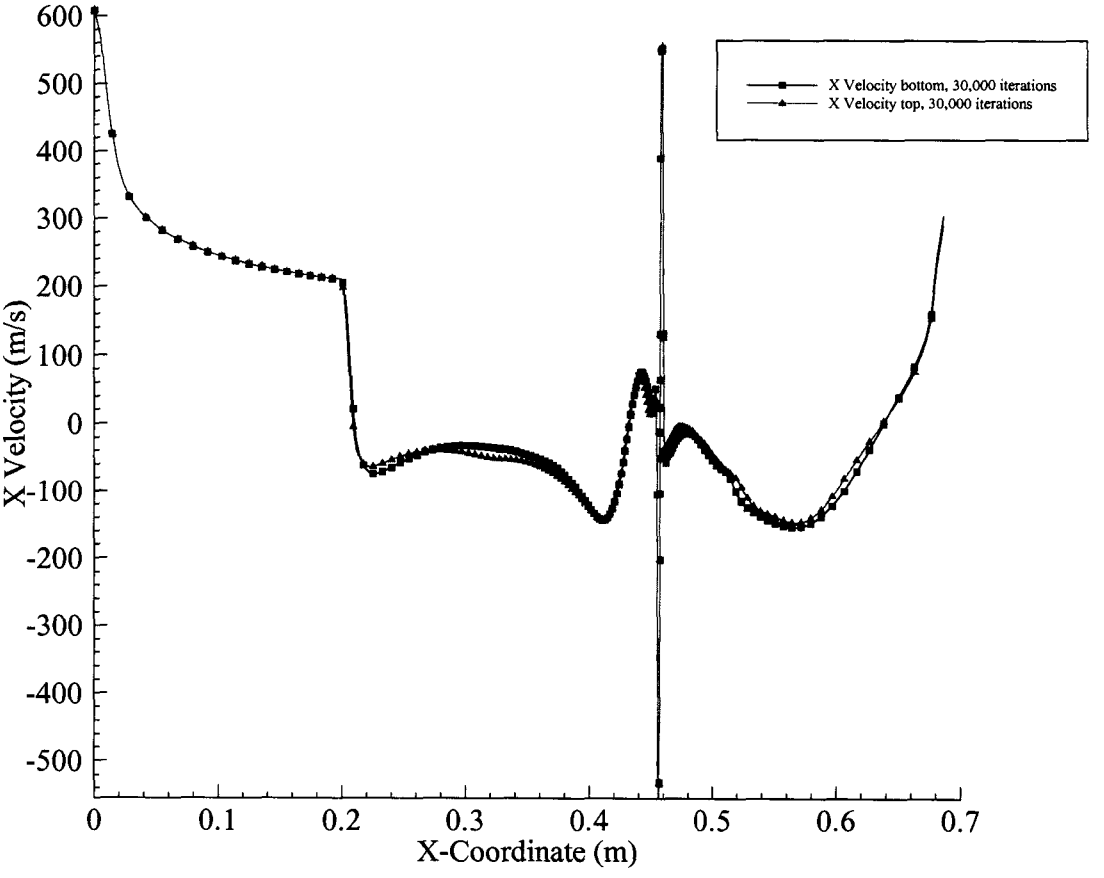

Figure 4.51 X velocity plot after 30,000 iterations using the long isolator, Po_j/P=480.8.

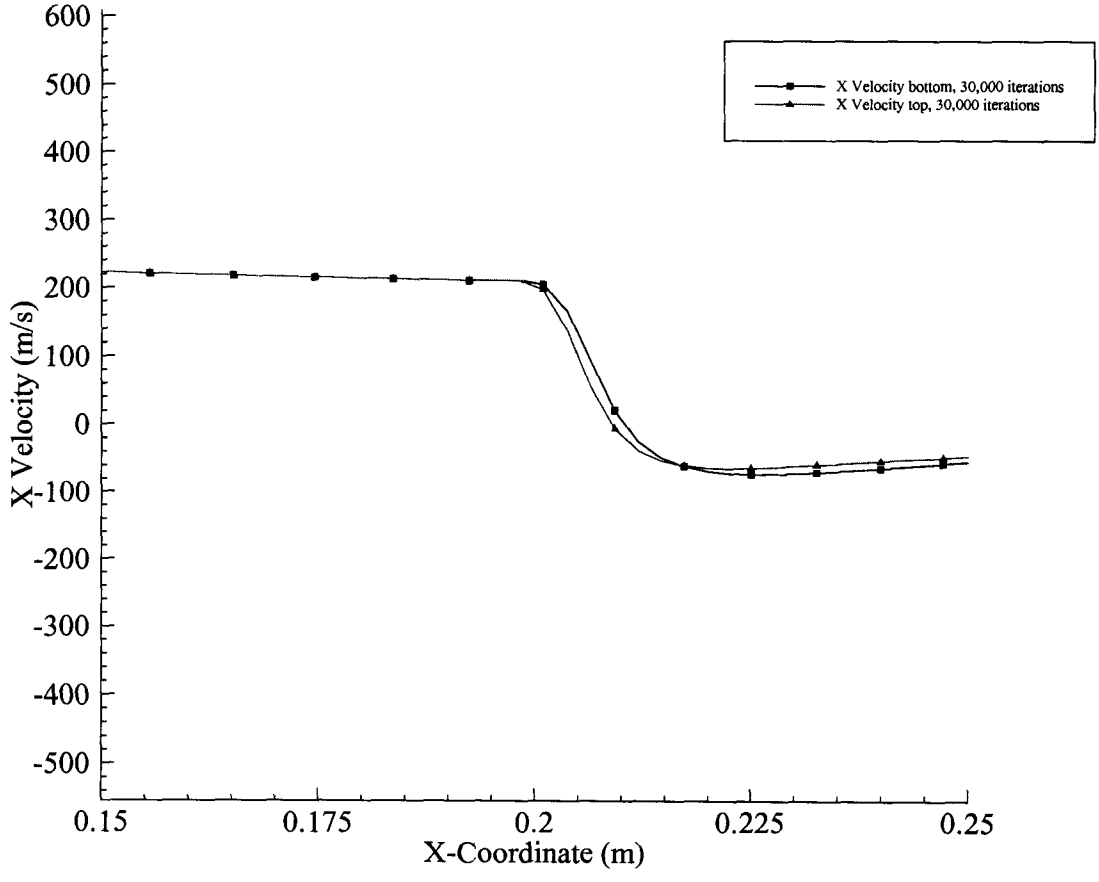

Figure 4.52 X velocity plot showing boundary layer separation after 30,000 iterations using the long isolator, Po_j/P=480.8.

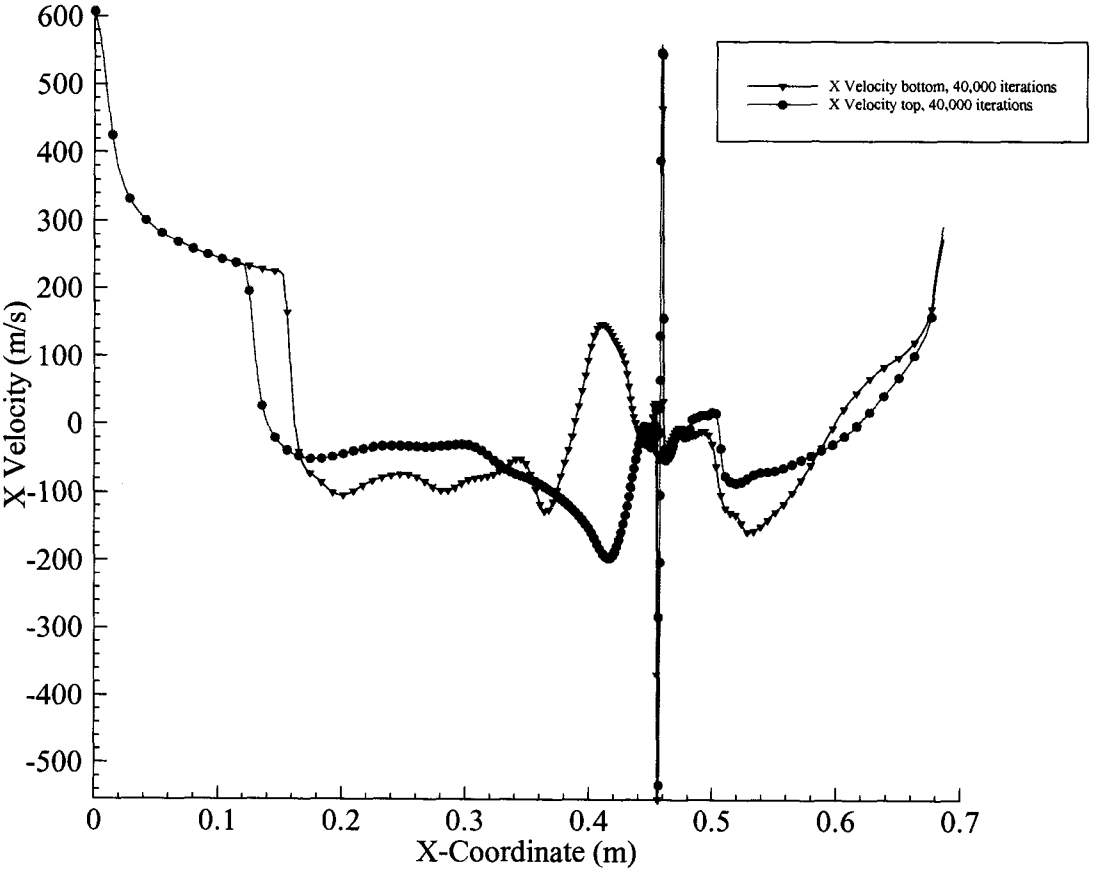

Figure 4.53 X velocity plot after 40,000 iterations using the long isolator, Po_j/P=480.8.

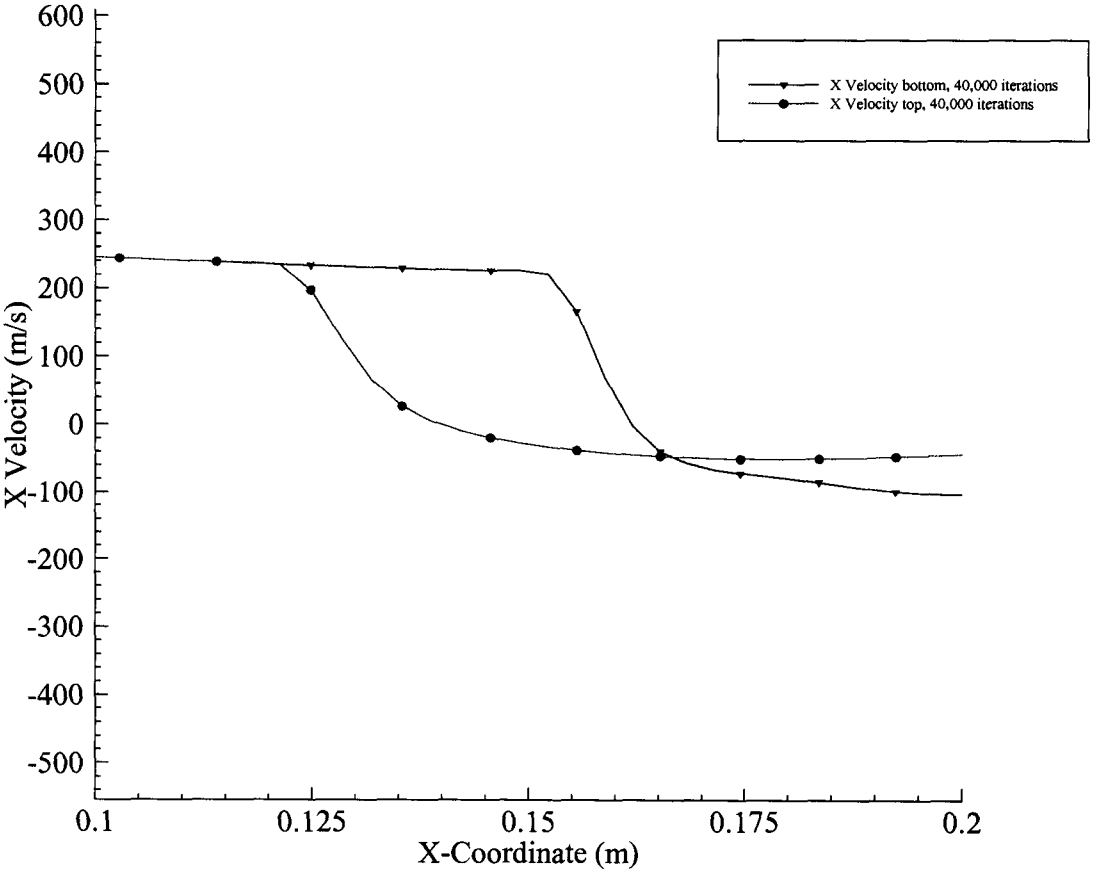

Figure 4.54 X velocity plot showing boundary layer separation after 40,000 iterations using the long isolator, Po_j/P=480.8.

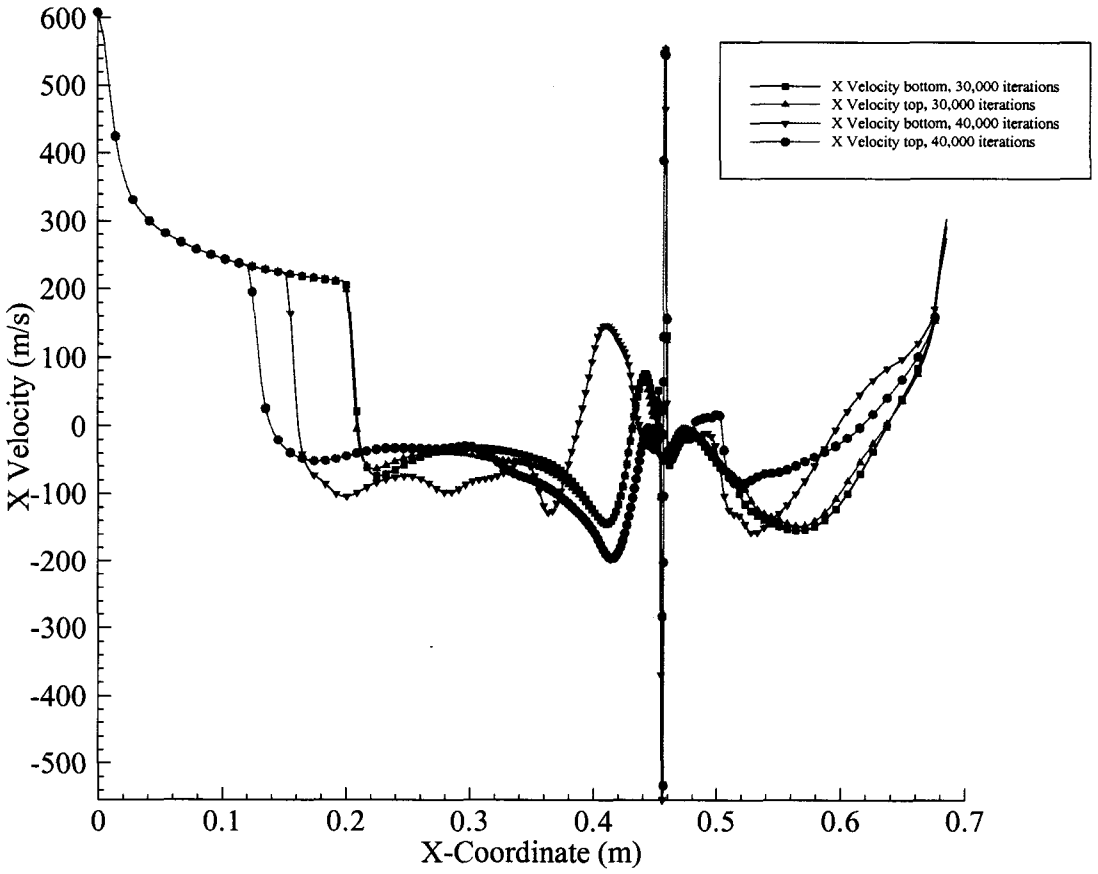

Figure 4.55 X velocity plot comparison using the long isolator, Po_j/P=480.8.

Separation point versus separation length has been plotted in Fig. 4.56. The separation points for the top and bottom walls for the 30,000 iteration case are much closer together than the 40,000 iteration case. Also notice how far the separation points move upstream as the number of iterations increased.

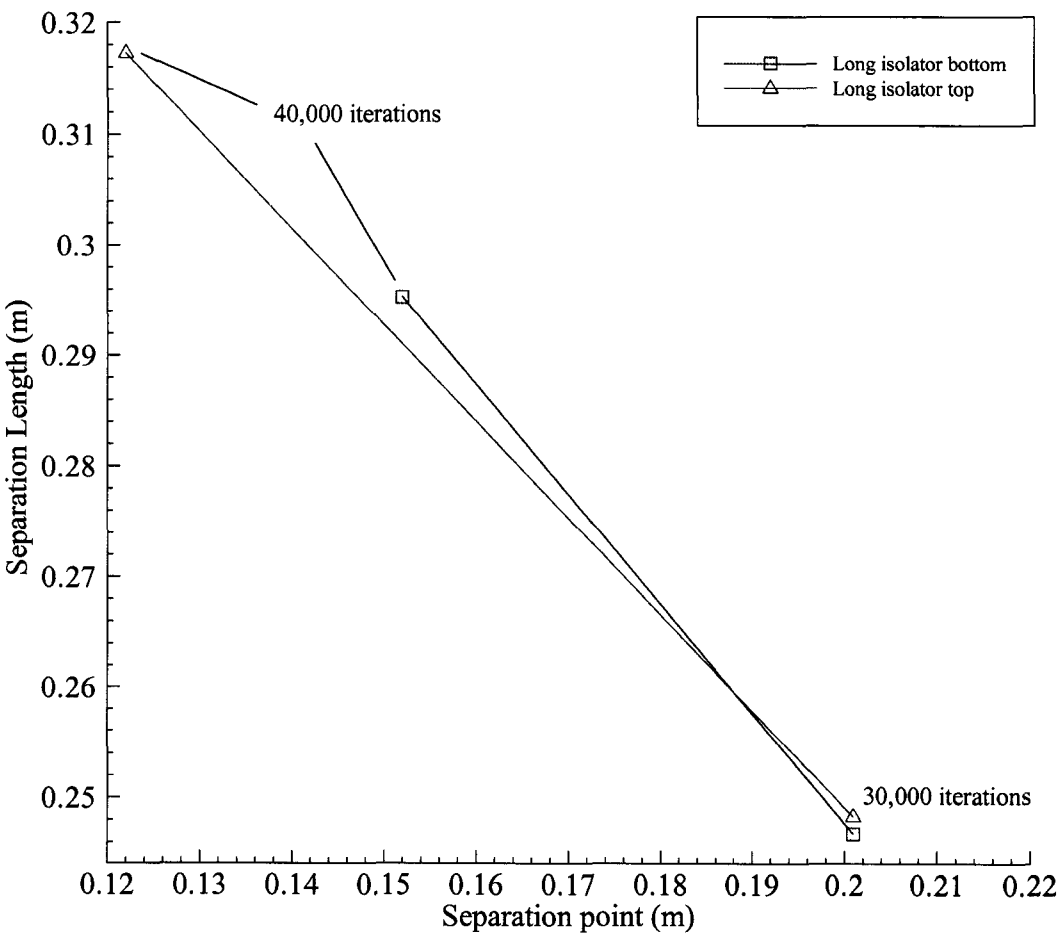

Figure 4.56 Separation point versus separation length for the long isolator, Po_j/P=480.8.

4.6 Longer Isolator Duct Results for $Po_j/P = 480.8$

This section is a continuation of the previous studies with the isolator region extended an additional 0.2286 m. This makes the distance of the isolator at 0.6858 m. Boundary conditions are maintained for the $Po_j/P = 480.8$ models. Figure 4.57 shows the geometry and grid for this study. Grid size for this study was 276,000 cells. Table 4.7 shows the boundary conditions.

Mach number contours are given in Fig. 4.58 for 29,700 and 50,900 iterations. The upstream interaction moves upstream as the case iterates. The Mach legend shows a difference in Mach number in the injector region. This can be attributed to the upstream interaction moving upstream and producing a larger circulation region or "bubble". The difference between the two can be seen. After 29,700 iterations, the upstream interaction is consistent with previous models, however after 50,900 iterations the flow moves much further upstream close to the inlet giving a unique shock train not seen in previous models. This is due to the longer isolator geometry. Notice the recirculation bubble on the bottom wall. It shows the flow in one region to be supersonic. Also, results for Fig. 4.58a appear to be symmetric, but results for Fig. 4.58b are clearly asymmetric.

Normalized static pressure contours are presented in Fig. 4.59. The classic shock train is present in both contours. The pressure rise is greater across the shock in Fig. 4.59b. The recompression shock is much more defined as well. The separation shock has moved further upstream after iterating more. The separation shock begins to oscillate forward and backward as the model iterates, never reaching a convergent state due to the high turbulence and shock wave formations. It is evident in Fig. 4.59b that the separation shock on the bottom separates before the top.

Figure 4.60 shows the mole fraction of N_2. In Fig. 4.60a we see that the Nitrogen is concentrated in the recirculation region near the injector, typical of previous mole fraction figures. As we continue after 20,300 iterations, in Fig. 4.60b, the upstream interaction has moved further upstream, however the Nitrogen mole fraction stays confined near the injector. The top wall region has a small percentage of Nitrogen being swept upstream. This is due a small pocket region in front of the injector, shown in Fig. 4.60b, where the recirculating "bubble" is further upstream. If you compare both figures of Fig. 4.60 we see that the recirculating region is closer to the injector in

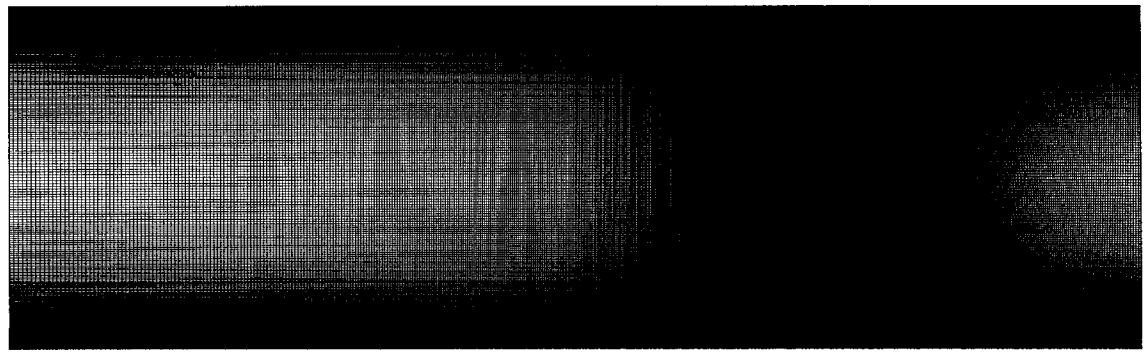

Figure 4.57 Geometry and grid for longer isolator.

Table 4.5 Boundary conditions for longer isolator

	Freestream Air	Nitrogen Injectant
M	3.5	1.0
P_t (kPa)	60.157	379.901
P_s (kPa)	0.789	200.637
T_t (K)	314.44	291.67
T_s (K)	91.67	243.33
Velocity (m/s)	670.56	317.906

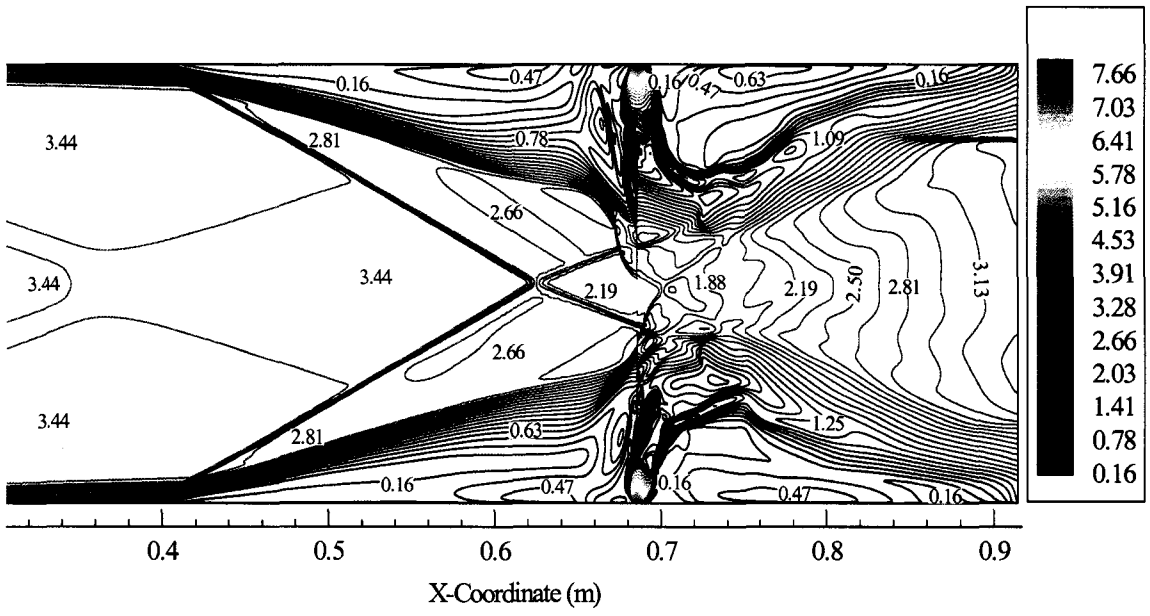

a. 29,700 iterations

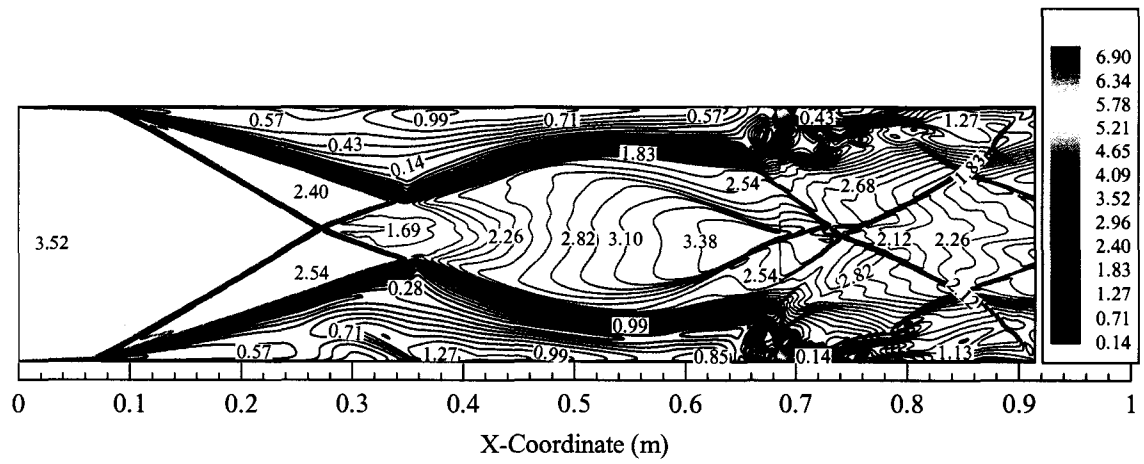

b. 50,900 iterations

Figure 4.58 Mach number contours for Po_j/P=480.8.

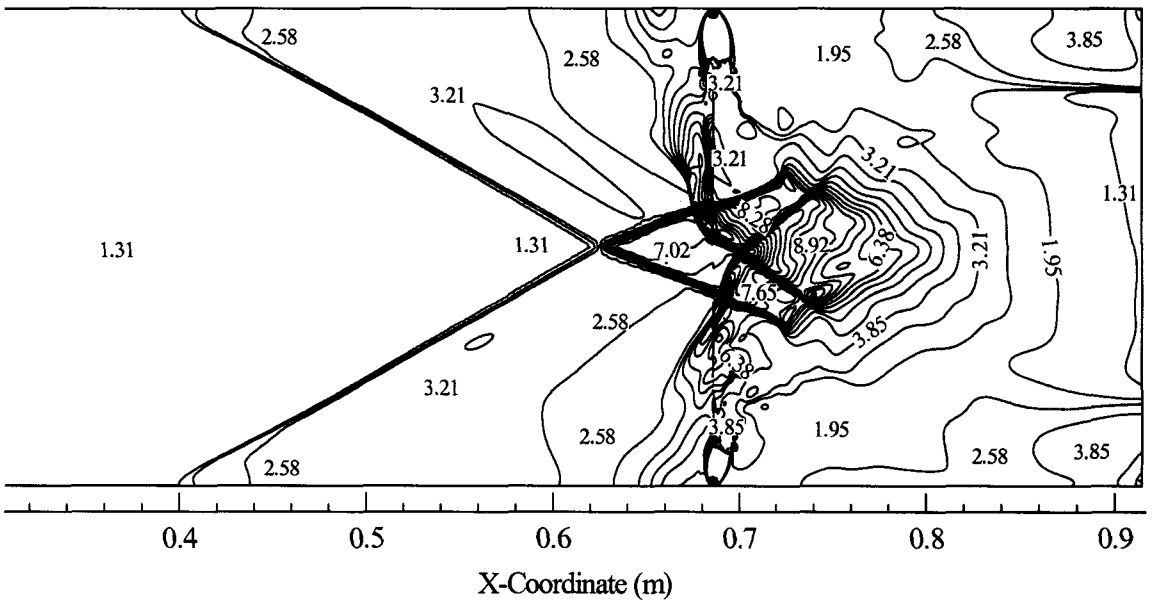

a. 29,700 iterations

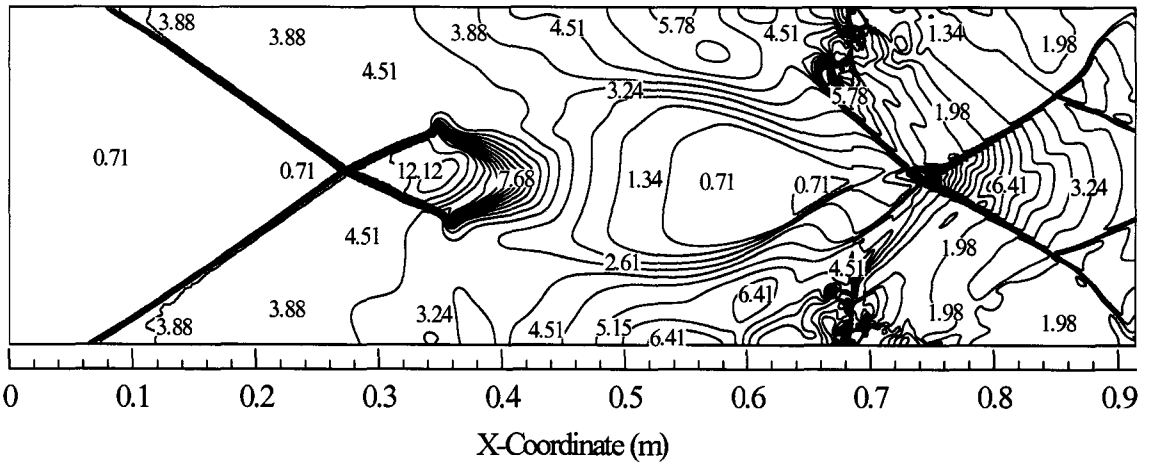

b. 50,900 iterations

Figure 4.59 Normalized static pressure contours for P_{oj}/P=480.8.

Fig. 4.60a than in Fig. 4.60b. This explains why Nitrogen, in Fig. 4.60b, is not being swept upstream as in previous Nitrogen mole fraction figures.

Velocity vector and streamline contours are shown in Fig. 4.61. The classic upstream vorticity is shown in Fig. 4.61a, as well as the downstream vorticity. Figure 4.61b shows the upstream circulation region being much larger than in previous velocity vector and streamline contour plots. The region is triangular shaped and since the vorticity does not reach to the forward injector region, Nitrogen is not circulated upstream as shown in the previous Fig. 4.60. Since the isolator region is longer this phenomena has occurred. The isolator was elongated to investigate this upstream reaction. Downstream there is very little vorticity in the recirculation region leeward of the injector.

Figures 4.62-4.64 examine the normalized static pressure at the walls after 29,700 and 50,900 iterations. Figure 4.62 is after 29,700 iterations. The pressure begins to rise rapidly at approximately 0.4m and reaches a plateau at approximately $Po_j/P=3$ before reaching the injector. Within the recirculating region the pressure varies due to the transition across the shock wave. Figure 4.63 shows the results after 50,900 iterations. The upstream separation shock has moved much further upstream. Notice that the bottom separates clearly before the top. The pressure ratio reaches a plateau at approximately $Po_j/P=4$ and then begins to fluctuate due to the shock train. Figure 4.64 shows the combination of the 29,700 and 50,900 iteration plots. The difference between the upstream separation shocks for both models is clearly shown. The 29,700 iteration model separated at approximately 0.4m while the 50,900 iteration model separates at approximately 0.08 m. The difference is calculated to be approximately 0.32m.

Velocity along the x-axis is presented for the longer isolator in Figs. 4.65-4.69. Figure 4.65 shows the whole domain after 29,700 iterations. We see that the separations occur approximately at 0.4m. A close up of the separation in Fig. 4.66 shows that the bottom separates approximately 0.025m further upstream than the top. As the case continues to iterate the separation moves upstream very close to the inlet as shown in Fig. 4.67. It is also shown much clearer that the bottom separation is further upstream than the top. Figure 4.68 shows the separation region. The bottom separates at approximately 0.0125m from the inlet and the top separates at approximately 0.075m from the inlet. The

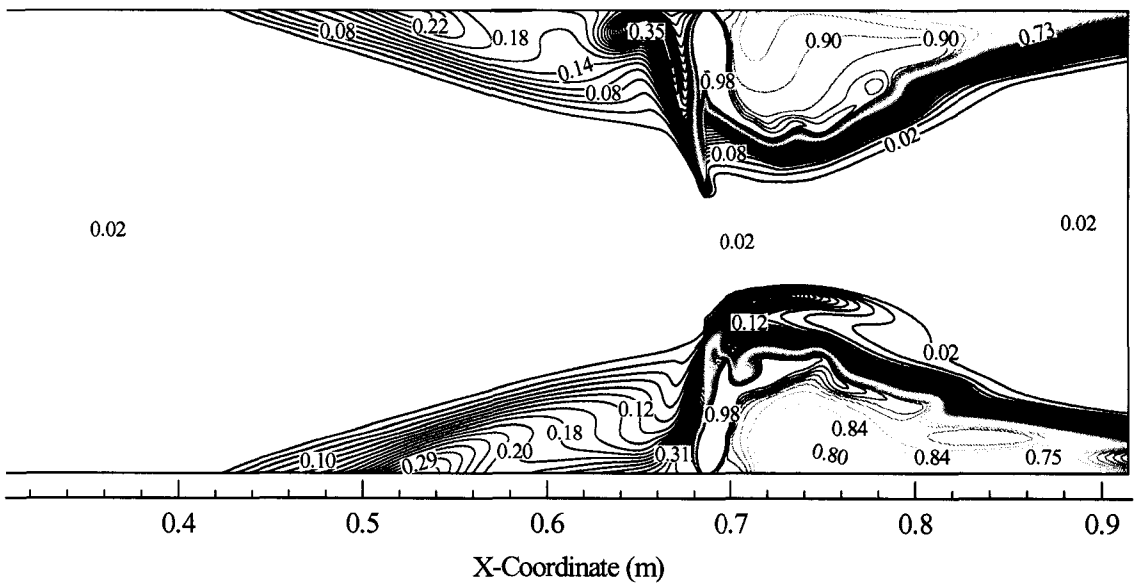

a. 29,700 iterations

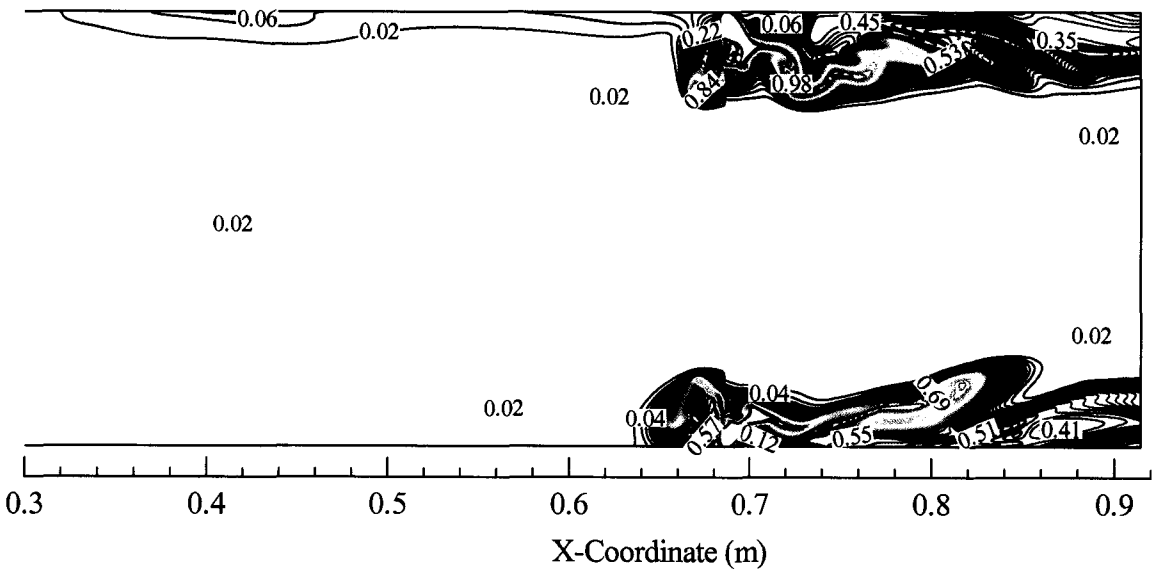

b. 50,900 iterations

Figure 4.60 Mole number contours for Po_j/P=480.8.

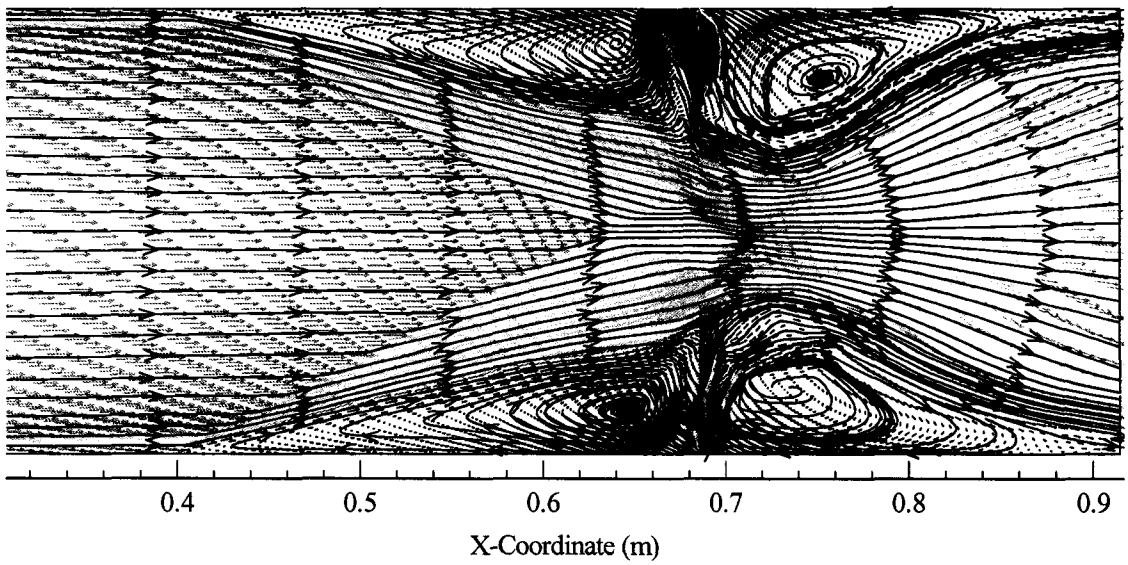

a. 29,700 iterations

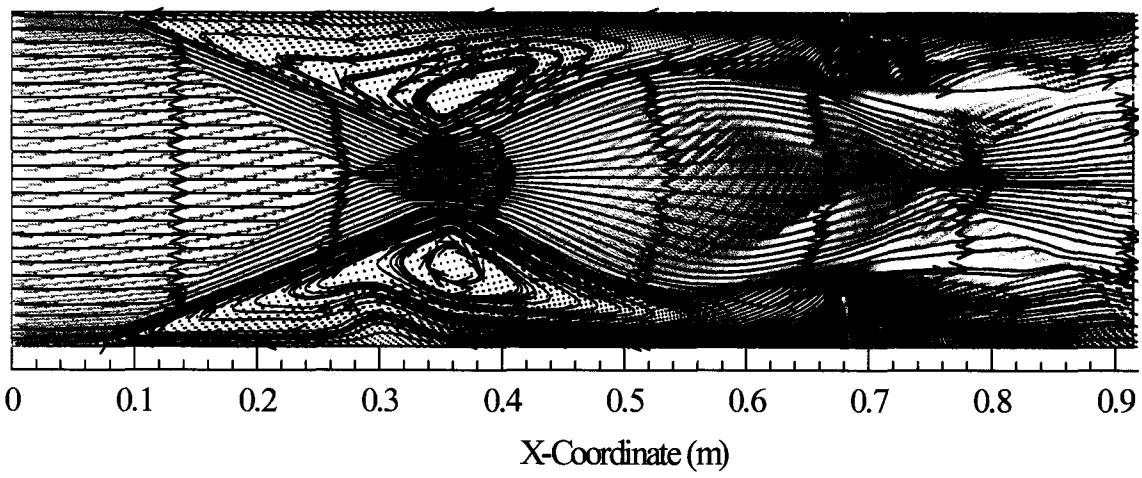

b. 50,900 iterations

Figure 4.61 Velocity vector and streamline contour plots for Po_j/P=480.8.

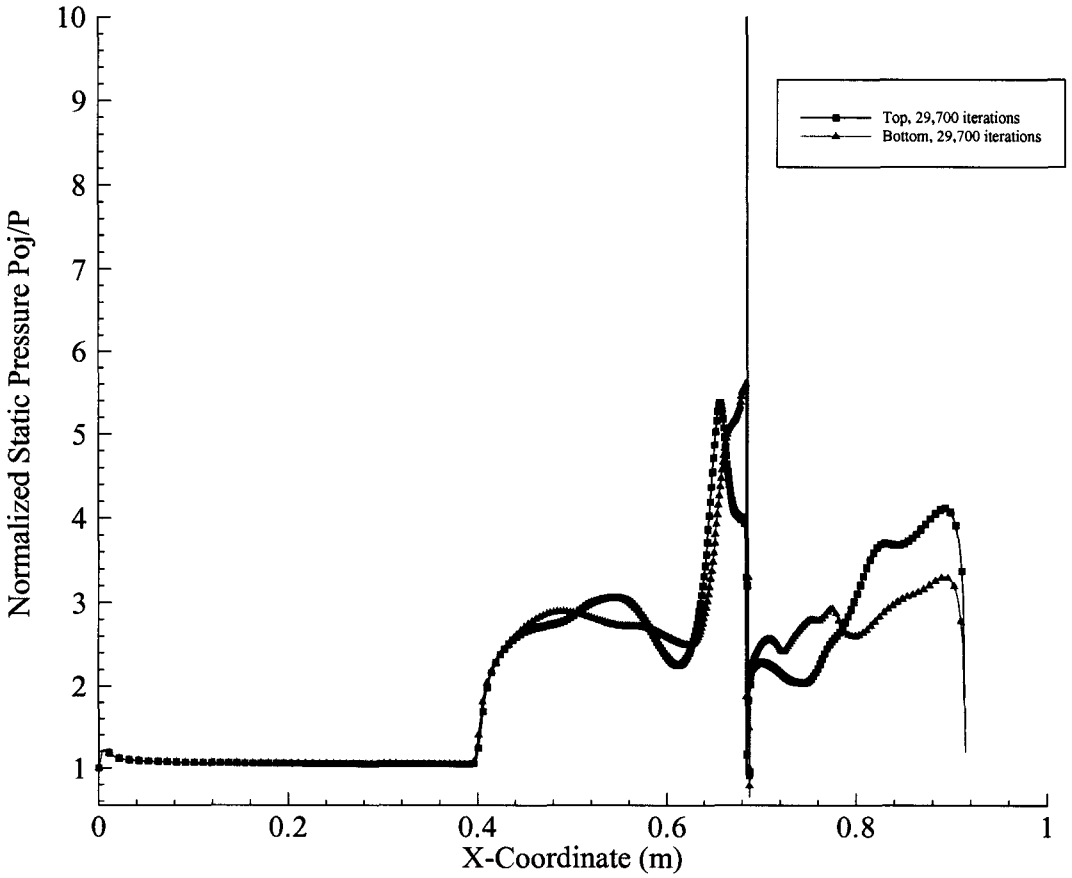

Figure 4.62 Normalized static pressure plot comparison using the longer isolator after 29,700 iterations, Po_j/P=480.8.

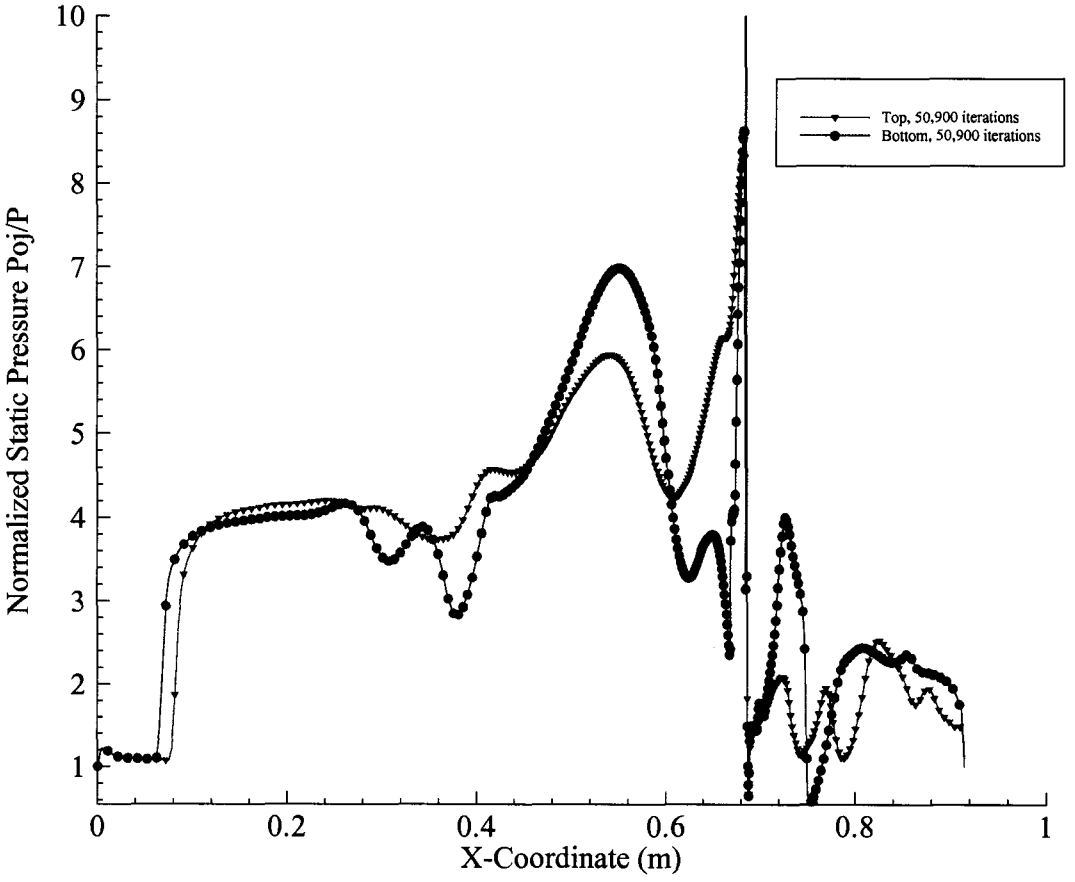

Figure 4.63 Normalized static pressure plot comparison using the longer isolator after 50,900 iterations, P_{oj}/P=480.8.

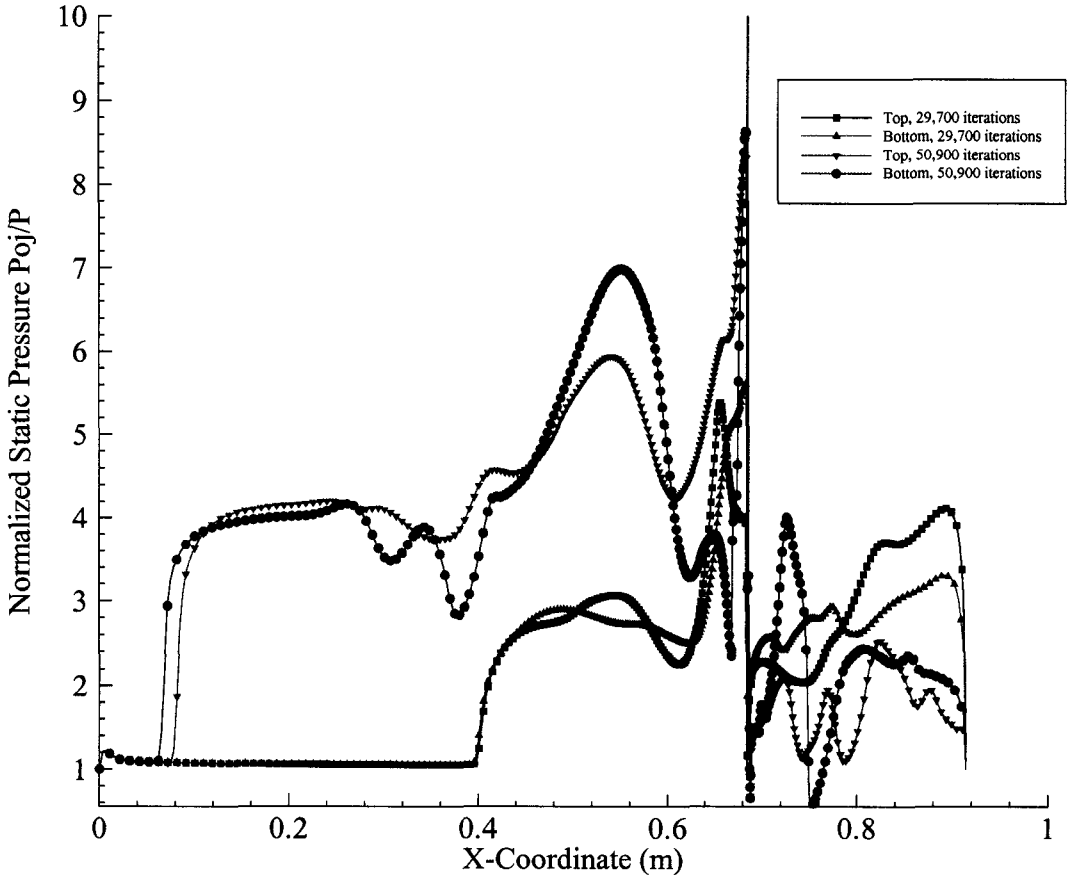

Figure 4.64 Normalized static pressure plot comparison using the longer isolator, P_{oj}/P=480.8.

difference is 0.0625m. Figure 4.69 combines both the 29,700 and 50,900 iteration models. The separation distance, approximately 0.3375m, is very large between both models. Fluctuations in velocity are seen within the separation region. This can be attributed to the turbulence created by the recirculation "bubbles".

Figure 4.70 illustrates the separation point versus separation length for the longer isolator models. The 29,700 iteration model shows how much closer together the separation points are as compared to the 50,900 iteration model. We see that the separation length for the 50,900 iteration case is approximately twice in length as compared to the 29,700 iteration case. If we continued to increase the isolator length, we would find that the separation shock would continue to move forward to a equilibrium point within the isolator. Further, the separation shock would then begin to oscillate downstream and then reach another equilibrium point and then reverse back upstream. This is a continuous process that never reaches a equilibrium state. Convergence is never achieved due to the shock/shock interactions that occur within the chamber. Further investigation into a longer isolator would be beneficial to the study of the upstream interaction and the scramjet engine.

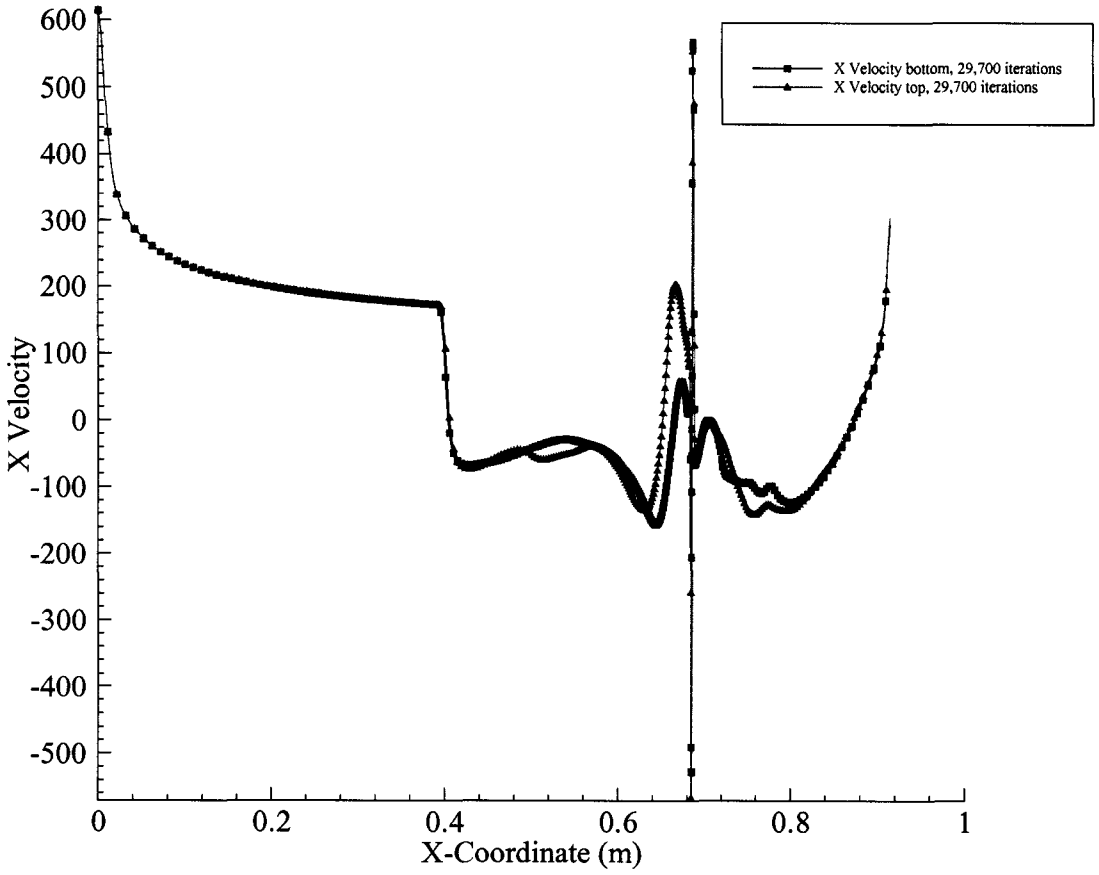

Figure 4.65 X velocity plot after 29,700 iterations using the longer isolator, Po_j/P=480.8.

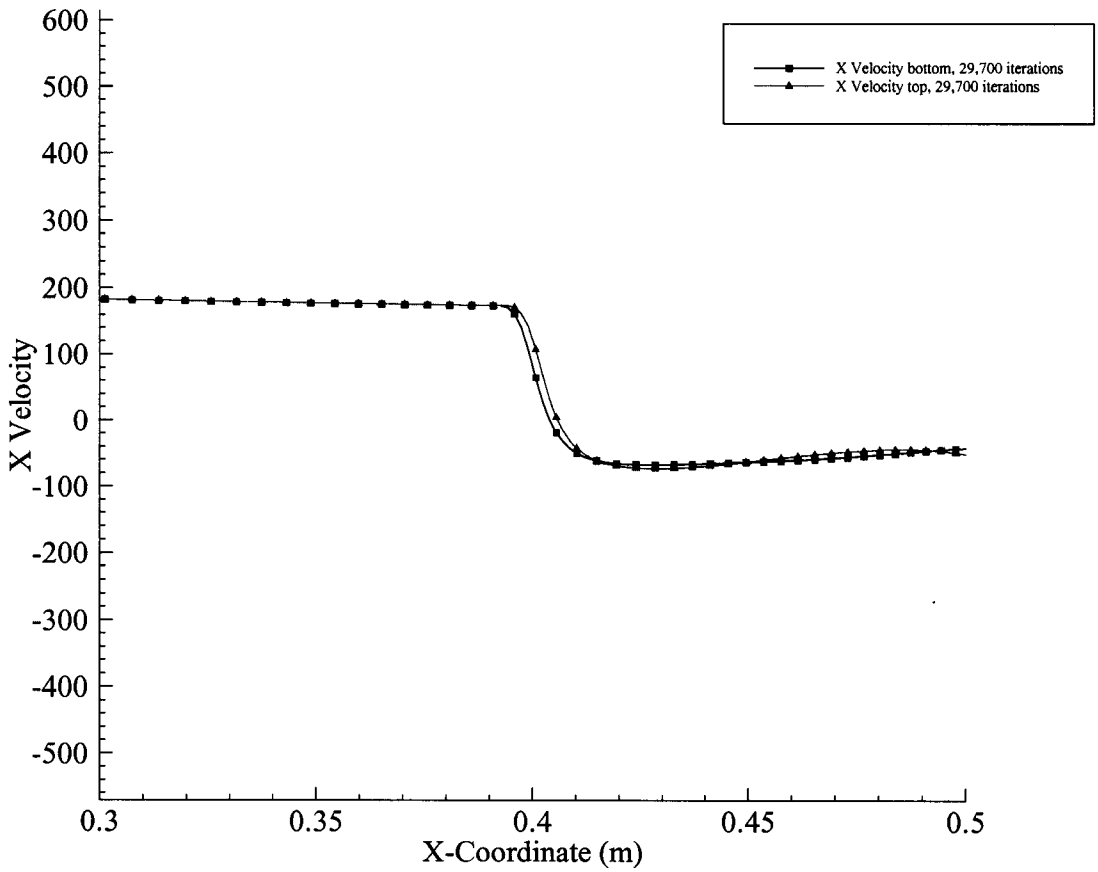

Figure 4.66 X velocity plot showing boundary layer separation after 29,700 iterations using the longer isolator, Po_j/P=480.8.

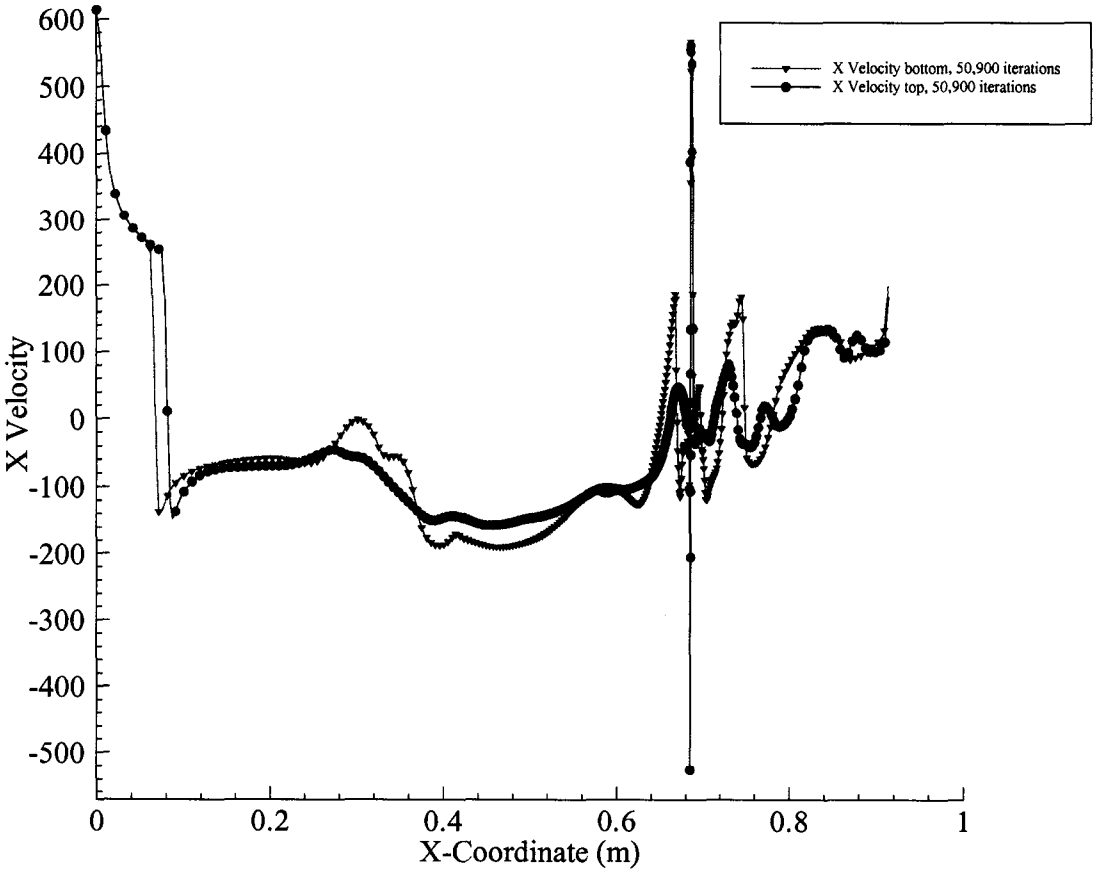

Figure 4.67 X velocity plot after 50,900 iterations using the longer isolator, Po_j/P=480.8.

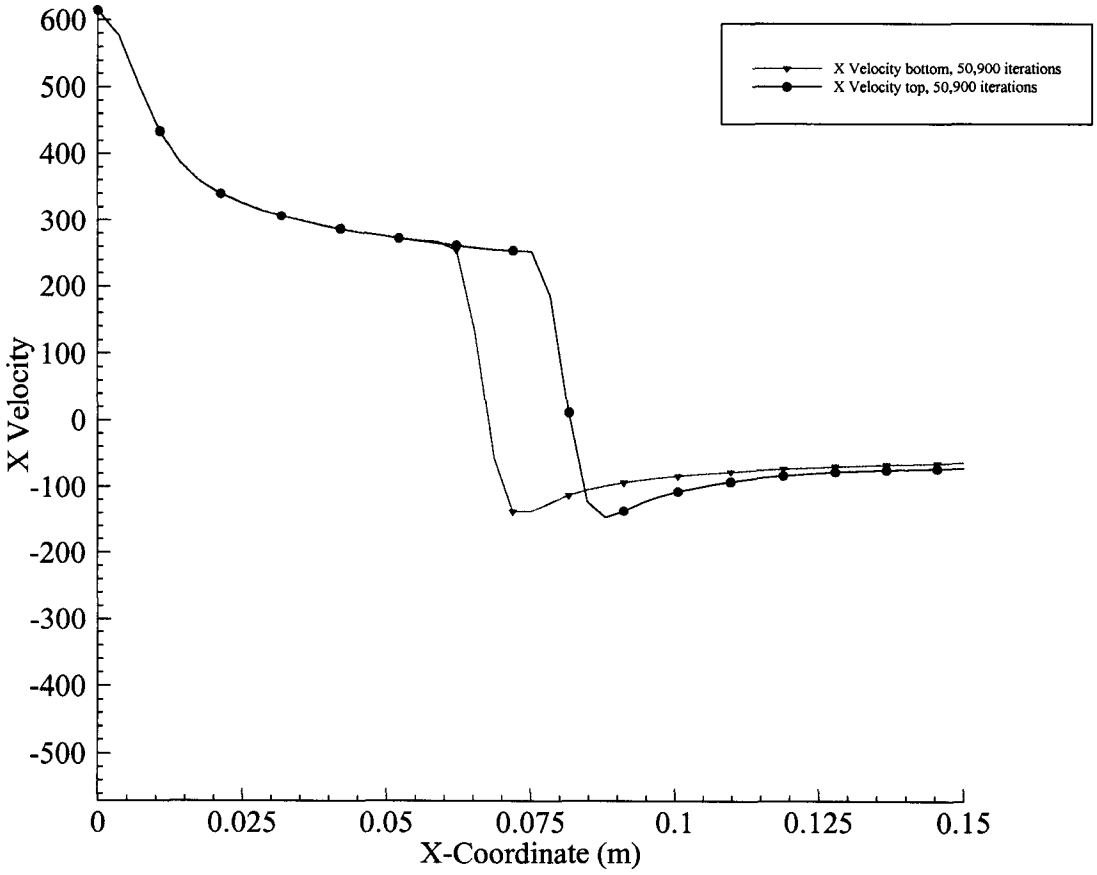

Figure 4.68 X velocity plot showing boundary layer separation after 50,900 iterations using the longer isolator, Po_j/P=480.8.

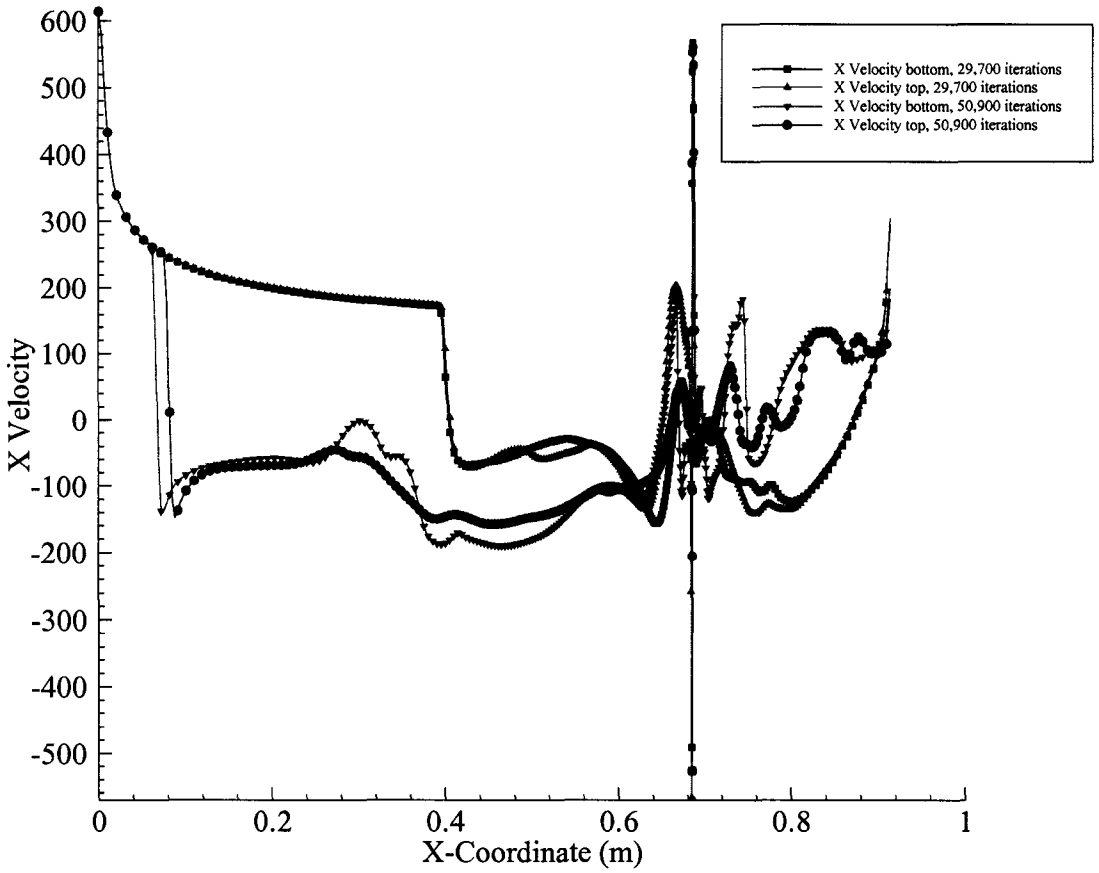

Figure 4.69 X velocity plot comparison using the longer isolator, Po_j/P=480.8.

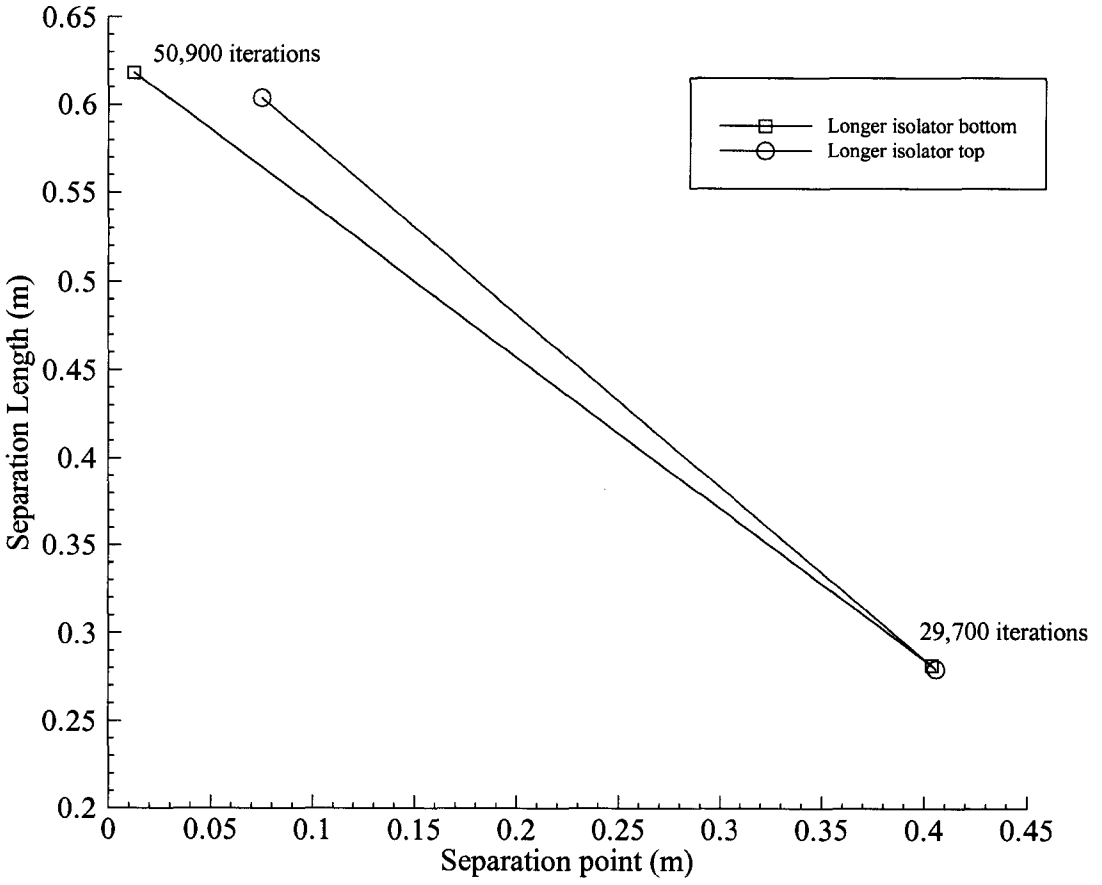

Figure 4.70 Separation point versus separation length for the longer isolator, $Po_j/P=480.8$.

Numerical simulation of two-dimensional transverse sonic injection of Nitrogen into a Mach 3.5 freestream has been investigated. The presence of the injected Nitrogen creates an oblique shock wave which separates upstream of the injector, thus creating the "upstream interaction". The results showed in the $Po_j/P=120.2$ study showed excellent agreement with the experimental results. With this shown, we conducted further investigation increasing the freestream-to-pressure ratio. As predicted, the upstream interaction moves further upstream creating larger eddy circulations. Lengthening the isolator proved beneficial in studying the upstream interaction. We showed that as the isolator length increased the upstream continued to work its way upstream until reaching an equilibrium point. The full duct results showed that as the pressure ratio increased the point where the separation occurred began to vary on the upper and bottom. This meant that the points of separation on the upper and lower wall were not the same and the symmetry assumption had collapsed. This was evident in the $Po_j/P=480.8$ study. Improvements in this study could include:

1. Introducing a backpressure at the exit to investigate how this affects the upstream interaction.
2. Further lengthening of the isolator region to investigate the upstream interaction.
3. Using various freestream-to-pressure ratios.
4. Changing the injector angle.

SECTION 5

SUDDEN EXPANSION RESULTS AND DISCUSSION

5.1 Introduction

Numerical results using the modified geometry of the Japan National Aerospace Laboratory (JNAL) combustion chamber experimental model are investigated. The modified geometry is shown in Fig. 5.1. The modified version has a constant diameter exit duct and compared to the JNAL version, it consists of an exit diffuser. The JNAL version geometry was shown in Fig 2.2. The entire domain was numerically modeled to investigate the upstream interaction based on three different freestream to injector pressure ratios. The numerical grid consists of 184,867 unstructured cells. A close up of the expansion and injector regions is shown in Fig. 5.2. Nitrogen gas was injected sonically 0.01263m from the top and bottom steps.

5.2 Results and Discussion

5.2.1 $Po_j/P=120.2$ Results

Mach number contours are given in Figs. 5.3 and 5.4 for 36,300 and 37,000 iterations. It is shown that the flow becomes asymmetric in each case. If we investigate each of the contour plots we see that for the 36,300 iteration model the upper wall separation shock separates further upstream than the lower wall separation shock. After further iterations we find at 37,000 iterations that the separation shock on the lower wall extends further than the upper wall separation shock.

Figures 5.5 and 5.6 show the normalized static pressure contour plots. Again the asymmetry is seen. Notice the large pressure rise in the shock/shock region and then again between the injectors. Also, downstream of the injector, the reattachment shocks are also asymmetric.

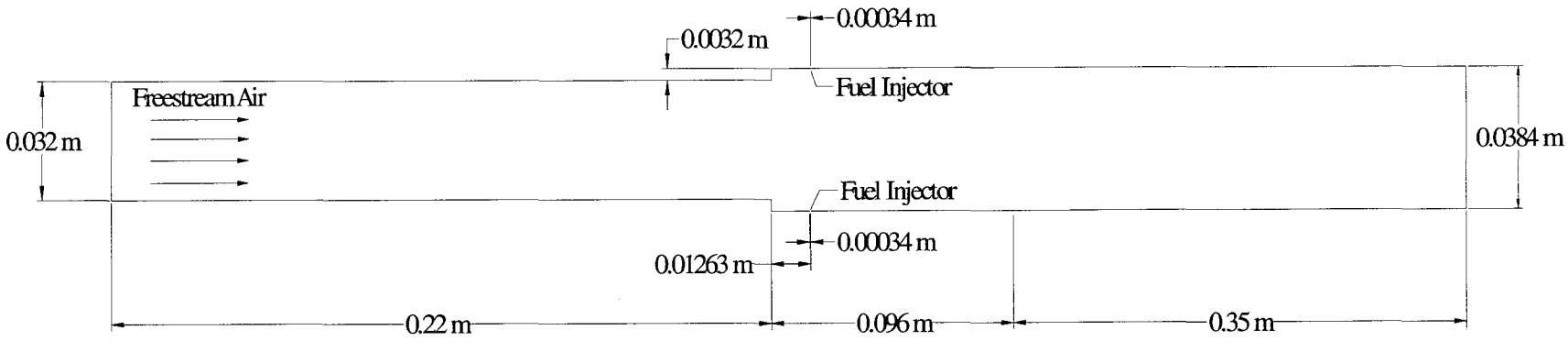

Figure 5.1 Geometry of modified JNAL combustion chamber experimental model.

Table 5.1 Boundary conditions for sudden expansion case $P_o/P=120.2$

	Freestream Air	Nitrogen Injectant
M	3.5	1.0
P_t (kPa)	240.627	379.901
P_s (kPa)	3.158	200.637
T_t (K)	314.44	291.67
T_s (K)	91.67	243.33
Velocity (m/s)	670.56	317.906

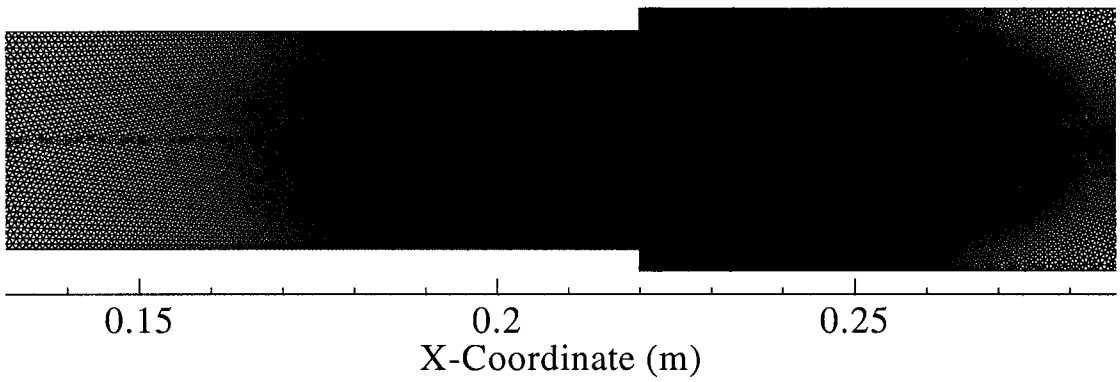

Figure 5.2 Close up of grid for sudden expansion case.

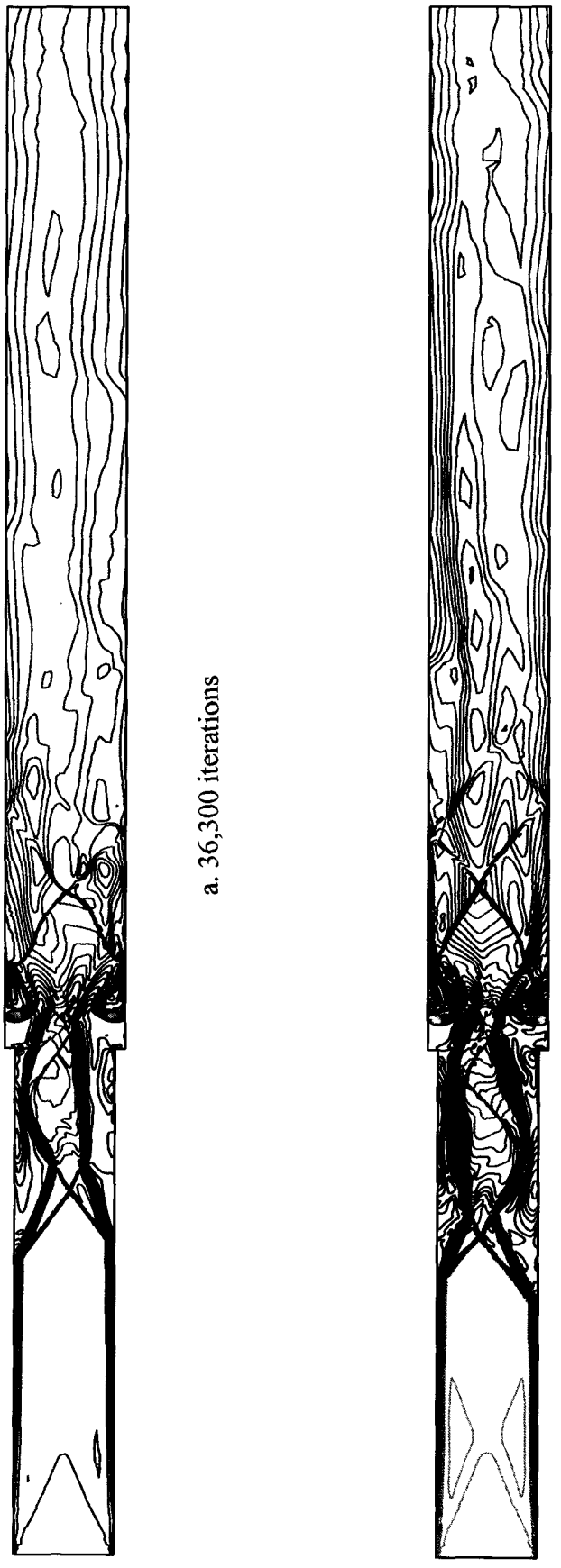

a. 36,300 iterations

b. 37,000 iterations

Figure 5.3 Mach number contour plots for the entire sudden expansion domain, $Po_j/P=120.2$.

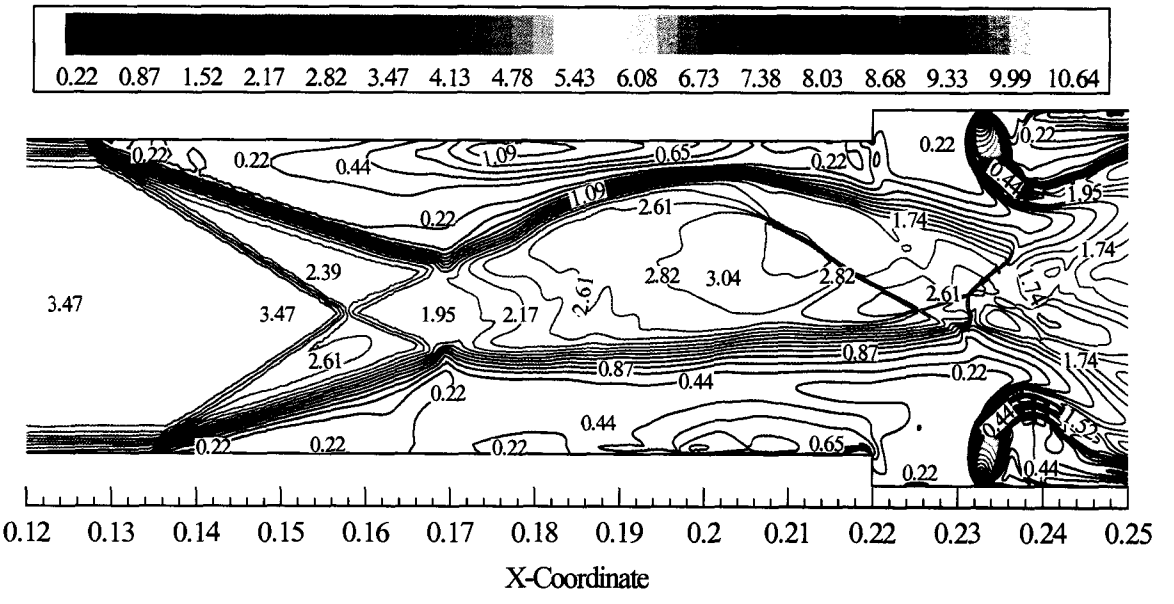

a. 36,000 iterations

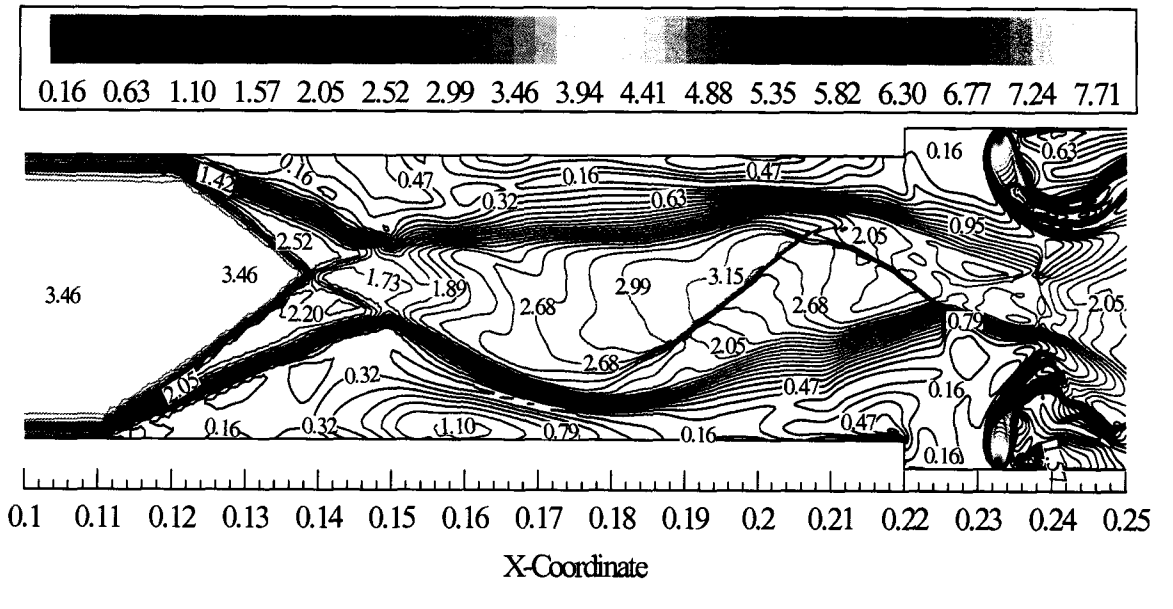

b. 37,000 iterations

Figure 5.4 Mach number contours for sudden expansion case, $Po_j/P=120.2$.

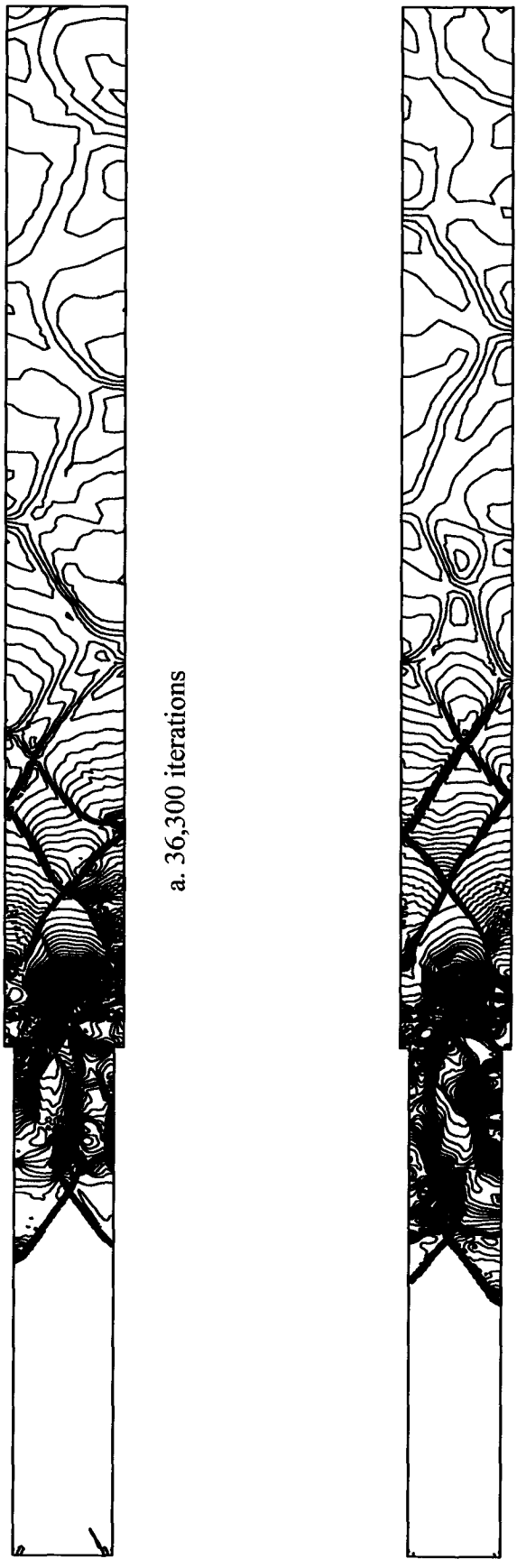

a. 36,300 iterations

b. 37,000 iterations

Figure 5.5 Normalized static pressure contour plots for the entire sudden expansion domain, $Po_j/P=120.2$.

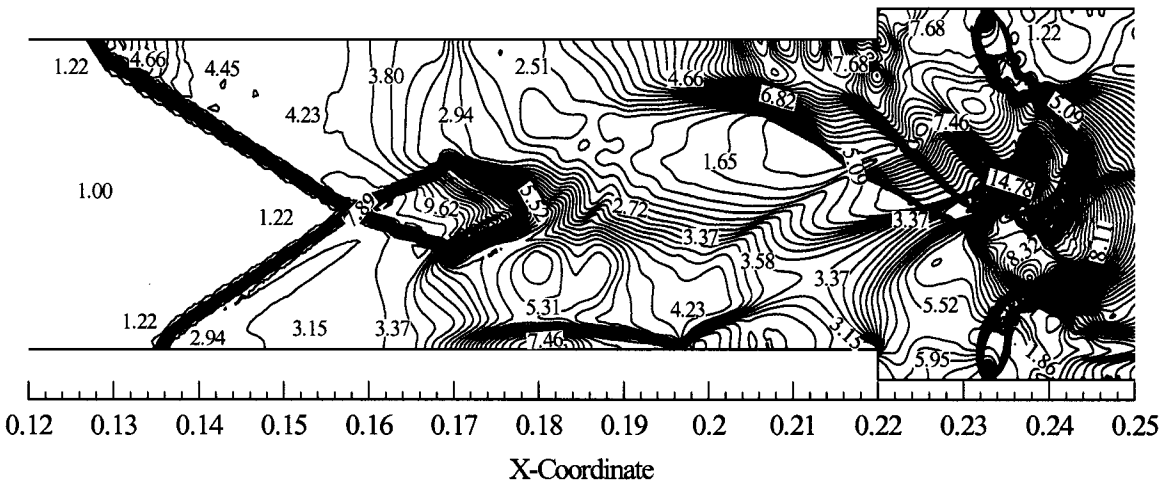

a. 36,000 iterations

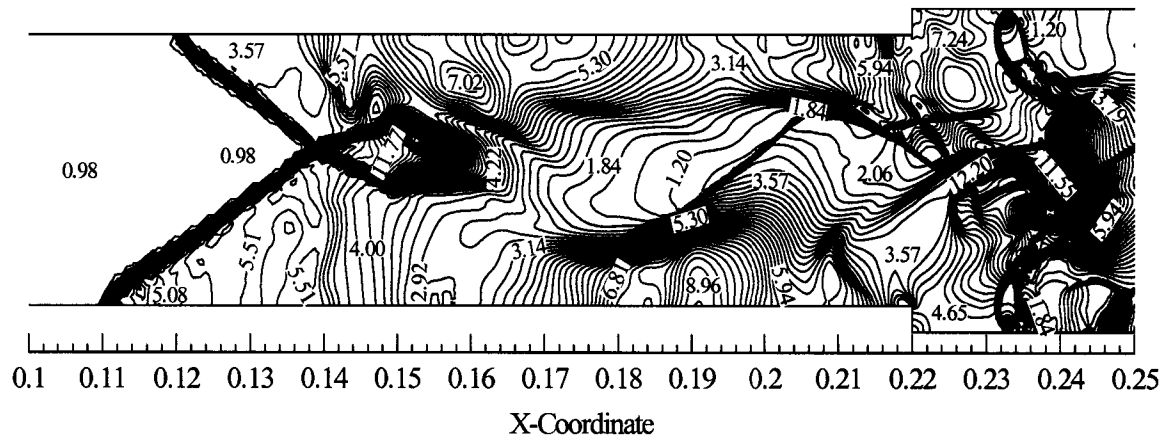

b. 37,000 iterations

Figure 5.6 Normalized static pressure contours for sudden expansion case, Po_j/P=120.2.

Mole fraction of N_2 is shown in Figs 5.7 and 5.8. The upstream interaction does not convect the nitrogen upstream due to multiple recirculation regions. These regions are tangent to each other, but the area is small. This can be shown more clearly with the velocity vector plots in Figs. 5.9 and 5.10. This small area is not large enough to convect the nitrogen from one circulation region downstream to the one upstream. Penetration of the nitrogen is approximately 3 step heights for both. Downstream we see that the nitrogen remains fairly close to the upper and lower walls.

Figures 5.11 and 5.12 give the velocity vector and streamline contour plots. Notice the large recirculation bubble on the upper wall in the 36,300 iteration model and then switching to the lower wall in the 37,000 iteration model. There is a large vortex bubble generated just upstream of the lower injector. Notice the flowfield bending due to the large recirculation regions.

Normalized static pressure is plotted along the x-axis in Figs 5.11-5.13. Notice the pressure plateau at the separated region is higher for the separation shocks that occur further upstream. This is evident in Fig. 5.13. The separation distance between both iteration models are nearly identical. Downstream we see that the turbulence decreases rapidly and oscillations of the pressure decrease.

Velocity along the x-axis is presented in Figs. 5.14-5.18. Comparison of the separation regions in Figs. 5.15 and 5.17 show that for the 36,300 iteration model that the top separates at approximately 0.128m and the bottom at approximately 0.134m. The difference is 0.006m. Comparison of the 37,00 iteration models shows that the top separates at approximately 0.11m and the bottom at approximately 0.12m. The difference is 0.01m.

a. 36,300 iterations

b. 37,000 iterations

Figure 5.7 Mole fraction of N_2 contour plots for the entire sudden expansion domain, $Po_j/P=120.2$.

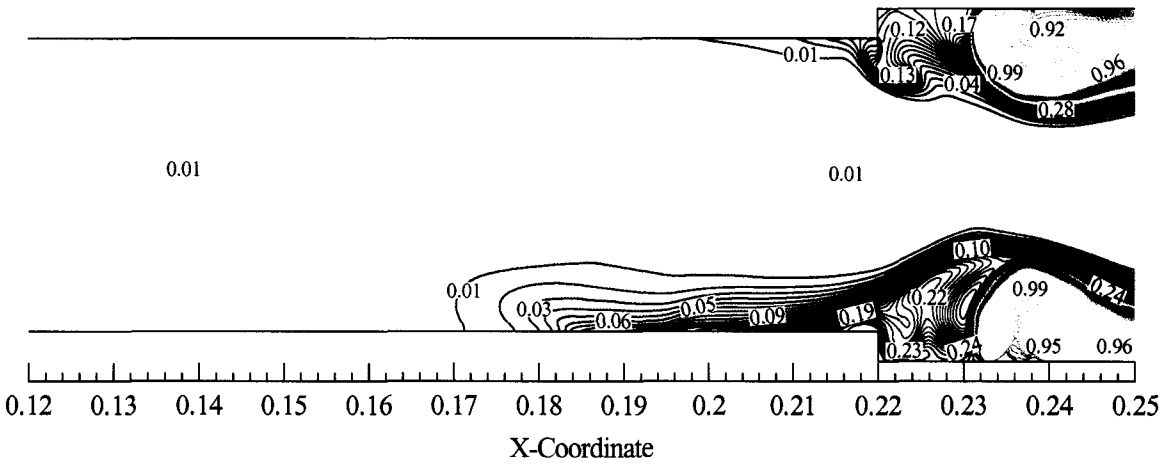

a. 36,000 iterations

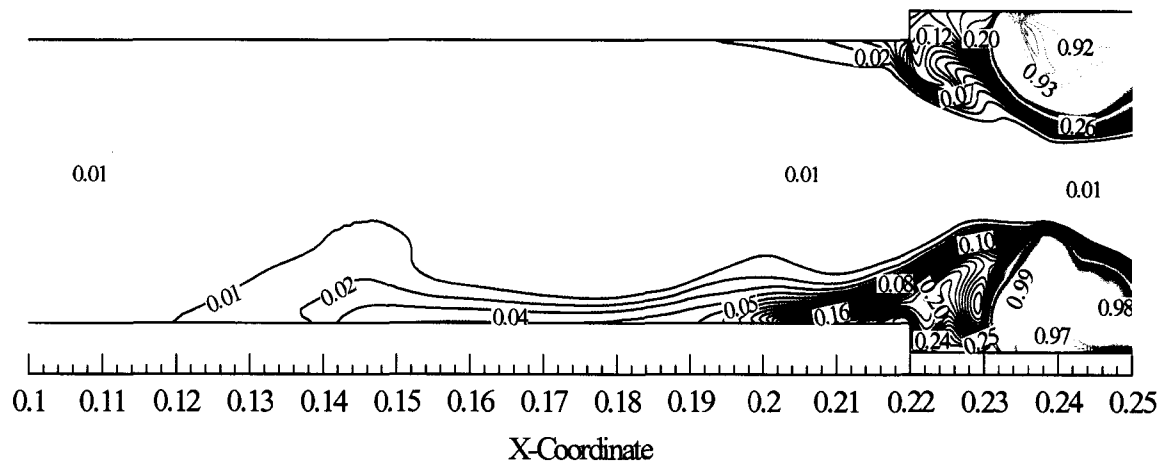

b. 37,000 iterations

Figure 5.8 Mole fraction of N_2 contours for sudden expansion case, P_{oj}/P=120.2.

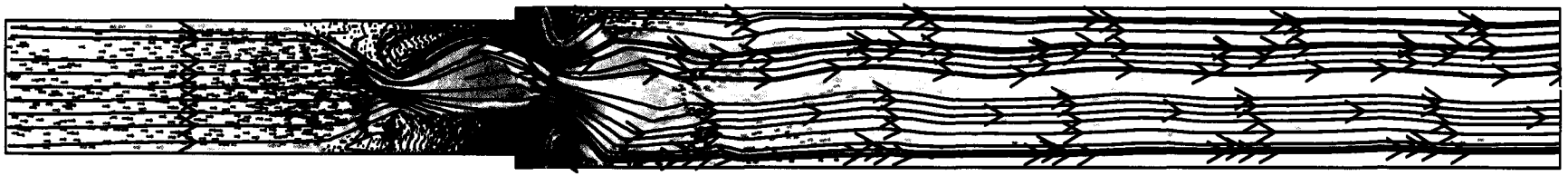

a. 36,300 iterations

b. 37,000 iterations

Figure 5.9 Velocity vector and streamline plots for the entire sudden expansion domain, $Po_j/P=120.2$.

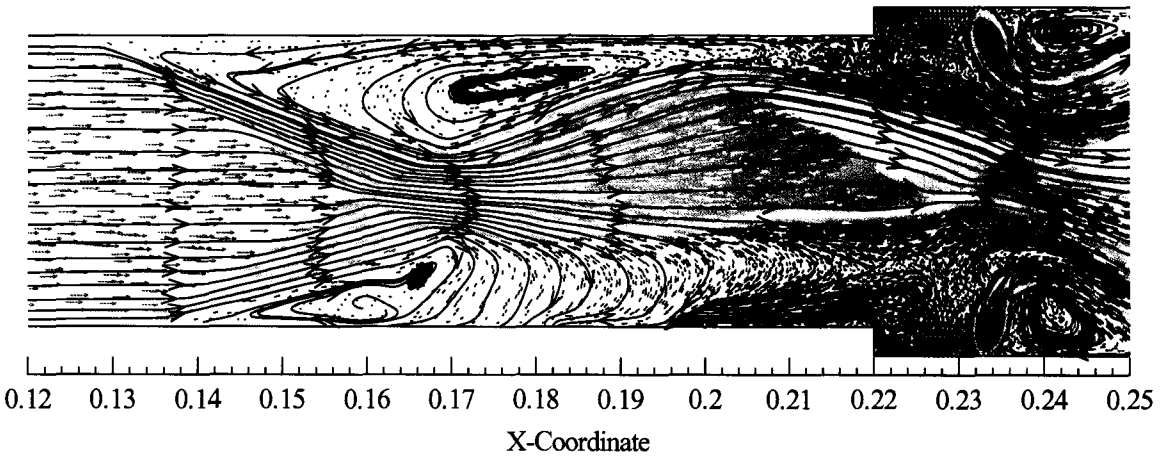

a. 36,300 iterations

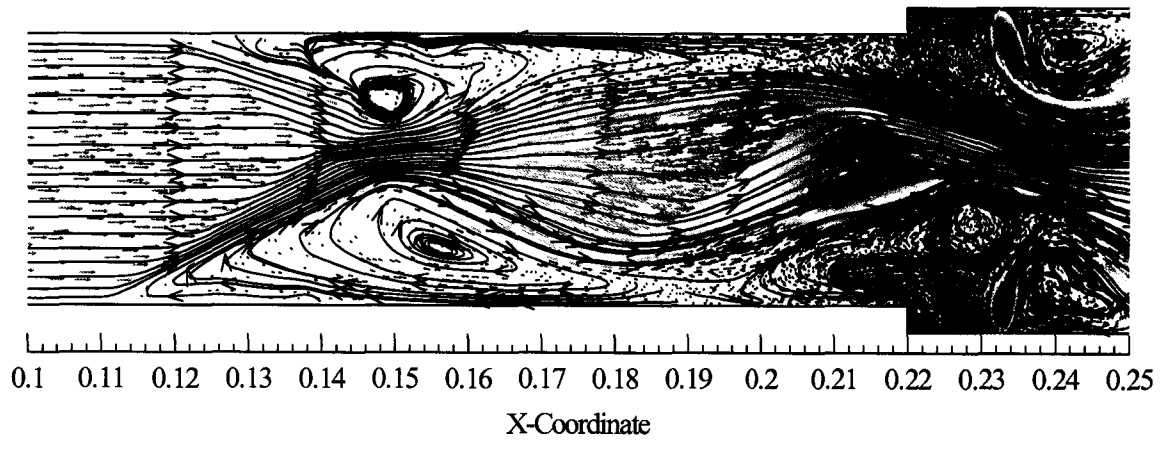

b. 37,000 iterations

Figure 5.10 Velocity vector and streamline plots for sudden expansion case, $Po_j/P=120.2$.

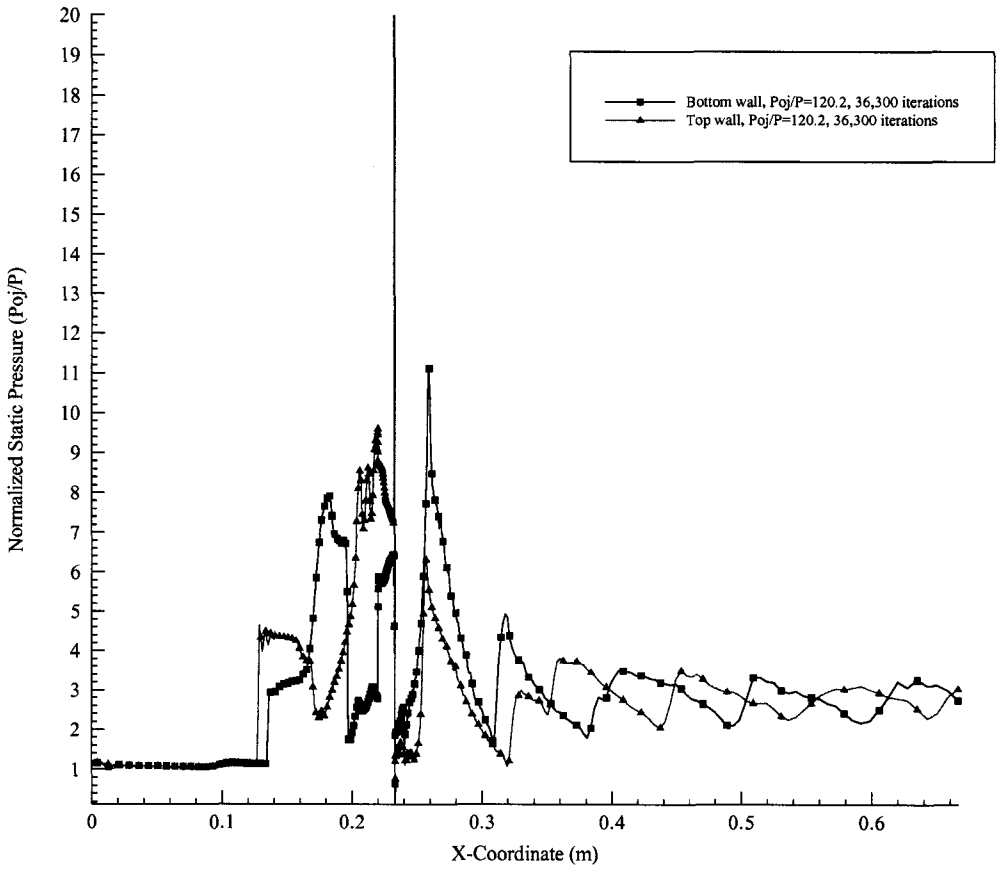

Figure 5.11 Normalized static pressure plot after 36,300 iterations, sudden expansion study, $Po_j/P=120.2$.

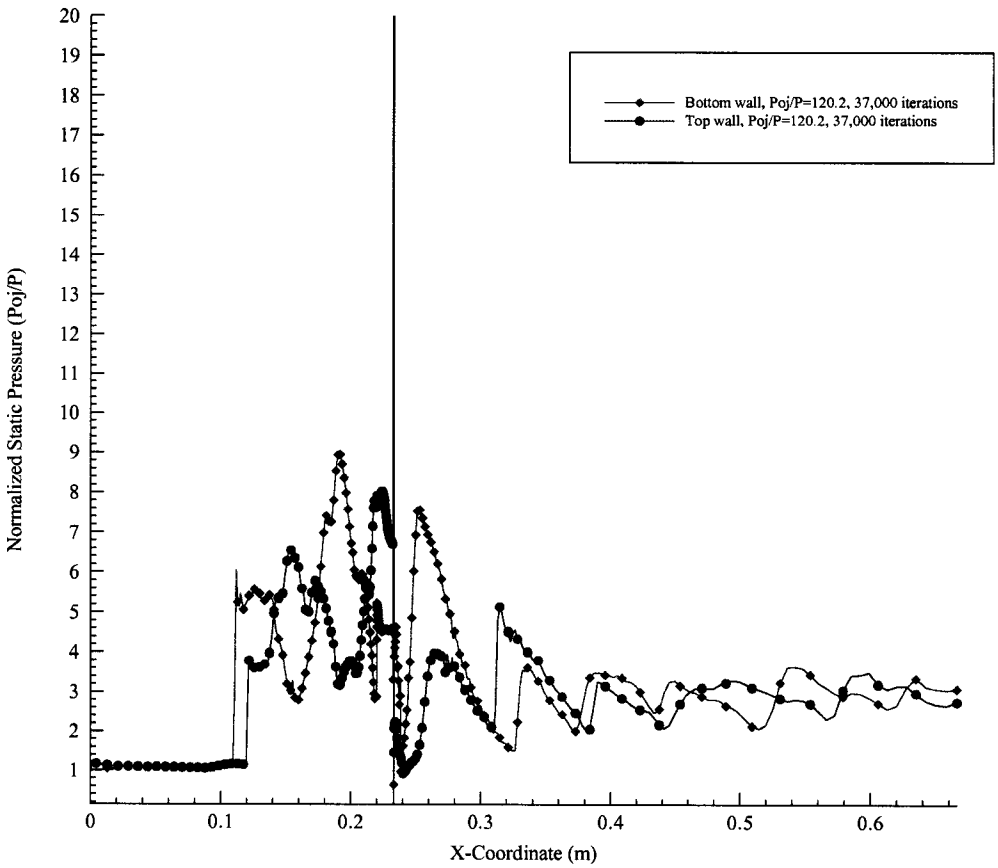

Figure 5.12 Normalized static pressure plot after 37,000 iterations, sudden expansion study, $P_{oj}/P=120.2$.

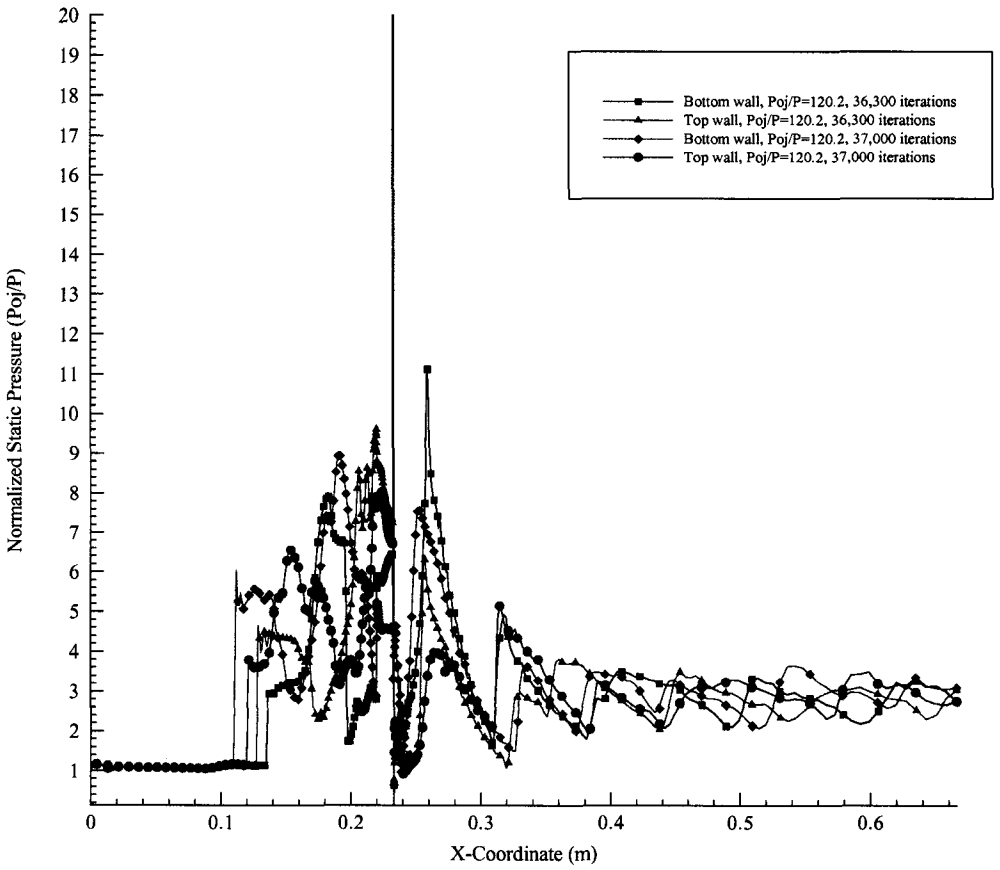

Figure 5.13 Combined normalized static pressure plot, sudden expansion study, $Po_j/P=120.2$.

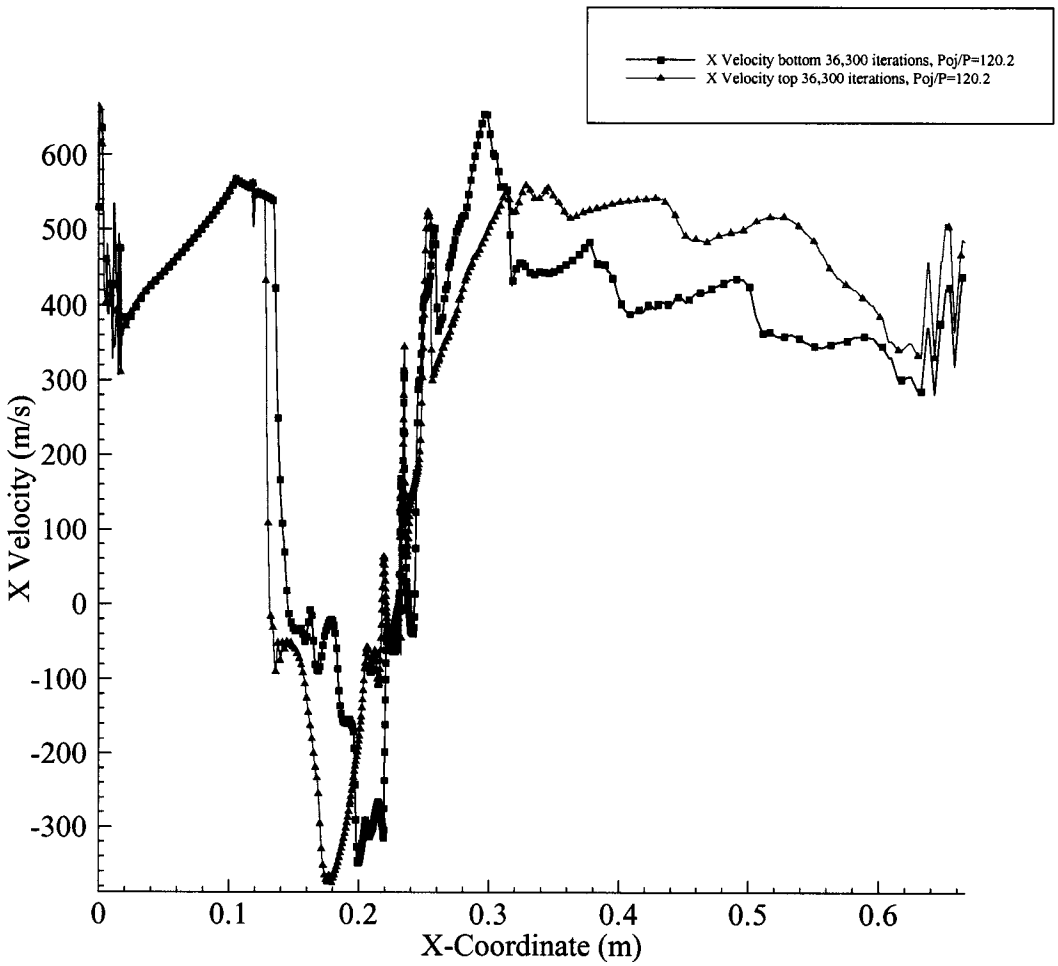

Figure 5.14 X velocity plot comparison after 36,300 iterations, sudden expansion study, $Po_j/P=120.2$.

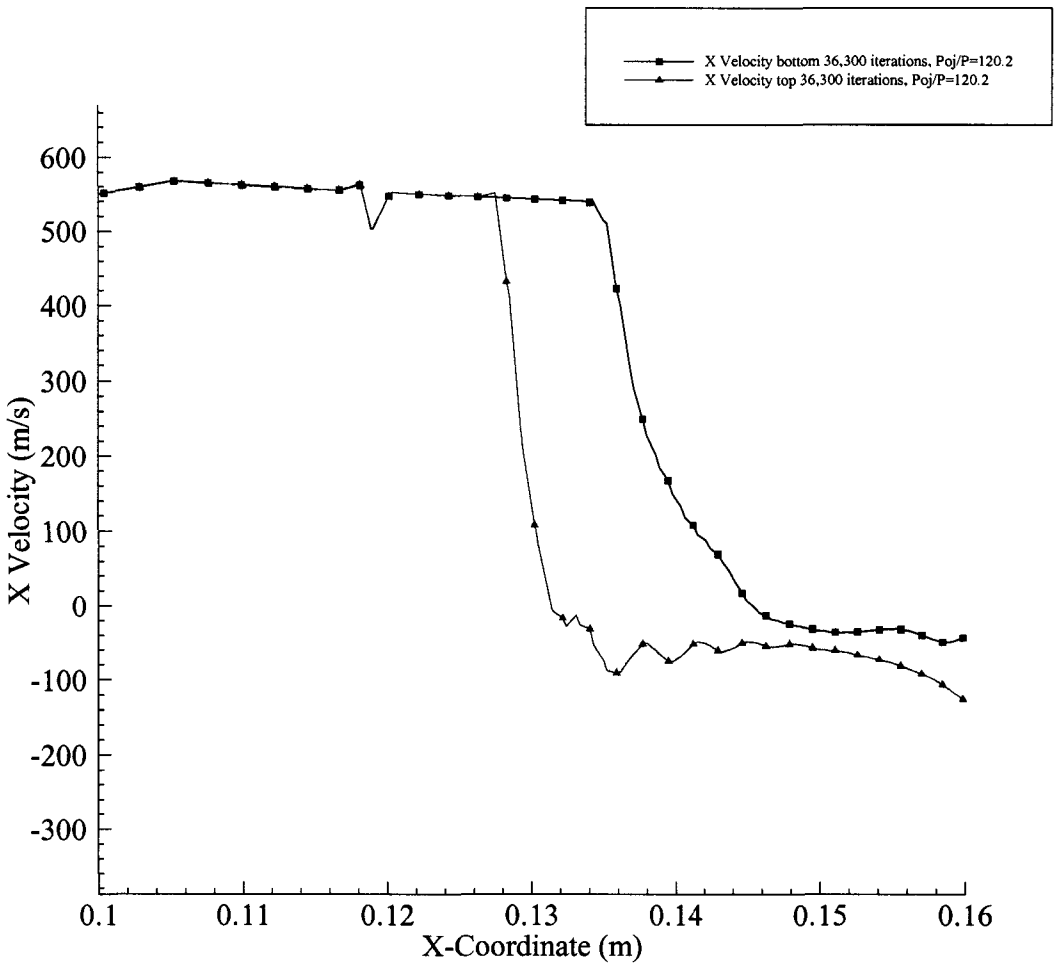

Figure 5.15 X velocity plot showing boundary layer separation after 36,300 iterations, sudden expansion study, P_{oj}/P=120.2.

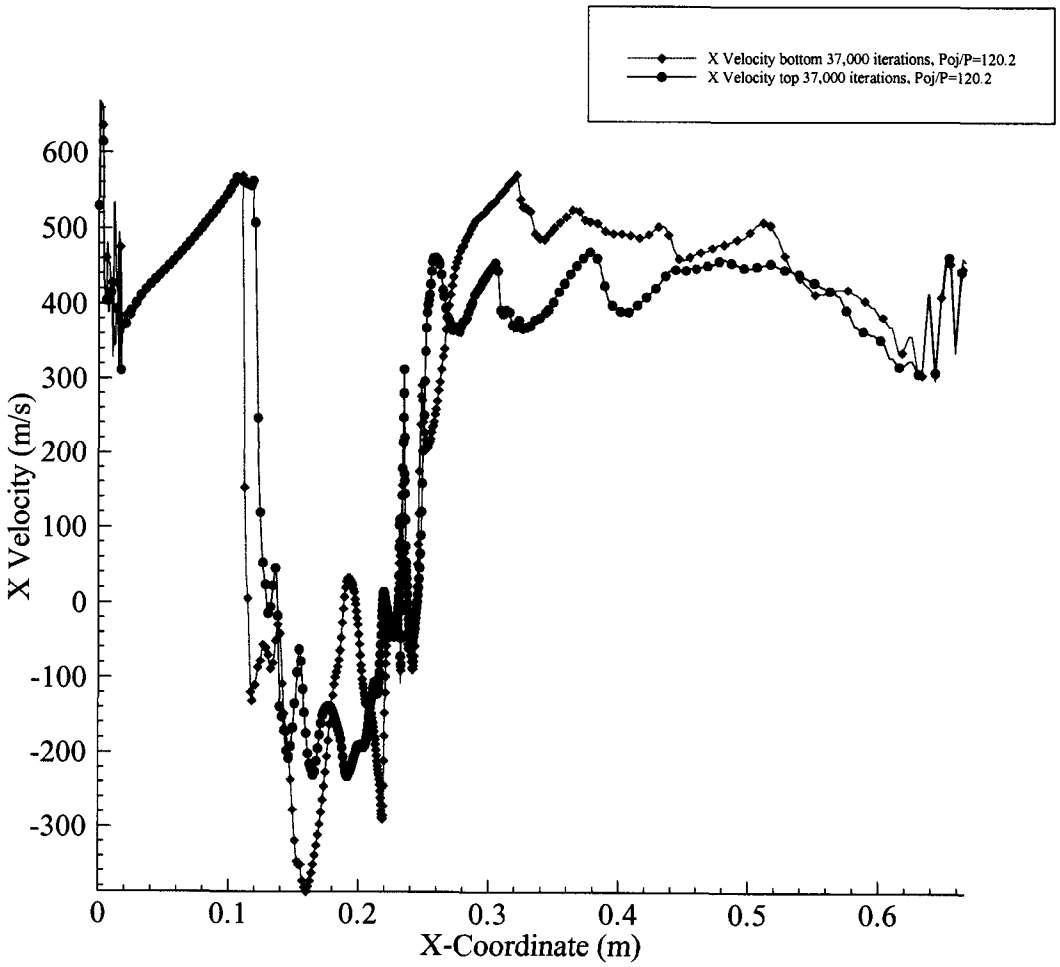

Figure 5.16 X velocity plot comparison after 37,000 iterations, sudden expansion study, $Po_j/P=120.2$.

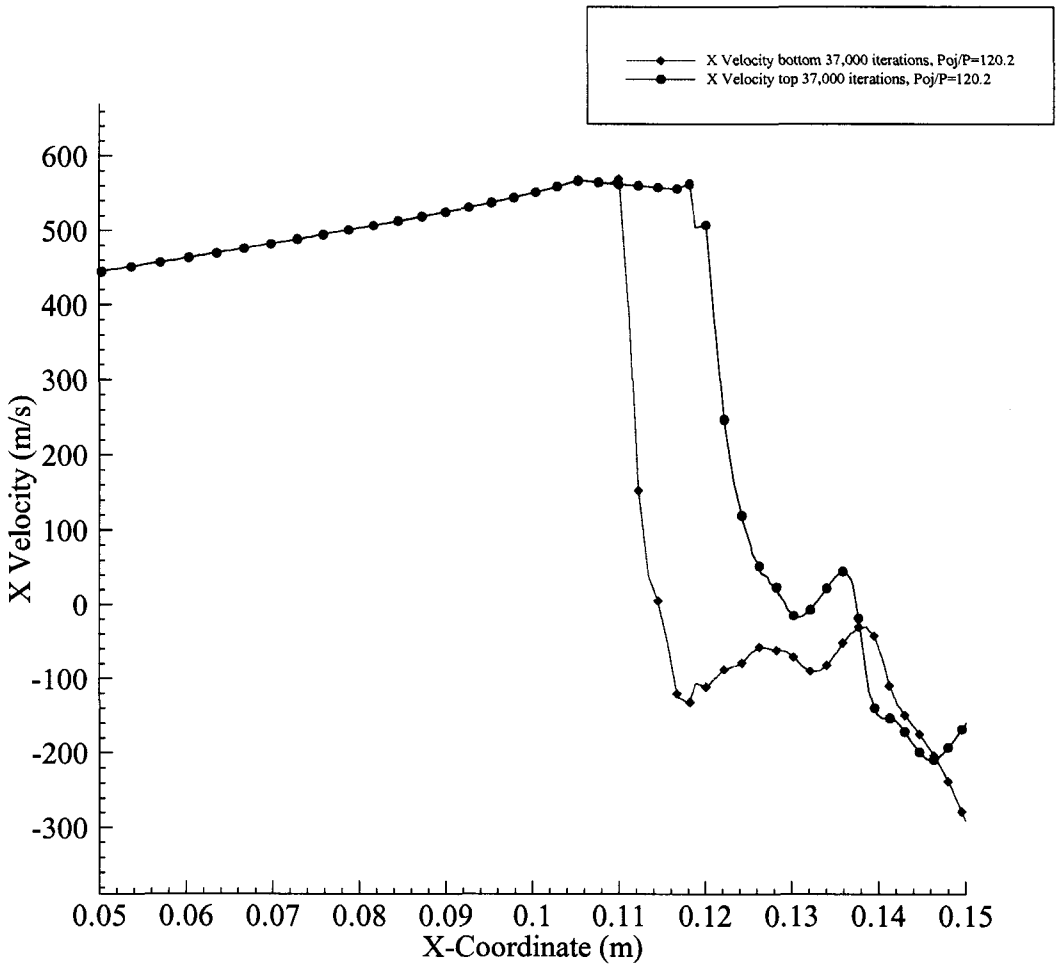

Figure 5.17 X velocity plot showing boundary layer separation after 37,000 iterations, sudden expansion study, P_{oj}/P=120.2.

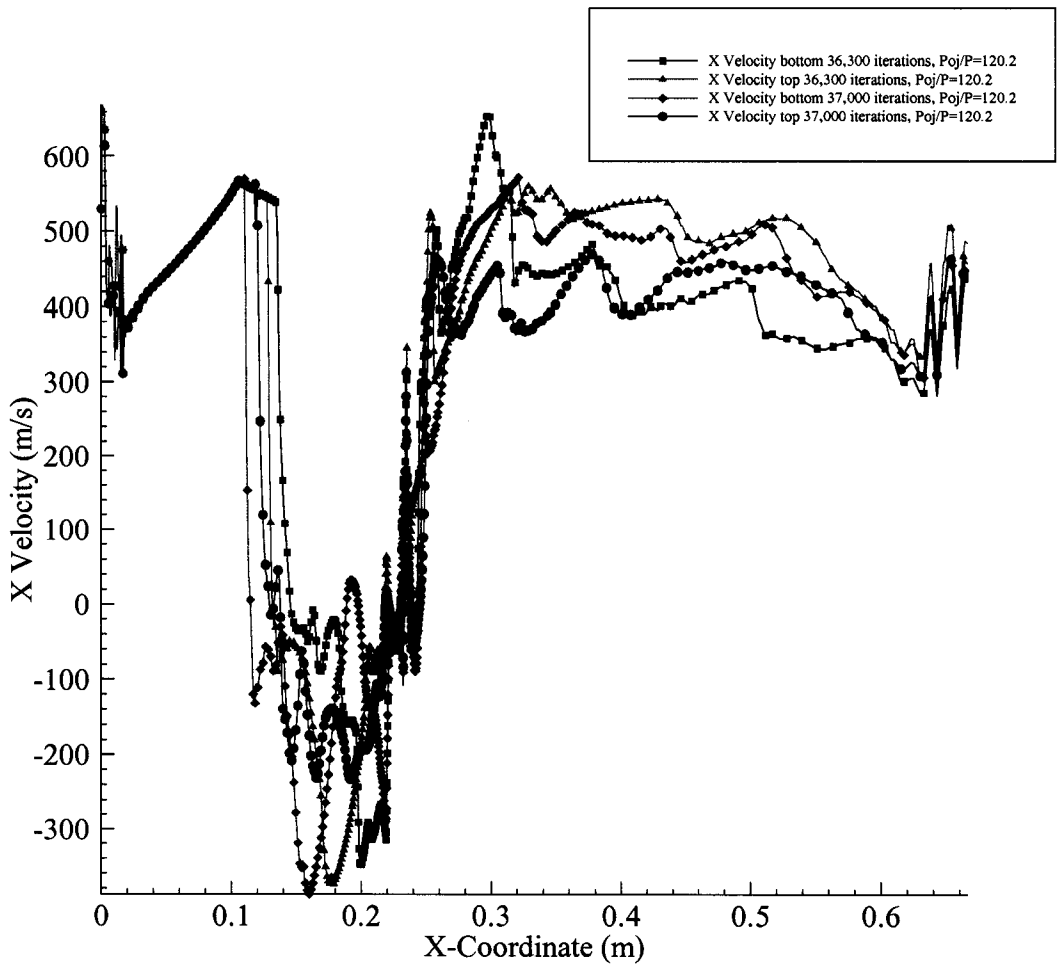

Figure 5.18 X velocity plot comparison, sudden expansion study, $Po_j/P=120.2$.

5.2.2 $Po_j/P=240.4$ Results

Boundary conditions of the $Po_j/P=240.4$ sudden expansion numerical model is shown in Table 5.2. Results are taken after 12,400 iterations and 17,500 iterations. Mach number contours are shown in Figs. 5.19 and 5.20. We see for the 12,400 iteration model that the separation is nearly symmetric. However, for the 17,500 iteration model it is evident that the flow is asymmetric. In Fig. 5.20a the Mach flowfield seems to be inconsistent as compared in Fig. 5.20b. This can be due to the nearly symmetric flowfield. And the fact that the separated flowfield may be switching walls

Figures 5.21 and 5.22 give the normalized static pressure contours. Notice the difference the upstream interaction between the two iteration models is along the x-axis. The shock/shock interaction region in Fig. 5.22a is not quite defined as in Fig. 5.22b. This is also due to the nearly symmetric flowfield.

Mole fraction of nitrogen is shown in Figs. 5.23 and 5.24. The convection of nitrogen through the recirculation regions is greater than for the $Po_j/P=120.2$ model. As shown in Fig. 5.24 where the recirculation bubbles meet the area is greater, therefore allowing the nitrogen to be convected upstream. Downstream mixing appears to be very turbulent and nitrogen is evident throughout the whole expansion height to a distance 0.32m downstream of the injectors.

Figures 5.25 and 5.26 give the velocity and streamline contour plots. After 12,400 iterations the upstream interaction regions are very small as compared to the 17,500 iteration model. This can be caused by the fact that the flowfield may be in the "buckling" phase. This phase is where the separation of the longer shock may be shortening and the opposite wall separation shock is lengthening. Figure 5.26b shows the recirculation regions are greater in detail. Notice that the area between the multiple recirculation regions are larger than in the $Po_j/P=120.2$ model. This in turn allows the nitrogen to be able to be convected upstream.

In the next Figs. 5.27-5.29, normalized static pressure is plotted along the x-axis. Normalized static pressure rise is greater by a ratio of 2 for the 17,500 iteration model than the 12,400 iteration model. This is seen in Fig. 5.29. Due to the shocktrain pressure oscillates upstream of the injectors. Leeward of the injectors normalized static pressure ratio oscillations begin to decrease.

Table 5.2 Boundary conditions for sudden expansion case $Po_j/P=240.4$.

	Freestream Air	Nitrogen Injectant
M	3.5	1.0
P_t (kPa)	120.314	379.901
P_s (kPa)	1.579	200.637
T_t (K)	314.44	291.67
T_s (K)	91.67	243.33
Velocity (m/s)	670.56	317.906

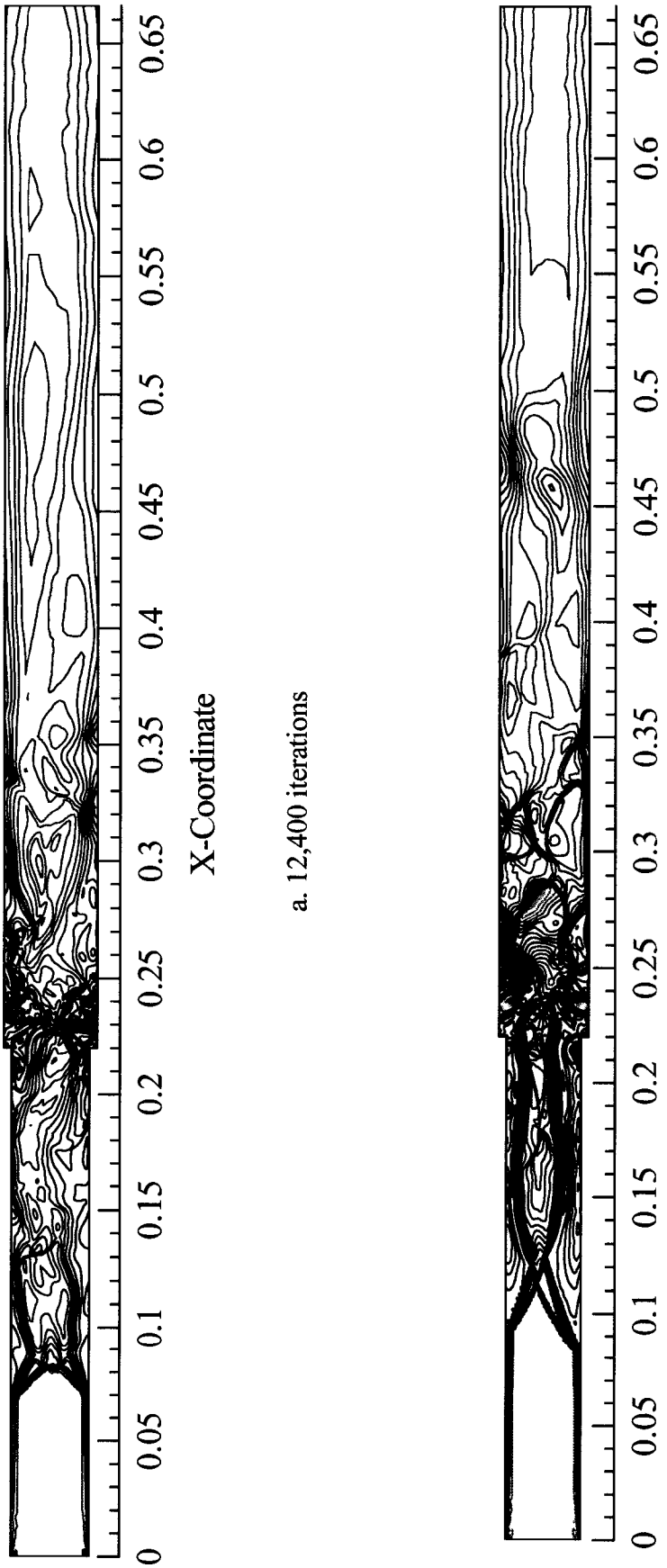

a. 12,400 iterations

b. 17,500 iterations

Figure 5.19 Mach number contour plots for the entire sudden expansion domain, $Po_j/P=240.4$.

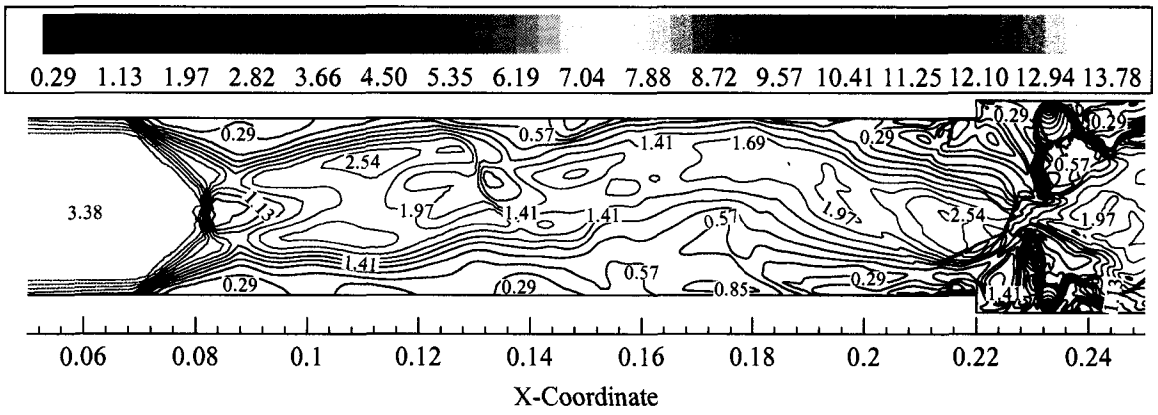

a. 12,400 iterations

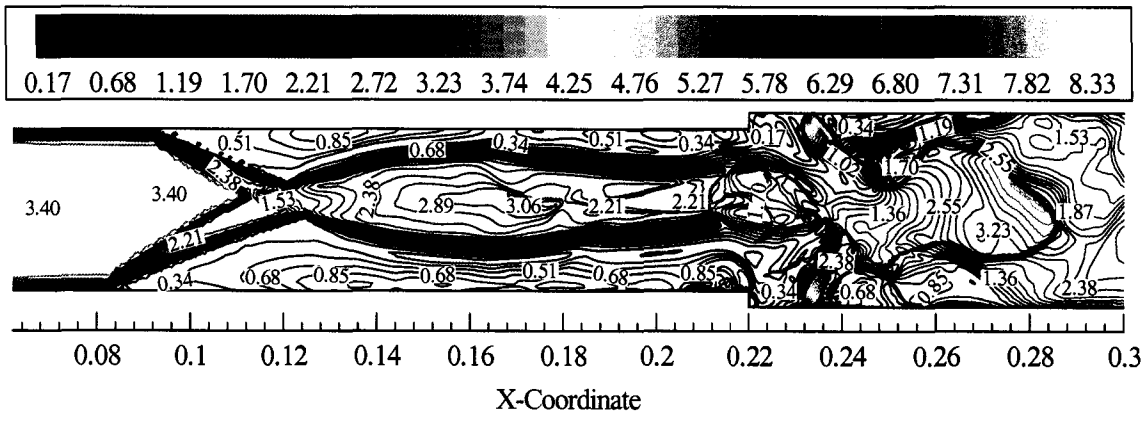

b. 17,500 iterations

Figure 5.20 Mach number contours for sudden expansion case, Po_j/P=240.4.

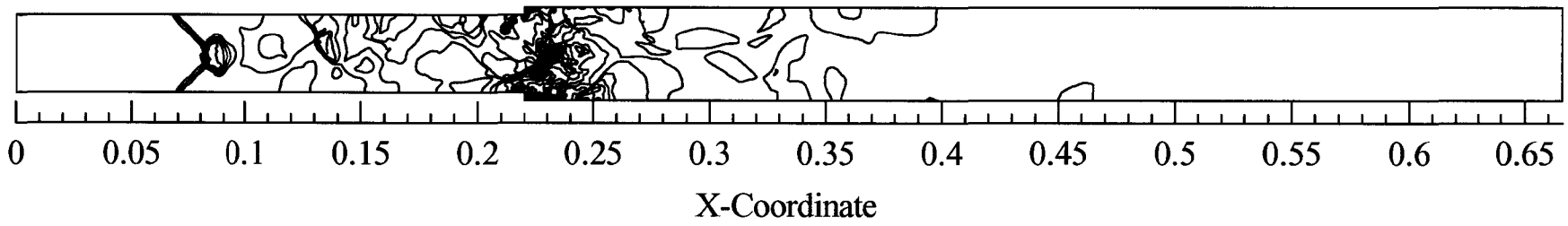

a. 12,400 iterations

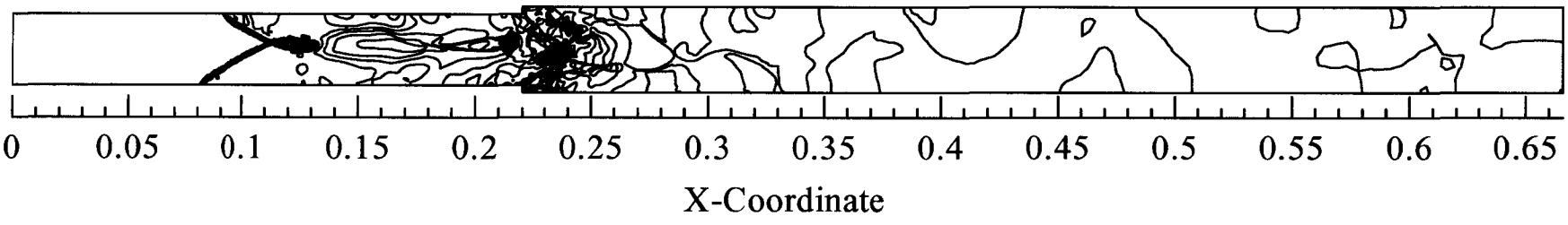

b. 17,500 iterations

Figure 5.21 Normalized static pressure contour plots for the entire sudden expansion domain, $Po_j/P=240.4$.

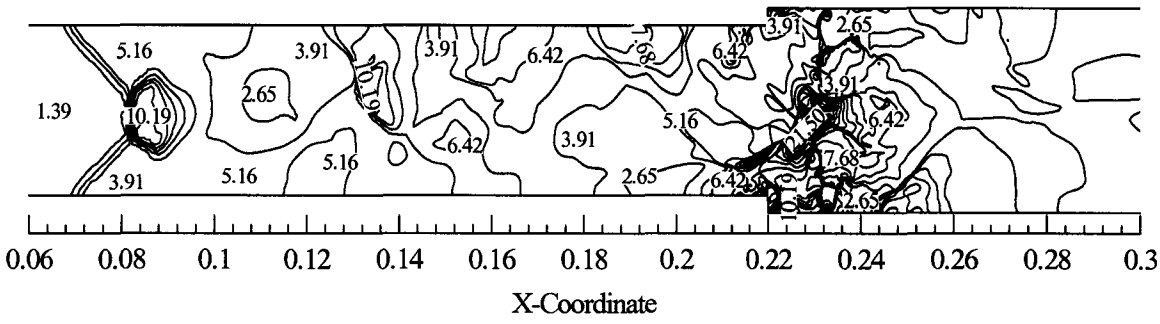

a. 12,400 iterations

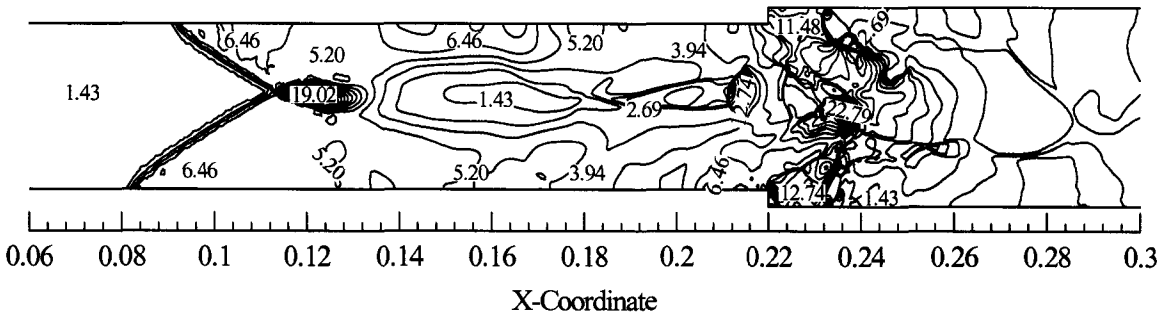

b. 17,500 iterations

Figure 5.22 Normalized static pressure contours for sudden expansion case, $Po_j/P=240.4$.

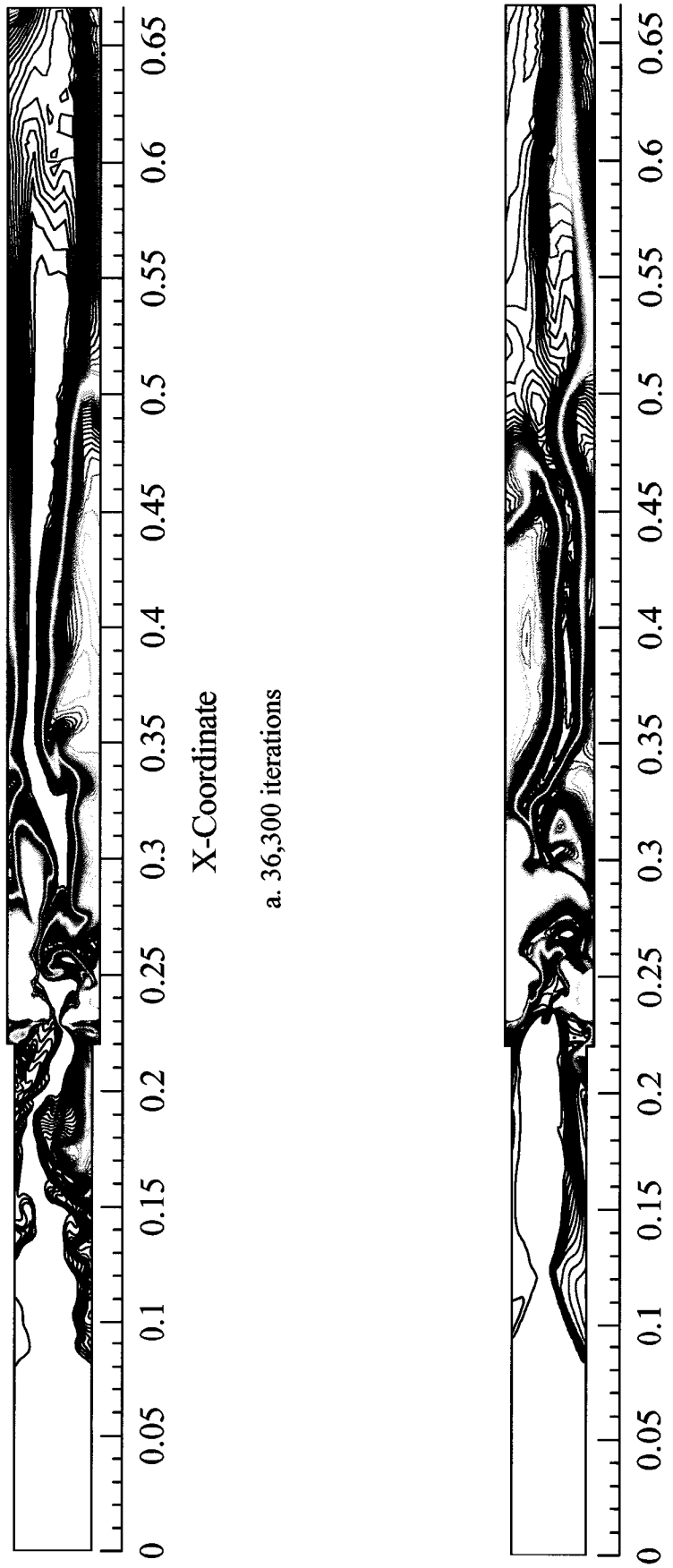

a. 36,300 iterations

b. 37,000 iterations

Figure 5.23 Mole fraction of N_2 contour plots for the entire sudden expansion domain, $Po_j/P=240.4$.

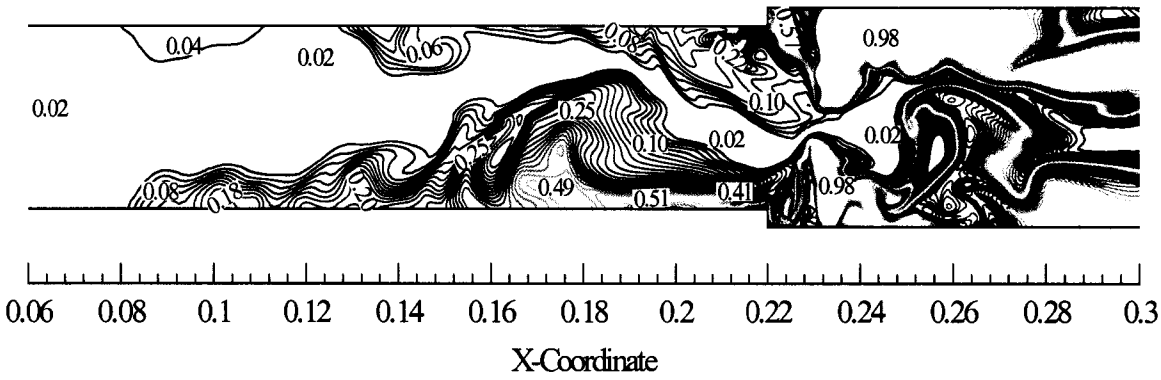

a. 12,400 iterations

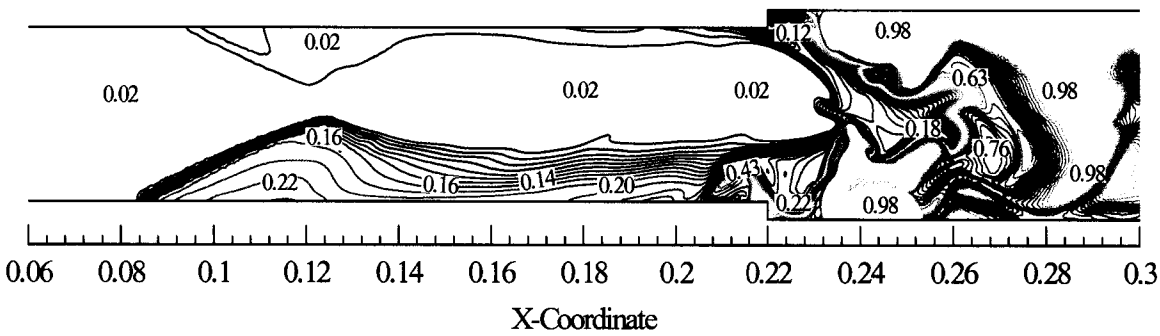

b. 17,500 iterations

Figure 5.24 Mole fraction of N_2 contours for sudden expansion case, $Po_j/P=240.4$.

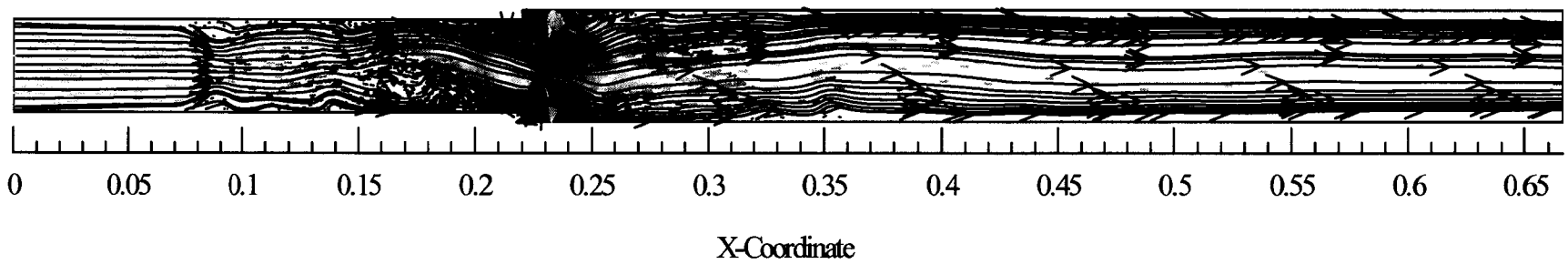

a. 12,400 iterations

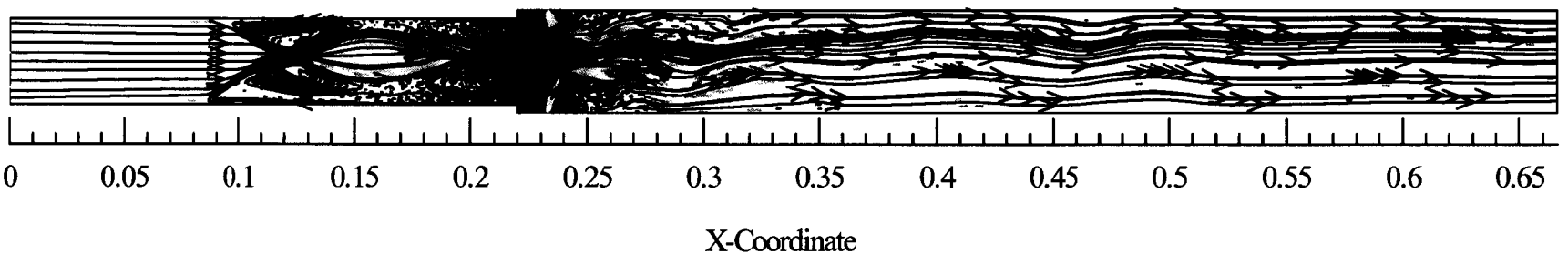

b. 17,500 iterations

Figure 5.25 Velocity vector and streamline plots for the entire sudden expansion domain, $Po_j/P=240.4$.

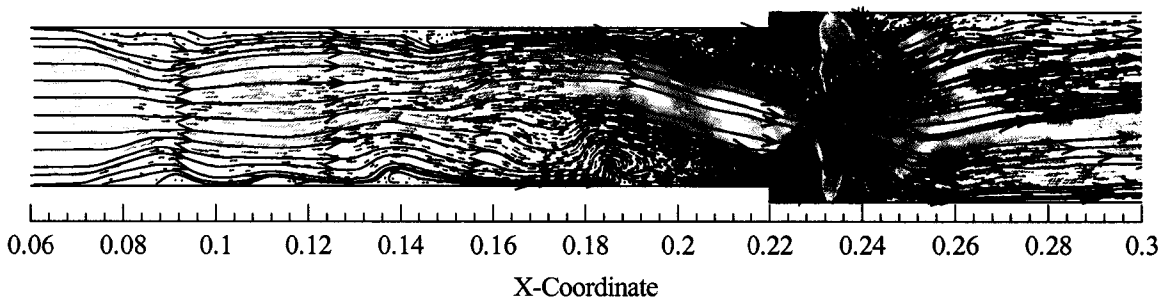

a. 12,400 iterations

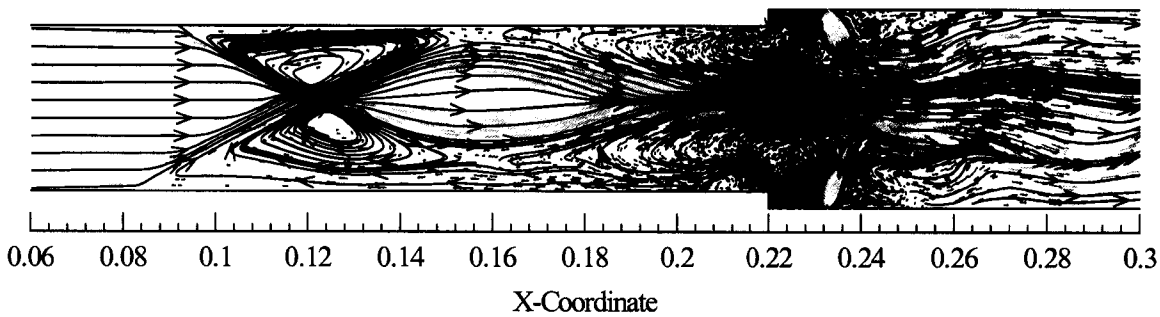

b. 17,500 iterations

Figure 5.26 Velocity vector and streamline plots for sudden expansion case, $Po_j/P=240.4$.

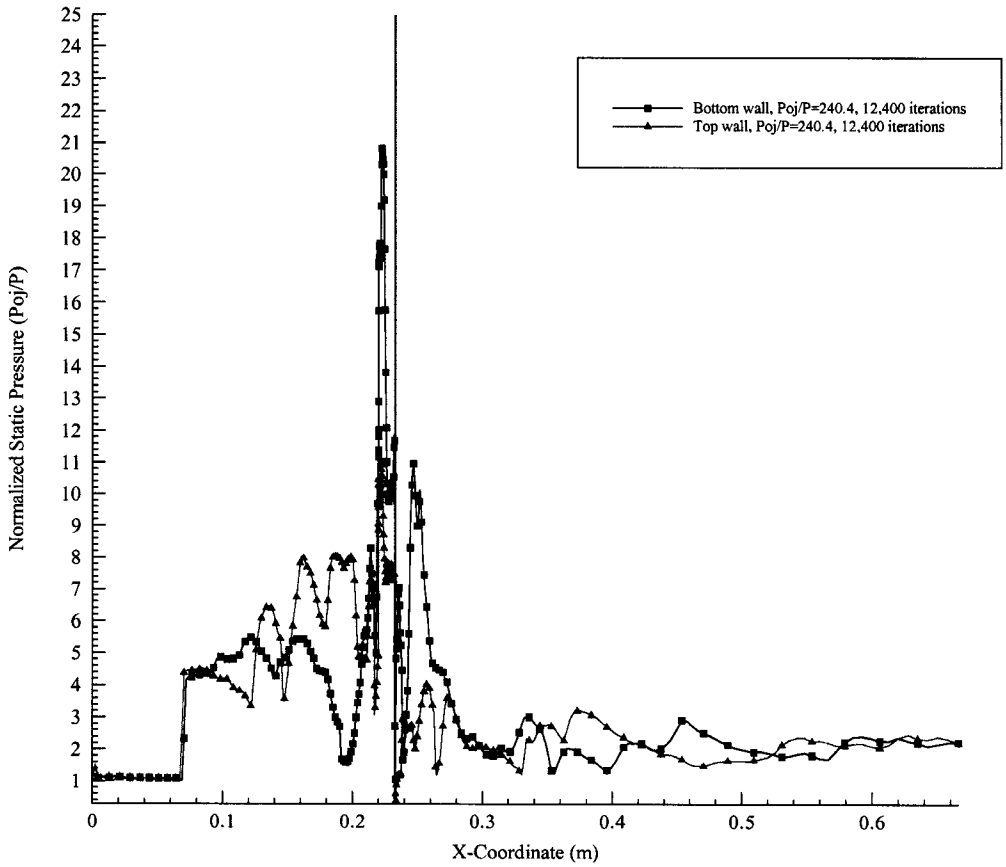

Figure 5.27 Normalized static pressure plot after 12,400 iterations, sudden expansion study, P_{oj}/P=240.4.

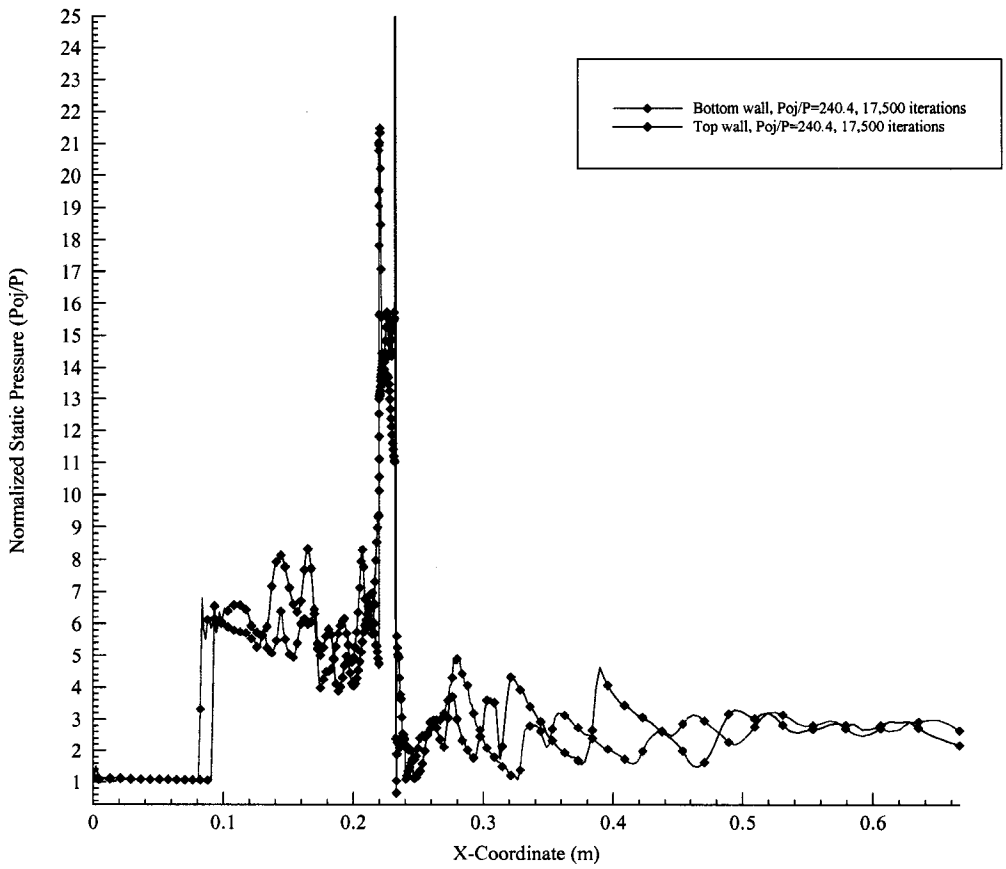

Figure 5.28 Normalized static pressure plot after 17,500 iterations, sudden expansion study, $Po_j/P=240.4$.

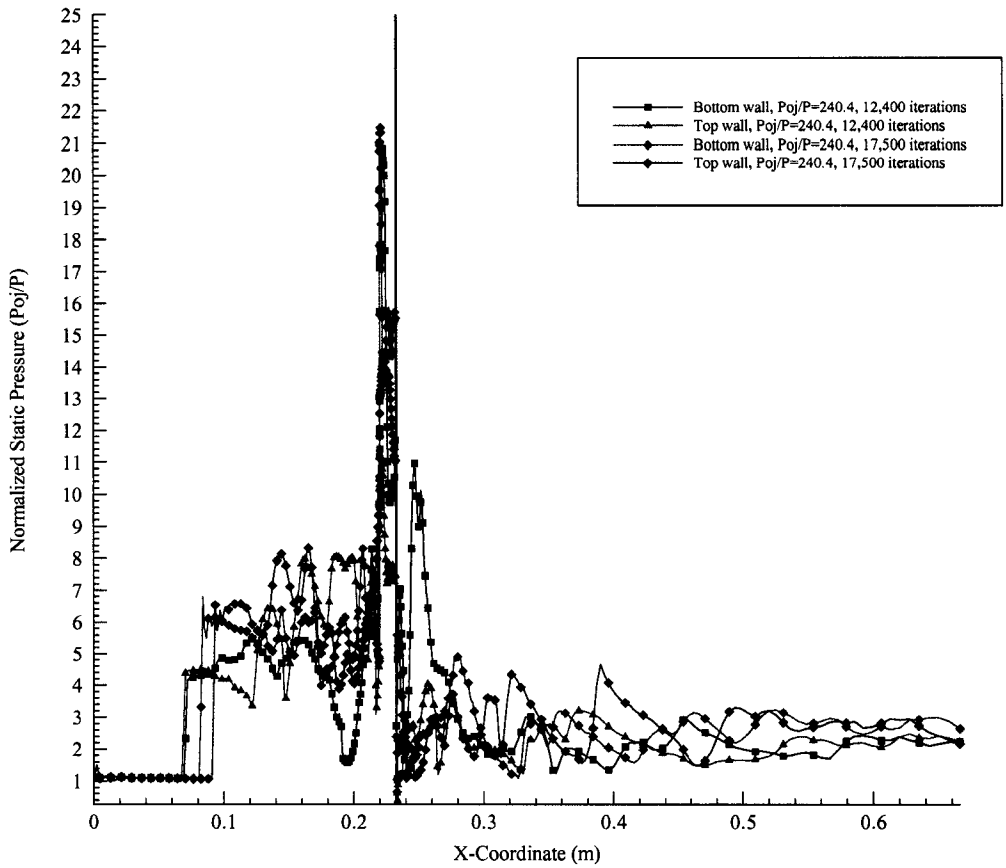

Figure 5.29 Combined normalized static pressure plot, sudden expansion study, $Po_j/P=240.4$.

Figures 5.30-5.34 investigate the velocity along the x-axis. Close up of the boundary layer separation region in Figs. 5.31 and 5.33 show that for the 12,400 iteration model the separation distance is much smaller as compared to the 17,500 iteration models. The upper wall separates at approximately 0.066m and the lower wall separates at approximately 0.068m in the 12,400 iteration model. This difference is very minimal and barely visible to the naked eye. For the 17,500 iteration model the lower wall separates at approximately 0.0809m and the upper wall separates at approximately 0.092m. The difference here is much greater at a distance of 0.0111m.

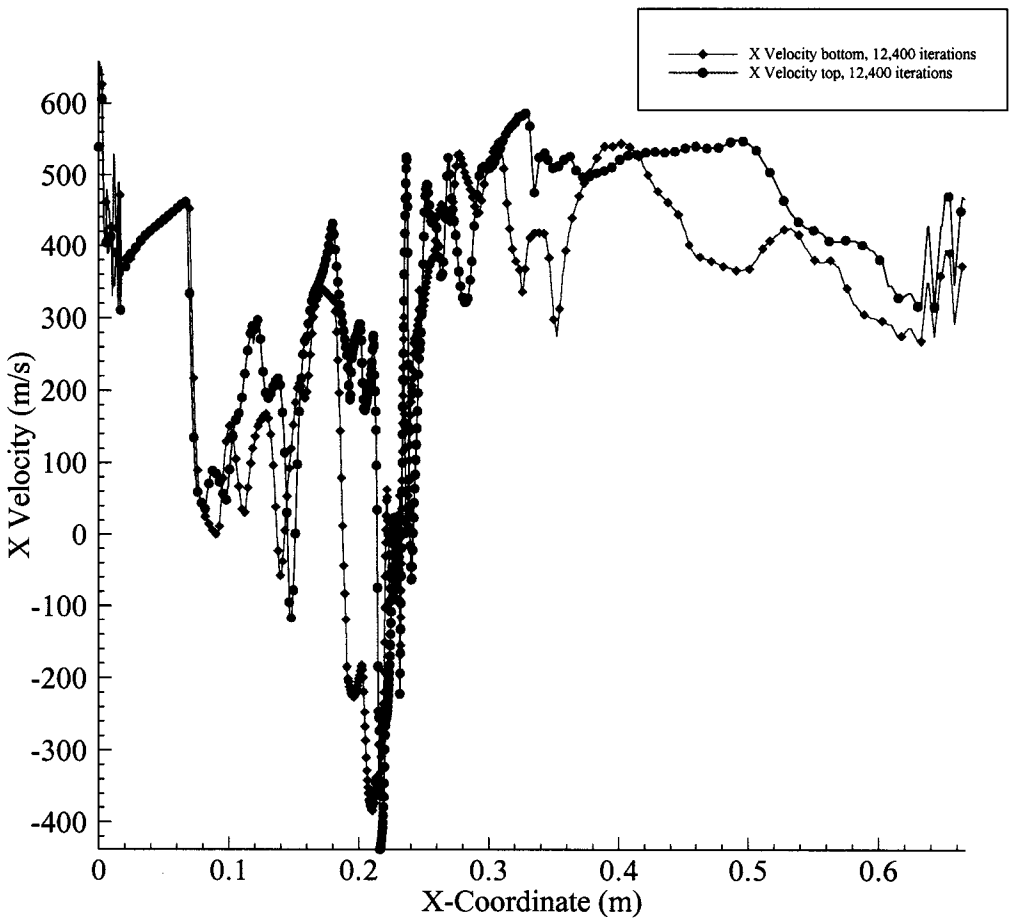

Figure 5.30 X velocity plot comparison after 12,400 iterations, sudden expansion study, $Po_j/P=240.4$.

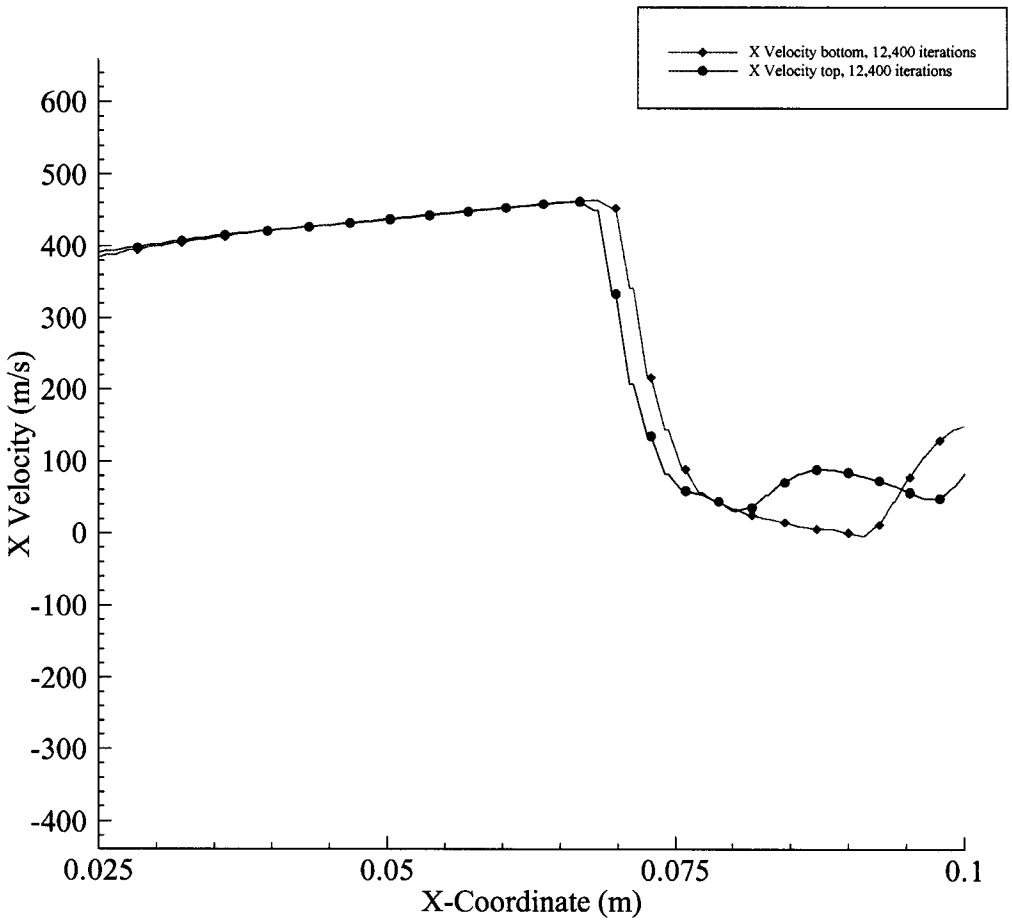

Figure 5.31 X velocity plot showing boundary layer separation after 12,400 iterations, sudden expansion study, Po_j/P=240.4.

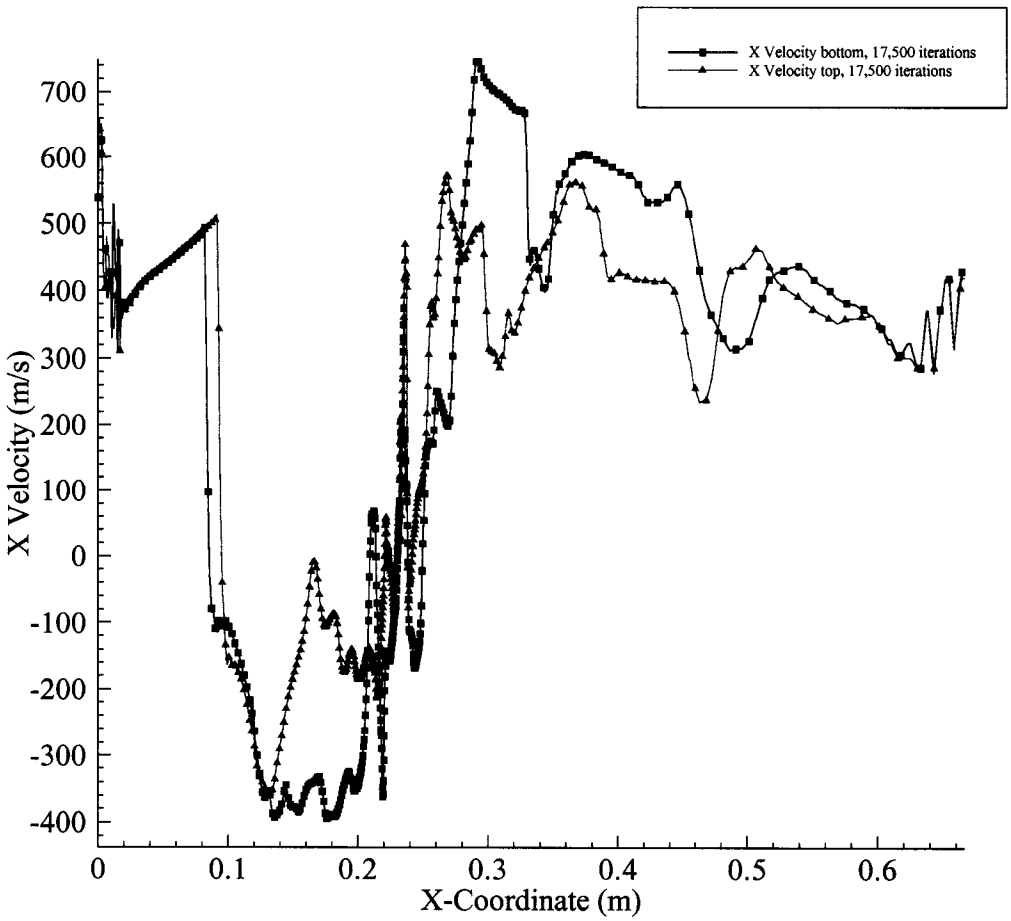

Figure 5.32 X velocity plot comparison after 17,500 iterations, sudden expansion study, Po_i/P=240.4.

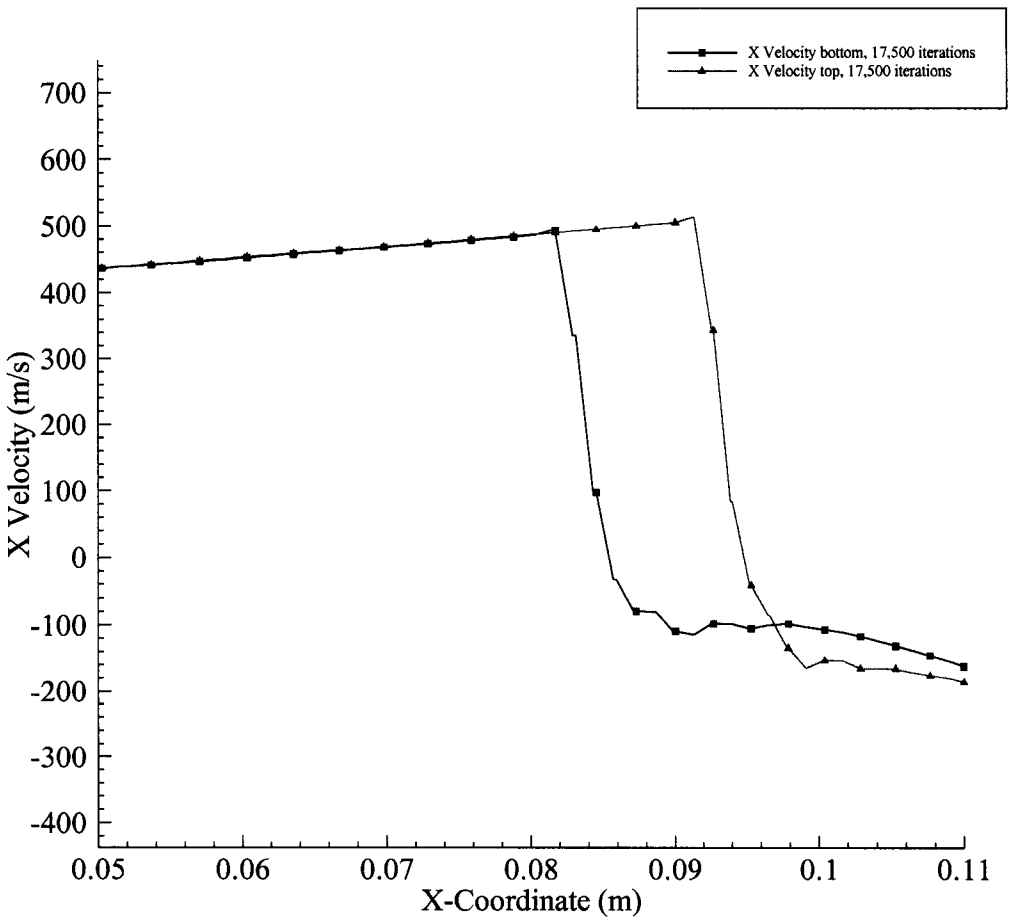

Figure 5.33 X velocity plot showing boundary layer separation after 17,500 iterations, sudden expansion study, Po_j/P=240.4.

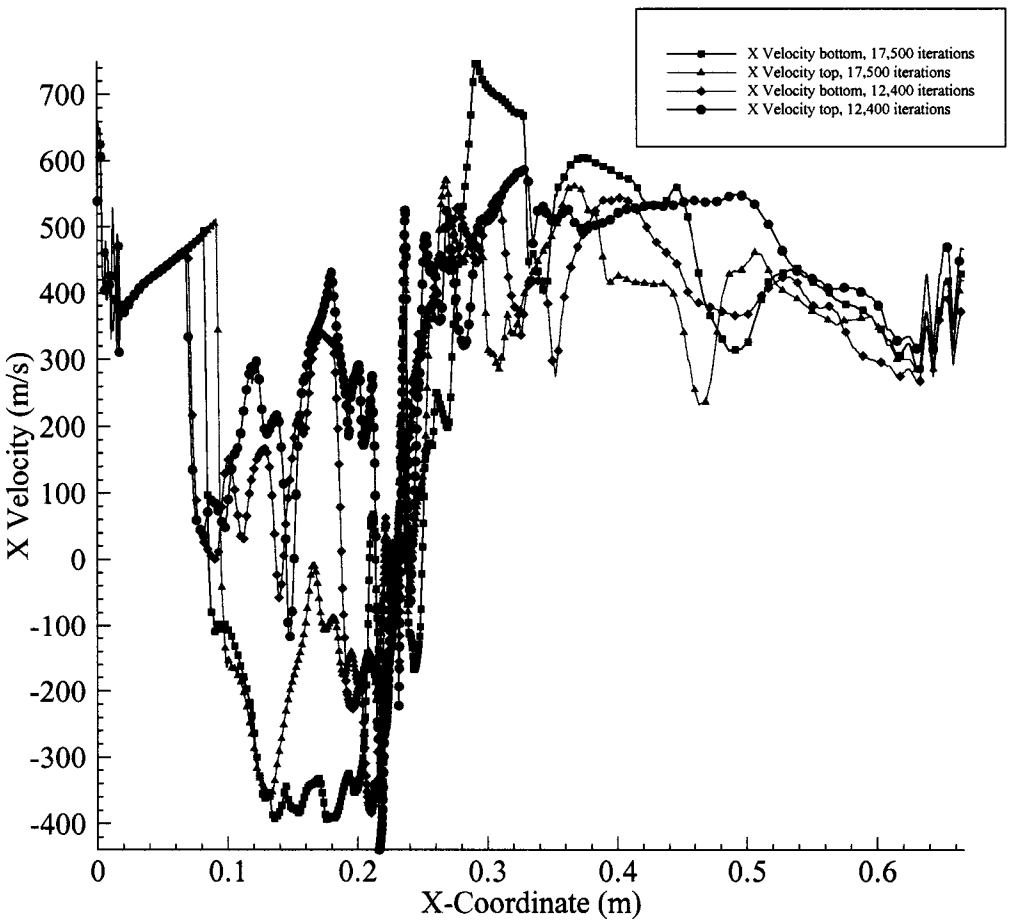

Figure 5.34 X velocity plot comparison, sudden expansion study, Po_j/P=240.4.

5.2.3 $Po_j/P=480.8$ Results

Boundary conditions of the $Po_j/P=480.8$ sudden expansion numerical model is shown in Table 5.3. Results are taken after 8,200 iterations and 8,500 iterations. Mach number contours are given in Figs. 5.35 and 5.36. Notice the injector barrel shocks in the injections are spread out farther than in the previous injector-to-freestream pressure ratio numerical models. The asymmetry is defined in both iteration cases.

Normalized static pressure contours are presented in Figs. 5.37 and 5.38. The classic separation shocktrain is present. Notice the presence of a normal shock forming at the sudden expansion steps. There is a large pressure rise to verify this. Again the recompression shock downstream shows asymmetry as well.

Figures 5.39 and 5.40 show the mole fraction of nitrogen. The upstream interaction convects the nitrogen upstream. Mole fractions in the recirculation regions are much greater than in previous models. This can be attributed to the higher injector-to-freestream pressure ratio. Mixing in the injector region is good. Nitrogen penetration is shown almost across the entire sudden expansion height.

Velocity along the x-axis is given in Figs 5.41 and 5.42. Large recirculation bubbles are shown in both models. The 8,500 iteration models recirculation region is so large that both the upper and lower recirculating regions extend across the entire isolator domain. The incoming air is allowed through however due to the large separation the flowfield is slowed greatly. Notice that the injectors due to the much larger injector-to-freestream pressure ratio have a larger "fan" than in previous models.

In Figs. 5.43-5.45 the normalized static pressure is plotted versus the x-axis. Again we see the classic pressure increase due to the separation shock. The bottom separates first in the 8,200 iteration model as compared to the top separating first in the 8,500 iteration model. Downstream of the injectors, the plots oscillate at a nearly constant rate with the upper and lower plots being in fair agreement with each other.

Velocity along the x-axis is shown in Figs. 5.46-5.50. Figures 5.47 and 5.49 show the boundary layer separation points. We see that for the 8,200 iteration model the lower plots separates at approximately 0.120m and the upper plot separates at approximately 0.1325m. The difference here is 0.0125m. For the 8,500 model we find that the upper plot

Table 5.3 Boundary conditions for sudden expansion case P_o/P=480.8

	Freestream Air	Nitrogen Injectant
M	3.5	1.0
P_t (kPa)	60.157	379.901
P_s (kPa)	0.789	200.637
T_t (K)	314.44	291.67
T_s (K)	91.67	243.33
Velocity (m/s)	670.56	317.906

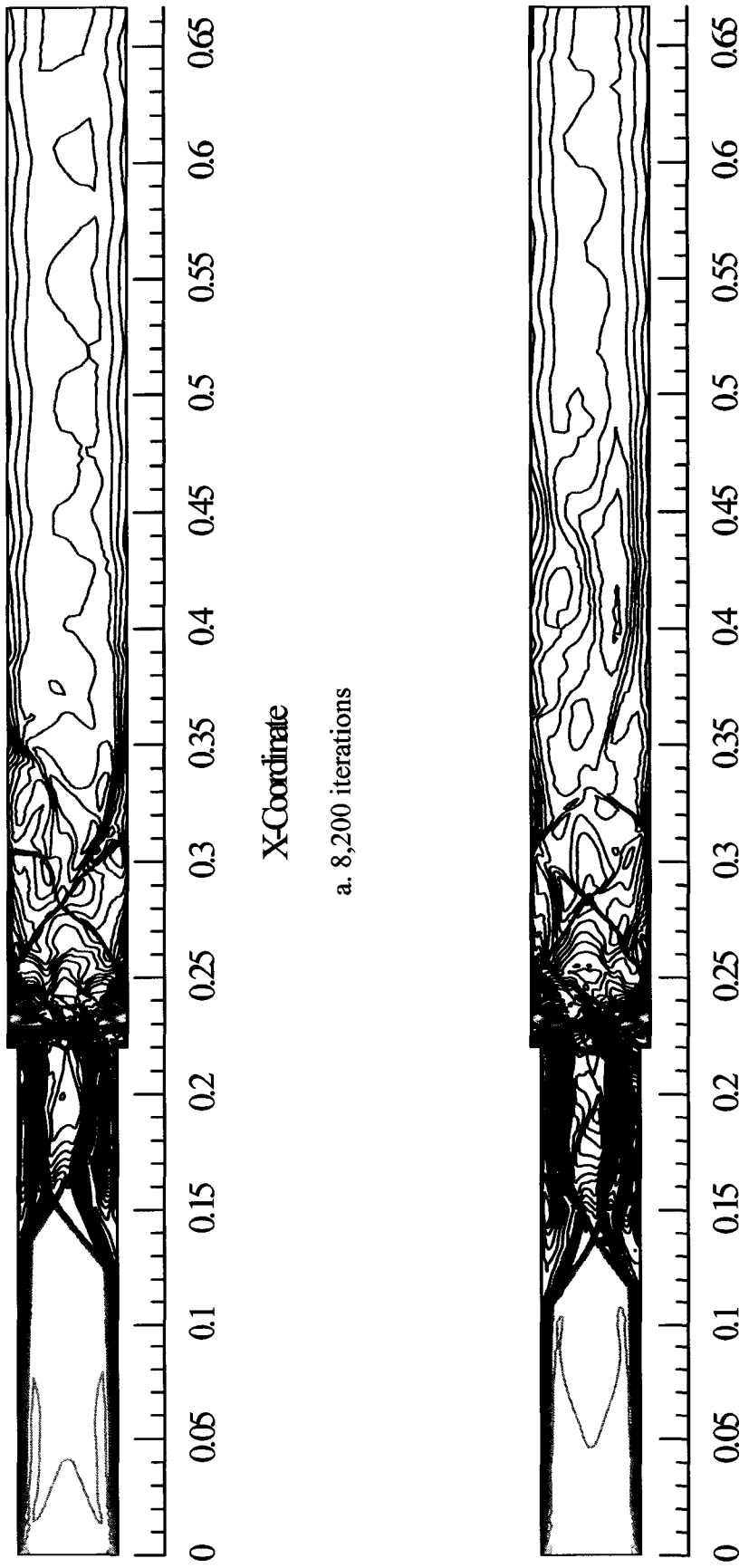

a. 8,200 iterations

b. 8,500 iterations

Figure 5.35 Mach number contour plots for the entire sudden expansion domain, Po_j/P=480.8.

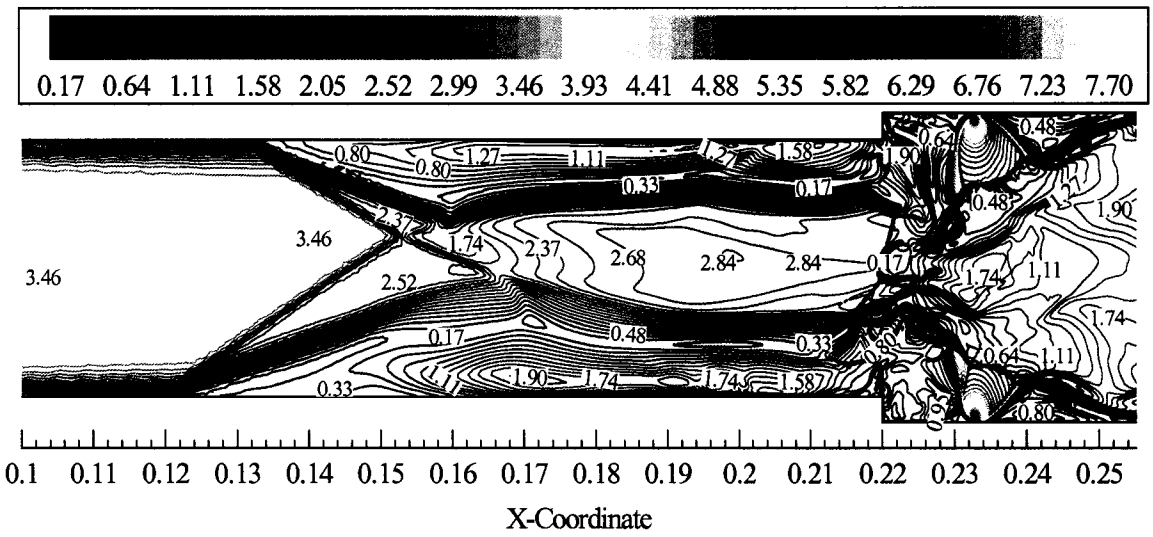

a. 8,200 iterations

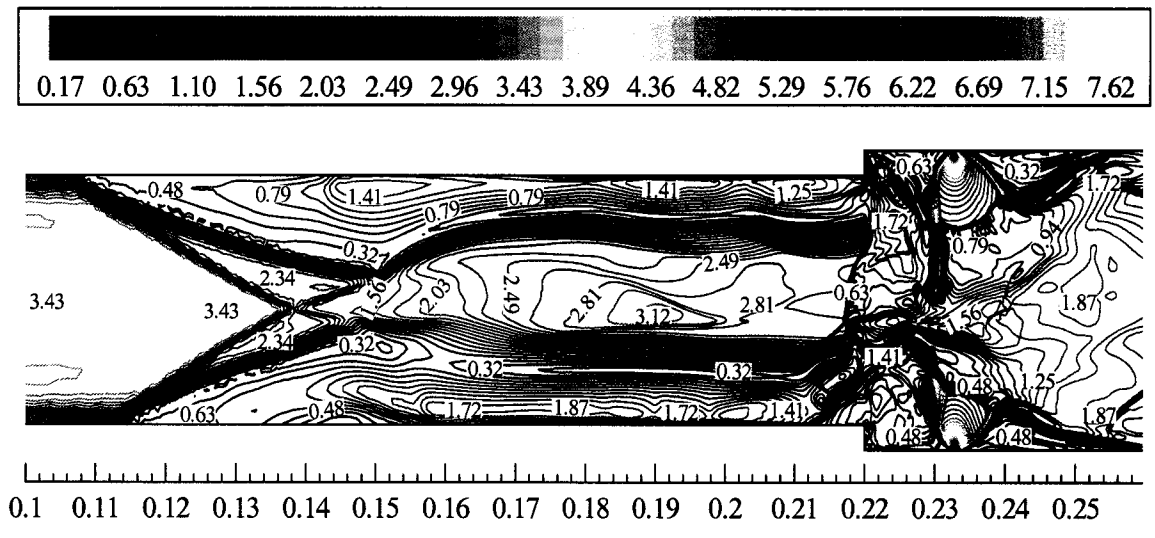

b. 8,500 iterations

Figure 5.36 Mach number contours for sudden expansion case, Po_j/P=480.8.

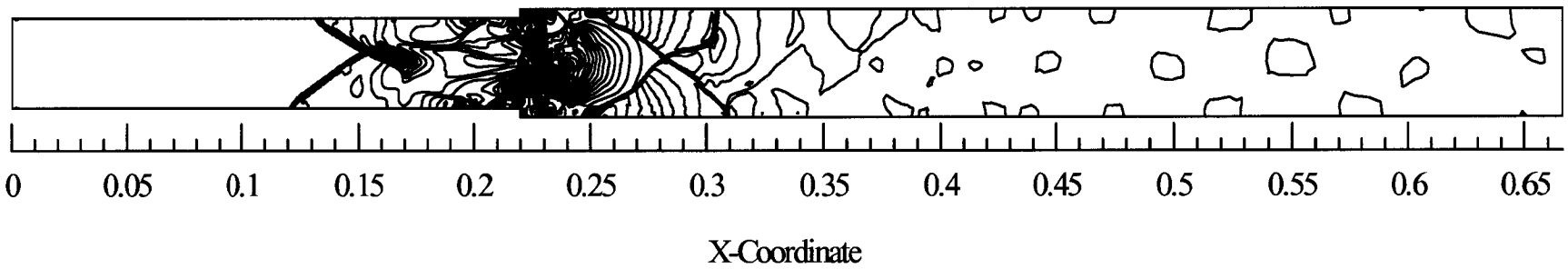

a. 8,200 iterations

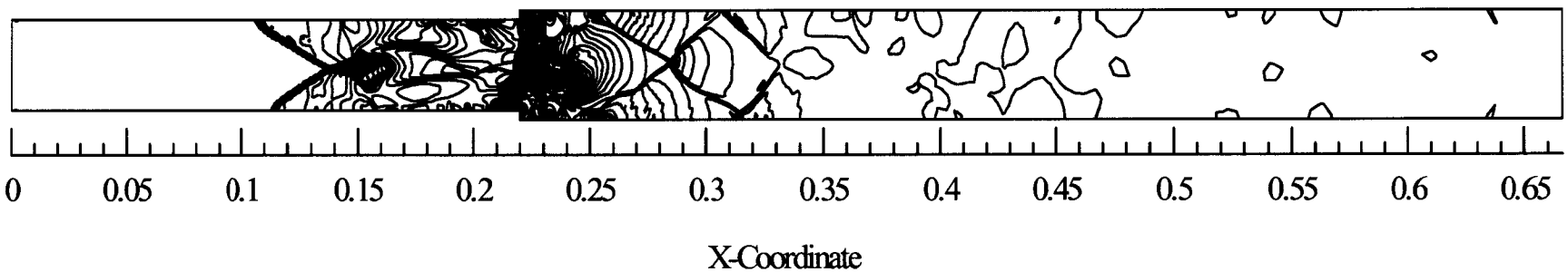

b. 8,500 iterations

Figure 5.37 Normalized static pressure contour plots for the entire sudden expansion domain, Po_j/P=480.8.

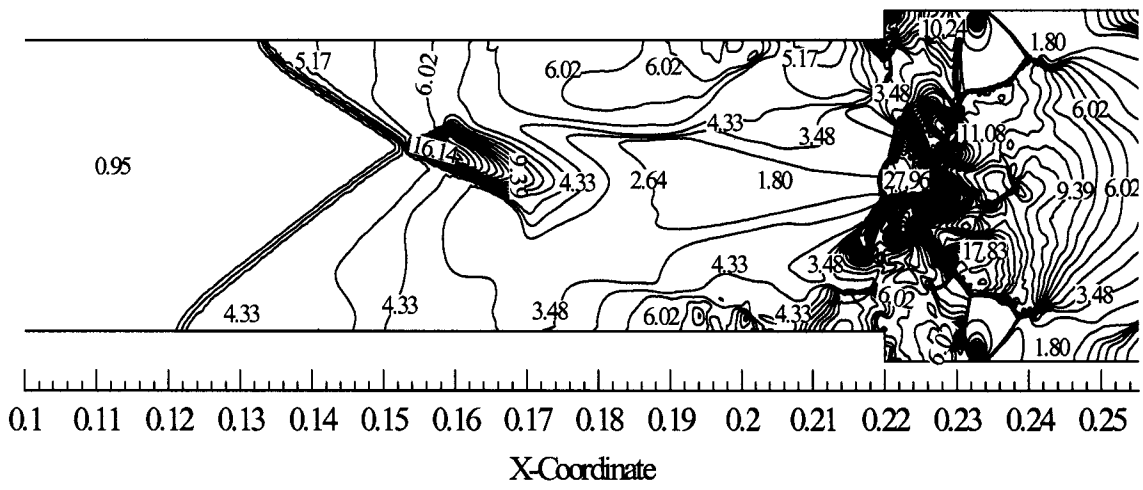

a. 8,200 iterations

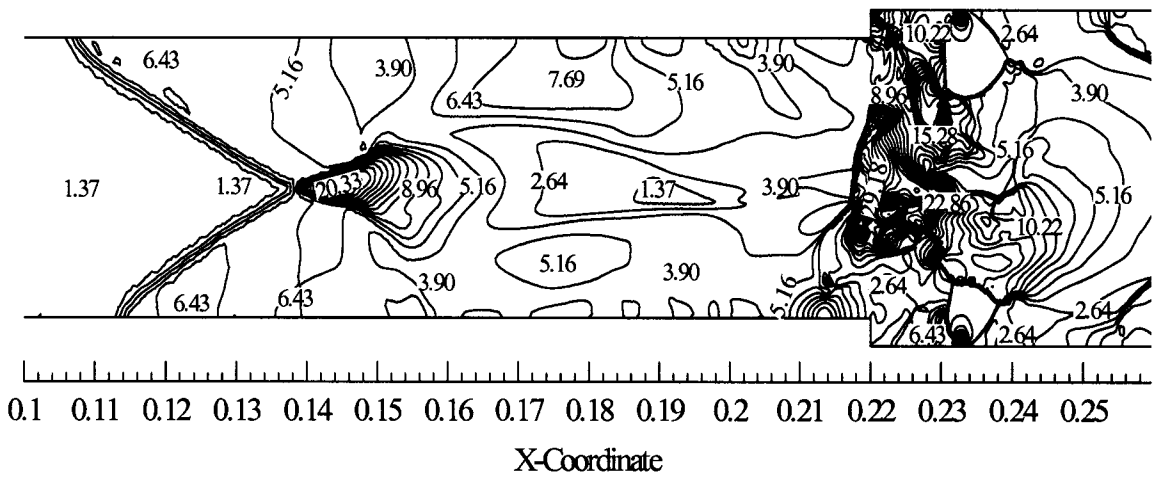

b. 8,500 iterations

Figure 5.38 Normalized static pressure contours for sudden expansion case, Po_j/P=480.8.

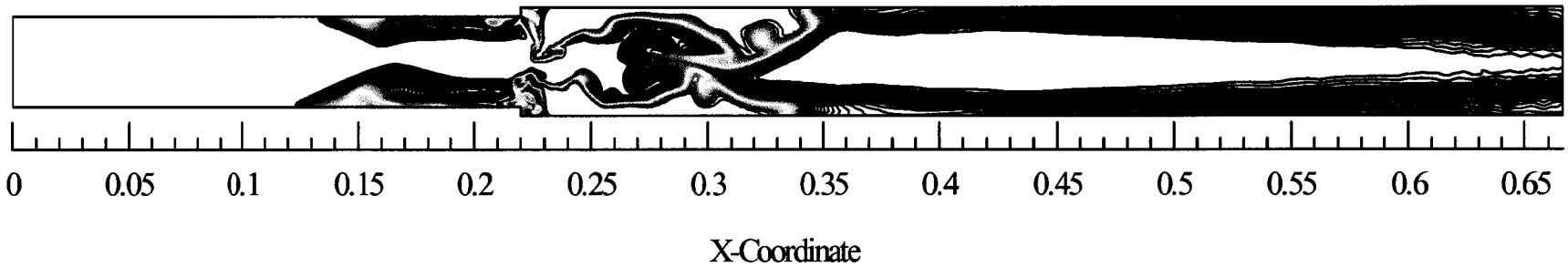

a. 36,300 iterations

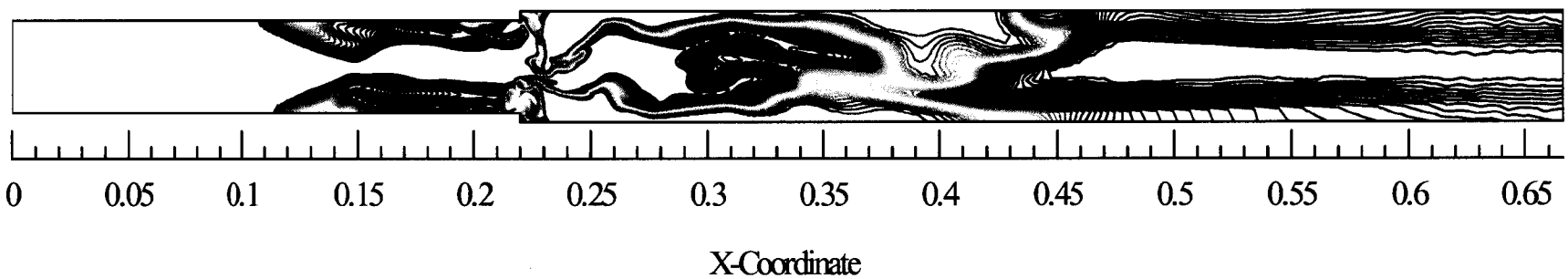

b. 37,000 iterations

Figure 5.39 Mole fraction of N_2 contour plots for the entire sudden expansion domain, Po_j/P=480.8.

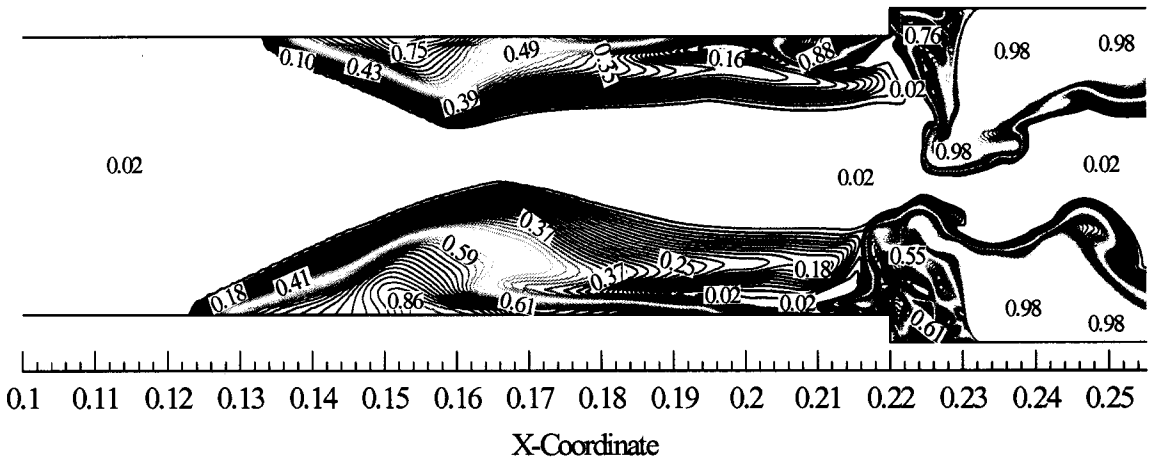

a. 8,200 iterations

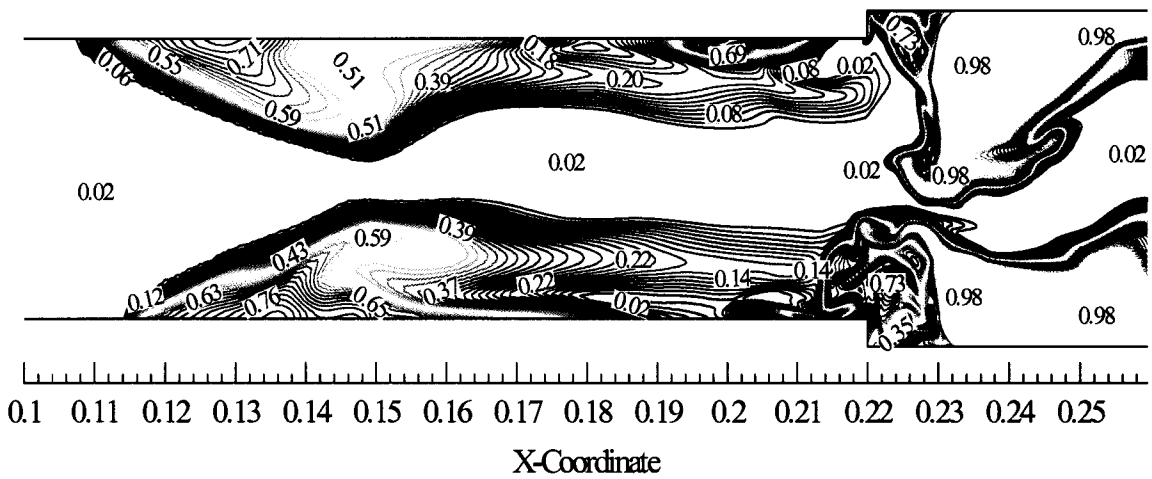

b. 8,500 iterations

Figure 5.40 Mole fraction of N_2 contours for sudden expansion case, Po_j/P=480.8.

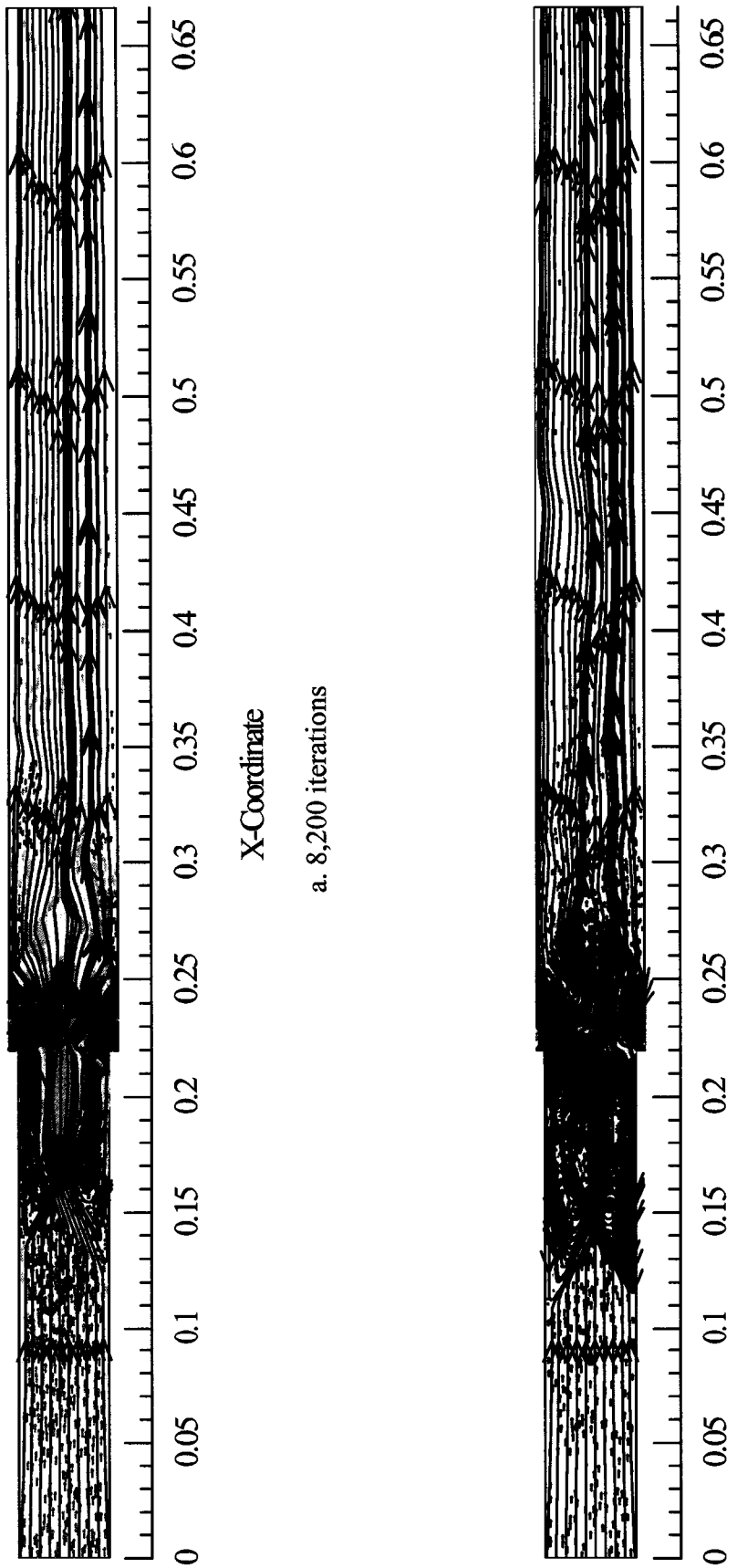

Figure 5.41 Velocity vector and streamline plots for the entire sudden expansion domain, Po_j/P=480.8.

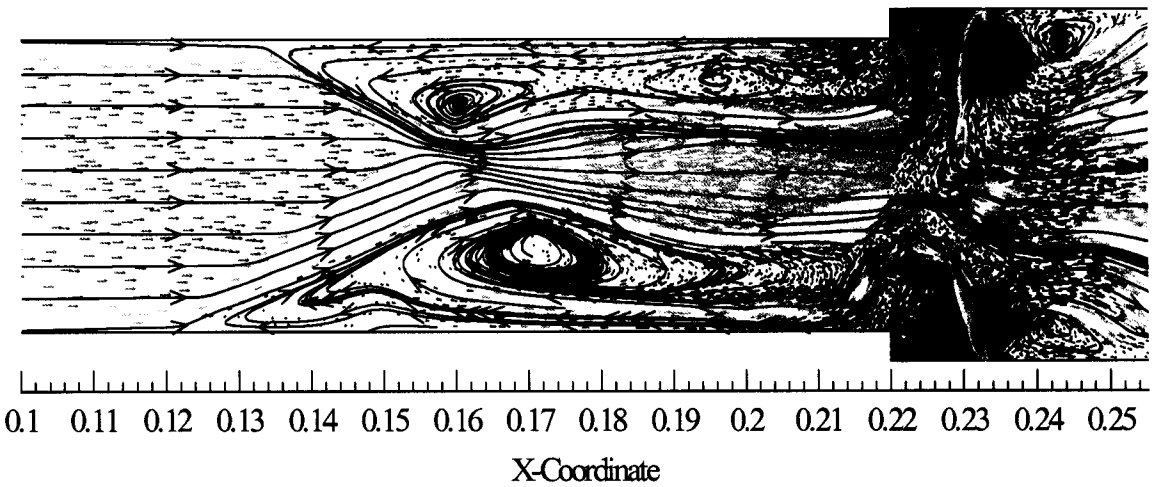

a. 8,200 iterations

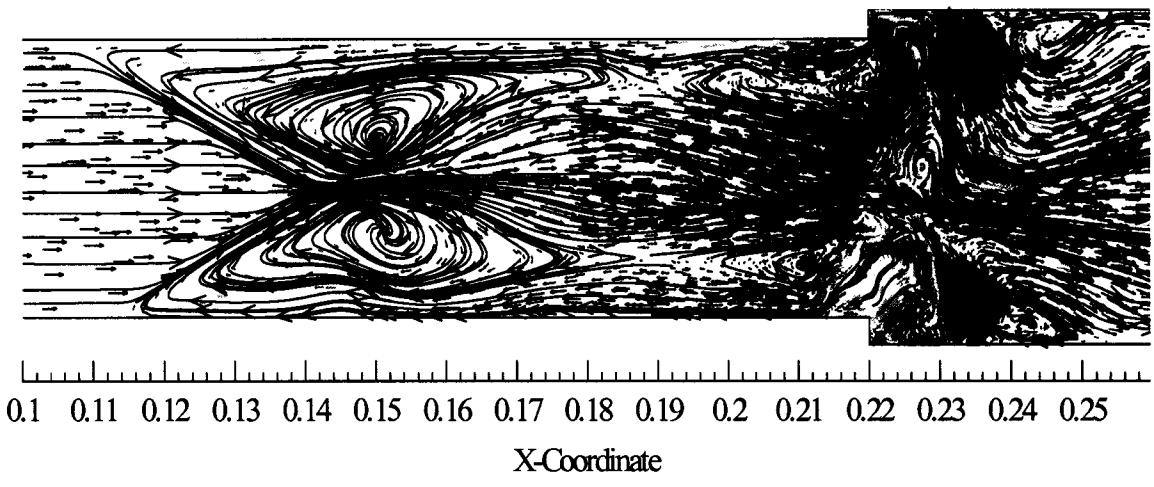

b. 8,500 iterations

Figure 5.42 Velocity vector and streamline plots for sudden expansion case, $Po_j/P=480.8$.

separates at approximately 0.1025m and the lower plot separates at approximately 0.110m. The difference between the two is 0.0075m.

The change from the upper to lower wall can be attributed to the flowfield buckling due to the high pressure rise and turbulent instability in the shock/shock interaction region. As the model iterated, the upstream interaction moved upstream within the isolator close to the leading edge then retreated leeward into the isolator. This cycle continue until the numerical model was stopped. The injected nitrogen blocks the flowfield causing the separated flow causing this phenomenon. As the separated flowfield continues upstream, it interacts with the freestream incoming air. The two reach an equilibrium point where then the separated flow retreats back into the isolator. The comparison of all the sudden expansion numerical models show that as the injector-to-freestream ratio is increased, asymmetry due to the separation shocktrain is present. It has been proven here that by using a non-reacting scheme the asymmetry is present as compared to other studies where reacting flows had been used.

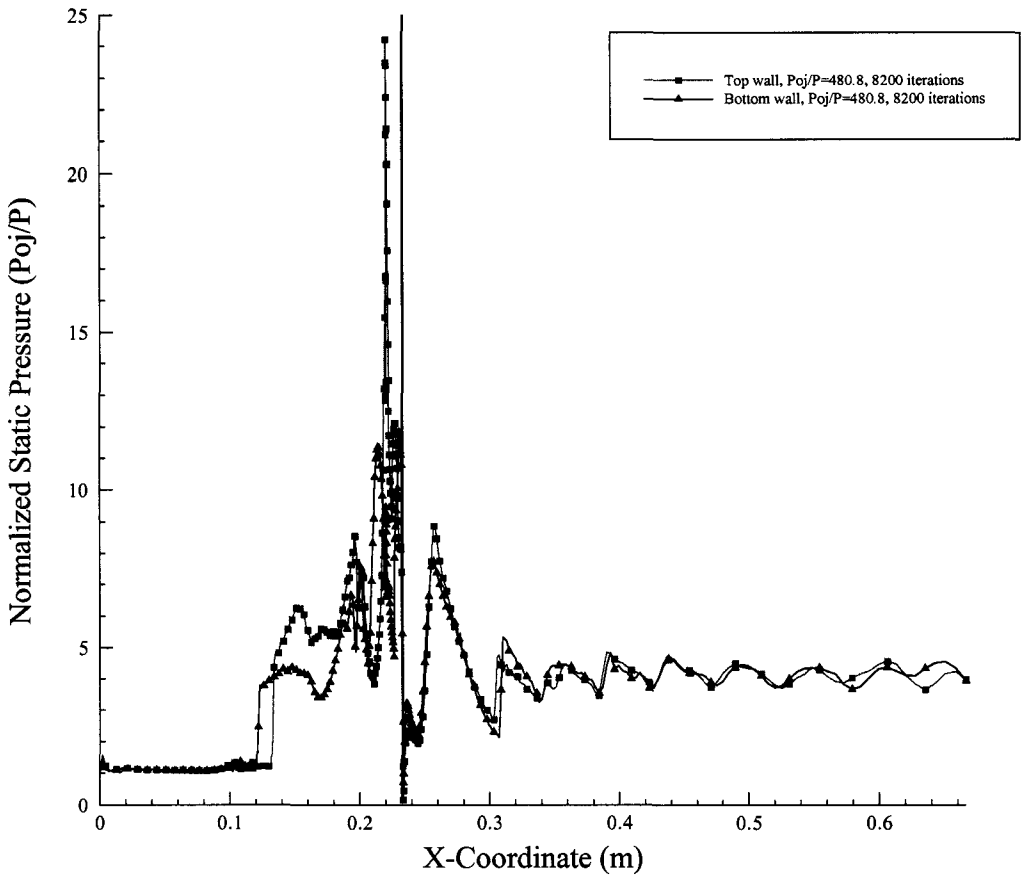

Figure 5.43 Normalized static pressure plot after 8,200 iterations, sudden expansion study, P_{oj}/P=480.8.

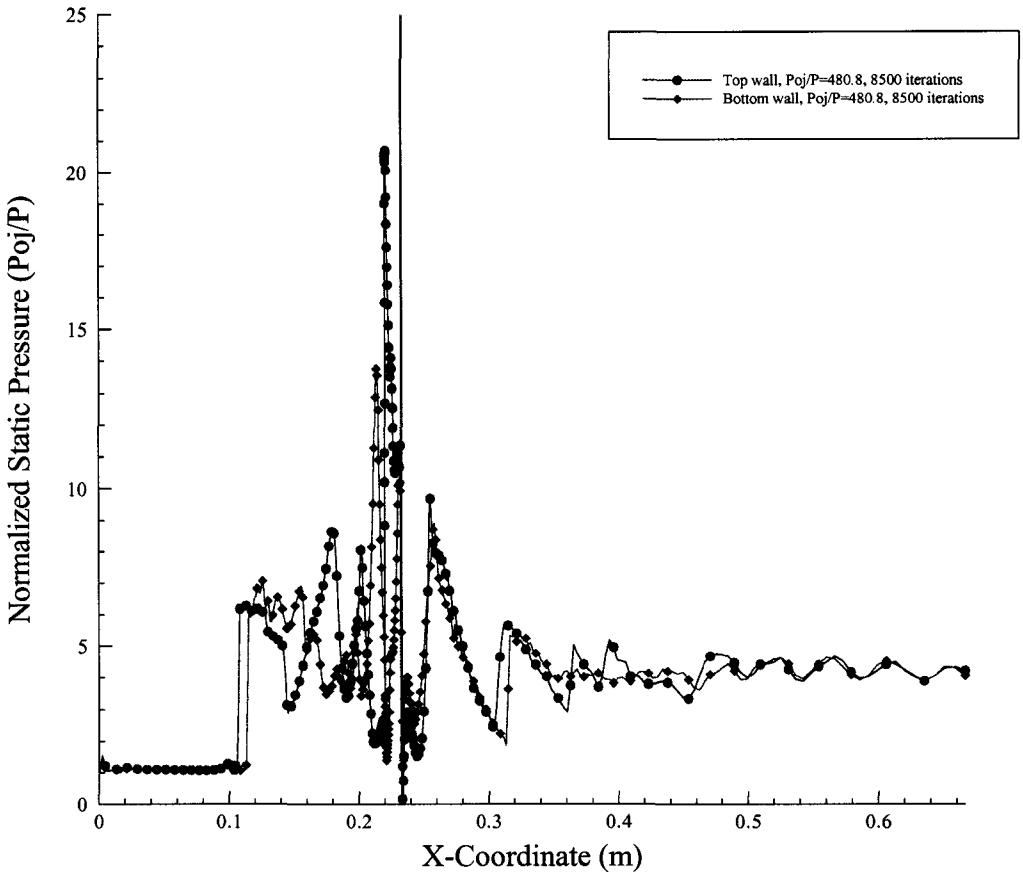

Figure 5.44 Normalized static pressure plot after 8,500 iterations, sudden expansion study, P_{oj}/P=480.8.

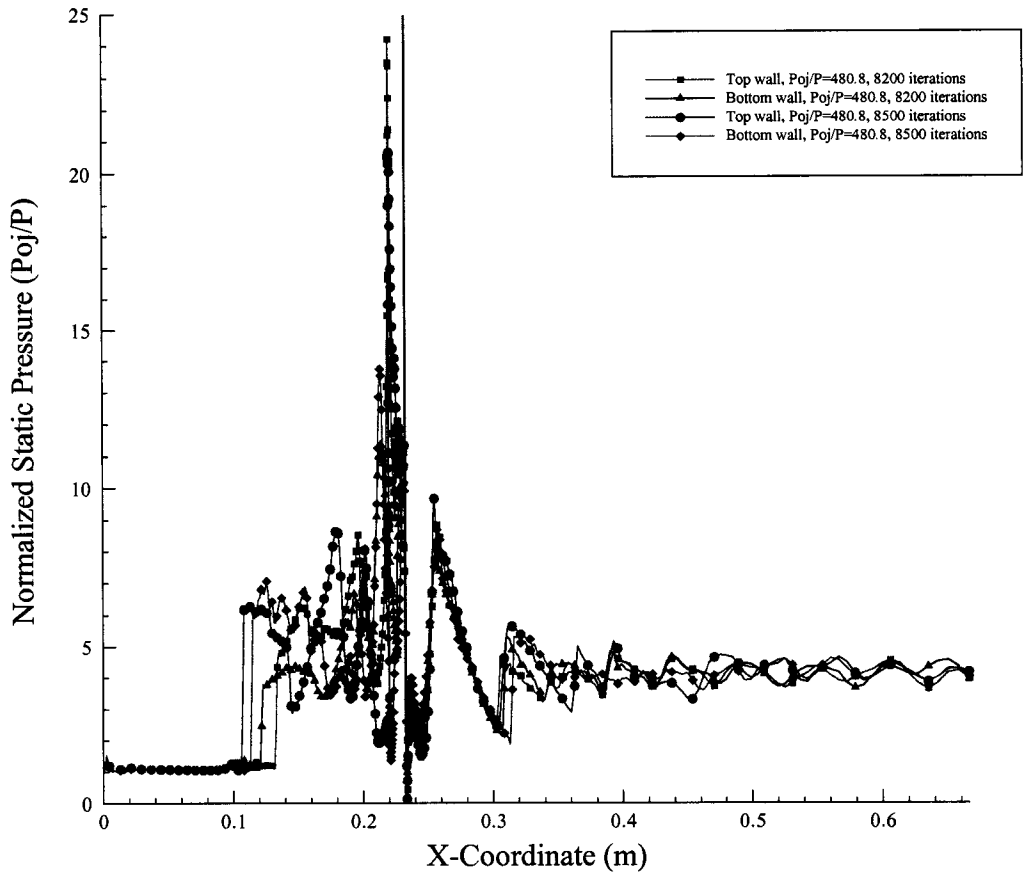

Figure 5.45 Combined normalized static pressure plot, sudden expansion study, P_{oj}/P=480.8.

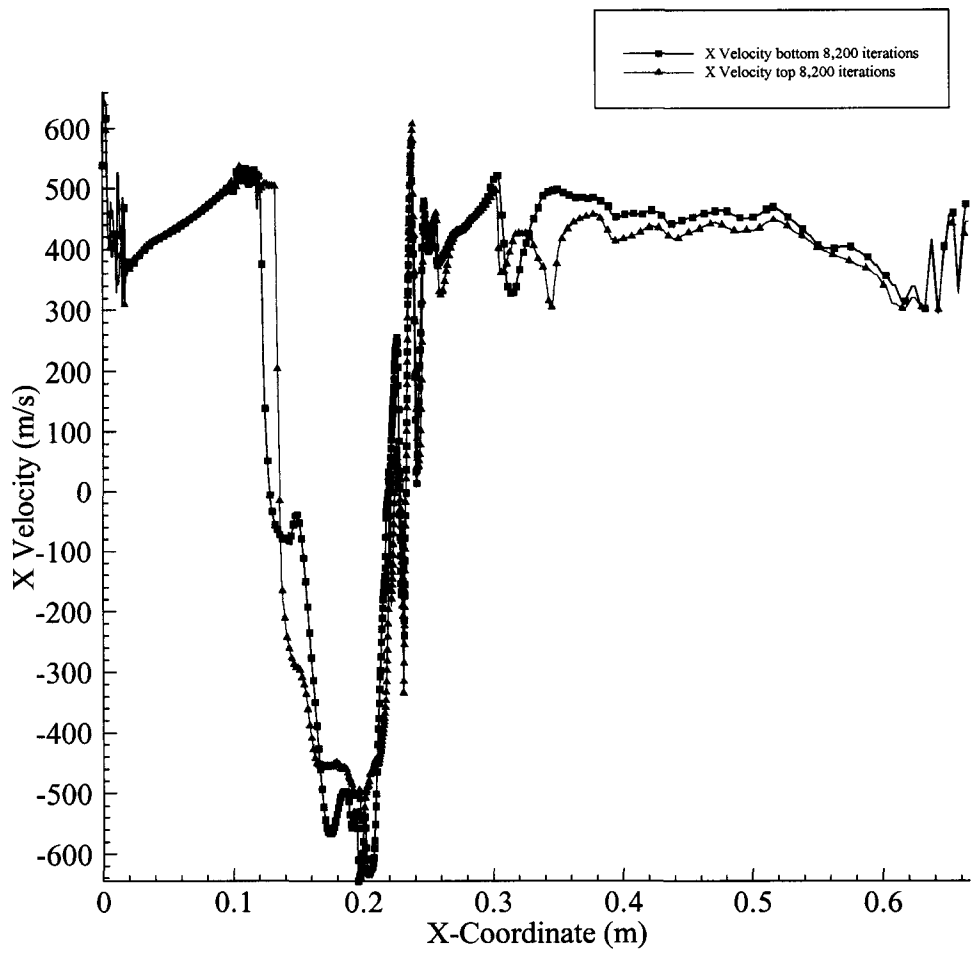

Figure 5.46 X velocity plot comparison after 8,200 iterations, sudden expansion study, Po_j/P=480.8.

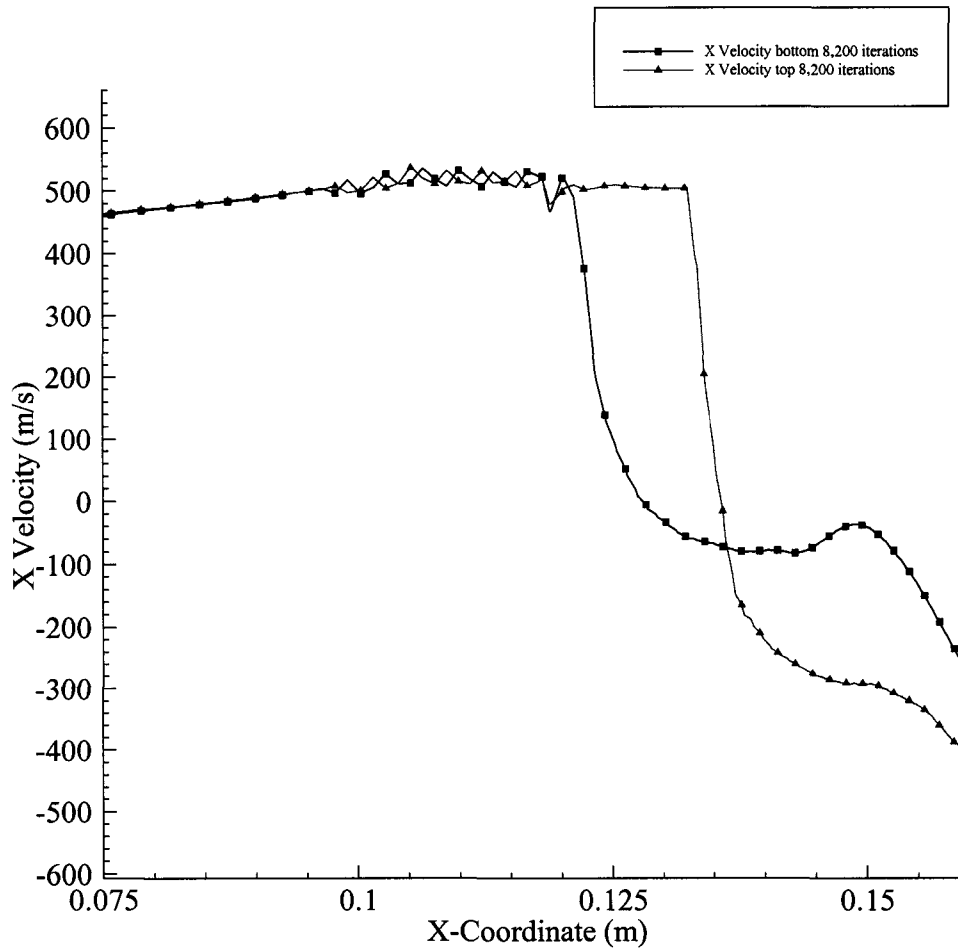

Figure 5.47 X velocity plot showing boundary layer separation after 8,200 iterations, sudden expansion study, Po_j/P=480.8.

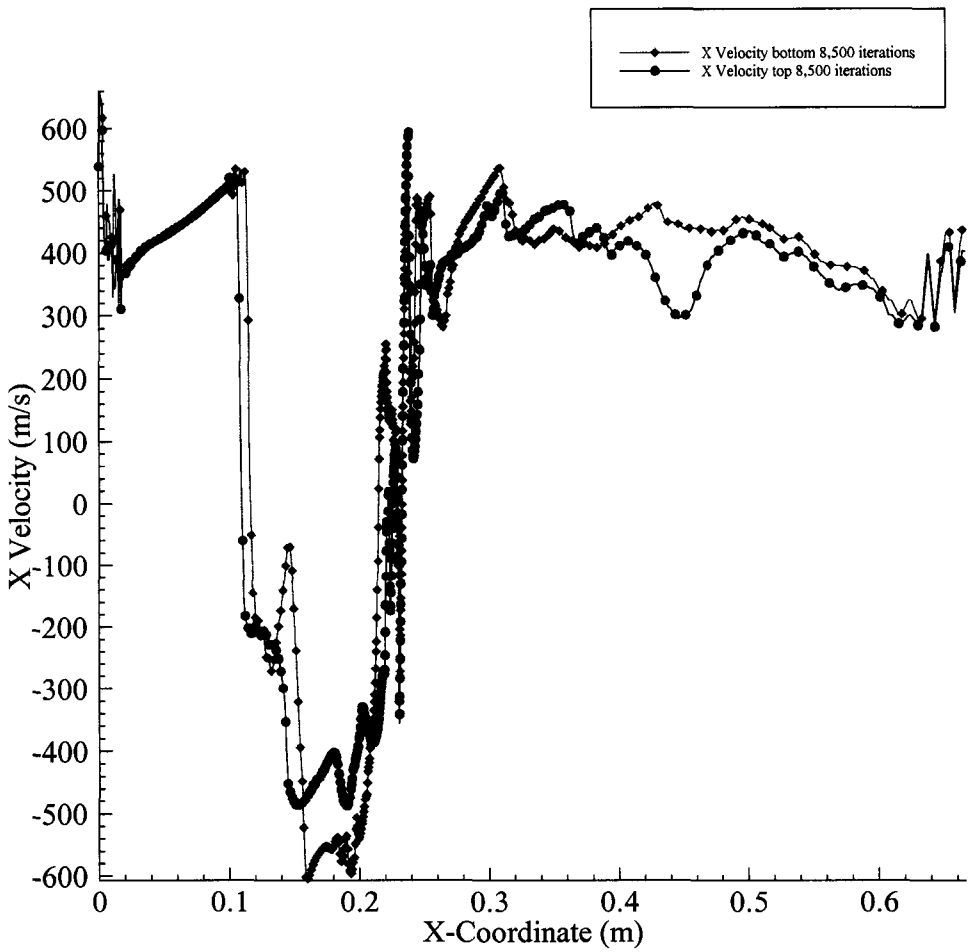

Figure 5.48 X velocity plot comparison after 8,500 iterations, sudden expansion study, Po_j/P=480.8.

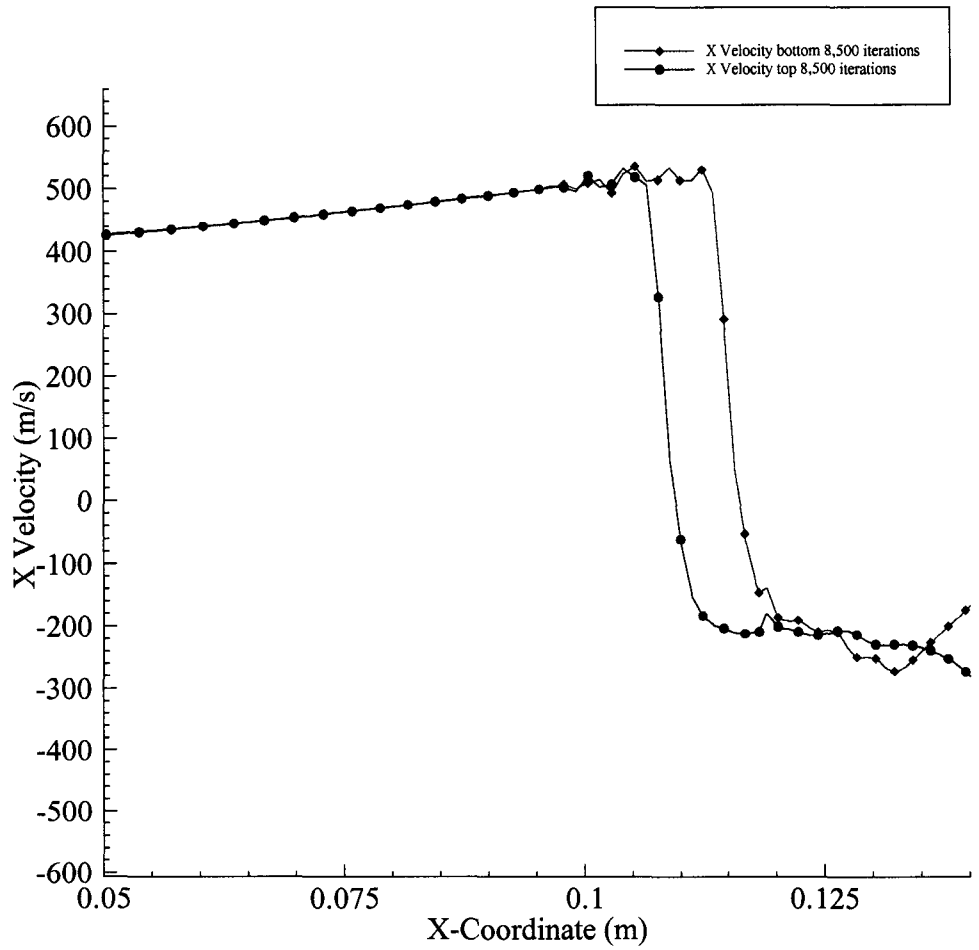

Figure 5.49 X velocity plot showing boundary layer separation after 8,500 iterations, sudden expansion study, Po_i/P=480.8.

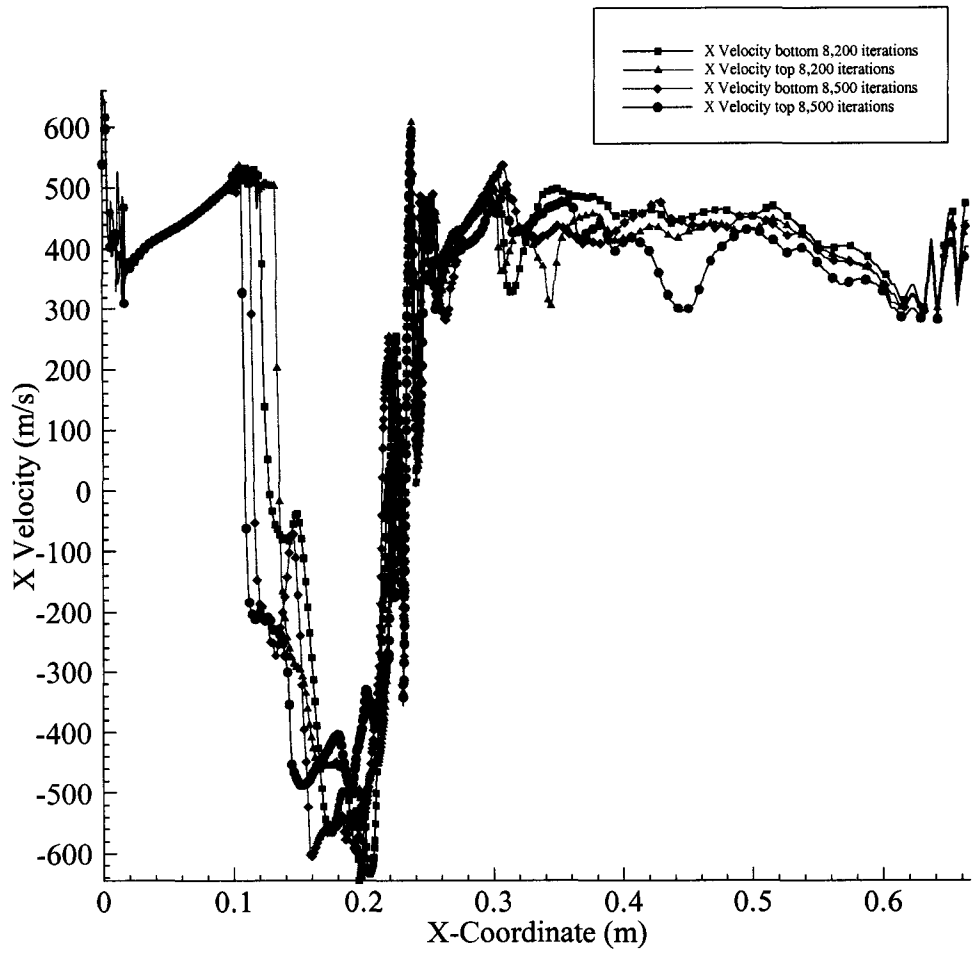

Figure 5.50 X velocity plot comparison, sudden expansion study, Po_j/P=480.8.

Numerical computation has been conducted using sudden expansion geometry. This geometry is a modified version of JNAL scramjet engine. Boundary conditions are the same as the constant area duct. The symmetry assumption has broken down in all studies. Also as the numerical convergence continues the separation would "jump" from one wall to the other. Meaning the asymmetry would be longer on one wall and shorter on the other and then after iterating the asymmetry would "flip". Changes in pressure within the separation region causing shear stresses within the boundary layer could be the culprit causing the asymmetry. The upstream interaction length increased as the freestream-to-injector pressure ratio increased. This was also shown in the constant area duct. The presence of the steps creates much more apparent asymmetric results. Just as in the constant area duct the same assumptions of why the upstream interaction occurs are that the turbulent shear stresses embedded within the boundary layer separation help create the separation and pressure or velocity fluctuations in the circulation regions and downstream help create the asymmetry. Improvements in this study could include:

1. Introducing a backpressure at the exit to investigate how this affects the upstream interaction.
2. Using a diffusing duct after the injectors. In other words using the original JNAL geometry.
3. Using various freestream-to-pressure ratios.
4. Changing the injector angle or position.
5. Increasing or decreasing injectant velocity

SECTION 6

CONCLUSION AND RECOMMENDATIONS

The use of Computational Fluid Dynamics (CFD) has been used to investigate all studies in the manuscript. The main purpose of this thesis was to investigate the upstream interaction caused by either injecting a gas into the freestream or by introducing a backpressure at the exit. Two-dimensional analysis has been presented using constant area duct, sudden expansion, and a test section with diffusing walls geometries. The constant area duct used both a symmetry wall assumption and a full domain assumption. The JNAL sudden expansion study produced asymmetric upstream interaction results. What was found during this study is listed below:

1. The use of a cold flow, or non-reacting flowfield showed that the upstream interaction symmetry assumption breaks down. Previous investigation[44] has believed this to be related to the viscous shear stresses within the boundary layer separation region.
2. As the freestream-to-pressure ratio increased, the upstream interaction length moved upstream eventually reached an equilibrium position and then began to move back downstream until reaching another equilibrium point and then switching direction to start the process over again.
3. Comparison of X velocity plots showed in detail the point of separation and thus showing the symmetry breakdown.
4. Numerical convergence was impossible to achieve due to the large oblique shock wave interactions.
5. Experimental data showed excellent agreement with numerical results for the $Po_j/P=120.2$ constant area duct study. Thus, we are allowed to assume that further numerical investigation will produce results similar to actual experimental results if and when conducted.
6. As numerical converging continued, it was shown in the sudden expansion studies that the upstream interaction length varied from on wall to the other. Meaning, the length of separation would "switch" or "jump" from the upper wall to the lower wall.

7. Flow blockage created by the separation regions and flowfield perturbations may contribute to the breakdown of the symmetry assumption.
8. Due to the symmetry breakdown, it would be wise to numerically simulate the entire domain to achieve correct results.
9. Further investigation using three-dimensional analysis would be beneficial in investigating the upstream interaction.

REFERENCES

1. Rogers, R.C., Capriotti, D.P., and Guy, R.W., "Experimental Supersonic Combustion Research at NASA Langley," AIAA Paper 98-2506, June 1998.
2. Fischer, K.E., Huebner, L.D., McClinton, C.R., Voland, R.T., and Witte, D.W., "Hyper-X Engine Design and Ground Test Program," AIAA 98-1532, April 1998.
3. Huebner, L.D., Rock, K.E., Rogers, R.C., and Voland, R.T., "NASA'S Hyper-X Scramjet Engine Ground Test Program," ISABE Paper 99-7214, September 1999.
4. Bittner, R.D., Cockrell, C.E., Dilley, A.D., Engelund, W.C., Frendi, A., and Jentink, T.N., "Integrated Aero-Propulsive CFD Methodology for the Hyper-X Flight Experiment," AIAA Paper 2000-4010, August 2000.
5. Crawford, J.L., McClinton, C.R., and Rausch, V.L., "Hyper-X: Flight Validation of Hypersonic Airbreathing Technology," ISABE Paper 97-7024, September 1997.
6. Freeman, D.C., McClinton, C.R., Rausch, V.L., and Reubush, D.E., "The NASA Hyper-X Program," 48th International Astronautical Congress, Turin, Italy, October 1997.
7. Matsuo, Y., Mizobuchi, Y., and Ogawa, S., "Parallel Numerical Simulation of Compressible Free Shear Layers in a Scramjet Engine," AIAA Paper 98-0963, January 1998.
8. Mohieldin, T., Olynciw, M., and Tiwari, S., "Convergence-Acceleration Technique for Dual-Mode Combustors Simulation," HX Report HX-845, October 2000.
9. Abdel-Salam, T.M., Mohieldin, T.O., and Tiwari, S.N., "Three-Dimensional Numerical Study of a Scramjet Combustor," AIAA Paper 2002-0805, January 2002.
10. Abdel-Salam, T.M., Mohieldin, T.O., and Tiwari, S.N., "Analysis of a Dual-Mode Scramjet Combustor," AIAA Paper 2001-3194, July 2001.
11. Abdel-Salam, T.M., Chaturvedi, S.K., Mohieldin, T.O., and Tiwari, S.N., "Mixing and Combustion in Scramjet Combustor with Raised and Relieved Ramps," AIAA Paper 2000-3709, July 2000.

12. Riggins, D.W., Rodriguez, C.G., and White, J.A., "Three-Dimensional Effects in Modeling of Dual-Mode Scramjets," AIAA Paper 2000-3704, July 2000.
13. Komuro, T., Kudo, K., Masuya, G., Chinzei., Murakami, A., and Tani, K., "Experiment on a Rectangular Cross Section Scramjet Combustor," National Aerospace Lab, NAL TR-1068, Tokyo, Japan, 1990.
14. Murakami, A., Komuro, T., and Kudo, K., "Experiment on a rectangular Cross Section Scramjet Combustor," National Aerospace Lab, NAL TR-1220, Tokyo, Japan, 1990.
15. Murakami, A., Komuro, T., and Kudo, K., "Experiment on a Rectangular Cross Section Scramjet Combustor (II)-Effects of Fuel Injector Geometry," National Aerospace Lab, NAL TR-1220, Tokyo, Japan, 1993.
16. Spaid, F.W., and Zukoski, E.E., "Secondary Injection of Gases into a Secondary Flow," *AIAA Journal*, Vol. 2, No. 10, Oct. 1964, pp.1689-1696.
17. Spaid, F.W., and Zukoski, E.E., "A Study of the Interaction of Gaseous Jets from Transverse Slots with Supersonic External Flows," *AIAA Journal*, Vol. 6, No. 2, Feb. 1968, pp. 205-212
18. Billig, F.S., and Schetz, J.A., "Penetration of Gaseous Jets Injected into a Supersonic Stream," *AIAA Journal*, Vol. 3, No 11, Nov. 1966, pp.1658-1665.
19. Billig, F.S., Lasky, M, and Orth R.C., "A Unified Analysis of Gaseous Jet Penetration," *AIAA Journal*, Vol. 9, No. 6, Jan.1971, pp. 1048-1058.
20. Billig, F.S., Orth, R.C., and Schetz, J.A., "The Interaction of Gaseous Jets in Supersonic Flow," NASA CR-1386, August 1965.
21. Povinelli, F.P., and Povinelli, L.A., "Correlation of Secondary Sonic and Supersonic Gaseous Jet Penetration into Supersonic Crossflows," NASA TN D-6370, June 1971.
22. Aso, A., and Okuyama, S., "Experimental Study on Mixing Phenomena in Supersonic Flows with Slot Injection," AIAA Paper 91-0016, January 1991.
23. Ando, Y., Aso, S., Fujimori, T., and Okuyama, S., "Two-Dimensional and Three-Dimensional Mixing Flow Fields in Supersonic Flow Induced by Injected Secondary Flows Through Transverse Slot and Circular Nozzle," AIAA Paper 93-0489, January 1993.

24. Aso, S., Kawano, S., and Inoue, K., "Experimental and Computational Studies on Two-Dimensional Supersonic Mixing Flow Physics," AIAA Paper 2002-0236, January 2002.
25. Toda, K., and Yamamoto, M., "Computation of Supersonic Turbulent Flowfield with Secondary Jet Normal to Freestream," AIAA Paper 98-0944, January 1998.
26. McClinton C.R., and Riggins, D.W., "Analysis of Losses in Supersonic Mixing and Reacting Flows," AIAA Paper 91-2266, June 1991.
27. Gerlinger, P., Algermissen, J., and Bruggemann, D., "Numerical Simulation of Mixing for Turbulent Slot Injection," *AIAA Journal*, Vol. 34, No. 1, Jan. 1996, pp. 73-78.
28. Holderman, J.D., Liscinsky, D.S., and True, B., "Experimental Investigation of Crossflow Jet Mixing in a Rectangular Duct," AIAA Paper 93-2037, June 1993.
29. Holderman, J.D., Liscinsky, D.S., True, B., and Vranos, A., "Experimental Study of Cross-Stream Mixing in a rectangular Duct," AIAA Paper 92-3090, July 1992.
30. Rizzetta, D., "Numerical Simulation of Slot Injection into a Turbulent Supersonic Stream," AIAA Paper 92-0827, January 1992.
31. Grasso, F., Magi. V., "Simulation of Transverse Gas Injection in Turbulent Supersonic Air Flows," *AIAA Journal*, Vol. 33, No. 1, Jan. 1995, pp. 56-62.
32. Ben-Yakar, A., Kamel, M., Morris, C., and Hanson, R.K., "Experimental Investigation of H_2 Transverse Jet Combustion in Hypervelocity Flows," AIAA Paper 97-3019, July 1997.
33. Baurle, R.A., Gruber, M.R., and Tam, C-J., "Numerical Study of Jet Injection into a Supersonic Crossflow," AIAA Paper 99-2254, June 1999.
34. Kallenberg, M., Von Lavante, E., and Zeitz, D., "Numerical Simulation of Supersonic Air Flow with Transverse Hydrogen Injection," AIAA Paper 99-4902, November 1999.
35. Hubbard, D.G., Lin, M., and Papamoschou, D., "Observations of Supersonic Transverse Jets," AIAA Paper 91-1723, June 1991.
36. Chocinski, D., Hachemin, J.V., and Leblanc, R., "Experimental/Computational Investigation of Supersonic Jet in Subsonic Compressible Crossflow," AIAA Paper 97-0714, January 1997.

37. Rodriguez, C.G., "Two-Dimensional, Compressible-Flow Test-Cases for the Validation of the VULCAN Flow-Solver," HX Report HX-763, November 1999.
38. Chen, T.H., Dutton, J.C., Gruber, M.R., and Nejad, A.S., "Bow Shock/Jet Interaction in Compressible Transverse Injection Flowfields," *AIAA Journal*, Vol. 34, No. 10, pp. 2191-2193.
39. Chrans, L.J., and Collins, D.J., "Stagnation Temperature and Molecular Weight Effects in Jet Interaction," *AIAA Journal*, Vol. 8, No. 2, Feb. 1970, pp. 287-293.
40. Barber, M.J., Schetz, J.A., and Roe, L.A., "Normal, Sonic Helium Injection Through a Wedge-Shaped Orifice into Supersonic Flow," *Journal of Propulsion and Power*, Vol. 13, No. 2, March-April 1997, pp. 257-263.
41. Drummond, J.P., and Weidner, E.H., "Numerical Study of Staged Fuel Injection for Supersonic Combustion," *AIAA Journal*, Vol. 20, No. 10, Oct. 1982, pp. 1426-1431.
42. Bowersox, R.B.W., Butler, T.A., and Meyer, M.J., "Compressible Turbulence Measurements in a Supersonic Boundary Layer with Impinging Shock Wave Interaction," AIAA Paper 97-0427, January 1997.
43. Rodriguez, C.G., "Asymmetry Effects in Numerical Simulation of Supersonic Flows with Upstream Separated Regions," AIAA Paper 2001-0084, January 2001.
44. Yang, S.Y., "Adaptive Refinement of the Supersonic Flow over a Backward-Facing Step," AIAA Paper 2001-3741, July 2001.
45. Ghia, K.N., and Papp, J.L., "Application of the RNG Turbulence Model to the Simulation of Axisymmetric Supersonic Separated Base Flows," AIAA Paper 2001-0727, January 2001.
46. Graves, J., Jr., and McDaniel, J.C., "Laser-Induced-Fluorescence Visualization of Transverse Gaseous Injection in a Nonreacting Supersonic Combustor," *AIAA Journal*, Vol. 4, No. 6, Nov.-Dec. 1988.
47. Durst, W.C., and Whitelaw, J.H., "Asymmetric Flows and Instabilities in Symmetric Ducts with Sudden Expansions", *Journal of Fluid Mechanics*, Vol. 84, 1978, pp. 13-31.

48. Abbott, D.E., and Kline, S.J., "Experimental Investigation of Subsonic Turbulent Flow Over Single and Double Backward Facing Steps", *Journal of Basic Engineering*, Sep. 1962, pp. 317-325.
49. Uenishi, K., Rogers, R.C., and Northam, G.B., "Three-Dimensional Numerical Predictions of the Flow Behind a Rearward-Facing Step in a Supersonic Combustor", AIAA Paper 87-1962, July 1987.
50. GAMBIT. Vers. 2.0. Computer Software. Fluent Inc., 1988-2001. IBM PC-WINNT 4.0, CD-ROM.
51. FLUENT User's Guide., Lebanon, NH: FLUENT, Inc, December 2001.
52. Dutton, D.C., and Carroll, B.F., "Characteristics of Multiple Shock Wave/Turbulent Boundary-Layer Interactions in Rectangular Ducts", *Journal of Propulsion*, Vol. 6, No. 2, March-April 1990, pp. 186-193.

BIOGRAPHY

Stephen Cromwell Coghill was born June 26th, 1975 in Richmond, Virginia. He graduated from Essex High School in Tappahannock in 1993. After two years at Rappahannock Community College in Warsaw, Virginia he transferred to Old Dominion University and was accepted in the mechanical engineering technology program. Stephen graduated in the summer of 1999 with his bachelor of science in mechanical engineering technology. He was one of four ODU engineering students chosen to participate at ODU's sister university Kyushu Institute of Technology in Kitakyushu Japan in an engineering design competition to design a friendlier blind man's cane.

In the fall of 1999 he was accepted into the mechanical engineering graduate program. He was awarded a research grant from NASA Langley Research Center in Hampton, Virginia to complete his thesis research. He worked part time at NASA Langley and at ODU while he was a graduate student. His research was associated with the Hyper-X program at NASA LaRC. He has also co-authored the following publications:

Mohieldin, T.O., Coghill, S.C., Carson, R., Luetke, N., Tiwari, S.N., "Numerical Study of Two- Dimensional Dual- Mode Scramjet Combuster", AIAA Paper 2003-7036, December 2003.